THE APPLICATION OF MAX-DOAS TO THE MEASUREMENT OF TROPOSPHERIC GASES AND AEROSOLS IN MARINE AND CONTINENTAL ENVIRONMENTS

JAMIE D. HALLA

A DISSERTATION SUBMITTED TO THE FACULTY OF GRADUATE STUDIES
IN PARTIAL FULFILMENT OF THE REQUIREMENTS
FOR THE DEGREE OF

DOCTOR OF PHILOSOPHY

GRADUATE PROGRAM IN CHEMISTRY
YORK UNIVERSITY
TORONTO, ONTARIO
JUNE 2013
© JAMIE D. HALLA, 2013

Abstract

Multi Axis Differential Optical Absorption Spectroscopy (MAX-DOAS) is a passive DOAS technique that uses scattered sunlight to determine differential slant column densities (DSCDs) of trace gas absorbers along multiple axes. MAX-DOAS measurements probe long path lengths, and when coupled with a radiative transfer model (RTM) to determine the average light path travelled, MAX-DOAS has the potential to yield trace gas vertical column densities (VCDs), aerosol optical depths, and trace gas and aerosol layer heights. Determination of DSCDs and VCDs have advantages over point-source measurements in that they are more sensitive to the total atmospheric load of a pollutant, and are relatively insensitive to variations in the boundary layer height. Two Canadian field campaigns: one from Saturna Island, BC, located in the Strait of Georgia; the other from Ridgetown, ON, in southwestern Ontario; employed a MAX-DOAS instrument to obtain spectra that were analyzed to yield DSCDs of NO_2, O_4 and HCHO. The measured spectra from Ridgetown were also compared to RTM calculations to yield NO_2 VCDs, aerosol

optical depths, and gas and aerosol layer heights. The method of determining NO_2 VCDs in this way was validated for the first time by comparison to composite VCDs derived from aircraft and ground-based measurements of NO_2, satellites, and a chemical model. The usefulness of the MAX-DOAS technique was extended further, using both DSCDs and VCDs, to include the interpretation of pollutant transport at Saturna and Ridgetown, and to provide an example of fumigation of elevated industrial pollutants brought to the surface at a lake breeze front at Ridgetown.

Acknowledgements

While working on this Ph.D. was, at times, a solitary task, I received a lot of support along the way. First and foremost I would like to acknowledge my primary supervisor, Dr. Robert McLaren. Without his support and guidance this thesis would not be possible. Next I would like to thank Dr. Thomas Wagner, my IMPRS advisor, for his help and advice in particular with regards to the details of DOAS analysis, radiative transfer modelling, and for welcoming me into his group during several research trips to Germany. Thanks to Dr. Jan Bottenheim for acting as my co-supervisor, and Dr. Geoff Harris for making up the third member of my regular thesis committee and introducing me to the IMPRS program, where I was honoured to work with DOAS experts in both Heidelberg and Mainz, including Dr. Ulrich Platt, whose hospitality was much appreciated. Dr. Jeff Brook must also be acknowledged for his valuable advice and guidance during the analysis of the BAQS-Met data set while I was a RAP student at EC, and Dr. Mark Wenig for his collaborations and guidance with respect to satellite DOAS. Furthermore, special

thanks to my examination committee including Dean's representative, Dr. Jochen Rudolph, my external examiner, Dr. Greg Evans from U of T, and my internal examiner Dr. Yongsheng Chen from Earth and Space Science and Engineering.

I must also thank my lab colleagues past and present. It has been a pleasure to work with and get to know them all: Ibraheem, Patryk, Zoë, Dan, Joy, Charlie, Nick, Pei, and the countless undergraduates who have came through our lab during my tenure as a Ph.D. candidate at York, plus the other members of the Centre for Atmospheric Chemistry and Chemistry, in particular Dr. Corinne Schiller, Carol Weldon, Mary Mamais, and Magy Baket, as well as Ryan D'Souza from U of T, Dr. Steffen Beirle from MPI-Mainz, Dr. Ossama Ibrahim from Heidelberg, Lok Chan from City U, and Dr. Jason O'Brien, Dr. Bruce Ainslie, and Kathy Hayden from EC. Dr. Carole Carpenter was and continues to be a true mentor, leader and friend, and I sincerely thank Dr. René Fourier for believing in me and giving me the opportunity to work with such great people. I am grateful for his help and am positive I would not have made it to this point without his efforts on my behalf! Special thanks to the brave few (Zoë and Riad) who proofread my entire thesis.

Most importantly, on a personal level I need to thank all my friends and family for supporting me throughout my studies and life. To my beautiful wife Oana and son Hudson you both bring me unbelievable happiness and have motivated me to be a better man. This thesis is dedicated to you both!

Table of Contents

List of Tables

List of Figures

Abbreviations

A - Attenuation factor

AERONET - AErosol RObotic NETwork

agl - *a*bove *g*round *l*evel

AMF - Air Mass Factor

AOD - Aerosol Optical Depth

asl - *a*bove *s*ea *l*evel

AURAMS - A Unified Regional Air-quality Modelling System

AVDC - Aura Validation Data Center

BAQS-Met - Border Air Quality and Meteorology Study

BLH_{eff} - effective Boundary Layer Height

CFCs - ChloroFluoroCarbons

CCD - Charge Coupled Device

COSPEC - COrrelation SPECtrometer

DAMF - Differential Air Mass Factor

$DAMF_{box}$ - Differential box Air Mass Factor

DANDELIONS - Dutch Aerosol and Nitrogen Dioxide Experiments for Validation of OMI and SCIAMACHY

DC - Dark Current

DOAS - Differential Optical Absorption Spectroscopy

DOASIS - DOAS Intelligent System

DMS - DiMethyl Sulphide

DSCD - Differential Slant Column Density

EA (α) - Elevation Angle

EC - Environment Canada

EDT - Eastern Daylight Time

ENVISAT - ENVIronmental SATellite

FRS - Fraunhofer Reference Spectrum

FWHM - Full Width Half Maximum

GEM - Global Environmental Multi-scale model

GEO - GEOmetrical approximation

GVRD - Greater Vancouver Region District

IT - Integration Time

LAADS - Level 1 and Atmospheric Archive and Distribution System

LED - Light-Emitting Diode

LFV - Lower Fraser Valley

LIDAR - LIght Detection And Ranging

MAX-DOAS - Multi AXis Differential Optical Absorption Spectroscopy

MBL - Marine Boundary Layer

MCARaTS - Monte Carlo Atmospheric Radiative Transfer Simulator

McArtim - Monte carlo Atmospheric radiative transfer inversion model

MODIS - MODerate resolution Imaging Spectroradiometer

OME - Ontario Ministry of the Environment

OMI - Ozone Monitoring Instrument

PAN - Peroxyl Acetyl Nitrate

PDT - Pacific Daylight Time

PM - Particulate Matter

$PM_{2.5}$ - Particulate Matter with aerodynamic diameter of up to 2.5 μm

PMT - PhotoMultiplier Tube

R - Residual

RASCAL - Rapid Acquisition SCanning Aerosol LIDAR

RAZI (ϕ) - Relative AZImuth angle

RSS - Residual Sum of Squares

RTM - Radiative Transfer Model

SCD - Slant Column Density

SCIAMACHY - SCanning Imaging Absorption spectroMeter for Atmospheric CHartographY

SCIATRAN - SCIAMACHY radiative TRANsfer model

SMOKE - Sparse Matrix Operator Kernel Emissions

SSA - Single Scattering Albedo

SZA (ϑ)- Solar Zenith Angle

TEOM - Tapered Element Oscillating Microbalance

TOA - Top Of the Atmosphere

TOAc - Top Of the Aircraft

TRACY - Trace gas RAdiative Monte Carlo Y(I)mplementation

UTC - Co-ordinated Universal Time

VCD - Vertical Column Density

VOCs - Volatile Organic Compounds

WD - Wind Direction

WISE - Wake-Induced Stagnation Effect

WS - Wind Speed

1 Introduction

Significant atmospheric research focuses on several topics that are highly relevant in our society. News reports dedicated to global warming and climate change, air quality indices, smog and UV levels, and the adverse health effects caused by air pollution, are broadcast on a daily basis. There have been some recent success stories and breakthroughs, such as the banning of chlorofluorocarbons (CFCs), the discovery of the ozone hole, the general acceptance that climate change is a real possibility and the improvement of pollution controls in industry and vehicles. Yet, today's scientists are still faced with a great challenge in understanding the long-term consequences of human interaction with the complex atmosphere that surrounds our Earth.

Our atmosphere is composed of four distinct layers, classified according to the vertical temperature profile. Within these layers, the ozone chemistry of the stratosphere and troposphere is of critical importance to the well-being of humans. With decreased ozone in the stratosphere there is an increase in the likelihood of skin

cancer, as the ozone layer protects man from harmful UV radiation, while tropospheric ozone is a major component of smog and is linked to respiratory illness, crop damage and infrastructure damage.

Along with ozone, nitrogen dioxide is a key atmospheric trace gas species to be measured in the stratosphere and troposphere because it is directly linked to the ozone chemistry occurring in both layers.

1.1 Stratospheric Ozone Chemistry

1.1.1 Chapman Mechanism

Ozone (O_3) is a substance that plays a huge role in shaping life on Earth as we know it. The stratospheric ozone layer, centered approximately 20 km above the earth's surface is of critical importance to mankind, since it acts as a filter protecting life from the harmful UV radiation of the sun. Its presence was determined in the 1920s using observations of solar UV spectra. In 1930 the foundation of ozone formation and ozone destruction in this layer was proposed by British scientist Sydney Chapman. The Chapman mechanism (Reactions (R1)-(R6)) originates due to the photolysis of O_2, whereby only high energy photons found at high altitude

have sufficient energy to photolyze O_2:

$$O_2 + h\nu(\lambda < 240nm) \rightarrow O(^3P) + O(^3P) \quad \text{(R1)}$$

The ground level triplet state $O(^3P)$ radicals produced then react rapidly with O_2, and a third body (e.g. N_2 or O_2):

$$O_2 + O(^3P) + M \rightarrow O_3 + M \quad \text{(R2)}$$

The ozone produced can photolyze since O_3 bonds are weaker than those in O_2:

$$O_3 + h\nu(\lambda < 320nm) \rightarrow O_2 + O(^1D) \quad \text{(R3)}$$

$$O(^1D) + M \rightarrow O(^3P) + M \quad \text{(R4)}$$

The net reaction of (R3) and (R4) is:

$$O_3 + h\nu \rightarrow O_2 + O(^3P) \quad \text{(R5)}$$

while ozone may also combine with $O(^3P)$:

$$O_3 + O(^3P) \rightarrow 2O_2 \quad \text{(R6)}$$

Reactions (R2) and (R5) have been found to be significantly faster than Reactions (R1) and (R6). Since there is a rapid interchange between O and O_3 in the faster reactions, these species are defined as odd oxygen ($O_x \equiv O_3 + O$). Assuming a steady state of O atoms produced via Reaction (R5) and consumed in (R2)

while neglecting the slow Reactions (R1) and (R6), a steady state of ozone in the stratosphere may be governed by the following relationship:

$$\frac{[O]}{[O_3]} = \frac{k_5}{k_2 C_{O_2} n_{air}^2} \tag{1.1}$$

where k_5 and k_2 are the rate constants of Reactions (R5) and (R2), C_{O_2} is the mixing ratio of oxygen and n_{air} is the number density of air (Jacob, 1999). By substituting measured values into the above equation this ratio is found to be significantly less than one in the stratosphere (e.g. 5×10^{-5} at 20 km) and O_3 is found to be the main component of the O_x family. The concentration of O_3 is controlled by the slow Reactions (R1) and (R6) and the lifetime of O_3 versus chemical loss is defined by the lifetime of O_x. The maximum ozone number density according to the Chapman mechanism is found at a height of around 20-30 km, which reflects the vertical dependence of O production via photolysis and the decreasing O_2 levels as a function of height. However, using this mechanism alone to describe the ozone layer is flawed because it significantly overpredicts the actual O_3 number density observed, even though it successfully reproduces the general shape of the ozone layer.

1.1.2 HO_x Loss Cycle

In the late 1950s it was found that catalytic cycles initiated by the oxidation of water vapour could represent a significant ozone sink in the stratosphere. Water vapour is transported into the stratosphere from the troposphere, and is produced in the stratosphere from the oxidation of methane (CH_4). Levels are typically between 3-5 ppm, which is not significant enough for it to compete with a third body in reaction with $O(^1D)$, but the production of the hydroxy radical (OH) initiates the following catalytic loss cycle in which O_3 is destroyed:

$$H_2O + O(^1D) \rightarrow 2OH \tag{R7}$$

$$OH + O_3 \rightarrow HO_2 + O_2 \tag{R8}$$

$$HO_2 + O_3 \rightarrow OH + 2O_2 \tag{R9}$$

The net reaction for (R8) and (R9) is:

$$2O_3 \rightarrow 3O_2 \tag{R10}$$

while this chain reaction is terminated by:

$$OH + HO_2 \rightarrow H_2O + O_2 \tag{R11}$$

The above cycle is called a HO_x loss cycle ($HO_x \equiv HO_2$, OH, H). In the 1950-60s, calculations assuming a steady state level of HO_x, estimated stratospheric H_2O

levels, and the rate constants for Reactions (R8)-(R11), found this cycle to be a significant ozone sink. Unfortunately, it did not fully explain the discrepancy between Chapman-modelled and observed stratospheric ozone levels.

1.1.3 NO_x Loss Cycle

The impact of nitrogen oxide radicals ($NO_x \equiv NO_2 + NO$) on the ozone layer became apparent in the late 1960s when several countries were planning on launching a stratospheric-flying supersonic aircraft fleet. A key component of aircraft exhaust is nitric oxide (NO) that is directly formed from combustion processes at temperatures over 2000 K:

$$O_2 + N_2 \rightarrow 2NO \tag{R12}$$

In the stratosphere NO reacts rapidly:

$$NO + O_3 \rightarrow NO_2 + O_2 \tag{R13}$$

As first suggested by Blacet (1952), the nitrogen dioxide (NO_2) produced photodissociates during the day to yield a $O(^3P)$ radical:

$$NO_2 + h\nu(\lambda < 430nm) \rightarrow NO + O(^3P) \tag{R14}$$

while O_3 may be reformed:

$$O_2 + O(^3P) + M \rightarrow O_3 + M \tag{R2}$$

The rapid cycling between NO and NO_2 in Reactions (R13) and (R14) has no net effect on O_3 levels. However, NO_2 may destroy ozone if Reaction (R13) forms a catalytic cycle with the following reaction:

$$NO_2 + O(^3P) \rightarrow NO + O_2 \qquad \text{(R16)}$$

The net reaction destroys O_3:

$$O_3 + O(^3P) \rightarrow 2O_2 \qquad \text{(R6)}$$

while the following termination reaction produces nitric acid during the daytime:

$$NO_2 + OH + M \rightarrow HNO_3 + M \qquad \text{(R18)}$$

Nitric acid may act as a reservoir for NO_x. It is eventually converted back to NO_2 via photolysis:

$$HNO_3 + h\nu \rightarrow NO_2 + OH \qquad \text{(R19)}$$

The sum of all gaseous inorganic nitrogen oxides; NO + NO_2 + HNO_3 + HONO + HO_2NO_2 + $CH_3COOONO_2$ + NO_3 + N_2O_5, plus other organic nitrogen-containing compounds, is commonly denoted as NO_y. Further reactions of NO_x and NO_y will be discussed with regards to their roles in tropospheric chemistry in the following section.

Overall, the discovery of the NO_x loss cycle for ozone via (R13) and (R16) was a critical lead in determining the missing sinks for stratospheric ozone, and

eventually led to the cancellation of supersonic commercial flights near the O_3 layer maximum. Stratospheric NO_2 concentrations and profiles have been shown to have large diurnal, seasonal and latitudinal variation (Kreher et al., 1995; Meena, 2005; Senne et al., 1996). In the Northern Hemisphere, maximum stratospheric column densities are typically observed in the summer with minimum values in the winter. For example, in 2005, the stratospheric NO_2 column densities in Pune, India, ranged from $\sim$1-4$\times10^{15}$ molec cm^{-2} (Meena, 2005).

In the 1970s, nitrous oxide (N_2O) a low-yield product of denitrification and nitrification that has no significant sink in the troposphere and is thus transported to the stratosphere, was found to react with $O(^1D)$:

$$N_2O + O(^1D) \rightarrow 2NO \qquad \text{(R20)}$$

It provides an additional NO source that may also ultimately lead to O_3 destruction. Even though this reaction is only responsible for 5% of the N_2O loss in the stratosphere, it is nonetheless believed to be of great importance. A recent paper by Ravishankara et al. (2009) suggested that N_2O is becoming one of the most important ozone-depleting substance in the stratosphere because it has a relatively large ozone depletion potential and high emission rates (no N_2O restrictions were stipulated in the Montréal Protocol).

1.2 Tropospheric Ozone Formation

1.2.1 NO_x Chemistry

NO_x chemistry plays a very important role in the chemistry of the troposphere. Nitrogen dioxide is a red-brown gas that is primarily responsible for the colour of photochemical smog, while nitric oxide is a colourless gas. Both NO (~90%) and NO_2 (~10%) are formed directly from combustion processes and lightning:

$$O_2 + N_2 \rightarrow 2NO \tag{R12}$$

$$2O_2 + N_2 \rightarrow 2NO_2 \tag{R22}$$

Global emissions of NO_x were approximately 49 TgN yr^{-1} in 1997, with most produced anthropogenically (63%) from automobiles, ships, power generation and incineration, while the remaining emissions were due to biomass burning, soil processes and lightning formation (Mueller and Stavrakou, 2005). Recent Canadian emission inventories of NO_x (2009-2010) estimate that approximately 2 TgN yr^{-1} is emitted, a staggering amount considering Canada's relatively small population (EC, 2012). Nitrogen dioxide in the troposphere may damage vegetation and human respiratory systems. In particular it may irritate the lung, lower resistance to infection, cause lung tumours, impair lung function and increase the frequency of bronchitis in children (Macfarlane et al., 2000; Witschi, 1975). Yet, atmospheric

scientists are mainly concerned with NO_x because its chemistry is solely responsible for all the anthropogenically produced ozone in the troposphere (Finlayson-Pitts and Pitts, 1999). High levels of tropospheric O_3 are linked to crop damage, decreased levels of flora, high hospital admission rates, greater asthmatic complications and even premature mortality, since it is a strong irritant that causes lung inflammation and reduces the lung's capacity and function (Lippmann, 1989). Background tropospheric O_3 mixing ratios are estimated to be between 30-40 ppb today (Finlayson-Pitts and Pitts, 1999), which is a substantial increase from the 19th century when global O_3 levels were only 10-15 ppb (Volz and Kley, 1988). This change coincides with the increase in fossil fuel combustion over the last 100 plus years.

In the troposphere, NO_2 photolyzes during the day to yield a $O(^3P)$ radical which then reacts rapidly with oxygen to form ozone:

$$NO_2 + h\nu(\lambda < 430nm) \rightarrow NO + O(^3P) \qquad \text{(R14)}$$

$$O_2 + O(^3P) + M \rightarrow O_3 + M \qquad \text{(R2)}$$

This reaction sequence is extremely important because it is believed to be the only significant pathway that yields O_3 in the troposphere (Finlayson-Pitts and Pitts, 1999). Nitric oxide may also directly react with ozone or oxygen:

$$NO + O_3 \rightarrow NO_2 + O_2 \qquad \text{(R13)}$$

$$2NO + O_2 \rightarrow 2NO_2 \qquad \text{(R26)}$$

In urban areas with a lot of vehicular traffic, ozone is reduced to low levels via Reaction (R13). Although it was originally believed to be an important reaction in the formation of NO_2 in the troposphere, Reaction (R26) is very slow ($k_{26} = 2.0\times10^{-38}$ cm^6 molecule^{-2} s^{-1}) and usually insignificant unless there is a huge concentration of NO present (e.g. the initial period a combustion plume emitted from a uncontrolled power plant enters the atmosphere).

In environments that do not contain organics, Reactions (R14), (R2), and (R13) control the concentrations of NO and NO_2, and are the major loss processes for NO_2 and O_3. A photostationary state is created whereby ozone is created and destroyed at exactly the same rate. Under such circumstances the ratio of concentrations of O_3, NO and NO_2 are constant, as shown in Equation 1.2. This relationship is called the Leighton ratio, named after the scientist who wrote a pioneering book on air pollution (Leighton, 1961):

$$\frac{[O_3][NO]}{[NO_2]} = \frac{j_{NO_2}}{k_{NO}} \qquad (1.2)$$

or as it is more commonly expressed as:

$$\frac{[NO_2]}{[NO]} = \frac{k_{NO}}{j_{NO_2}}[O_3] \qquad (1.3)$$

The ratio of concentrations is expected to change throughout the course of the day, since j_{NO_2} is dependent on the solar zenith angle.

1.2.2 Oxidation of CO and Volatile Organic Compounds

As early as 1969, it had been suggested that the OH radical actually drives the daytime chemistry in both polluted and clean environments (Heicklen et al., 1969; Weinstock, 1969). This is because OH initiates the oxidation of carbon monoxide (CO) and volatile organic compounds (VOCs). It may be formed by the photodissociation of O_3 to produce $O(^1D)$ followed by reaction with H_2O:

$$O_3 + h\nu(\lambda < 320nm) \rightarrow O_2 + O(^1D) \quad \text{(R3)}$$

$$H_2O + O(^1D) \rightarrow 2OH \quad \text{(R7)}$$

even though $O(^1D)$ reacts much faster with a third body (e.g. N_2 or O_2) to form $O(^3P)$ via Reaction (R4). In the troposphere, the water content is much higher than the stratosphere and Reaction (R7) gains importance. In 1 atm of air with 50% relative humidity at 298 K, approximately 10% of the $O(^1D)$ reacts with H_2O via Reaction (R7) to form OH.

The OH radical is also produced through the photodissociation of nitrous acid (HONO) or hydrogen peroxide (HOOH):

$$HONO + h\nu(\lambda < 370nm) \rightarrow OH + NO \quad \text{(R29)}$$

$$HOOH + h\nu \rightarrow 2OH \quad \text{(R30)}$$

The OH radicals formed may then react with CO, according to the following reaction mechanism:

$$CO + OH \rightarrow CO_2 + H \quad \text{(R31)}$$

$$H + O_2 + M \rightarrow HO_2 + M \quad \text{(R32)}$$

$$HO_2 + NO \rightarrow NO_2 + OH \quad \text{(R33)}$$

$$NO_2 + h\nu \rightarrow NO + O(^3P) \quad \text{(R14)}$$

$$O_2 + O(^3P) + M \rightarrow O_3 + M \quad \text{(R2)}$$

with a net reaction of:

$$CO + 2O_2 \rightarrow CO_2 + O_3 \quad \text{(R36)}$$

As seen from Reaction (R36) the net effect of CO oxidation is the HO_x and NO_x catalyzed formation of tropospheric ozone, while both NO_x and OH are conserved. The above mechanism is valid when the reaction of HO_2 with NO (R33) dominates compared to the loss of HO_x through the formation of HOOH:

$$HO_2 + HO_2 \rightarrow HOOH + O_2 \quad \text{(R37)}$$

The OH radical may also react with methane, according to a similar mechanism:

$$CH_4 + OH \rightarrow CH_3 + H_2O \quad \text{(R38)}$$

$$CH_3 + O_2 \rightarrow CH_3O_2 \quad \text{(R39)}$$

$$CH_3O_2 + NO \rightarrow NO_2 + CH_3O \quad \text{(R40)}$$

$$CH_3O + O_2 \rightarrow HO_2 + HCHO \quad \text{(R41)}$$

$$HO_2 + NO \rightarrow NO_2 + OH \quad \text{(R33)}$$

$$2NO_2 + h\nu \rightarrow 2NO + 2O(^3P) \quad 2\times\text{(R14)}$$

$$2O_2 + 2O(^3P) + M \rightarrow 2O_3 + M \quad 2\times\text{(R2)}$$

Net Reaction:

$$CH_4 + 4O_2 + h\nu \rightarrow HCHO + 2O_3 + H_2O \quad \text{(R45)}$$

Other potential reactions (termination steps) that may occur include:

$$CH_3O_2 + CH_3O_2 \rightarrow CH_3OOCH_3 + O_2 \quad \text{(R46)}$$

$$CH_3O_2 + HO_2 \rightarrow CH_3OOH + O_2 \quad \text{(R47)}$$

In the above mechanism, the tropospheric formation of ozone is again catalyzed by HO_x and NO_x chemistry, but also produces formaldehyde (HCHO) as a daughter compound. Formaldehyde, which has been linked to eye and respiratory tract irritation (McGwin et al., 2010), is stable, relative to the radical species, but it will oxidize or photolyze to accelerate ozone formation (via HO_x chemistry) and produces CO as a stable product that can also be oxidized, as previously described.

$$HCHO + OH \rightarrow CHO + H_2O \quad \text{(R48)}$$

$$HCHO + h\nu(\lambda < 325nm) \rightarrow CHO + H \quad \text{(R49)}$$

$$HCHO + h\nu(\lambda > 325nm) \rightarrow CO + H_2 \quad \text{(R50)}$$

$$CHO + O_2 \rightarrow CO + HO_2 \quad \text{(R51)}$$

Additional hydrocarbons (RH) and many other VOCs will also react with OH to produce alkylperoxy radicals (RO_2) and produce tropospheric ozone using a similar pathway to those previously described:

$$RH + OH \rightarrow R + H_2O \quad \text{(R52)}$$

$$R + O_2 \rightarrow RO_2 \quad \text{(R53)}$$

$$RO_2 + NO \rightarrow RO + NO_2 \quad \text{(R54)}$$

$$RO + O_2 \rightarrow R_1CHO + HO_2 \quad \text{(R55)}$$

$$RO + O_2 \rightarrow R_1C(O)R_2 + HO_2 \quad \text{(R56)}$$

$$RO + O_2 \rightarrow \alpha R_1CHO + \beta R_1C(O)R_2 + HO_2 \quad \text{(R57)}$$

$$HO_2 + NO \rightarrow NO_2 + OH \quad \text{(R33)}$$

$$2NO_2 + h\nu \rightarrow 2NO + 2O(^3P) \quad 2\times\text{(R14)}$$

$$2O_2 + 2O(^3P) + M \rightarrow 2O_3 + M \quad 2\times\text{(R2)}$$

Net Reaction:

$$RH + 4O_2 + h\nu \rightarrow \alpha R_1CHO + \beta R_1C(O)R_2 + H_2O + 2O_3 \quad \text{(R61)}$$

At high VOC/NO_x ratios (NO is unavailable), the following termination steps occur:

$$R_1O_2 + R_2O_2 \rightarrow R_1OOR_2 + O_2 \quad \text{(R62)}$$

$$R_1O_2 + HO_2 \rightarrow ROOH + O_2 \quad \text{(R63)}$$

$$HO_2 + HO_2 \rightarrow HOOH + O_2 \quad \text{(R37)}$$

At low VOC/NO_x ratios there is a loss of OH due to the high NO_2 present:

$$OH + NO_2 + M \rightarrow HNO_3 + M \quad \text{(R18)}$$

1.2.3 Ozone Control Strategies

In cities and polluted rural areas, there is a significant supply of NO_x and VOCs such that the ozone-producing reactions described earlier are both relevant and effective. The ozone formation mechanism is non-linear. Depending on the relative amounts of NO_x and VOCs, two distinct situations for ozone production occur; NO_x and VOC limited regimes (Figure 1.1). A reduction in NO_x or VOC emissions does not guarantee a reduction in O_3. The determination of which regime a region or city lies in is thus an important consideration when determining effective strategies for pollution control. This is because for the NO_x limited case (high VOC, low NO_x), reductions in NO_x will lower ozone production, while reductions in VOC levels

have little effect. For the VOC limited case (low VOC, high NO_x), NO_x reductions may, at times, actually increase O_3 production, while VOC reductions lower O_3 production. Urban environments are often VOC limited since they contain direct sources of NO_x, while rural environments are NO_x limited since they have few NO_x sources, but significant natural VOC emissions and perhaps also VOCs from an urban air mass that had been transported a long distance. This interpretation is a general guideline only and specific cases must be studied with care to determine the actual scenario present. In particular, the effect of natural VOC emissions such as isoprene, α-pinene, or β-pinene may significantly alter this relationship.

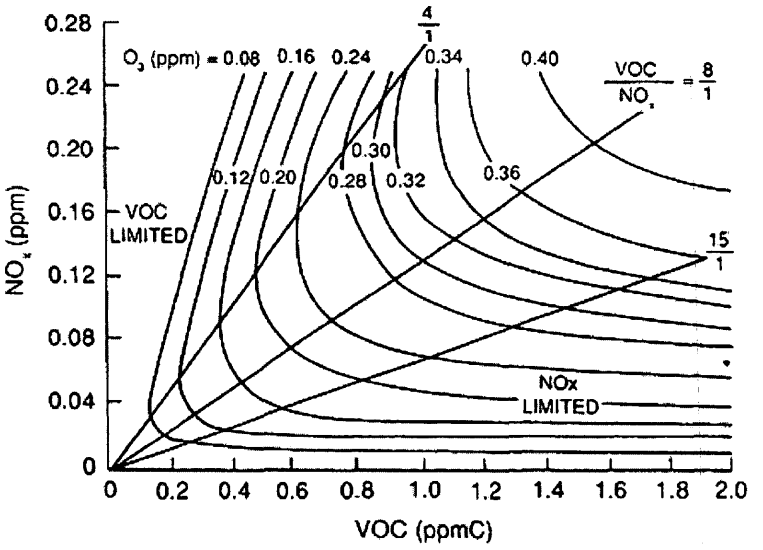

Figure 1.1: Representative ozone isopleth diagram, adapted from Dodge (1977). The ozone production rate (in ppm) is listed for the corresponding isopleths. Solid diagonal lines represent VOC/NO_x ratios of 4, 8, and 15 respectively.

1.2.4 Nighttime Chemistry

Nighttime chemistry in polluted areas is dominated by reactions of the nitrate radical (NO_3), dinitrogen pentoxide (N_2O_5), and subsequent reactions that form nitric acid and chlorine-containing photolabile species. The first reported measurements of NO_3 in the troposphere were done using Differential Optical Absorption Spectroscopy (DOAS), a technique which will be described in Section 1.3. These studies found levels greater than 300 ppt, one hour after sunset (Noxon et al., 1980; Platt et al., 1980b). Other studies have shown NO_3 to be important at significantly lower levels. Generally, NO_3 is less reactive than OH with VOCs, but there are several species for which NO_3 is a competing or dominant sink. Within the continental boundary layer in Europe for instance, Geyer et al. (2001) estimated that 55% of the 50 observed VOCs were oxidized from OH, followed by 28% from NO_3 and 17% from O_3 initiation.

The NO_3 radical is formed when NO_2 levels typically build up after sunset and photolysis has stopped:

$$NO_2 + O_3 \rightarrow NO_3 + O_2 \tag{R66}$$

while during the daytime NO_3 readily undergoes photolysis via visible light:

$$NO_3 + h\nu(\lambda < 700nm) \rightarrow NO + O_2 \tag{R67}$$

$$NO_3 + h\nu(\lambda < 580nm) \rightarrow NO_2 + O(^3P) \tag{R68}$$

NO_3 reacts rapidly with NO:

$$NO_3 + NO \rightarrow 2NO_2 \tag{R69}$$

acts as a nighttime oxidant oxidizing VOCs:

$$NO_3 + VOC \rightarrow products \tag{R70}$$

and reacts with dimethyl sulphide (DMS), the most abundant biological sulphur compound emitted into the atmosphere:

$$NO_3 + (CH_3)_2S \rightarrow products \tag{R71}$$

In the marine boundary layer (MBL) of the North Atlantic Ocean, NO_3 is a more efficient sink for DMS at night than OH is during the day (Allan et al., 2000). NO_3 also reacts reversibly with NO_2 to form dinitrogen pentoxide:

$$NO_3 + NO_2 \rightleftharpoons N_2O_5 + heat \tag{R72}$$

This equilibrium is temperature dependent and N_2O_5 is often an important nighttime sink for NO_x. The hydrolysis of N_2O_5 on aerosols is an important global pathway for the conversion of NO_x to HNO_3 (Dentener and Crutzen, 1993):

$$N_2O_5 + H_2O(p) \rightarrow 2HNO_3(p, g) \tag{R73}$$

In this case, HNO_3 may act as a permanent sink for NO_x as it can be removed via dry or wet deposition. The above reaction may also occur in the gas phase but the

existence of the reaction in this phase is highly uncertain (Mentel et al., 1996):

$$N_2O_5 + H_2O(g) \rightarrow 2HNO_3(g) \quad \text{(R74)}$$

In marine environments, it has also been discovered that N_2O_5 can react with sea salt (NaCl):

$$N_2O_5 + NaCl(s, aq) \rightarrow ClNO_2(g, aq) + NaNO_3(aq) \quad \text{(R75)}$$

$$ClNO_2 + h\nu \rightarrow Cl + NO_2 \quad \text{(R76)}$$

$$Cl + RH \rightarrow HCl + R \quad \text{(R77)}$$

Nocturnal chlorine radical reservoir species such as nitryl chloride ($ClNO_2$) may play an important role in the oxidation chemistry of the atmosphere, as the NO_2 and R generated will react as described earlier. As such, the relative importance of $ClNO_2$ is currently under investigation by research teams in North America and Europe (Mielke et al., 2011; Phillips et al., 2012; Riedel et al., 2012)

Nitrous acid is a species that builds up during the nighttime and plays a key role in the polluted atmosphere (Harris et al., 1982). The photolysis of HONO (R29) is often the major source of OH in the morning boundary layer (Platt et al., 1980a) and has been estimated to contribute 17-34% of the total OH production integrated over 24 h in polluted environments (Alicke et al., 2002, 2003). Although HONO levels typically decline during the day, several studies show residual levels at mid-day that suggest a significant daytime source of HONO (Kleffmann et al., 2003;

Zhou et al., 2002). A complete understanding of the sources and sinks of HONO during the day and night has remained elusive. It is believed to be emitted directly from combustion with a $HONO/NO_x$ ratio usually below 0.01 (Kurtenbach et al., 2001). Observations in the nocturnal boundary layer indicate a significant HONO source (Harrison and Kitto, 1994) with a negative HONO gradient and positive NO_2 gradient with respect to the height above ground (Harrison et al., 1996; Stutz et al., 2002; Wang et al., 2006), while laboratory studies provide evidence in support of a heterogeneous reaction of NO_2 on a range of surfaces including glass, steel and teflon (Finlayson-Pitts et al., 2003; Lammel, 1999).

Generally, the consensus is that HONO forms from the reaction of NO_2 on surfaces with the following stoichometry:

$$NO_2 + NO_2 + H_2O \rightarrow HONO + HNO_3 \qquad \text{(R78)}$$

Recently our research group proposed a HONO formation mechanism (Wojtal et al., 2011) based on the reaction of NO_2 on ambient aqueous surfaces that is consistent with Reaction (R78).

1.3 Differential Optical Absorption Spectroscopy

Differential Optical Absorption Spectroscopy (DOAS) is a spectroscopic technique used to detect various trace gases in the stratosphere and troposphere (Plane and Smith, 1995; Platt, 1994; Platt and Stutz, 2008). Its development is credited to Ulrich Platt and Dieter Perner (Perner et al., 1976; Platt et al., 1979) who initially made DOAS measurements using artificial light, although similar experiments around the same time utilized natural light sources (Noxon, 1975; Noxon et al., 1979). The application of the DOAS technique has led to the direct detection of several gases for the first time including OH, HONO, NO_3, BrO, IO and CHOCHO (Alicke et al., 1999; Hausmann and Platt, 1994; Perner and Platt, 1979; Perner et al., 1976; Platt and Perner, 1980; Platt et al., 1980b; Sanders et al., 1988; Volkamer et al., 2005) in the troposphere, as well as BrO and OClO in the stratosphere (Sanders et al., 1993; Solomon et al., 1989, 1993). Several other trace gases such as NO_2, ClO, O_3, SO_2, CS_2, H_2O, NH_3 and HCHO have also been detected using DOAS (Ahmed and Kumar, 1992; Edner et al., 1990; Noël et al., 1999; Platt and Perner, 1980; Platt et al., 1979; Tuckermann et al., 1997). Since this remote sensing technique measures the composition of ambient air in the atmosphere without interaction with the atmosphere itself, DOAS measurements are also able to measure reactive radical species such as NO_2, NO_3, OH, BrO, ClO and IO simultaneously.

As such, DOAS can be an extremely powerful analytical measurement technique in the field of atmospheric chemistry.

The application of DOAS stems directly from the Beer-Lambert Law. It describes the absorption of electromagnetic radiation (light) by matter and may be expressed as:

$$I(\lambda) = I_0(\lambda)e^{-\sigma(\lambda)cL} \tag{1.4}$$

where $I(\lambda)$ is the intensity of light after it passes through a trace gas layer with absorber of concentration c and thickness L. $I_0(\lambda)$ is the initial light intensity, while $\sigma(\lambda)$ is the absorption cross section of the absorber. The light source may either be artificial (lamp) or natural (sun or moon), while the matter which absorbs the light is the earth's atmosphere, containing both aerosols and trace gases.

Equation 1.4 may be rearranged to obtain a quantity defined as the optical density, D:

$$D \equiv ln\left(\frac{I_0(\lambda)}{I(\lambda)}\right) = \sigma(\lambda)cL \tag{1.5}$$

If the path length and appropriate cross section are known, the concentration of the trace gas absorber may be found:

$$c = \frac{D}{\sigma(\lambda)L} \tag{1.6}$$

In the real atmosphere, absorptions from other trace gases, Rayleigh and Mie scattering, and turbulence effects must also be considered. The resulting form of the

Beer-Lambert Law becomes significantly more complicated:

$$I(\lambda) = I_0(\lambda)e^{[-L(\sum_i \sigma_i(\lambda)c_i)+\varepsilon_R(\lambda)+\varepsilon_M(\lambda)]} \times A(\lambda) \tag{1.7}$$

where $\varepsilon_R(\lambda)$ is the Rayleigh scattering extinction coefficient, $\varepsilon_M(\lambda)$ the Mie scattering extinction coefficient, $A(\lambda)$ the attenuation factor and $\sum_i \sigma_i(\lambda)c_i$ the absorption by all molecules (i^{th} term). The attenuation factor $A(\lambda)$ describes the broad wavelength-dependent transmission of the optical system used and turbulence effects.

The elegance of the DOAS technique is that it separates the above light extinction effects and allows the trace gas absorptions to be analyzed separately. This is accomplished by using the differential absorption, which is the part of the absorption that varies rapidly with wavelength, as opposed to the components that vary broadly with wavelength (ε_R, ε_M, and A). Figure 1.2B shows a comparison between the component of the absorption cross section that varies slowly with λ, denoted as σ^B, and the component that changes rapidly with λ, denoted as σ' (differential absorption cross section). These two components add to form the overall absorption cross section:

$$\sigma(\lambda) = \sigma^B(\lambda) + \sigma'(\lambda) \tag{1.8}$$

Similarly, the optical density may also be separated into a slowly varying component D_B, and a differential component D' (Figure 1.2A), which add to form the overall

optical density D:

$$D = D_B + D' \tag{1.9}$$

By fitting D and σ with appropriate polynomials to eliminate D_B and σ^B, the differential optical density D' and the differential absorption cross section σ' can be isolated. This is crucial because Rayleigh and Mie scattering processes are only represented in the D_B and σ^B terms. This allows the trace gas absorptions of interest to be separated from aerosol extinction processes, provided that their electronic spectra have rapidly varying cross sections. This requirement usually limits DOAS to small molecules of several atoms.

The concentration of a particular absorber may then be determined by replacing the optical density and absorption cross section with their differential counterparts:

$$c = \frac{D'}{(\sigma'(\lambda)L)} \tag{1.10}$$

The calculation of the concentration of trace gases from Equation 1.10 is the basis of the standard DOAS technique first used by Platt et al. (1979). However, since several trace gases may absorb in the same spectral region, a numerical fitting procedure must be used to separate them. For multiple species, a least squares fit is used to extract the slant column density (SCD) of each absorbing species:

$$SCD \equiv cL \tag{1.11}$$

$$\sum_{\lambda=a}^{b}(D' - \sigma'_c \cdot SCD_c)^2 = R \tag{1.12}$$

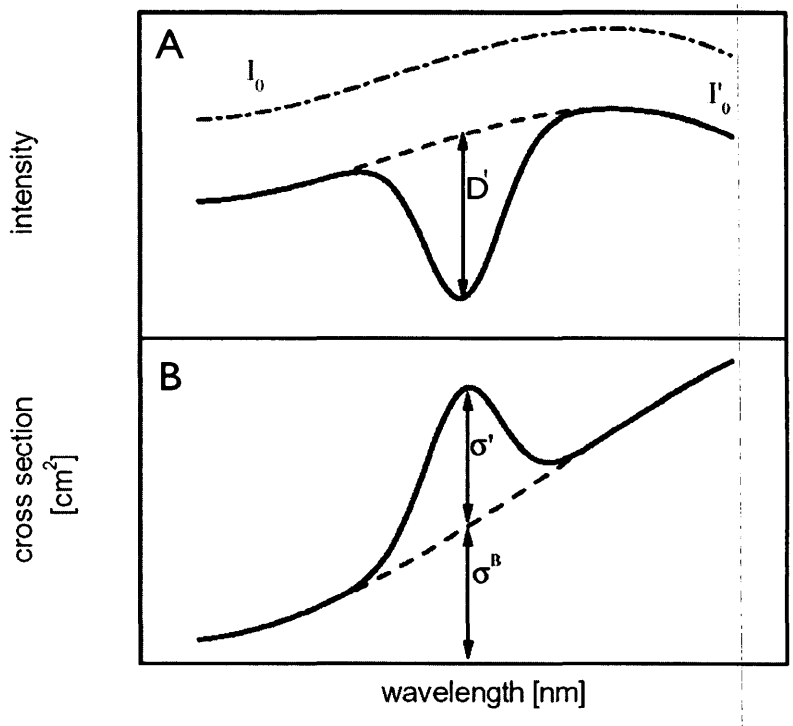

Figure 1.2: The differential optical density (D′) and differential absorption cross section (σ'). The top panel (A) shows how the differential optical density (D′) is determined. The bottom panel (B) shows how the differential absorption cross section (σ') is found by removing the broad band component (σ^B) from the absorption cross section (σ). This figure is a modified version of the original figure found in Platt and Stutz (2008)

where over the wavelength range a to b, σ'_c is the experimentally-determined differential absorption cross section of species c, SCD_c is the slant column density of species c, and R, is the residual of the fit. Ideally, the residual would only contain instrumental noise, but in practicality lowering the residual to acceptably low levels is adequate for fitting most species. Various software programs (e.g. DOASIS and WinDOAS) exist to perform the DOAS fitting procedure described above. Here the DOAS polynomial was fit to the logarithm of an appropriate reference spectra divided by the absorption spectra measured in the field to determine D', while differential absorption cross sections (σ'_c) were calculated by applying the DOAS polynomial to the required cross sections found in the literature.

Figure 1.3 provides examples of different trace gas absorption cross sections measured in the lab. As may be seen from this figure, several trace gas species may be detected simultaneously using DOAS. However, it should be noted that often in order to detect certain gases, spectrometers with small wavelength ranges must be used. In the field then, more than one spectrometer is often required to detect certain gases simultaneously (e.g. NO_3 and NO_2).

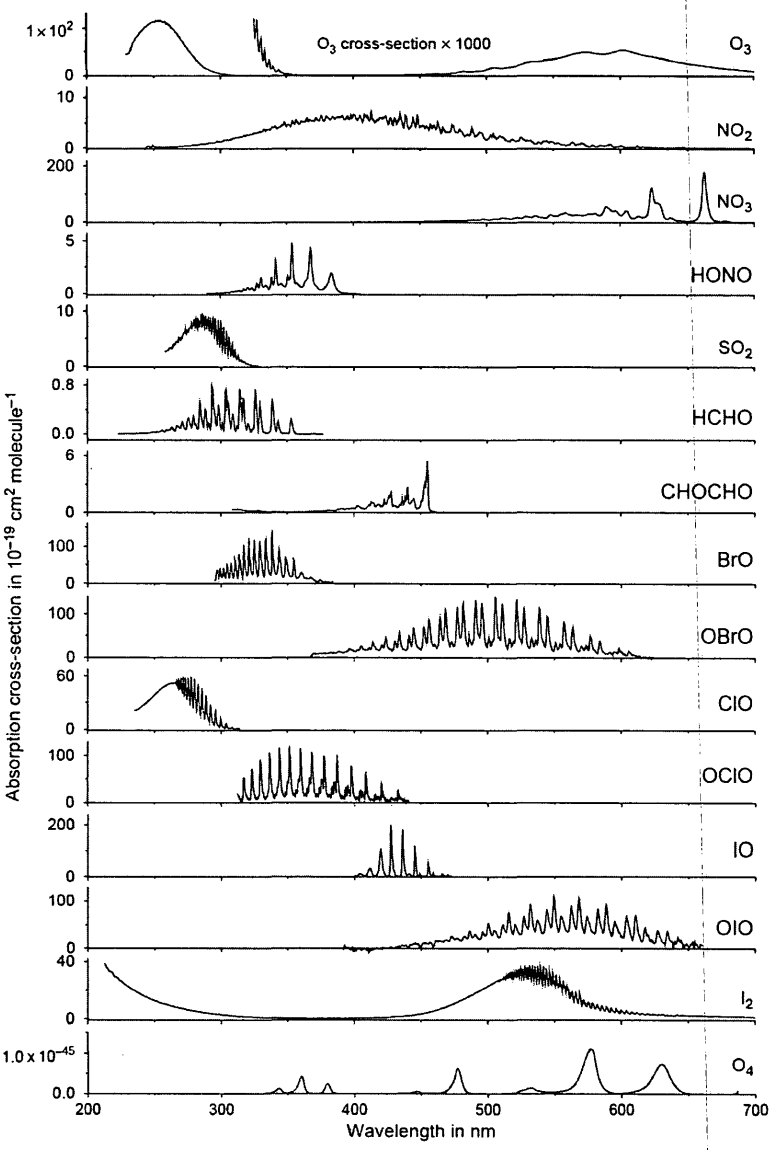

Figure 1.3: Examples of absorption cross sections currently used in DOAS trace gas retrievals. Figure courtesy of L. Vogel, Universität Heidelberg, Germany (personal communication).

1.3.1 Active DOAS

DOAS experiments may be classified either as active or passive. The term active refers to the light source being artificial, as opposed to being a passive or natural light source such as the sun or moon. Standard active DOAS experiments have three main advantages; the path lengths are well-defined, experiments may be run day or night, and wavelengths under 300 nm may be examined (Platt and Stutz, 2008). However, they often require more complex optical arrangements, and require greater maintenance and power, when compared to passive systems. In order to set up an active DOAS experiment three basic components are often used; a continuous light source (such as a light-emitting diode (LED) or Xe arc lamp), a reflector (although this is not mandatory, it is used to double the effective light path and reduce turbulence effects), and a spectrometer (typical detector types include photomultiplier tubes (PMTs), photodiode arrays, and charged-coupled devices (CCDs)). Figure 1.4 provides a schematic of a typical active DOAS experimental setup, which consists of a Xe arc lamp light source, an optical system (telescope and retro-reflectors), and a CCD spectrometer connected to the optical system via a fiber optic and to a laptop computer via USB connection.

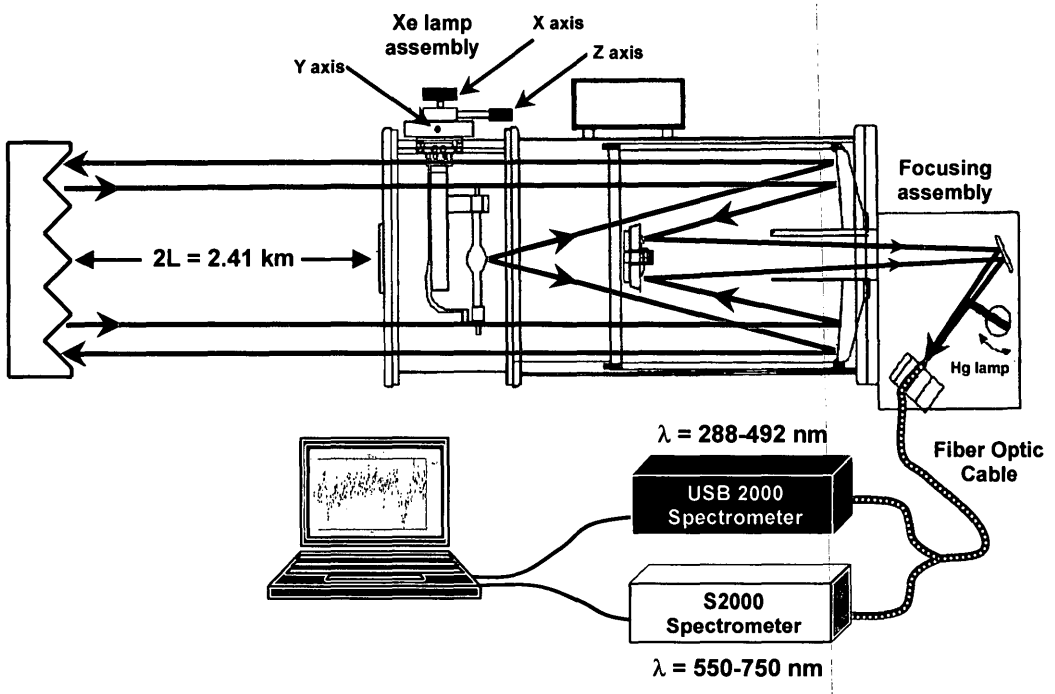

Figure 1.4: A typical active DOAS instrumental setup. A Xe arc lamp is used to send light to the retro-reflector assembly located 1.2 km away. The retro-reflector sends the light back to the CCD spectrometer (either USB2000 or S2000) as shown, providing a total path length of 2.41 km.

1.3.2 Passive DOAS

Current passive DOAS techniques may be first traced back to early scattered sunlight absorption spectroscopy measurements. The first vertical profiles of ozone were determined using the "Umkehr" technique, an example of passive absorption spectroscopy using ozone absorption features at four distinct wavelengths (Götz et al.,

1933). This technique was extended to wider spectral ranges with the invention of the COSPEC (COrrelation SPECtrometer) technique in the late 1960s (Davies, 1970), a technique that has been implemented for over three decades to study NO_2 and SO_2 (Hoff, 1992; Stoiber and Jepsen, 1973). More recently, the passive DOAS technique was developed. Early measurements were performed in the zenith direction (90°) exclusively to measure stratospheric absorbers, since the radiative transfer modelling used to determine vertical column densities was straightforward, and the radiative transfer modelling for tropospheric conditions was not yet available. These measurements focused on stratospheric NO_2, O_3, OClO, BrO and IO (Noxon, 1975; Noxon et al., 1979; Solomon et al., 1989; Wittrock et al., 2000), while active DOAS was used for tropospheric measurements. Passive DOAS instruments are also capable of measuring off-axis (i.e. at angles less than the zenith). The first such measurements were performed to measure OClO over Antarctica during twilight (Sanders et al., 1993). Other off-axis measurements coupled with direct moon measurements were used to determine stratospheric and tropospheric profiles of NO_3 (Smith and Solomon, 1990; Weaver et al., 1996). Today there are several passive DOAS instruments used in the field that include off-axis, zenith-sky, aircraft, satellite and multiple axis configurations. A comprehensive overview of the history of passive DOAS measurements may be found in Platt and Stutz (2008).

1.4 Multi AXis Differential Optical Absorption Spectroscopy

Multi AXis Differential Optical Absorption Spectroscopy (MAX-DOAS) is a passive DOAS technique that measures scattered sunlight from different off-axis viewing directions to ultimately determine the tropospheric vertical column density of various trace gas species (Hönninger et al., 2004). Compared to previous passive DOAS experiments which employed either a zenith or one fixed off-axis viewing direction, MAX-DOAS offers the additional advantage of obtaining information with respect to the vertical distribution of trace gases, as it combines the aforementioned advantages of passive DOAS with several new innovations. By comparing the results of tropospheric radiative transfer models with MAX-DOAS measurements, information on the vertical distribution of both aerosols and trace gases is obtained.

To understand how MAX-DOAS systems yield the above information, the critical geometry is shown in Figure 1.5. A telescope is placed at ground level (or on the top of a building or mountain), and it is capable of rotating from an angle parallel to the horizon (0°) to the zenith (90°). This angle is known as the telescope elevation angle (EA or α). Sunlight enters the atmosphere at a certain angle depending on the time of day and season. This angle, defined by the angle between the sun and the zenith, is called the solar zenith angle (SZA or ϑ). If a single light scattering approximation is made (multiple scattering is more likely) then an apparent slant

column density for a given elevation angle (SCD_α) may be defined as the trace gas concentration integrated along the effective light path (Figure 1.5):

$$SCD_\alpha = \int c(s)ds \tag{1.13}$$

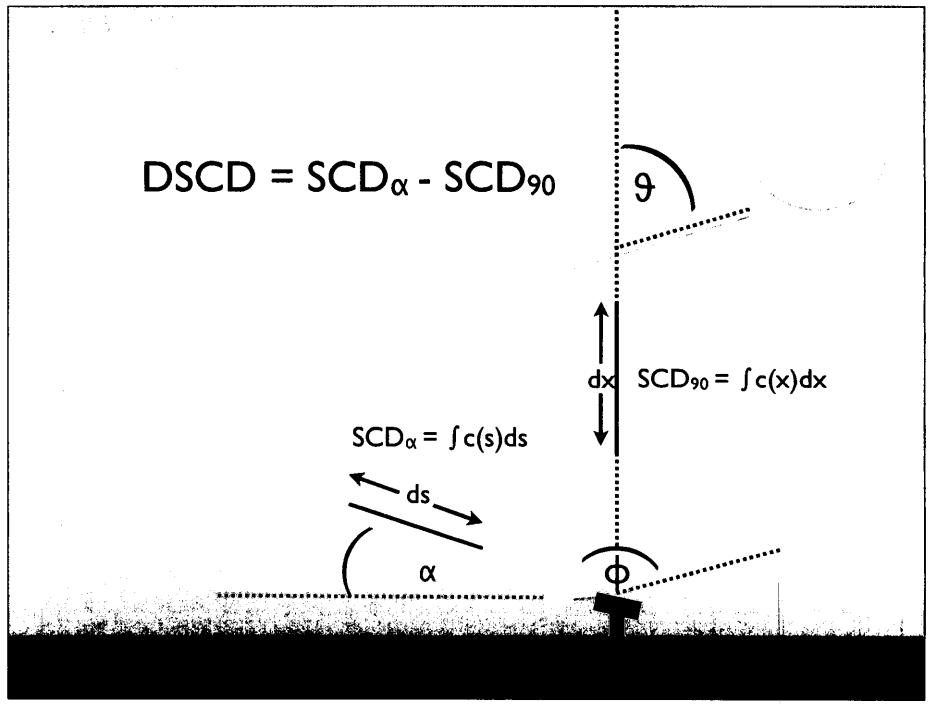

Figure 1.5: MAX-DOAS geometry. The primary result of a MAX-DOAS retrieval is the differential slant column density (DSCD) of a trace gas, which depends on the elevation angle (α), solar zenith angle (ϑ) and relative azimuth angle (ϕ).

For a tropospheric absorber, the longest effective path length is found when pointing the telescope at low elevation angles, while zenith measurements ($\alpha = 90°$) have significantly smaller light paths through the troposphere and have SCDs that are

usually dominated by stratospheric absorbers. The zenith angle measurements may then be used as references to eliminate the effect of stratospheric absorbers on the SCDs and are traditionally known as Fraunhofer Reference Spectra (FRS). The primary result of a MAX-DOAS retrieval then is the differential slant column density (DSCD):

$$DSCD = SCD_{\alpha} - SCD_{90} \tag{1.14}$$

$$DSCD = SCD_{\alpha} - FRS \tag{1.15}$$

As can be seen in Figure 1.5, the DSCD depends not only on the trace gas amount, but also on the α of the measurement, the ϑ of the sun, and relative azimuth angle (RAZI or ϕ) between the sun and the direction the telescope is pointed, as well as the FRS used. Ideally, the FRS subtracted should be taken at exactly the same time so that the above variables are identical, but in practicality the FRS is usually taken after a series of lower angle measurements. If the time difference between these measurements is small this approach is valid. Since the SCDs vary with λ, α, ϑ, and ϕ, it is useful to convert SCDs into vertical column densities (VCDs), as these quantities are independent of the above parameters:

$$VCD = \int c(z)dz \tag{1.16}$$

This conversion is accomplished by the use of an Air Mass Factor (AMF). The AMF is defined as the enhancement of the SCD in relation to the VCD (Solomon

et al., 1987):

$$AMF(\lambda, \vartheta, \alpha, \phi) \equiv \frac{SCD(\lambda, \vartheta, \alpha, \phi)}{VCD} \tag{1.17}$$

and when it is known (usually determined via radiative transfer modelling) the corresponding VCDs may be obtained:

$$VCD = \frac{SCD(\lambda, \vartheta, \alpha, \phi)}{AMF(\lambda, \vartheta, \alpha, \phi)} \tag{1.18}$$

When using a single scattering assumption, the AMF may be approximated as:

$$AMF \approx \left[a \cdot \frac{1}{sin\alpha} + (1 - a) \cdot \frac{1}{cos\vartheta} \right] \tag{1.19}$$

where a is the fraction of the total vertical trace gas column below the scattering altitude. As shown in Figure 1.6A, for a tropospheric absorber the AMF may be approximated as $1/\sin\alpha$, showing a strong dependence on the elevation angle, while for a stratospheric absorber the AMF is approximated by $1/\cos\vartheta$, showing a strong dependence on the solar zenith angle (Figure 1.6B). It must be stressed that this geometrical approximation assumes single scattering only and is generally only applied to measurements where $\alpha \geq 20°$. For low elevation angles, this approximation is rarely valid because the presence of aerosols in the atmosphere causes multiple scattering to dominate. Most often radiative transfer models are used to calculate the AMFs necessary to convert SCDs into tropospheric VCDs.

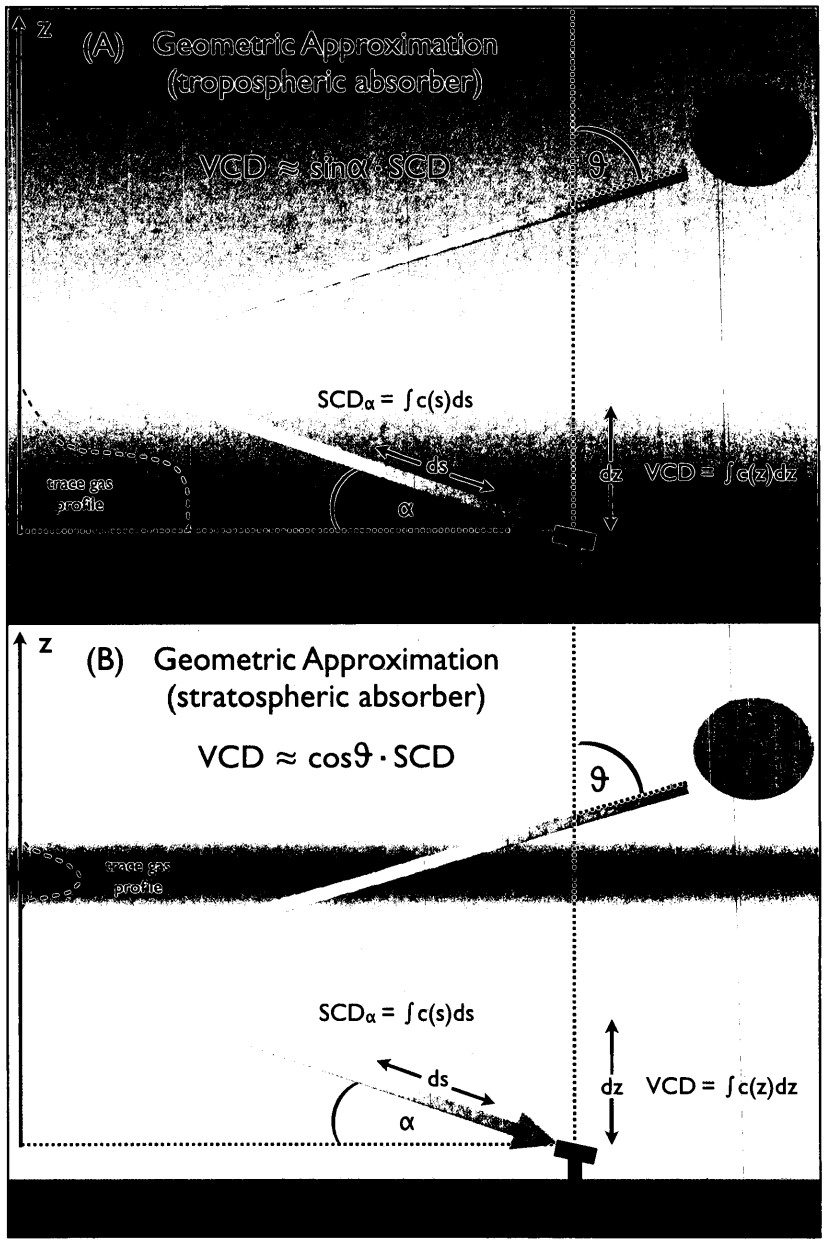

Figure 1.6: Geometrical VCD approximations for tropospheric and stratospheric absorbers, assuming single scattering only. For a tropospheric absorber (A), the AMF is approximated as $1/\sin\alpha$, and hence the VCD $\approx \sin\alpha \cdot$SCD for $\alpha \geq 20°$. For a stratospheric absorber (B), the AMF is approximated as $1/\cos\vartheta$, and hence the VCD $\approx \cos\vartheta \cdot$SCD for $\alpha \geq 20°$.

1.4.1 MAX-DOAS Progession

Hönninger and Platt (2002) were the first to utilize the Multiple AXis (MAX) feature in DOAS measurements performed during the spring of 2000 in Alert, Nunavut, Canada. First, BrO DSCDs were determined at multiple elevation angles and then BrO vertical profile information, namely the most probable BrO layer height, was found by comparing these results with values determined from a single scattering Monte Carlo radiative transfer model. These measurements showed a strong anti-correlation between BrO and O_3 within the boundary layer and demonstrated the potential of this new DOAS technique. Hönninger et al. (2004) also produced a significant review paper that highlighted the MAX-DOAS studies performed at that time. Radiative transfer model calculations using the Monte Carlo radiative transfer model TRACY (von Friedeburg, 2003) were used to systematically study the effects of changing profile shapes, ground albedo, aerosol load, and aerosol type on the AMF determined, as a function of elevation angle or solar zenith angle. The technical requirements for making MAX-DOAS measurements, including the advantages and disadvantages of sequential or simultaneous operation, and the possible applications of the technique, including tracking nearby emission patterns from a point source, looking into smog episodes in valleys, or studying active halogen release on salt surfaces were highlighted. Several of the methods used or forecasted

in this paper have now become feasible and relevant in the DOAS community today.

A MAX-DOAS, with a 2-D CCD chip, was used for the first time to monitor NO_2 emissions next to a highway in Heidelberg, Germany, during the spring of 2001 (von Friedeburg et al., 2005). The 2-D chip allowed measurements to be collected from eight multiple headings simultaneously (as opposed to sequential measurements). The goal of this study's measurements was to obtain a set of real-world NO_2 emissions that could be compared to current emission estimates determined from existing models, while exploring the potential for MAX-DOAS to detect pollutants spatially across a motorway plume. The NO_2 DSCDs determined were generally higher for measurements that traversed the plume (~50% higher) than those containing only background NO_2. When comparing measurements at different elevation angles, for headings pointed outside of the plume those measurements with the lowest elevation angles generally had the highest DSCDs, however when the measurement headings were pointed into the plume this trend was not always observed. The authors explained this phenomenon by increased aerosol levels at lower heights within the plume that increased light extinction (and hence reduced the effective light path length) for measurements at lower elevation angles. They came to the conclusion that the influence of aerosols on MAX-DOAS measurements was much higher than originally expected.

This result stressed the need to understand the aerosol levels present when inter-

preting MAX-DOAS results. Comparing DSCDs of trace gases from day to day may be inaccurate if aerosol levels change significantly. Wagner et al. (2002, 2004) first proposed a method of comparing O_4 DSCDs and radiative transfer model results to quantify aerosol levels. More importantly, this method was used to determine the most effective light path for MAX-DOAS measurements. Sinreich et al. (2005) utilized this approach to obtain aerosol extinction coefficients, NO_2 vertical column densities, atmospheric boundary layer heights and NO_2 mixing ratios from O_4 and NO_2 MAX-DOAS measurements, during the summer of 2003 in Heidelberg. First, measured O_4 DSCDs were converted to AMFs and manually compared to AMFs determined using the Monte Carlo radiative transfer model TRACY to yield aerosol extinction coefficients and define the most probable light path for the MAX-DOAS measurements. This information was then used to model NO_2 AMF ratios with TRACY that were compared to measured NO_2 DSCDs ratios ($\alpha = 2°/20°$) yielding NO_2 VCDs and approximate boundary layer heights.

Wittrock et al. (2004) and Heckel et al. (2005) used similar approaches to determine NO_2 VCDs and mixing ratios, and HCHO VCDs and mixing ratios respectively, using MAX-DOAS measurements taken in Ny-Ålesund, Norway, 2002 and in the Po-Valley, Italy, 2002. Measured O_4 VCDs were compared to VCDs calculated via a full spherical Picard iterative radiative transfer model SCIATRAN (Rozanov et al., 2001) to determine the most appropriate aerosol conditions. This

aerosol information was then used to determine NO_2 or HCHO VCDs for various modelled trace gas profiles. The modelled profiles were varied until a consistent solution between modelled and measured VCDs was found.

Sinreich et al. (2007) used MAX-DOAS to detect glyoxal (CHOCHO) in New England, USA, at the MIT campus and over the Atlantic Ocean, using the approach applied in Sinreich et al. (2005). Although the DSCD detection limits were quite high ($1\sigma = 3.00\times10^{14}$ molec cm^{-2}), CHOCHO DSCDs and VCDs were determined and shown to be substantially higher ($\sim$2.5 times higher) over the ocean than inland.

The information content gleaned from the collection of studies described above represented a significant advance from previous active or passive DOAS experiments. In particular, the NO_2, HCHO and CHOCHO VCDs determined play an important role in satellite validation. Unfortunately, performing the radiative transfer modelling was a very time consuming process, and for accurate AMF determinations several parameters such as the solar zenith angle, elevation angle, wavelength, ground albedo and multiple scattering (Mie and Rayleigh) must be considered. Different groups also utilize unique radiative transfer models (e.g. TRACY, SCIATRAN, McArtim, MCARaTS, VECTOR, LIDORT) and this may introduce further error, although comparison studies (Hendrick et al., 2006; Wagner et al., 2007) have shown good agreement between models (ranging from 2-14% depending

on conditions). Simple aerosol extinction profiles were often assumed to be either "box" profiles or those with exponential decay, and in certain studies only one DSCD/DAMF ratio was used to determine the boundary layer height (as opposed to performing inversions with multiple elevation angles). Once an aerosol extinction coefficient was determined it was used for a given time span (e.g. one complete day), although aerosol conditions often vary, and other factors such as the SZA and RAZI also vary throughout the daytime having an impact on the AMF. In principle then, the same inversion analysis has to be done for every measurement of the day, a considerable task if performed manually.

Irie et al. (2008) were the first to retrieve tropospheric aerosol profiles using MAX-DOAS measurements and radiative transfer modelling in Japan. Their approach was to model the aerosol extinction coefficient by separating the aerosol profile into three distinct regions; F_1 = 0-1 km, F_2 = 1-2 km, and F_3 = 2-3 km; plus an exponential decay starting at 3 km until 100 km. Look up tables were created using a Monte Carlo Atmospheric Radiative Transfer Simulator (MCARaTS) to create O_4 AMFs at 476 nm that correspond to various combinations of F, τ (aerosol optical depth), SZA, RAZI and EA. Then by using an optimal estimation method, measured MAX-DOAS O_4 AMFs were compared to modelled AMFs to determine aerosol extinction coefficients and aerosol profiles. Results were compared with LIDAR and sky radiometer measurements and showed good agreement

(~30%) for the F_1 region (0-1 km). Similar studies and results were found by Lee et al. (2009), who made measurements off the west coast of Korea at 356 nm, and Irie et al. (2009), who performed their retrieval again in Japan, this time at multiple wavelengths (354 and 476 nm). Since these publications, research groups in Belgium and Germany have employed other radiative transfer models (LIDORT and SCIATRAN) with similar optimal estimation methods to determine aerosol properties (Clémer et al., 2010; Rozanov et al., 2001; Zieger et al., 2011). These approaches however require the use of *a priori* values. Selecting these values is not a trivial task that can easily cause unrealistic or biased results (Frieß et al., 2006). An alternative method was developed by Li et al. (2010). This approach uses a linear least squares minimization between measured and modelled O_4 AMFs to determine aerosol properties and does not require any *a priori* assumptions. It uses a simple parameterization of the aerosol extinction coefficient with three variables: τ, the aerosol optical depth, H, the aerosol layer height, and f, the fraction of aerosol within H. Results correlated nicely with humidity-corrected nephelometer data. Furthermore, in a comparison study that took place in the Netherlands, this method proved the most accurate in determining aerosol extinction coefficient values, while alternative methods employing optimal estimation proved more accurate in determining aerosol optical depth values (Zieger et al., 2011).

In this dissertation, an original two-step approach to determine NO_2 VCDs from

MAX-DOAS measurements is outlined, applied to a data set on a routine basis, and validated with other field measurements (Halla et al., 2011). The first step makes use of measured O_4 DSCDs and the RTM McArtim (Monte carlo Atmospheric radiative transfer inversion model) to obtain aerosol conditions for each MAX-DOAS measurement, following the approach introduced by Li et al. (2010). This aerosol information is then used as input to McArtim for the calculation of NO_2 AMFs that are ultimately compared to the measured MAX-DOAS SCDs to obtain NO_2 VCDs. In addition to the NO_2 VCDs, aerosol optical depth (τ) values, aerosol layer heights (H_{aer}) and gas layer heights (H_{gas}) are also determined and compared to values determined from other standard techniques.

1.5 Dissertation Outline

MAX-DOAS measurements were taken in two unique locations in Canada: Saturna Island, British Columbia and Ridgetown, Ontario. By using the standard DOAS evaluation technique, trace gas DSCDs for NO_2, O_4 and HCHO were determined. The strength of this experimental technique was then explored by coupling the DSCDs with radiative transfer modelling and inversion techniques to yield aerosol optical depths, aerosol layer heights, NO_2 VCDs and NO_2 layer heights. These values were compared to other standard techniques such as chemiluminescence, satel-

lite DOAS and active DOAS. It is often at this point where many MAX-DOAS studies end their discussion. In this dissertation, the utility of the MAX-DOAS analytical technique is examined further and used to help describe and understand the interactions of both chemical and meteorological phenomena in the troposphere. Following this introduction, Chapter 2 describes the experimental apparatus used to make all MAX-DOAS measurements in the field, plus the DOAS fitting methods employed; Chapter 3 provides results and discussion from the Saturna field study; Chapter 4 provides results and discussion from the BAQS-Met field study; and Chapter 5 concludes the dissertation by providing general conclusions and areas to focus on in the future.

2 Experimental

2.1 MAX-DOAS Instrumental Setup

A custom MAX-DOAS instrument, built by D. Majonis, was used for both field campaigns. This instrument (Figure 2.1) used a 1 m focal length Newtonian telescope (Sky Watcher, f/5) with a 20 cm diameter primary concave mirror to measure scattered sunlight. A stepper motor controlled the elevation angle over the range of 0° (horizon) to 90° (zenith) with an error of ± 0.2°, and a custom fiber optic coupler was added into the telescope eyepiece to couple light from the secondary mirror into the fiber optic that transferred light to a miniature CCD spectrometer. Either the Ocean Optics 2000 or 2000^{+} spectrometer was used and was cooled either via a mini-fridge or Peltier cooling unit. The spectrometer data was transferred to a PC via USB connection, while a LabVIEW program, written by D. Majonis, automated the measurement sequence including light level determination, integration times, collection and storage of averaged spectra, and movement of the telescope elevation angle by stepper motor prior to the next measurement. Every

measurement began with an automatic and quick determination of light level. This information was used to adjust the integration time of the measurement automatically, ensuring that all measurements had an approximately equal level of signal. For further details with regards to the specific MAX-DOAS set ups used and supporting instrumentation present at each field study, consult the individual chapters.

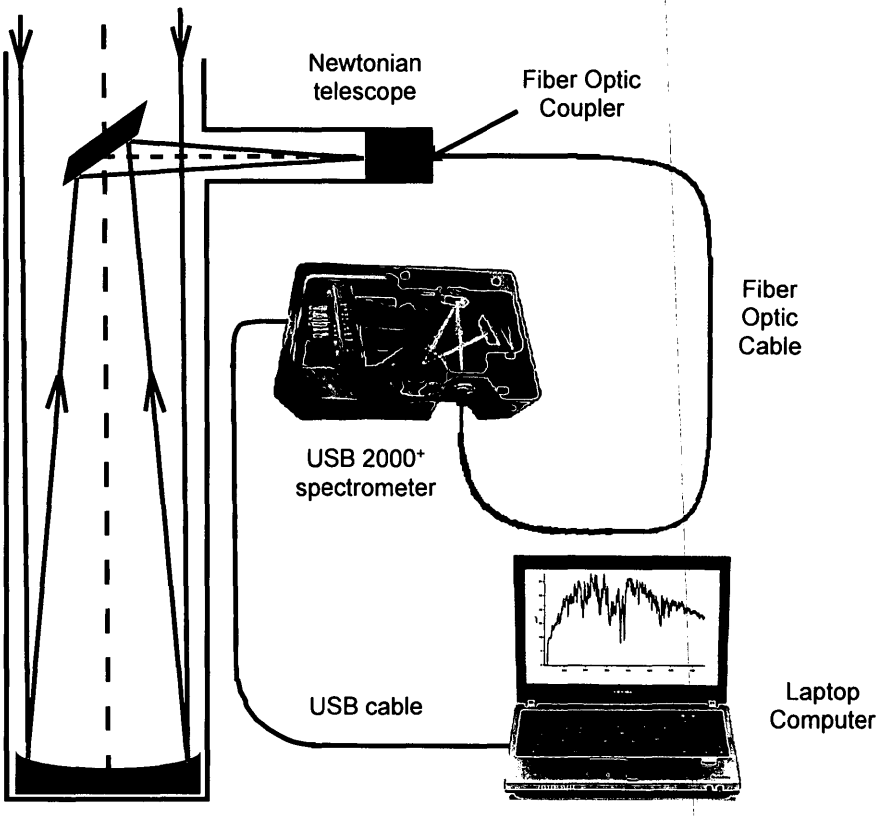

Figure 2.1: The MAX-DOAS instrumental setup.

2.2 DSCD Fit Retrievals

Two specific programs (WinDOAS and DOASIS) were used to perform DOAS fits that yielded DSCD values for NO_2, O_4 and HCHO (Fayt and van Roozendael, 2011; Kraus, 2006). Both use fitting algorithms based on the Levenberg-Marquard method (Levenberg, 1944). This method of a least squares fit uses an iterative combination of a linear component for the retrieval of the trace gas absorptions and a non-linear part that accounts for possible spectral shifts between the measured spectrum and the reference spectrum used in order to minimize the residual of the DOAS fit (Equation 1.12) and yield the required DSCDs for a given wavelength range.

However, before a raw spectrum (measured by a CCD) may be fit, it must be corrected for electronic offset and dark current. An electronic offset is an artificial electronic signal automatically added by the spectrometer to a given spectrum so that negative intensity values are not read by the detector. Negative values cannot be handled by the analog-digital converter since any negative value would be read as a "0" and introduce large error. An offset measurement is performed by measuring a spectrum in the dark with a very short integration time (IT) (e.g. 3 ms) and several scans (e.g. 10,000). Figure 2.2 gives an example of an offset spectrum for the Ocean Optics USB 2000 spectrometer. Offset decreases with increasing

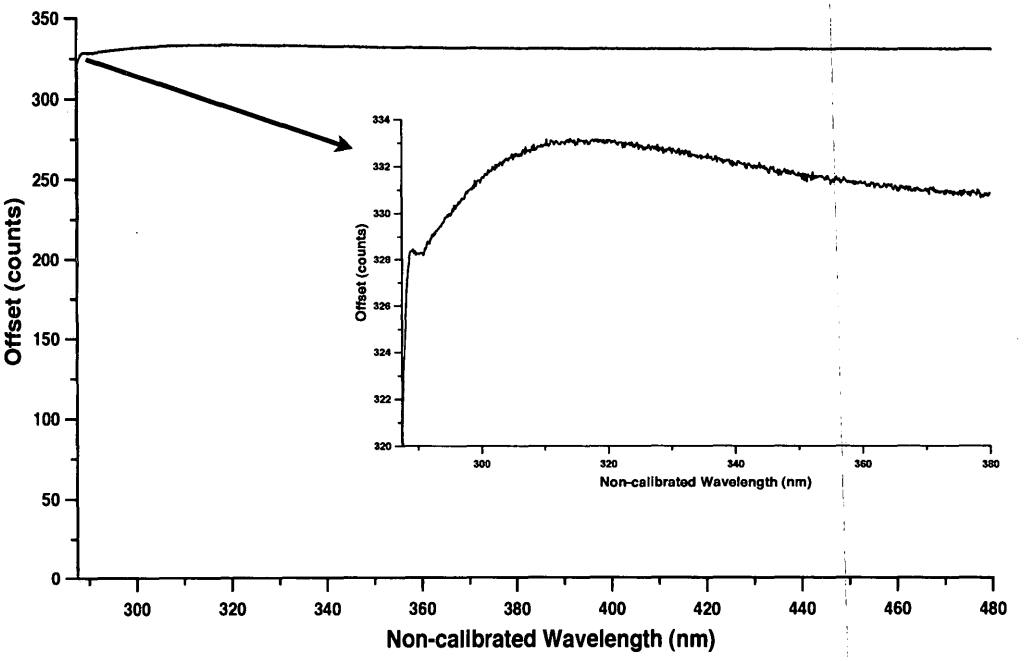

Figure 2.2: Example of an electronic offset spectrum from the USB 2000 spectrometer. This spectrum was taken in the dark using 10,000 scans and an integration time of 3 ms. The offset in this case is relatively constant around 331 counts, except for the feature seen below 290 nm to ~380 nm (see inset).

temperature (Figure 2.3B) for the USB 2000. It should be background subtracted from each raw spectrum, so that the actual signal processed is due to incoming light without any electronic background.

Dark current may be defined as the rate at which electrons accumulate in each pixel of the CCD detector due to thermal action; it is proportional to the Boltzmann factor $e^{E_i/kT}$. Figure 2.4 gives an example of a dark current spectrum from the USB

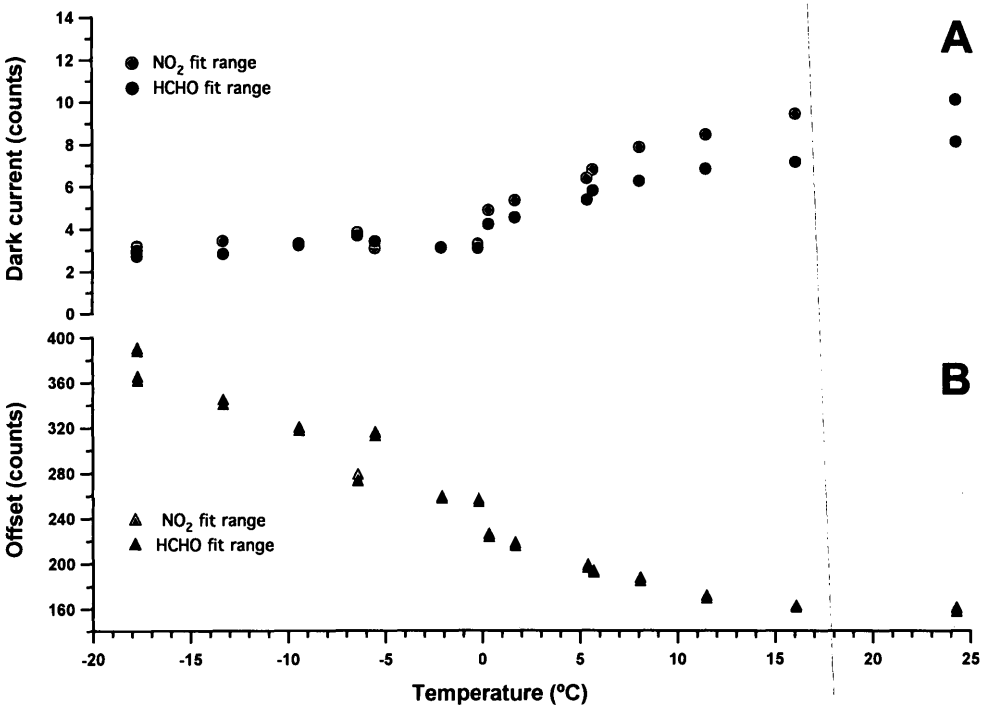

Figure 2.3: Dark current and offset for the USB 2000 spectrometer as a function of temperature. The top panel (A) shows the average dark current for two fit ranges, NO_2: 410-435 nm and HCHO: 335-357 nm; the bottom panel (B) shows the offset values for the same fit ranges.

2000. Dark current increases with the integration time of a given measurement and exponentially with temperature (Figure 2.3A). Generally, the spectrometer is cooled to lower the dark current, and one scan in the dark with a very long IT (e.g. 30 s) is performed daily to use as base for correcting dark current (DC). Individual spectra are then corrected for both offset and dark current according to

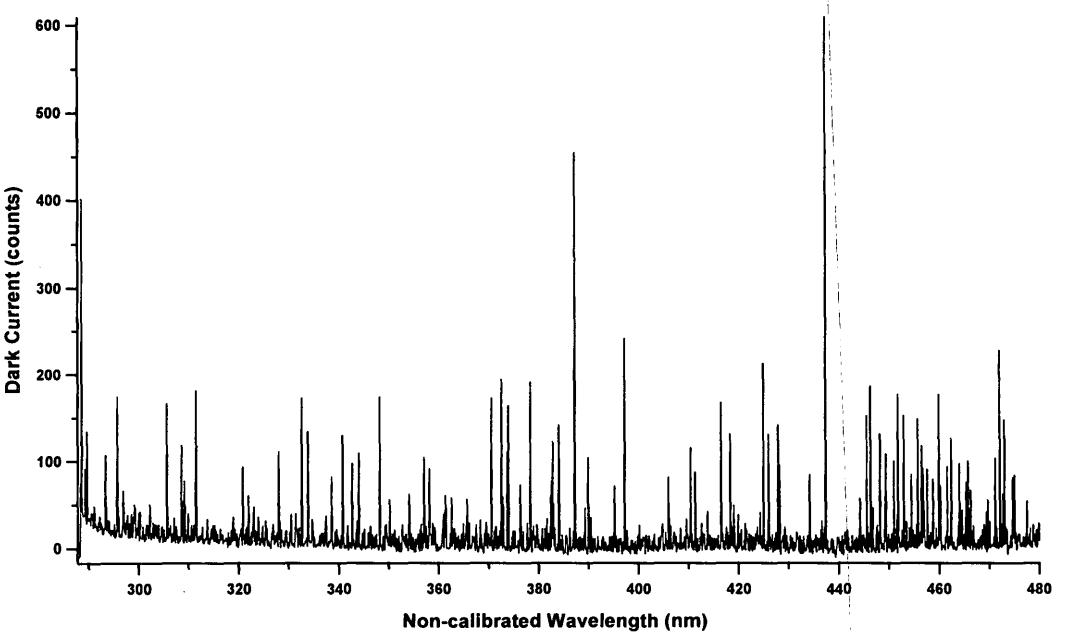

Figure 2.4: Example of a dark current spectrum for the USB 2000 spectrometer. This spectrum was taken using 1 scan and an integration time of 30 s.

the following equation:

$$M_i^* = M_i - O_i - \left[\frac{IT_i}{IT_{DC_i}}\right] DC_i \tag{2.1}$$

where M_i is the raw measurement spectrum for the i^{th} spectrum, O_i is the daily electronic offset, IT_i is the integration time (ms) of the raw measurement spectrum for the i^{th} term, IT_{DC_i} is the integration time (ms) of the dark current measurement (i.e. 30,000 ms), DC_i is the daily dark current measurement and M_i^* is the fully corrected measurement spectrum for the i^{th} term to be used in the subsequent

DOAS analysis. Although this correction is technically not 100% accurate because dark current is slightly dependent on the saturation level of each CCD pixel (Stutz, 1991), it is approximately correct.

These fully corrected spectra (M_i^*) are now fit using WinDOAS. The quality of the fit is largely governed by the choice of reference spectrum used. Fraunhofer lines are a set of several hundred dark lines that appear against the bright background of the continuous solar spectrum and are produced by the absorption of light by cooler gases in the sun's outer atmosphere at frequencies corresponding to the atomic transitions of these gases. A Fraunhofer reference spectrum (FRS) is required in every MAX-DOAS fit to account for these strong absorptions (Figure 2.5). Without such a spectrum it would be impossible to detect the much smaller absorptions for trace gases like NO_2, O_4 or HCHO. An ideal FRS is taken with an elevation angle of 90° (zenith) in a time period where there is little or no trace gas present in the most probable light path from the sun to the MAX-DOAS detector.

Furthermore, a Ring spectrum calculated directly from the chosen FRS using DOASIS, is also included as a pseudo absorber in each spectral fit (Figure 2.6). The Ring effect (Grainger and Ring, 1962) may be described as the "filling in" of Fraunhofer lines in the spectra of scattered sunlight as compared to direct sunlight. It is caused by the rotational Raman scattering of atmospheric molecules. The Ring effect reduces the optical depth of the observed Fraunhofer lines and therefore

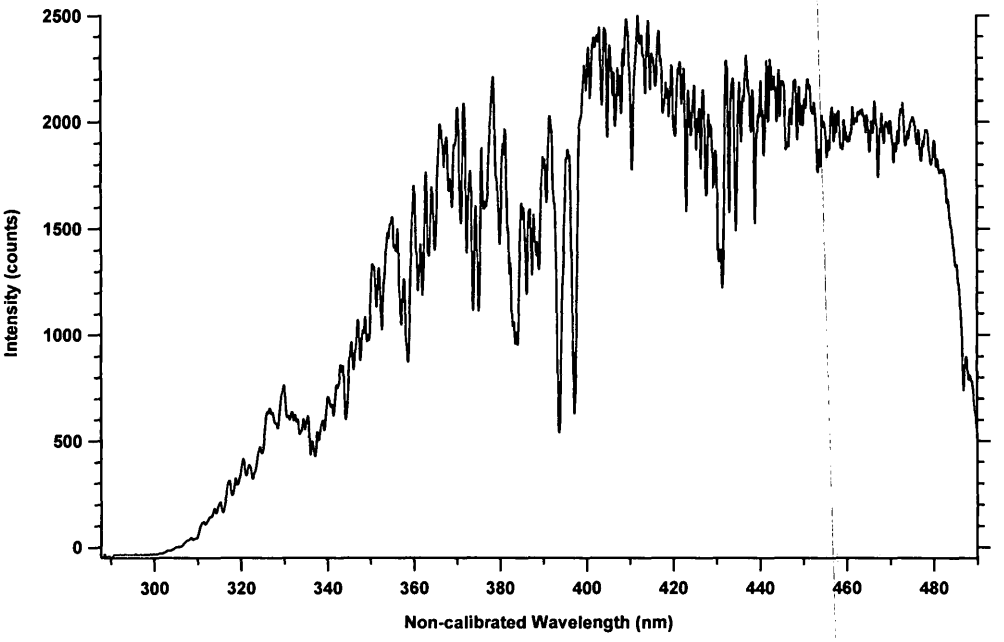

Figure 2.5: Example of a Fraunhofer Reference Spectrum (FRS) taken with the USB 2000 spectrometer. This FRS was taken on August 2, 2005 at 12:41 PDT during the Saturna Island field study.

must also be corrected for because some trace gas absorptions may be one or two orders of magnitude smaller than the Ring effect itself.

Next, all experimentally determined absorption cross sections required to fit the various trace gases species under investigation must be adapted to match the instrument's resolution. All adaptations were performed using the WinDOAS software, and all required absorption cross sections were convolved, except for O_4, which was interpolated. Convolution of the absorption cross sections is required because the laboratory instruments used to determine these cross sections have a much higher

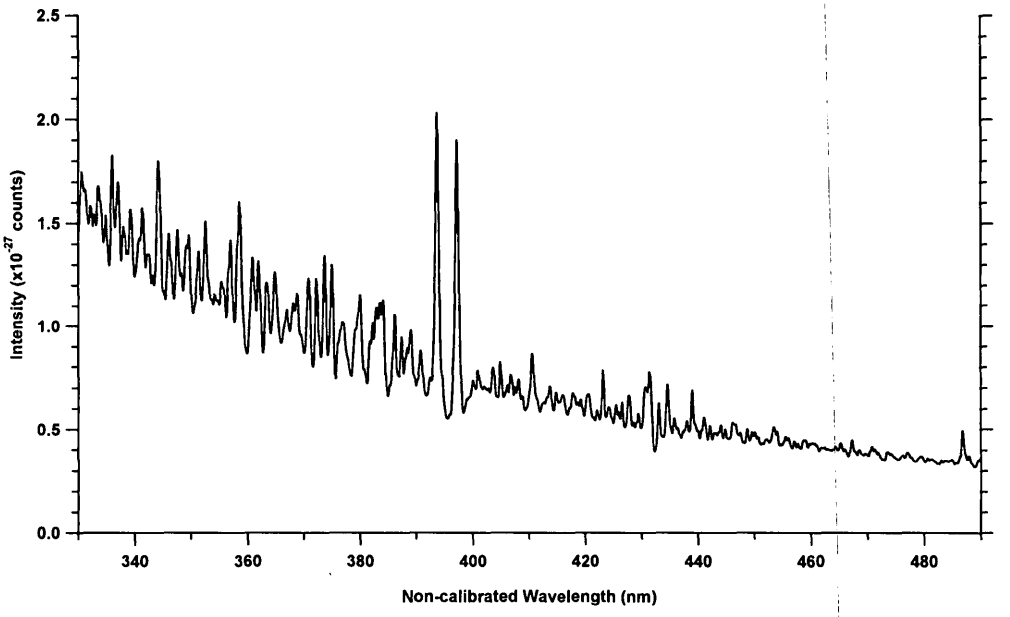

Figure 2.6: Example of a Ring spectrum created using DOASIS from an FRS taken with the USB 2000 spectrometer. The FRS used to create this Ring spectrum was taken on August 2, 2005 at 12:41 PDT during the Saturna Island field study.

spectral resolution than the spectrometer in the MAX-DOAS instrument. The slit function (represented by the full width half maximum, FWHM) used for the convolution of a particular trace gas is determined via a calibration of the FRS with the Kurucz solar spectrum (Kurucz et al., 1984) and changes as a function of temperature and wavelength (Figure 2.7). The result of such a calibration using the Ocean Optics USB 2000^{+} spectrometer on June 20, 2007 provides a Gaussian slit function (Figure 2.8) of approximately 0.50 nm for NO_2 (fit range: 410-435 nm) and approximately 0.65 nm for HCHO (fit range: 335-357 nm).

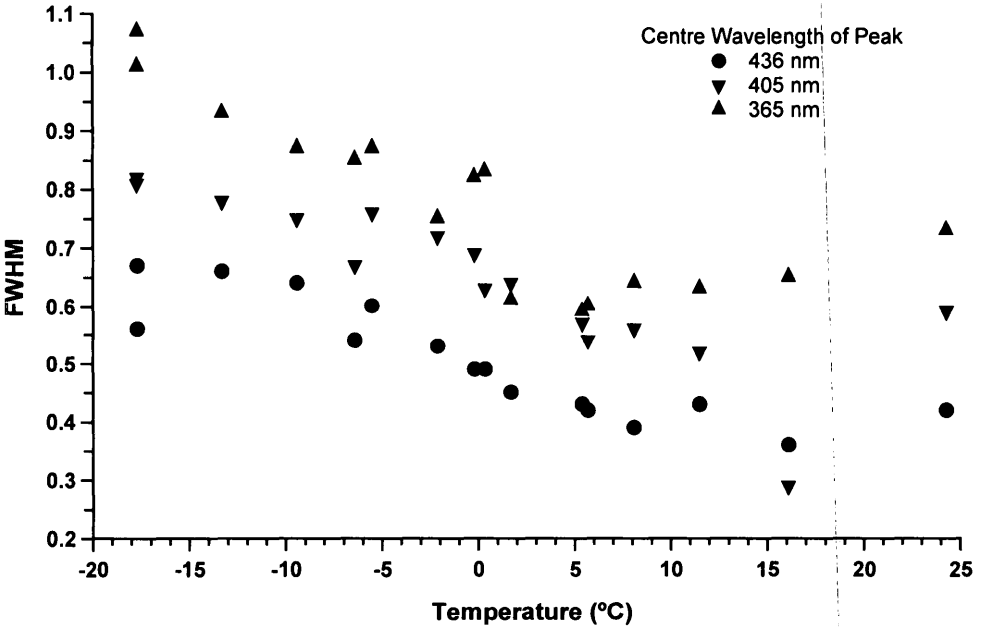

Figure 2.7: Full Width Half Maximum (FWHM) values as a function of temperature for the USB 2000. Three wavelength values representing the spectral peaks for a Mercury lamp at 436 nm, 405 nm and 365 nm are shown to demonstrate the differences in slit function with temperature and wavelength.

The actual convolution procedure uses an instrument function to broaden the features of the experimentally determined absorption cross sections:

$$\sigma^*(\lambda) = H \cdot \sigma(\lambda) = \int \sigma(\lambda') \cdot H(\lambda - \lambda') d\lambda' \tag{2.2}$$

where σ^* is the convolved absorption cross section, H the instrument function and σ the absorption cross section measured in the lab. Figure 2.9 gives an example of a NO_2 absorption cross section (Vandaele et al., 1998) and the resulting convolved NO_2 absorption cross section to be used in the subsequent DOAS fit.

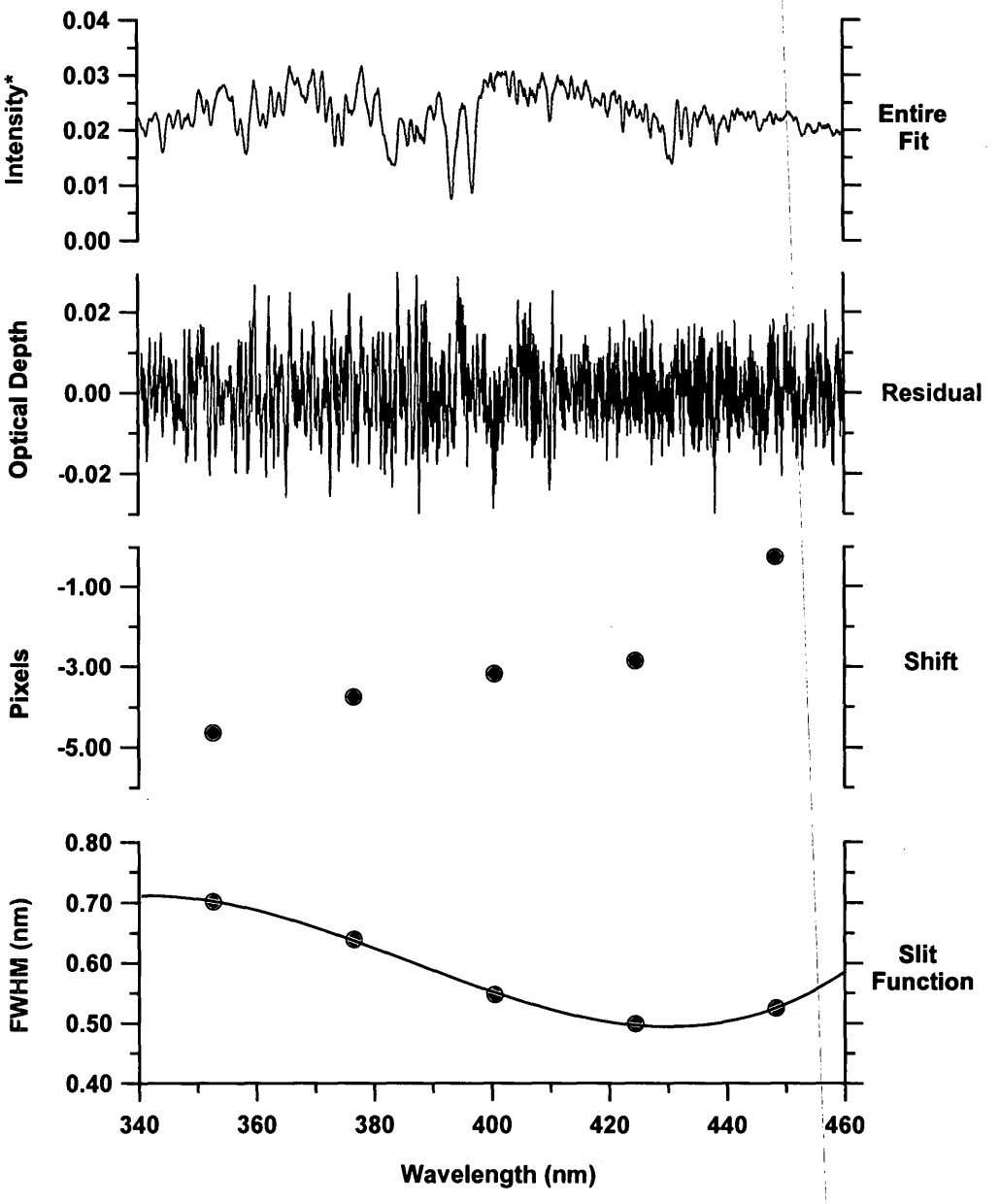

Figure 2.8: Sample of a wavelength calibration using the Kurucz spectrum and data from June 20, 2007. Each fit is done in a separate sub-window. Red lines and points represent measured values, while black lines are the corresponding fits for the respective items shown. The units for the entire fit are arbitrary units of intensity, while the units for the residual are optical depth units.

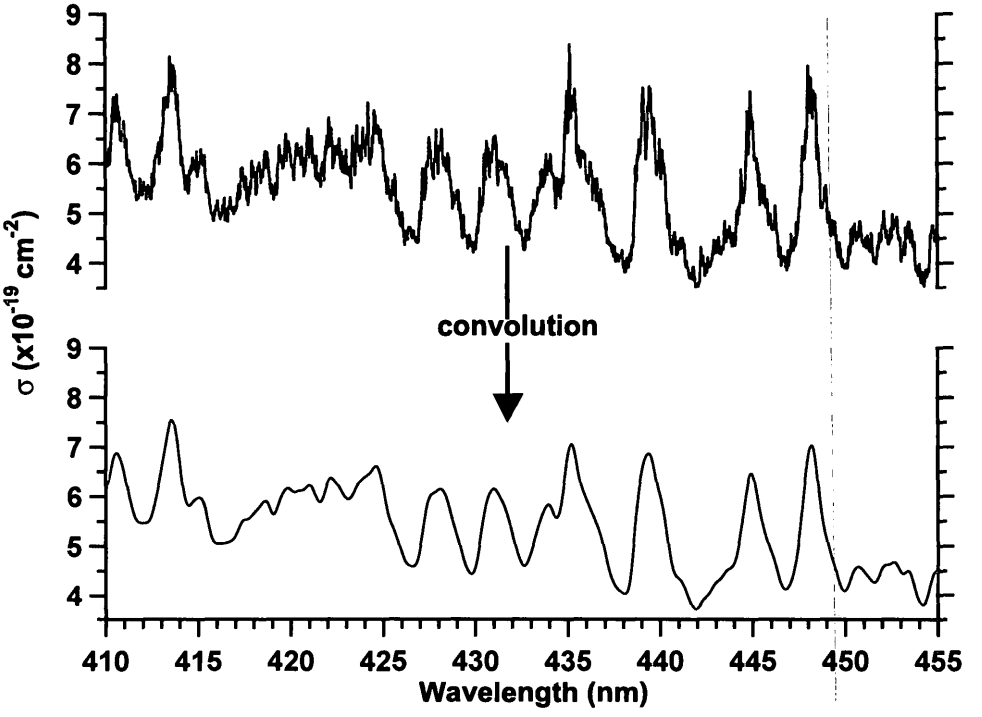

Figure 2.9: Sample of NO_2 absorption cross section (σ) before and after convolution. The original NO_2 absorption cross section used was taken from Vandaele et al. (1998).

For some convolved absorption cross sections, such as NO_2 and O_3, a further correction is required that takes into account the solar I_0 effect. The solar spectrum (I_0 spectrum) has a large variation in its intensity due to the Fraunhofer lines (the absorption and emission lines from the sun). This causes a discrepancy between the absorption of traces gases measured in the field using scattered sunlight and their absorption measured in the laboratory using a light source with a constant spectrum. To correct for the I_0 effect, a new I_0-corrected convolved cross section

is used for NO_2 and O_3 only, and was calculated with WinDOAS according to the following equations (Johnston, 1996):

$$\sigma^*_{I_0}(\lambda, T, P, SCD) = -ln\left[\frac{I^*(\lambda)}{I^*_0(\lambda)}\right] \cdot \frac{1}{SCD} \tag{2.3}$$

where

$$I^*_0(\lambda) = I_0(\lambda) \cdot H \tag{2.4}$$

$$I^*(\lambda) = H \cdot I(\lambda) = H \cdot (I_0(\lambda) e^{-\sigma(\lambda,T,P)\cdot SCD}) \tag{2.5}$$

and $\sigma^*_{I_0}$ is the I_0-corrected convolved cross section, $I^*_0(\lambda)$ is a convolved high resolution solar spectrum, $I^*(\lambda)$ is a convolved synthetic absorption spectrum calculated from $I_0(\lambda)$, the high resolution solar spectrum (Kurucz et al., 1984) and the absorption of the trace gas under investigation for a given slant column density. The SCD values used for NO_2 and O_3 were 2.5×10^{16} molec cm^{-2} and 1.0×10^{20} molec cm^{-2} respectively, typical values for most environments. This correction is only required for NO_2 and O_3 because for other trace gases their absorptions are either too weak or their absorption structures are too broad-banded for the absorption signal to change significantly due to the I_0 effect.

Finally, once the raw spectra are corrected for dark current and offset, an appropriate FRS and Ring spectra are prepared, and the required cross sections are convolved, WinDOAS was used to determine DSCDs for the trace gas species under investigation within wavelength ranges that have the strongest differential struc-

tures. A "DOAS" polynomial was chosen (3rd or 4th order) to remove the broad band component (Chapter 1, Section 1.3) and an additional polynomial was added to remove effects from stray light. For example, NO_2 is typically fit in the wavelength range 410-435 nm with a 3rd order polynomial, convolved NO_2 and O_3 spectra, and appropriate FRS and Ring spectra. Further details with respect to the specific fitting scenarios for NO_2, O_4 and HCHO for the Saturna Island and Ridgetown data sets may be found within those individual chapters.

2.2.1 DSCD Variations

As described earlier, the primary result of a MAX-DOAS retrieval is the differential slant column density (DSCD):

$$DSCD = SCD_{\alpha} - SCD_{90} \tag{1.14}$$

$$DSCD = SCD_{\alpha} - FRS \tag{1.15}$$

As can be seen in Chapter 1, Figure 1.5, the DSCD depends on the trace gas amount, α, ϑ, ϕ and the FRS used. Ideally, the FRS subtracted should be taken at exactly the same time so that the above variables are identical, but in practice the FRS is usually taken after a series of lower angle measurements. If the time difference between these measurements is small this approach is valid. For example,

in the case of NO_2, a single FRS (a 90° spectrum taken near solar noon) may be used for all fitting scenarios:

$$DSCD_k = SCD_\alpha - SCD_{90} = SCD_\alpha - FRS_k \tag{2.6}$$

where the SCD_α represents the slant column density measured at elevation angles not equal to 90° and FRS_k is the slant column density of a 90° elevation angle measurement. NO_2 $DSCD_k$ fits were exclusively used during the BAQS-Met field study (Chapter 4).

Ideally, the FRS would be absorption free. However, in the absence of such a spectrum, the FRS, taken as a zenith measurement at solar noon on a clean day, is used as the background for all NO_2 fitting scenarios. The light path through the stratosphere varies greatly as a function of SZA, with a large increase in path length for glancing angles of solar light through the atmosphere. As a result, there is a large enhancement in the NO_2 DSCDs during twilight periods in the early morning and evening, when using this noon-hour FRS exclusively. In order to determine the tropospheric DSCD, this "stratospheric effect" for trace gases like NO_2 that are abundant in the stratosphere, must be accounted for. To do this a polynomial is fit to all 90° measurements for each day as a function of time (t) (Figure 2.10). The value of this polynomial was subtracted from each measurement (with $\alpha < 90°$) to

yield a tropospheric DSCD*:

$$DSCD^*(t) = DSCD(t) - poly(t) \tag{2.7}$$

Finally, when using a FRS reference spectrum, there is still a small amount of absorption due to the troposphere gas present in this relatively short path. To further correct the DSCD* an additional term was added to yield the fully corrected tropospheric ΔSCD:

$$\Delta SCD = DSCD^* + ADD \tag{2.8}$$

where ADD is an additional term used to estimate the amount of tropospheric trace gas in the FRS. This procedure was exclusively used for the NO_2 ΔSCDs determined during the Saturna field study.

Alternatively, a daily FRS, taken under the same conditions was used to determine $DSCD_d$ values for O_4 and HCHO:

$$DSCD_d = SCD_\alpha - SCD_{90} = SCD_\alpha - FRS_d \tag{2.9}$$

where FRS_d is the slant column density of a daily 90° elevation angle measurement taken at a time closest to solar noon each day. The $DSCD_d$ may be considered an alternative form of the differential slant column density.

A third approach may be used in cases where high precision is required. In this case, a "closest in time" 90° measurement from the same series (e.g. α = 90°, 30°,

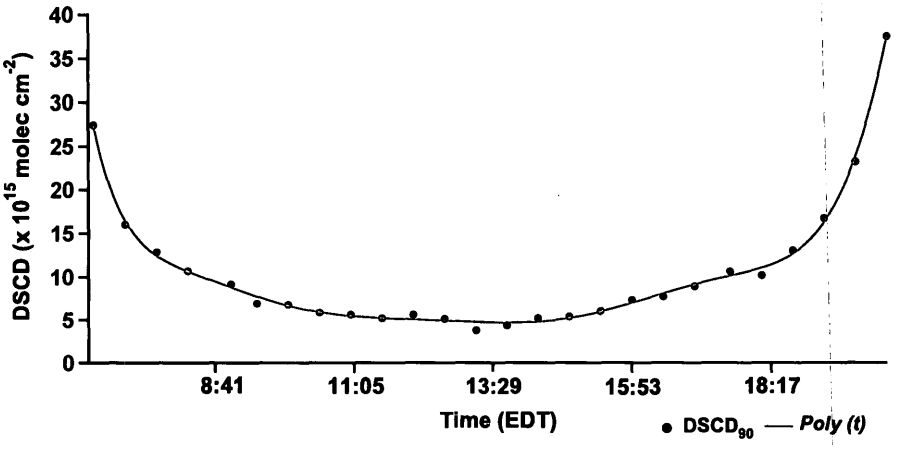

Figure 2.10: Example of a polynomial correction, *poly(t)*, for $DSCD_k$ or $DSCD_d$. This polynomial correction was used for June 29, 2007 at Ridgetown. Solar noon on this day was at 13:29 EDT.

10°, 6°, 4°, 2°) is used as the FRS reference to be included in the fit scenario for all other members of the series, yielding the $DSCD_s$:

$$DSCD_s = SCD_\alpha - SCD_{90} = SCD_\alpha - FRS_s \tag{2.10}$$

where FRS_s is the slant column density of the 90° elevation angle measurement for the given series under investigation.

Lastly, in some cases a similar quantity known as dSCD was calculated:

$$dSCD = DSCD_\alpha - DSCD_{90} \tag{2.11}$$

Both the $DSCD_s$ and the dSCD have the advantage of eliminating the "stratospheric effect". The dSCD is often easier to calculate however, since either $DSCD_k$ or $DSCD_d$ values can yield dSCDs quickly, as opposed to fitting each measurement

series with a new FRS, which is very time consuming if done manually. The $DSCD_s$ and dSCD may be considered alternative forms of the differential slant column density, analogous to $DSCD_k$ or $DSCD_d$.

In the following chapters, when generally describing the differential slant column density, the term DSCD will be used. In this context, it will encompass the $DSCD_k$, $DSCD_d$ and $DSCD_s$ cases. However, when dealing with individual trace gases (NO_2, O_4, HCHO) the use of $DSCD_k$, DSCD*, ΔSCD, $DSCD_d$ and dSCD will be used to differentiate the exact method used to determine the differential slant column density for that particular gas. It should be noted that for the $DSCD_k$ and $DSCD_d$ cases, the time dependent stratospheric correction (yielding DSCD*) is required for trace gases that absorb in the stratosphere, and the corresponding polynomial is subtracted. When determining the $DSCD_s$ or dSCD no further correction is required since the stratospheric contribution is cancelled out, provided the time difference between the SCD_α and SCD_{90} measurement is small. As such, the final DSCD found (regardless of the method applied) contains mainly the tropospheric component of the gas in question, and may be considered a $DSCD_{trop}$ value. The $DSCD_{trop}$ values determined during two distinct field studies were interpreted whenever possible, and during the BAQS-Met study they were also used for comparison to DAMFs determined via radiative transfer modelling.

3 Saturna Island Field Study

3.1 Introduction

The Lower Fraser Valley (LFV) is composed of the part of southwestern BC spanning the Canada/US border at 49°N that includes Vancouver and the surrounding communities that extend northward to the Coast Mountains, southward to the Cascade Ranges and eastward until the city of Hope (Figures 3.1 and 3.8). Its topographic features, which are similar to the Los Angeles basin, lead to complex meteorology and air pollutant transport (Snyder and Strawbridge, 2004). The region experiences the interaction of urban, suburban, marine, biogenic and agricultural emissions of pollutants and their subsequent transformation in ambient air. In the summertime, the valley experiences episodes of elevated ozone and fine particulate matter (PM) producing smog that results in reduced visibility and harmful health effects (Brauer and Brook, 1997). Not surprisingly then, two major intensive field campaigns have been conducted in the LFV with the goal of understanding the chemistry and meteorology involved in the formation and transport of ozone and

aerosols in this region, PACIFIC '93 and 2001 (Li, 2004; Steyn et al., 1997).

For three weeks during the summer of 2005, active and MAX-DOAS instrumentation was set up on Saturna Island, one of the Gulf Islands located in the Strait of Georgia. From this vantage point, nighttime NO_3 and NO_2 mixing ratios were measured via active DOAS and used to determine the N_2O_5 in the MBL, and assess its role in the nighttime chemistry and halogen activation while etablishing its link to the air quality in the LFV (McLaren et al., 2010). Furthermore, using the HONO and NO_2 active DOAS nighttime results, a new conceptual model for HONO formation on aqueous surfaces was recently proposed (Wojtal et al., 2011). This chapter however, will focus solely on the interpretation of NO_2 slant column densities determined from MAX-DOAS measurements at Saturna. It will: *i*) examine the diurnal NO_2 slant column density profile, *ii*) examine the potential difference between weekday and weekend measurements, *iii*) establish a link between NO_2 slant columns densities in the Strait of Georgia and maximum ozone levels in the LFV, *iv*) determine the significance of the stagnation of pollutants in the Strait of Georgia in relation to the build-up and processing of air pollutants, and *v*) use a case study to highlight the unique information content gleaned from MAX-DOAS that is not available from other point-source measurements.

3.2 Experimental

3.2.1 East Point, Saturna Island

DOAS measurements were taken at a ground site 23 m *asl* located at East Point, Saturna Island (48.79°N, 123.22°W). An Environment Canada weather station, at a height of 24.4 m *asl*, is also located at East Point, in close proximity to the MAX-DOAS and active DOAS telescopes (48.78°N, 123.04°W). Meteorological observations from this station, including wind direction and wind speed were obtained from the National Climate Data Archive (EC, 2012). Saturna Island is situated at the confluence of the northwest-southeast and northeast-southwest arms of the Strait of Georgia (Figure 3.1). It is between the Lower Mainland of BC (which is 20 km to the east) and Vancouver Island, has an area of 96 km^2, and a permanent population of 350. There are very few direct anthropogenic sources on the island, especially at East Point, although the site is directly influenced by marine vessel traffic, since major international shipping channels that lead to the Strait of Juan de Fuca and the open Pacific Ocean pass closely by. The identity, distance and direction to major urban areas from the measurement site include: Vancouver, BC (55 km NNW), Victoria, BC (46 km SSW), Bellingham, WA (41 km E) and Seattle, WA (142 km SSE).

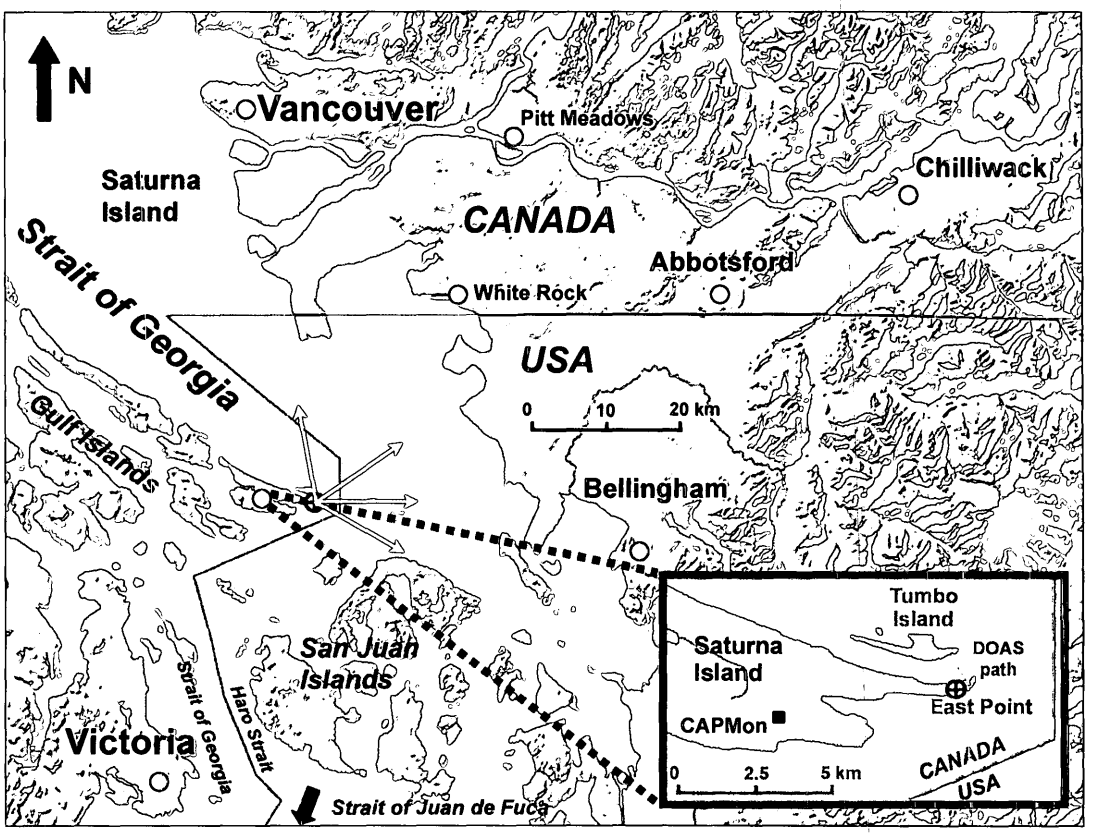

Figure 3.1: Saturna Island and the surrounding region. The MAX-DOAS instrument was located at East Point, adjacent to the active DOAS telescope. Yellow arrows identify the various directional headings the MAX-DOAS was pointed. The inset identifies the exact location of the active DOAS telescope at East Point, Saturna, while its retro-reflector was on Tumbo Island.

3.2.2 The MAX-DOAS Instrument and Retrieval

The general MAX-DOAS instrumental set up used at East Point was described in detail in Chapter 2 (see Section 2.1 and Figure 2.1) . A Newtonian telescope used a

stepper motor to control the elevation angle from 0° to 90° with an error of ±0.2°. For these experiments the fiber optic had a 400 μm diameter and was optimized for λ = 250-800 nm, while the spectrometer employed was the Ocean Optics USB 2000 with a grating #10 and a 25 μm slit, optimizing it for use in the wavelength range of 288-492 nm. The spectrometer was cooled using a mini-fridge to approximately -5°C, while the elevation angles were varied and the data was acquired using the custom LabVIEW program described earlier. The series of elevation angles chosen and the directional headings for these measurements were varied often. The specific combinations headings and elevation angles used each day may be seen in Table 3.1. Measurements were made from July 21 to Aug 8, 2005. Sunrise and sunset (PDT ≡ Pacific Daylight Time = UTC-7) at this location during the period were 5:46 (±11 min) and 20:51 (±11 min) respectively.

All spectra were corrected by subtracting an electronic offset and dark current (see Chapter 2, Section 2.2). These corrected spectra were then analyzed using the well-known DOAS technique (Plane and Smith, 1995; Platt, 1994; Platt and Stutz, 2008). A wavelength calibration using WinDOAS (Fayt and van Roozendael, 2011) was performed by fitting a noon-time (12:41 PDT) zenith FRS_k taken on a clean day (August 2, 2005), to a high resolution solar spectrum (Kurucz et al., 1984) that was convolved with the instrument's slit function. A Ring spectrum (Grainger and Ring, 1962) was calculated from the FRS_k with DOASIS (Kraus, 2006). The

Table 3.1: Headings and elevation angle series used at East Point, 2005

Date	Heading	EA Series
21/07	330°	(2°-90°)
22/07	330°	(90°-20°-10°-5°-2°), (90°-20°-10°-5°-0°),(2°-90°)
23/07	330°	(2°-90°),(90°-20°-10°-5°-1°),(1°-90°)
24/07	65°	(1°-90°)
	90°,135°	(1°-90°-1°)
	330°	(90°-20°-10°-5°-1°)
25/07	330°,135°,65°	(90°-20°-10°-5°-1°)
26/07	330°	(90°-20°-10°-5°-1°)
27/07	330°	(90°-20°-10°-5°-1°)
	330°,65°	(90°-1°-1°-5°-10°-20°)
28/07	65°	(90°-1°-1°-5°-10°-20°)
	65°,330°,90°,135°	(90°-0.5°-1.25°-2°-2.75°-3.5°-4.25°-5°)
29/07	330°	(90°-0.5°-1.25°-2°-2.75°-3.5°-4.25°-5°)
30/07	330°,65°	(90°-0.5°-1.25°-2°-2.75°-3.5°-4.25°-5°)
31/07	65°	(90°-0.5°-1.25°-2°-2.75°-3.5°-4.25°-5°)
01/08	330°	(90°-0.5°-1.25°-2°-2.75°-3.5°-4.25°-5°)
02/08	65°	(90°-0.5°-1°-1.5°-2°-2.5°-3°-4°-5°), (90°-60°-40°-20°)
03/08	65°,330°	(90°-0.5°-1°-1.5°-2°-2.5°-3°-4°-5°)
	65°	(90°-60°-40°-20°)
04/08	330°	(0.5°-1°-1.5°-2°)
	135°,65°	(90°-0.5°-1°-1.5°-2°-2.5°-3°-4°-5°)
05/08	65°	(90°-0.5°-1°-1.5°-2°-2.5°-3°-4°-5°), (1°-90°)
	330°	1° (repeating), (90°-0.5°-1.25°-2°-2.75°-3.5°-4.25°-5°)
06/08	65°	(90°-0.5°-1°-1.5°-2°-2.5°-3°-4°-5°)
	65°,330°	(90°-1°)
07/08	65°,90°	(90°-0.5°-1°-1.5°-2°-2.5°-3°-4°-5°)
	135°,330°	(90°-1°)
08/08	65°	(90°-1°)

NO_2 and O_3 (223 K and 243 K) absorption cross sections (Bogumil et al., 2003; Vandaele et al., 1998) were convolved (including the I_0 effect) using WinDOAS to match the instrument's resolution, while the O_4 cross section (Greenblatt et al., 1990) was interpolated. To determine the NO_2 $DSCD_k$ for each spectrum, a 3rd order polynomial, the logarithm of the FRS_k, the Ring spectrum, convolved NO_2, convolved O_3 (223 K) and an additive polynomial (stray light) were fit to the logarithm of the corrected measurement spectrum using WinDOAS in the fit range 410-435 nm. Figure 3.2 gives a sample fit yielding a NO_2 $DSCD_k$ of 5.03×10^{16} molec cm^{-2} on Aug 6, 2005, 14:23 PDT with an elevation angle of 1°. The NO_2 $DSCD_k$ detection limit was $\sim7\times10^{15}$ molec cm^{-2} calculated using two times the average fit error. All NO_2 $DSCD_k$ values at East Point were converted to ΔSCDs using the procedure described in Chapter 2, Section 2.2.1. Specifically, $DSCD^*$ values were determined by subtracting time dependent polynomial values from the $DSCD_k$ values. The polynomial used was determined from fitting the FRS spectra taken on August 1, 3, 4 and 5. Finally, ΔSCDs were determined by adding a constant value (ADD = 1.31×10^{15} molec cm^{-2}). This ADD value was determined by using the ground level NO_2 mixing ratio from active DOAS (2.1 ppb) at the time of the FRS_k measurement and assumed that the tropospheric component of FRS_k had a light path of 250 m.

To determine the HCHO $DSCD_d$ for each spectrum, a 4th order polynomial,

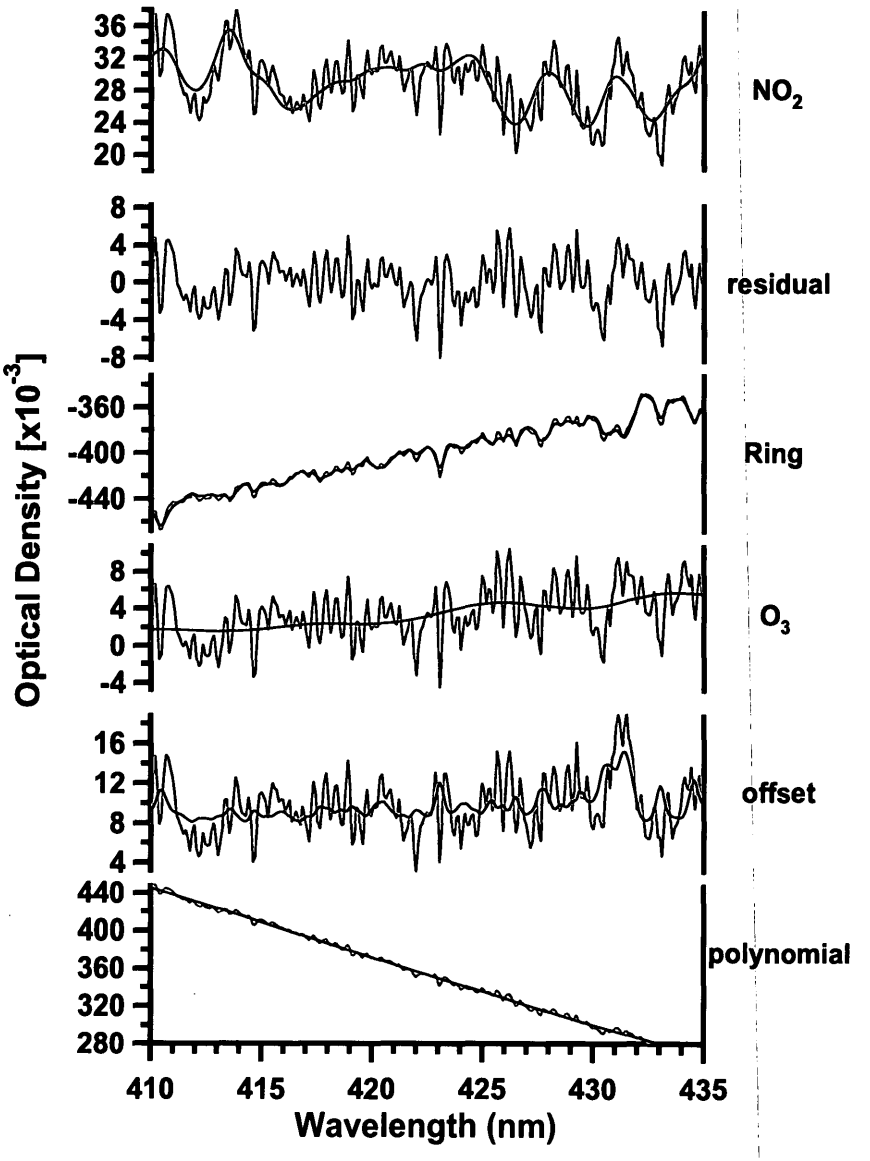

Figure 3.2: NO_2 MAX-DOAS fit retrieval for a measurement with $\alpha = 1°$ on Aug 6, 2005, 14:23 PDT. This fit, performed between 410-435 nm, includes the NO_2 and O_3 absorption cross sections, plus a 3rd order polynomial, offset polynomial, FRS_k, and Ring. The residual of the fit is shown in the second panel. For each remaining panel the black line represents the DOAS fit, and the red line represents the DOAS fit plus the residual of the species examined.

the logarithm of the FRS_d, the Ring spectrum, interpolated O_4, convolved NO_2, convolved O_3 (223 K and 243 K), convolved BrO (Wilmouth et al., 1999), convolved HCHO (Meller and Moortgat, 2000), and an additive polynomial were fit to the logarithm of the corrected measurement spectrum using WinDOAS in the fit range 335-357 nm. Figure 3.3 gives a sample HCHO fit for Aug 5, 2005, 17:58 PDT with an elevation angle of 3.5° that yields a $DSCD_d$ of 8.90×10^{16} molec cm^{-2}. The HCHO $DSCD_d$ detection limit was $\sim 3 \times 10^{16}$ molec cm^{-2} calculated using two times the average fit error. All HCHO $DSCD_d$ values were converted to dSCDs, as described in Chapter 2, Section 2.2.1. Table 3.2 gives a summary of the fit ranges, cross sections, FRS, Ring, and polynomials used for NO_2 and HCHO.

Table 3.2: MAX-DOAS fit scenario overviews for NO_2 and HCHO.

Trace Gas Fit	Fit Range (nm)	Cross Sections in the fit scenario	FRS and Ring	Degree of Polynomials	Offset Polynomial
NO_2	410-435	NO_2 & O_3(223 K)	August 2	3rd	constant
HCHO	335-357	HCHO, NO_2, BrO O_3(223K, 243 K), O_4	Daily	4th	constant

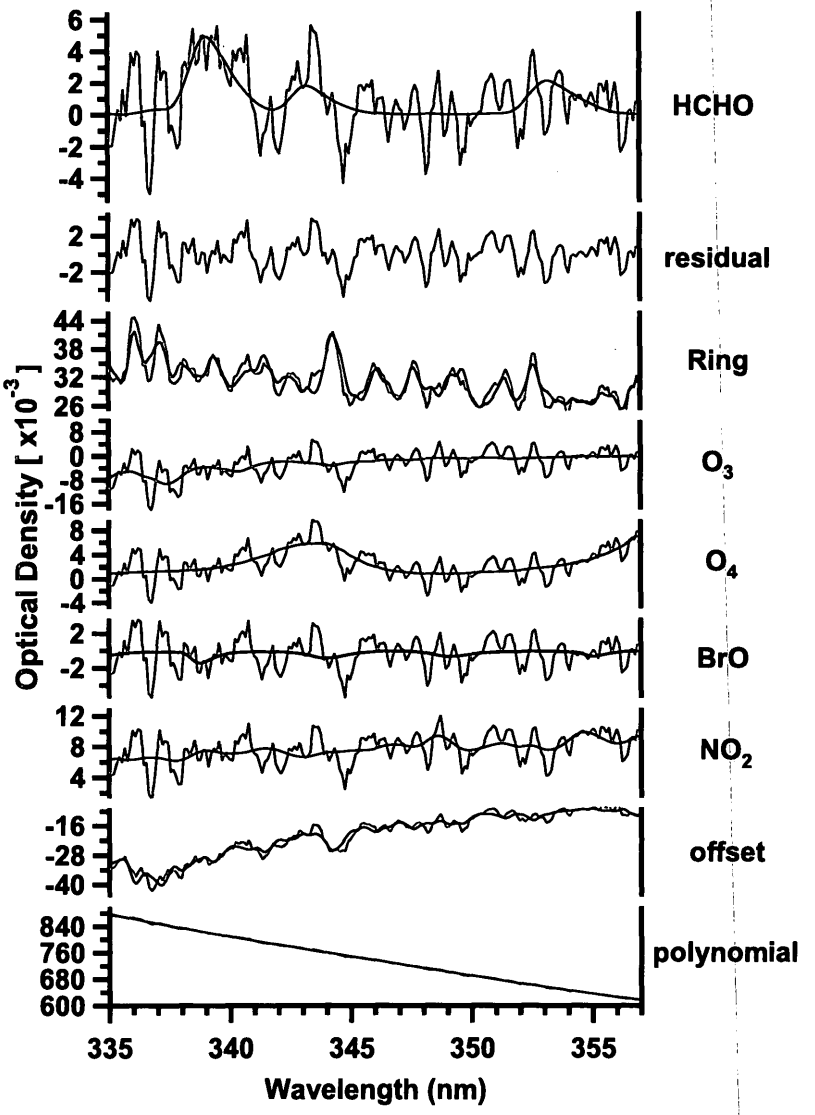

Figure 3.3: HCHO MAX-DOAS fit retrieval for a measurement with $\alpha = 3.5°$ on August 5, 2005, 17:58 PDT. This fit, performed between 335-357 nm, includes the HCHO, O_4, NO_2, BrO and two O_3 absorption cross sections (shown here as the difference between them), plus a 4th order polynomial, offset polynomial, FRS_d, and Ring. The residual of the fit is shown in the second panel. For each remaining panel the black line represents the DOAS fit, and the red line represents the DOAS fit plus the residual of the species examined.

3.2.3 The Active DOAS Instrument and Retrieval

DOAS measurements were made using a modified DOAS 2000 instrument by TEI (Chapter 1, Figure 1.4). The instrument utilizes a 150 W high pressure Xe-arc lamp and a coaxial Cassegrain telescope. The outgoing beam is collimated by the outer portion of the 20 cm primary telescope mirror. The beam traverses through the open atmosphere and is reflected from a retro-reflector composed of 7 × 5 cm corner cube reflectors. The DOAS retro-reflector was located on Tumbo Island (Figure 3.1, inset) at an elevation of 6 m *asl.* The total path length was 2.4 km, with the majority of the path (2.1 km) over the ocean at a mean elevation of 15 m *asl.* The return beam is focused by the inner portion of the primary mirror onto a modified detector system including a bifurcated quartz fiber optic (Ocean Optics) with dual 400 μm fibers, each fiber leading to a different fiber optic spectrometer. One spectrometer was optimized for NO_2 and UV absorption features (USB 2000, grating #10, 288-492 nm, 1800 lines mm^{-1}, 2048 element CCD, 25 μm slit, UV2 upgrade, L2 lens) with optical resolution of ~0.8 nm and one was optimized for NO_3 absorption in the red end of the visible spectrum (S2000, λ_{blaze} = 750 nm, 550-835 nm, 1200 lines mm^{-1}, 2048 element CCD, 25 μm slit, L2 lens) with an optical resolution of ~0.6 nm. A small diffuser was installed in the entrance end of the fiber to lower atmospheric turbulence noise (Stutz and Platt, 1997). The

spectrometers were both cooled to -5°C in a portable freezer.

The measured spectra were fit for NO_2 using two methods depending on which spectrometer was connected to the DOAS telescope. When using the S2000 spectrometer during the daytime (~6:00-21:00 PDT), the fit was performed by Joy McCourt using custom software designed by TEI Inc., and included a convolved NO_2 spectrum (Voigt et al., 2002), a lamp reference and a low-pass filter (which acted as the DOAS polynomial) in the fit range 422.7-438.3 nm. When using the USB 2000 spectrometer during twilight hours (~6:00-8:00 PDT and ~19:00-21:00 PDT), the fit was performed by Patryk Wojtal using DOASIS, and included a convolved NO_2 spectrum (Voigt et al., 2002), a lamp reference, and a 3rd order DOAS polynomial in the region from 422-435.5 nm. The NO_2 detection limit was ~2 ppb, taken as 2σ of the residual of an average fit.

3.3 Interpretation of NO_2 ΔSCDs and VCDs

3.3.1 Overview of ΔSCDs

Figure 3.4 provides an overview of the NO_2 ΔSCDs obtained under cloud-free conditions during the entire field study. Since there were no rainy days or power outages during the campaign, the only missing daytime periods were from July 22-24 when instrumental errors led to uncertain results, namely ΔSCD_{90} values that were

substantially higher than the ΔSCD_{90} values determined during the rest of the campaign. The cause for this "baseline shift" was unknown and these suspect results were subsequently discarded. It should be mentioned here that all measurements taken during the study at the 0.5° elevation angle (see Table 3.1) were not included in Figure 3.4 as they were found to be unreliable and were discarded. Aside from a few exceptions, the ΔSCDs measured at this angle were consistently lower than measurements at higher EAs within the same measurement series. To help explain this trend, the radiance (when $\lambda \approx 340$ and ≈ 480 nm) of these measurements was examined. It was found that the radiance at 0.5° was significantly smaller than the radiance for the higher elevation angles. Based on this result it is reasonable to conclude that when $\alpha = 0.5°$ the telescope collected some light that did not travel exclusively through the air just above the ocean, and may have collected some light that had been reflected from the ocean's surface. All other MAX-DOAS measurements taken during the study at higher EAs were included since their radiance was found to be significantly larger than the 0.5° measurements.

The remaining NO_2 ΔSCDs ranged from 0-2.6×10^{17} molec cm^{-2}, while the ΔSCDs within a given measurement sequence often varied substantially with EA. For example, the average $DSCD_1$ was 1.1×10^{17} molec cm^{-2} while the average $DSCD_5$ was 4.0×10^{16} molec cm^{-2}, for the entire study. For most individual measurement series (Table 3.1) the NO_2 ΔSCDs determined were larger for lower ele-

vation angles. This is to be expected because usually the tropospheric light path is much larger for smaller EAs than larger EAs. Figure 3.5 plots the NO_2 ΔSCDs vs. EA (α = 1°, 2° and 5°) in a box and whisker format, for all valid measurements made during the study, whereby the top of each box represents the 75th percentile, the middle line within each box is the median, the bottom of each box is the 25th percentile and the error bars represent the 95th and 5th percentile for each EA. This figure clearly shows that the 95th, 75th, 50th, 25th and 5th percentile NO_2 ΔSCD levels all become progressively smaller when α is increased from 1° to 5°. This is in agreement with a geometrically approximated AMF for a tropospheric absorber, which assumes a homogeneous air mass and single scattering, and predicts that the average tropospheric light path increases with decreasing EA according to a $1/\sin\alpha$ dependence (Chapter 1, Equation 1.19).

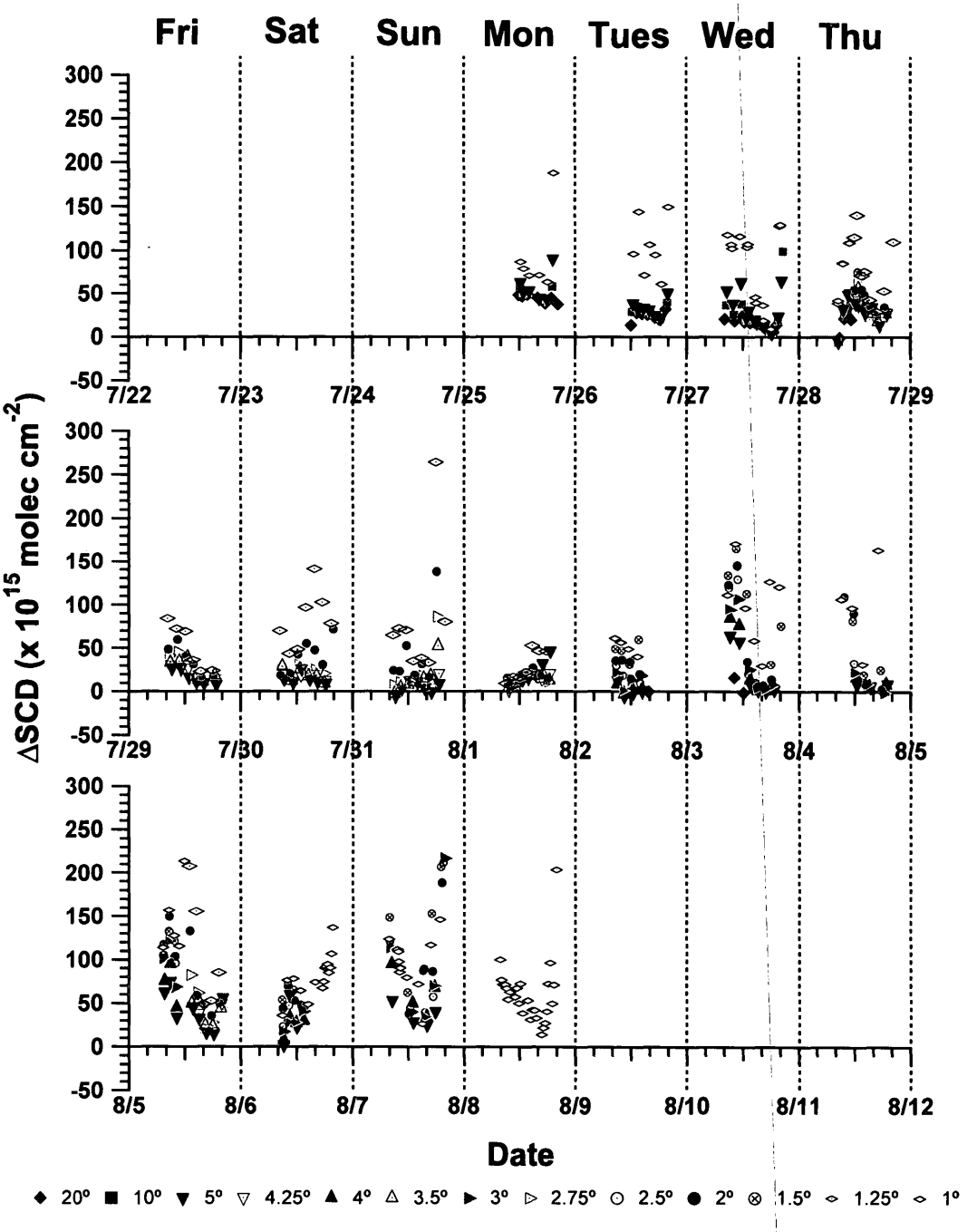

Figure 3.4: Overview of NO_2 ΔSCDs under clear conditions at East Point, Saturna Island, July 25-Aug 8, 2005.

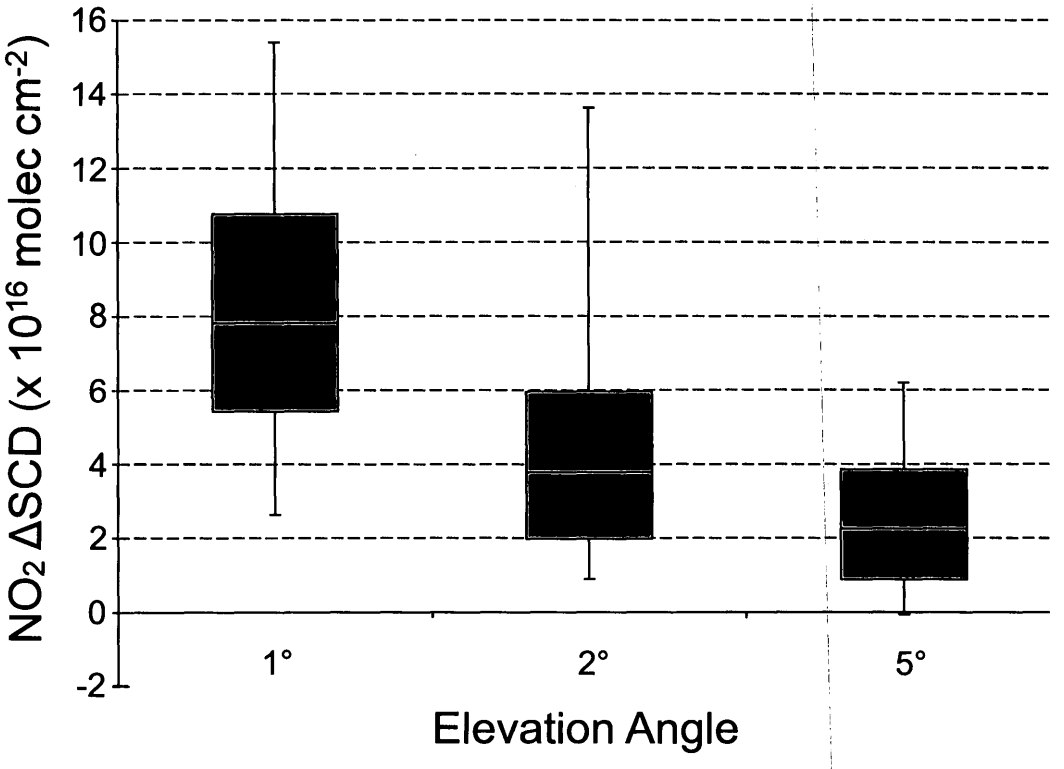

Figure 3.5: Box and whisker plot of NO_2 ΔSCD vs. Elevation Angle at East Point, Saturna Island. The solid horizontal line within each box represents the median, the top and bottom of the boxes represent the 75th and 25th percentiles, and the error bars correspond to the 95th and 5th percentile.

3.3.2 Diurnal Behaviour of NO_2

Figure 3.6 depicts the diurnal behaviour of the NO_2 mixing ratios from active DOAS and the NO_2 ΔSCDs ($\alpha = 1°$) at East Point for the entire study. For comparison purposes, the mixing ratio determined from a standard chemiluminescence instrument at station T13 (North Delta) is also shown (see Figure 3.8). Here the median for NO_2 mixing ratios and ΔSCDs at East Point were taken according to one hour time bins and marked at the mid-point time of each bin, while the median for each hour at T13 is displayed directly. The NO_2 ΔSCDs measured from Saturna and the NO_2 mixing ratios found at T13 showed similar diurnal patterns. A broad peak was seen for both the NO_2 ΔSCDs and mixing ratios from approximately 10:00-13:00 PDT daily. This coincident peak may be due to the outflow of NO_2 from the LFV into the Strait of Georgia since the MAX-DOAS instrument is measuring NO_2 at an average distance of approximately 20 km away from East Point (under low aerosol conditions) while the North Delta station is $\sim$30 km away from Saturna. The highest daily NO_2 ΔSCDs or mixing ratios occurred in the early evening hours just before sunset (19:00-20:00 PDT), a situation that also occurred at Saturna Island itself (as seen from active DOAS measurements at East Point). During the late afternoon/early evening the SZA is at its largest daily value yielding the longest light path through the stratosphere. However, the MAX-DOAS analysis method

used to yield the ΔSCDs presented here was designed specifically to subtract the stratospheric component, so these increases are believed to be due to real increases in tropospheric NO_2. Unlike the MAX-DOAS ΔSCDs, the mixing ratios at East Point do not show enhanced morning levels and show only small increases in NO_2 during the afternoon after 16:00 PDT, with maximum daily values between 17:00 and 20:00 PDT. The larger slant column densities and mixing ratios at this time, for all measures, may be partly due to lower NO_2 photolysis rates.

As theory predicts, the 1° ΔSCDs were generally higher than the 2° or 5° cases (not shown) and the broad peak between 10:00-13:00 PDT was not seen for the other EAs. This is likely due to the fact that the average light path of a MAX-DOAS ΔSCD_1 measurement is much longer than for the other EAs (i.e. $\sim$ 20 km assuming single scattering and low aerosol levels). In this case, the MAX-DOAS ΔSCD_1 measures NO_2 that is much closer to the LFV coastline then the higher EA ΔSCDs (or the active DOAS). Hence, the similarity between the diurnal NO_2 pattern seen at T13 and that seen from ΔSCD_1 measured from Saturna. The MAX-DOAS may be capturing urban outflow into the Strait of Georgia, while the NO_2 mixing ratios determined from active DOAS were insensitive to this outflow (and insensitive to most of the NO_2 from ship traffic in the Strait). The low NO_2 mixing ratios found at East Point truly represent the minimal background levels of NO_2 found locally on this small island.

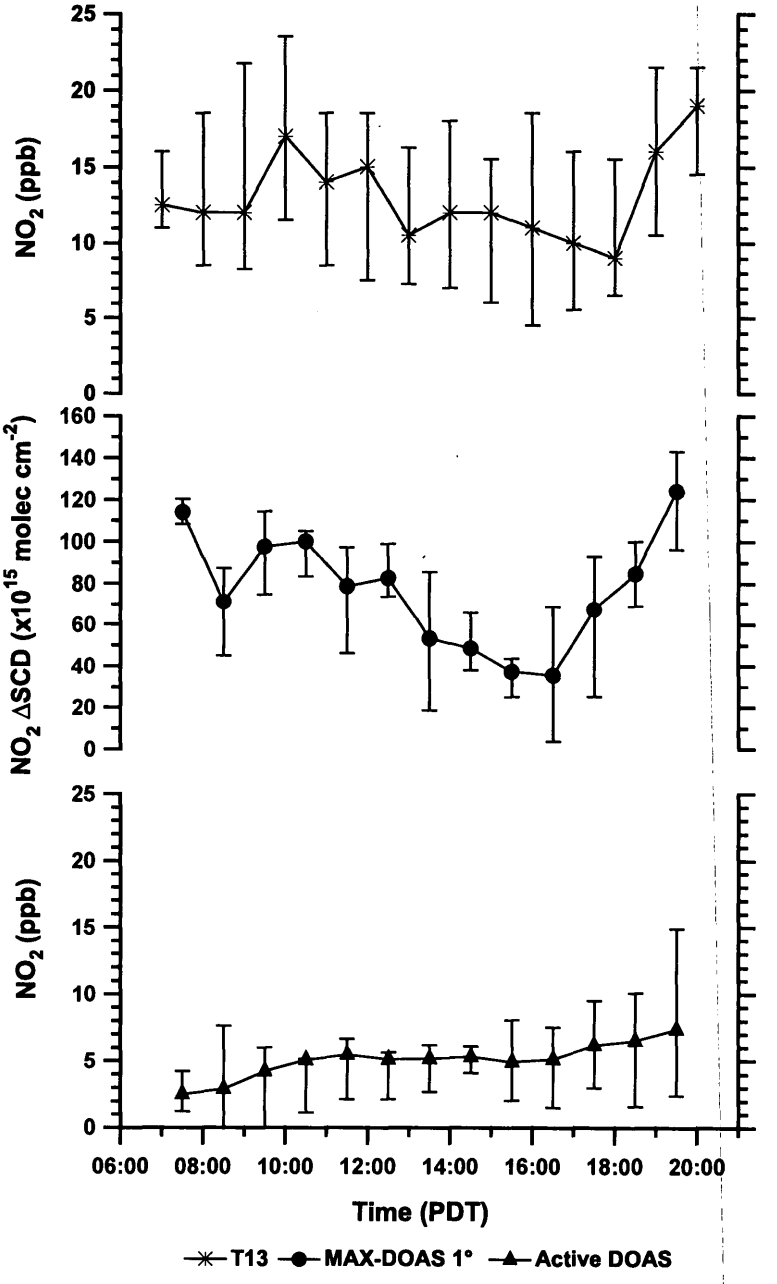

Figure 3.6: Diurnal behaviour of NO_2 ΔSCDs ($\alpha = 1°$) and mixing ratios at East Point, Saturna Island and mixing ratios at Station T13. The median mixing ratios and ΔSCDs are shown for 1 hour bins, while the hourly median mixing ratios at T1 are directly displayed. Error bars represent the 75th and 25th percentiles.

3.3.3 Differences between the Weekend and Weekdays

In urban areas, NO_x emissions are often lower during the weekend than weekdays. This may lead to higher O_3 levels on the weekend days versus the weekdays (Cleveland et al., 1974; Lebron, 1975). To examine the possibility of a "weekend effect" the median NO_2 mixing ratios for selected stations in the LFV (Figure 3.8) and the NO_2 mixing ratios found from active DOAS at Saturna were examined for weekend days (N = 4) and weekdays (N = 11). Table 3.3 shows that in all cases the median weekend NO_2 mixing ratios were lower than the median weekday NO_2 mixing ratios. The weekend to weekday NO_2 ratio ranged from a low of 0.5±0.6 for station T15 (Surrey East) to a high of 1.0±0.5 for station T1 in downtown Vancouver. In many cases this ratio was not statistically significant at the 90% confidence level. The result for the downtown station is reasonable since one could expect significant activity in the downtown core even during weekend periods since the T1 chemiluminescence NO_x (NO_2) monitor is located in a tourist area.

MAX-DOAS results are also displayed in Table 3.3 for the most commonly studied EAs of 1°, 2° and 5° and also show lower median NO_2 ΔSCDs on the weekend versus weekday. The weekend to weekday ΔSCD ratios here were 0.7±0.5, 0.4±0.8 and 0.4±1.3 for the 3 EAs respectively. The higher ratio for the $DSCD_1$ values was possibly due to the longer path length of these measurements, reflecting

a situation where more NO_2 over the Strait was measured versus the higher EA cases that have a great proportion of the NO_2 measured in the light path coming from local sources (that were low at East Point). Based on the NO_2 mixing ratios and ΔSCD values alone, there is the possibility of a "weekend effect" for O_3 in the LFV. To examine this further, the maximum O_3 levels at the same stations used for the NO_2 analysis were determined for the same weekend and weekday periods (not shown). Higher O_3 levels were seen on the weekend versus the weekday at the downtown stations T1 and T4 (Table 3.3). These areas are most likely VOC limited for O_3 formation and a reduction in NO_x (NO_2) in these areas consequently leads to higher O_3 levels (weekend effect). However, for stations T33, T12 and T29 (the less urban, more rural areas of Abbotsford, Chilliwack and Hope) the weekend O_3 levels are lower than weekday levels ("anti-weekend effect"). These stations are likely situated in NO_x limited regions and the weekend reduction of NO_x (NO_2) results in decreased O_3, as seen by the minimum O_3 weekend to weekday ratios of 0.9$\pm$0.4 (T33 - Abbotsford and T29 - Hope) and 0.9$\pm$0.5 (T12 - Chilliwack). Finally, station T15, slightly east of the city in Surrey East, had a maximum O_3 weekend to weekday ratio of 1.04$\pm$0.34, perhaps signifying that this domain is somewhere close to the border between a VOC limited and NO_x limited regime for O_3 formation. Unfortunately, O_3 data was not available at East Point for the duration of the study so that the determination of whether East Point lies in a

VOC or NO_x limited regime was not possible. However, this determination will be assessed in an alternative way in Section 3.5. The hypothesis that stations T33, T12 and T29 are NO_x limited with respect to O_3 formation is a useful result that will be used in the subsequent analysis described in Section 3.3.5. To more accurately confirm or deny the presence of this "weekend effect" a much larger sample size should be taken in the future because the errors for NO_2 and O_3 ratios are quite high at the 90% CI.

Table 3.3: Weekend and weekday median NO_2 mixing ratios, NO_2 ΔSCDs, and weekend to weekday ratios for NO_2 and O_3.

Method	Location	EA	NO_2 Median Weekend (χ) (or ΔSCD)	NO_2 Median Weekday (χ) (or ΔSCD)	NO_2 Median Ratio $\frac{Weekend}{Weekday}$	O_3 Max Ratio $\frac{Weekend}{Weekday}$
DOAS	Saturna	N/A	4.2±0.7	5.0±1.7	0.8±0.3	N/A
CL	T1 - Vancouver	N/A	17.5±3.1	18.0±9.1	1.0±0.5	1.1±0.7
CL	T4 - Kensington	N/A	8.5±10.4	14.4±7.4	0.6±0.8	1.1±0.7
CL	T15 - Surrey East	N/A	4.5±3.5	8.5±6.3	0.5±0.6	1.0±0.3
CL	T33 - Abbotsford	N/A	4.0±3.1	6.5±4.3	0.6±0.6	0.9±0.4
CL	T12 - Chilliwack	N/A	4.8±2.1	7.5±2.9	0.6±0.4	0.9±0.5
CL	T29 - Hope	N/A	4.3±1.2	6.0±1.8	0.7±0.3	0.9±0.4
MAX-DOAS	Saturna	1°	9.0±4.6	12.8±7.4	0.7±0.5	N/A
MAX-DOAS	Saturna	2°	4.7±7.4	10.8±8.6	0.4±0.8	N/A
MAX-DOAS	Saturna	5°	1.2±3.1	3.2±7.3	0.4±1.3	N/A

*The units for the weekend and weekday median NO_2 mixing ratios (χ) and ΔSCDs are ppb and $\times 10^{16}$ molec cm^{-2} respectively. The NO_2 median mixing ratios were calculated from 6:00-21:00 PDT, while the O_3 mixing ratios used for the O_3 max ratio were the maximum daily O_3 values. CL stands for chemiluminescence, and the station locations for T1, T15, T33, T12 and T29 are shown in Figure 3.8. All errors were calculated for the 90% confidence interval.

3.3.4 NO_2 VCDs

Figure 3.7 shows the average NO_2 tropospheric vertical column density in the LFV determined via the OMI satellite (see Chapter 4, Section 4.2.5 for details) for the period of July 22-Aug 8, 2005. Unlike the ground level measurements (Section 3.3.5, Figure 3.9), the highest NO_2 VCDs are not located in the most urban areas such as downtown Vancouver but rather in the suburbs east of the city, with a hot spot approximately centered around Pitt Meadows (VCD $\approx 1.4 \times 10^{16}$ molec cm^2). When NO_2 is measured with a point-source instrument, NO_2 levels are higher near downtown due to high NO_x emissions and a low boundary layer that is close to the ocean. Moving further inland and to the east, the boundary layer is likely higher which leads to lower NO_2 mixing ratios but not necessarily smaller VCDs (Hayden et al., 1997). In fact, emissions to the east of Vancouver are still high and NO_2 may continue to build up as additional time is made available for photochemical processing. This may help to explain the spatial distribution of NO_2 VCDs seen in Figure 3.7. The average NO_2 VCDs determined contain a low number of data points and measurements were only taken between 13:30 and 14:30 PDT, but similar distributions were found when yearly and seasonal data for the summertime were similarly plotted (not shown). This suggests that the vertical burden of pollutants east of Downtown Vancouver may be higher than shown via conventional

point-source measurement techniques. With higher NO_2 VCDs east of Vancouver, the potential for greater O_3 formation in these less urban and/or rural areas is a strong possibility. Conversely, the average NO_2 VCD in the Strait of Georgia appears to be almost one order of magnitude lower ($3\text{-}4\times10^{15}$ molec cm^2). As described in Chapter 1, the vertical column density may also be estimated under clear sky conditions by using the measured NO_2 ΔSCDs (with $\alpha \geq 20°$) and an approximated air mass factor (see Equation 1.19). Four geometrically approximated VCDs were determined using the $DSCD_{20}$ values taken on the three days that had 20° EA measurements taken between 13:30 and 14:30 PDT (July 25-27). The average VCD_{GEO} found was 5.2×10^{16} molec cm^2, substantially higher than what was seen from the OMI satellite. There are several plausible reasons for this discrepancy including the limited number of measurements made when $\alpha = 20°$ during the hour of the OMI overpass, and the possibility of high aerosol levels in the Strait, which would make this geometrical approximation invalid. However, as will be discussed in detail below, the impact of the NO_2 found in the Strait of Georgia on the LFV is likely more substantial than what is seen from the OMI satellite overview shown in Figure 3.7.

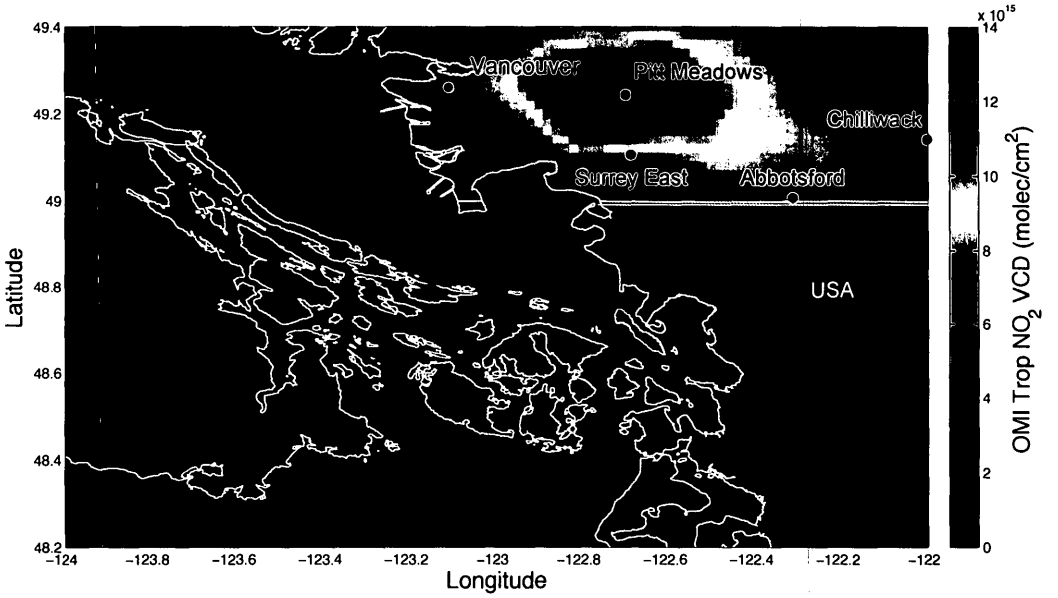

Figure 3.7: OMI NO_2 VCDs in the LFV. The VCDs were averaged for July 22-Aug 8, 2005 using a 0.02° × 0.02° grid and a daily overpass between 13:30 and 14:30 PDT. Figure courtesy of L. Chan, City U, Hong Kong (personal communication).

3.3.5 Relationship between NO_2 ΔSCDs and O_3 Formation in the Lower Fraser Valley

In order to search for a link between the accumulation of NO_2 in the Strait of Georgia and ozone formation in the Lower Fraser Valley, an observational analysis using ozone data at multiple monitoring stations in the valley and NO_2 ΔSCDs determined from measurements at Saturna Island was performed. The hypothesis to be tested is that the effect of enhanced NO_2 ΔSCDs at Saturna would only be correlated to enhanced ozone in the valley if there was substantial transport of marine air from the Strait into the valley via sea breezes and if ozone formation is NO_x limited. To determine what days during the field study had sea breezes, the meteorological observational data from six stations were examined (Figure 3.8). Using the criteria shown in Equations 3.1 and 3.2, similar to those in Snyder and Strawbridge (2004), only days where a sea breeze was present were used for the analysis described below.

$$Inflow(seabreeze) \equiv 180° < WD < 330° \tag{3.1}$$

$$Outflow(landbreeze) \equiv 0° < WD < 120° \tag{3.2}$$

Furthermore to assess the transport of marine air from the Strait to the LFV, evidence of sustained inflow for several hours, and wind speeds > 5 km h^{-1} at all six stations were required to retain data from individual days for this analysis. Only

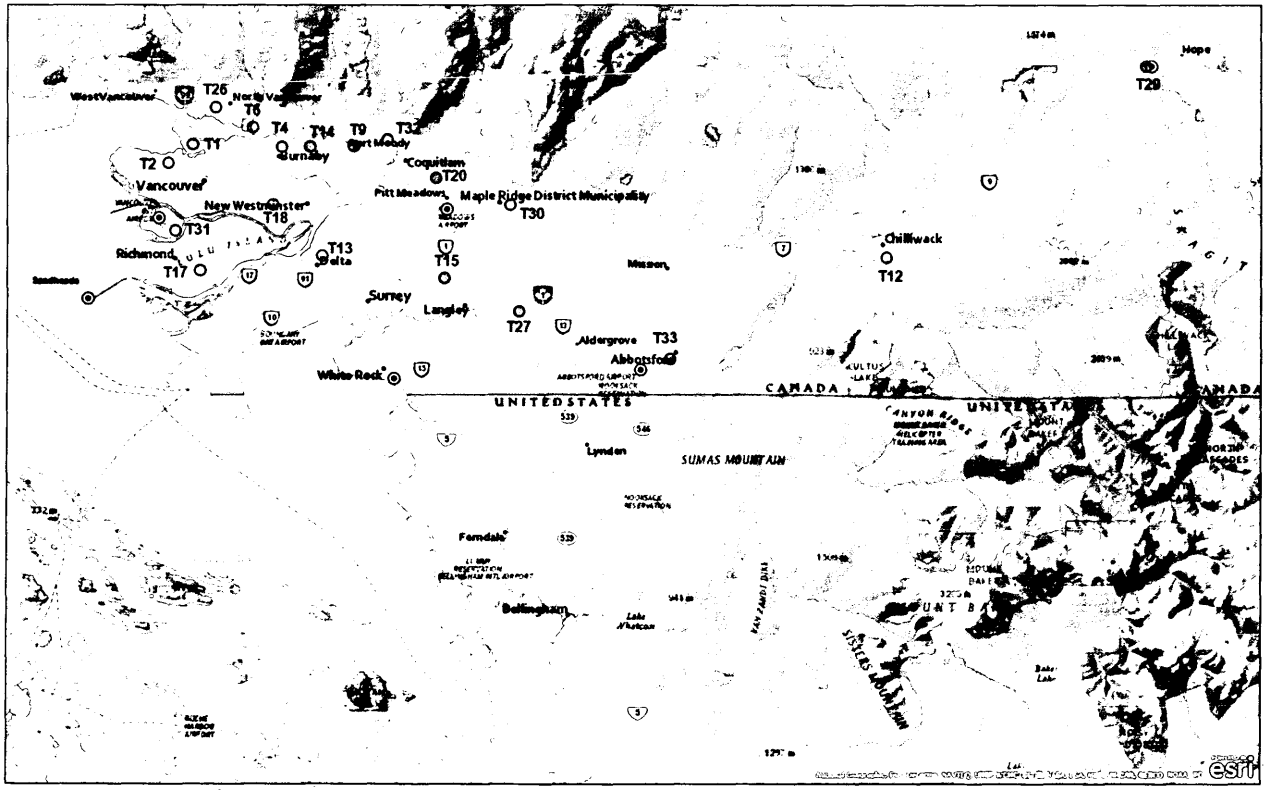

Figure 3.8: Map of the Lower Fraser Valley (LFV) with key monitoring stations shown. Grey circles represent air quality monitoring stations, circles with black dots represent Environment Canada climate stations, and the circle with the red dot signifies the MAX-DOAS instrument location on East Point, Saturna Island.

NO_2 ΔSCDs measured at the 1° and 5° elevation angles were considered since these angles were consistently taken on the highest number of days during the campaign and hence represent the largest possible data sets available from the EAs used (Table 3.1). From the complete data set of 15 days, 7 days fit the criteria: July 27 and 28, and Aug 2, 3, 5, 6 and 7. The average wind vectors (WD = wind direction, WS = wind speed) for the afternoon hours (12:00-16:00 PDT) on these days were: Vancouver International (WD = 280°, WS = 16.0 km h^{-1}), Sandheads (WD = 282°, WS = 15.5 km h^{-1}), Pitt Meadows (WD = 237°, WS = 6.7 km h^{-1}), White Rock (WD = 232°, WS = 7.1 km h^{-1}), Abbotsford (WD = 233°, WS = 10.8 km h^{-1}) and Hope (WD = 280°, WS = 18.6 km h^{-1}). A general observation of the meteorological analysis is that sea breezes start and finish earlier for stations close to the coast, versus stations further inland.

Figure 3.9A shows the average NO_2 mixing ratio measured at ground level at each station for the selected days during the 7:00-10:00 PDT time range ($\overline{\chi}_{NO_2}$). The overall average mixing ratio of NO_2 for all stations in the LFV was 12.3 ppb. The highest average NO_2 values were found at urban stations T1 (24.8 ppb), T6 (23.0 ppb), and T26 (17.5 ppb), while the lowest values were found in the rural, less densely populated communities of Langley (T27 - 6.4 ppb), Abbotsford (T33 - 6.9 ppb), Chilliwack (T12 - 7.5 ppb), and Hope (T29 - 6.0 ppb).

The maximum daily O_3 mixing ratio may be defined as $\chi^*_{O_3}$. Figure 3.9B shows

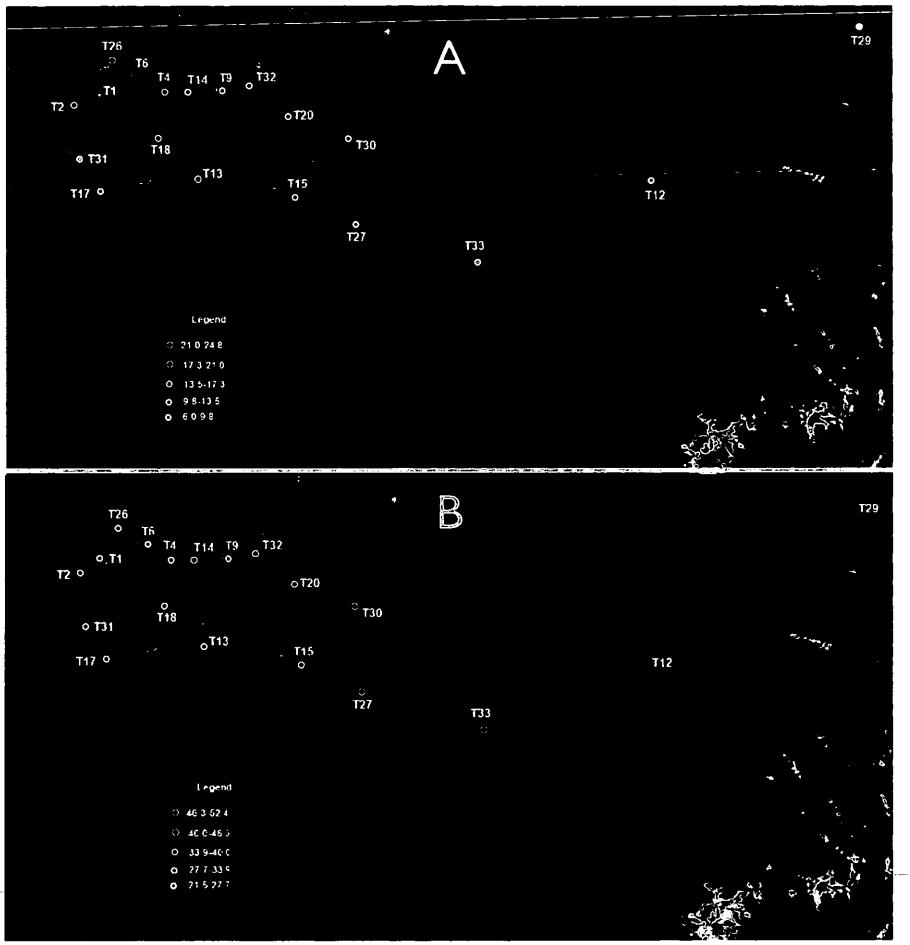

Figure 3.9: Average NO_2 ($\overline{\chi}_{NO_2}$) and average daily maximum O_3 ($\chi^*_{O_3}$) measured at ground level from stations in the LFV for the time period of July 27 and 28, and Aug 2, 3, 5, 6 and 7, 2005. Panel A depicts the average $\overline{\chi}_{NO_2}$ for the selected days during the 7:00-10:00 PDT time period, while panel B depicts the average $\chi^*_{O_3}$ on those same days. The values shown in the legend are in units of ppb.

the average $\chi^*_{O_3}$ measured at each station for the selected days. The average $\chi^*_{O_3}$ for these stations was 35.7 ppb. The lowest average $\chi^*_{O_3}$ values were found in urban stations (T1 - 21.6 ppb and T6 - 25.6 ppb), while the highest average values were found at stations in Abbotsford (T33), Chilliwack (T12), and Hope (T29) with values of 43.7 ppb, 47.0 ppb, and 52.4 ppb respectively. Figure 3.10 displays the average diurnal ozone values for representative stations in downtown Vancouver and the LFV. In this figure only the seven days with significant sea breezes were averaged. One clear trend seen is that the daily O_3 peaks later in the day and at higher values for stations further downwind of the Georgian Strait.

These results are somewhat predictable since in urban areas such as downtown Vancouver there are significant sources of NO_x. The NO present will typically consume the available O_3 resulting in very low ozone levels. In urban areas such as this the additional flux of NO_x from the Georgian Strait (measured by MAX-DOAS as an NO_2 ΔSCD) will not necessarily result in increased O_3 values, but may in fact lower O_3 (Chapter 1, Figure 1.1). Conversely, in rural areas that are NO_x limited, the titration of O_3 with NO becomes less significant as direct NO_x sources are low. Meanwhile the reactions of RH, HO_2, RO_2 and other VOCs become more relevant. If additional NO_x from the Strait is introduced into rural environments in the LFV it will likely result in increased O_3 (Figure 1.1), as the transported NO_x is given further time to process and react with these VOCs (Jiang et al., 1997).

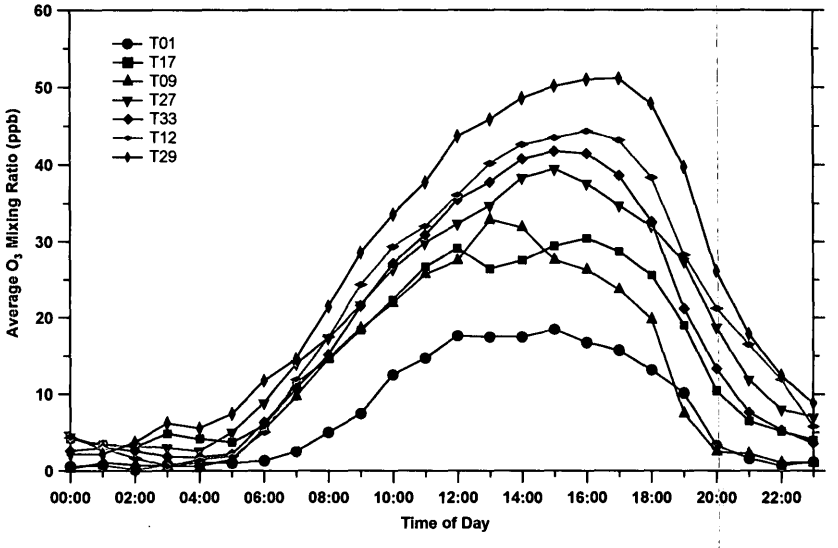

Figure 3.10: Average diurnal O_3 mixing ratios for representative stations in the LFV. The average O_3 values for each hour were determined for the seven selected days during the field campaign that had evidence of a sustained sea breeze.

For each air quality monitoring station in the LFV shown in Figure 3.8, a regression analysis was performed between the daily maximum 1 hour average O_3 mixing ratio value ($\chi^*_{O_3}$) and the average NO_2 ΔSCD between 7:00 and 10:00 PDT ($\overline{\Delta SCD}_{NO_2}$) on the selected days. The full results of these regressions are shown in Table 3.4. A sample of these regressions (with $\alpha = 1°$) using a few representative stations is shown in Figure 3.11. Linear regression analysis was used to determine the slope of the relationship $d\chi^*_{O_3}/d\overline{\Delta SCD}_{NO_2}$. A zero slope indicates no effect while a slope of statistical significance (p-value ≤ 0.05) indicates that there is a correlation between the NO_2 found in the Strait and ozone formation in the valley.

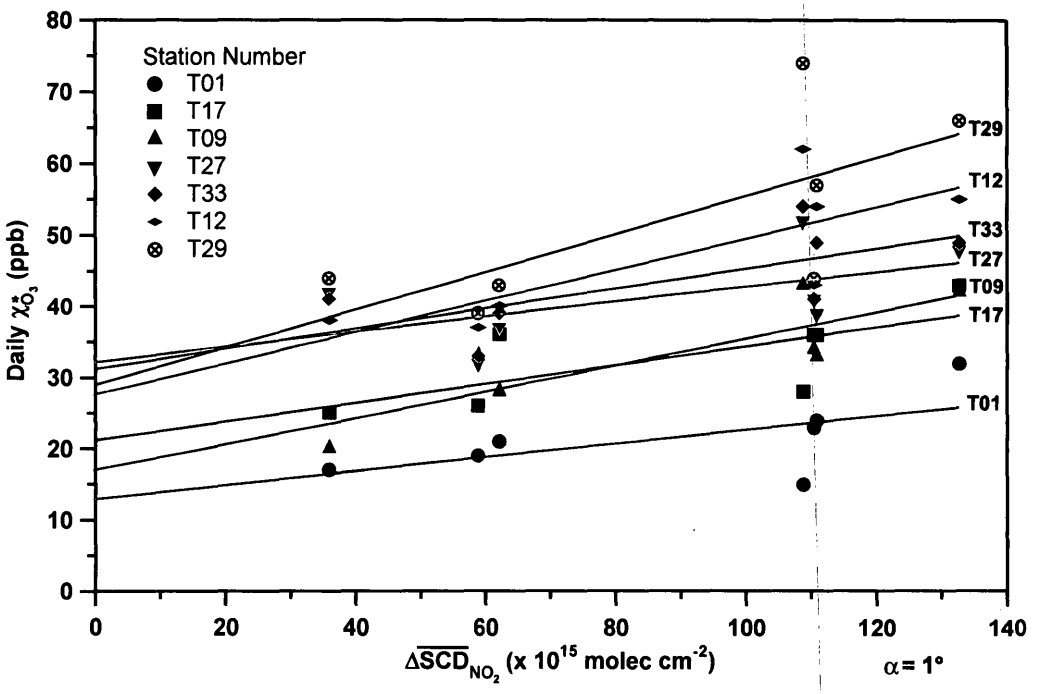

Figure 3.11: Correlation of daily $\chi^*_{O_3}$ and $\overline{\Delta SCD}_{NO_2}$ (1°) seen at monitoring stations in the LFV. The ΔSCDs were averaged daily over the time period 7:00-10:00 PDT. This analysis only includes the seven days in which a significant sustained sea breeze was observed.

Figure 3.12A shows the $d\chi^*_{O_3}/d\overline{\Delta SCD}_{NO_2}$ ($\alpha = 1°$) for each station in the LFV. Values are generally low for stations within the downtown core of Vancouver. The addition of further NO_2 from the Strait of Georgia does not seem to result in increased O_3 production since this area is most likely VOC limited. In the suburbs and for stations located further downwind the correlations are noticeably greater. This may be due to the fact that O_3 formation in these regions is NO_x limited (with a higher VOC/NO_x ratio) and in a regime where the addition of NO_2 may

now result in increased O_3 production. The greatest $d\chi^*_{O_3}/d\overline{\Delta SCD}_{NO_2}$ values are found at station T12 (Chilliwack) and T29 (Hope). Both stations are located far from large urban centers and are relatively far from Saturna. They, along with T33 (Abbotsford) are most likely in NO_x limited regimes and the addition of NO_2 in these areas should result in increased O_3. With each successive station (Abbotsford, Chilliwack, Hope) additional time is made available for photochemical processing and one would expect to see increased O_3 production at each successive station down the valley. The results shown in Figure 3.12A confirm this hypothesis as the $d\chi^*_{O_3}/d\overline{\Delta SCD}_{NO_2}$ was 1.41, 2.19, and 2.66×10^{-16} ppb molec^{-1} cm^2 respectively for these stations, all above the average value of 1.33×10^{-16} ppb molec^{-1} cm^2. This same trend was also seen for $d\chi^*_{O_3}/d\overline{\Delta SCD}_{NO_2}$ ($\alpha = 5°$), although the statistical significance of the 5° regressions was generally less than for the 1° case. These statistics will be discussed in detail below.

For comparison purposes, Figure 3.12B displays the change in the daily maximum 1 hour average O_3 mixing ratio ($d\chi^*_{O_3}$) divided by the change in the average NO_2 mixing ratio ($d\overline{\chi}_{NO_2}$), measured at each corresponding station, between 7:00 and 10:00 PDT on the selected days ($d\chi^*_{O_3}/d\overline{\chi}_{NO_2}$). The values in the downtown core were relatively low with the exceptions of stations T31 and T17 (1.69, 1.59). Similar to the correlations using the NO_2 $\overline{\Delta SCD}$s, the suburbs generally had larger slopes than the downtown core, except that the rural stations of Abbotsford, Chill-

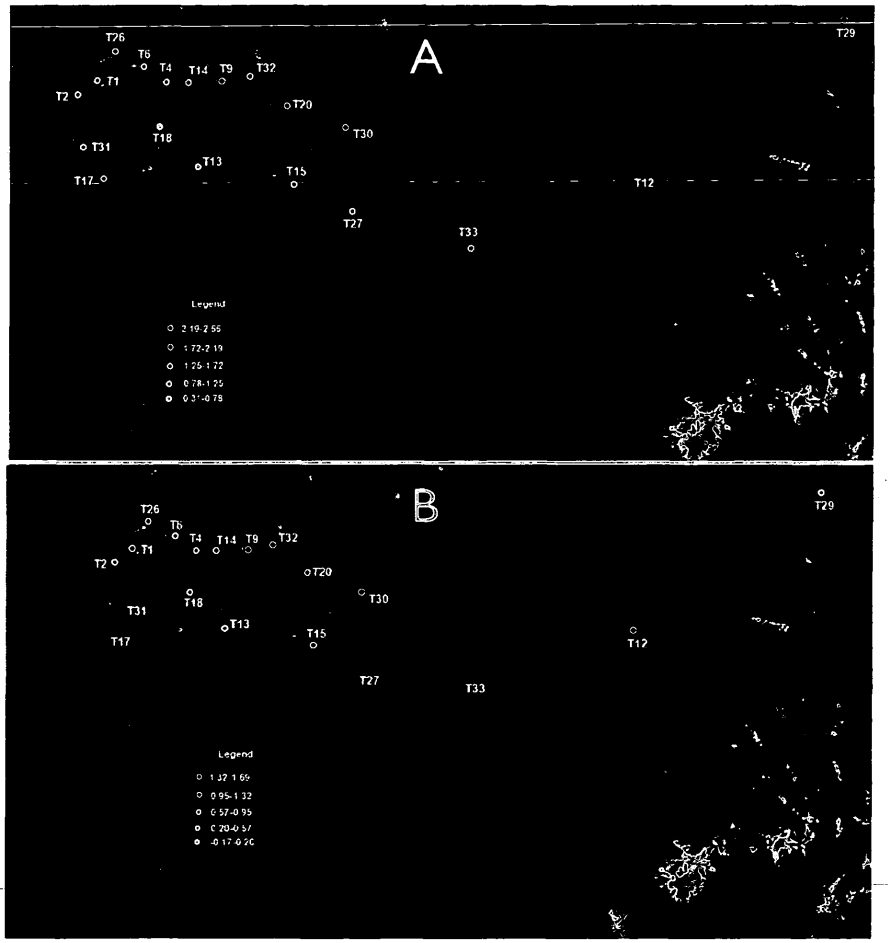

Figure 3.12: Correlation of $\chi^*_{O_3}$ and $\overline{\Delta SCD}_{NO_2}$ ($\alpha = 1°$) or $\overline{\chi}_{NO_2}$ on the same day seen at monitoring stations in the LFV. The NO_2 ΔSCDs and mixing ratios were averaged daily over the time period 7:00-10:00 PDT. Panel A displays the slope for $d\chi^*_{O_3}/d\overline{\Delta SCD}_{NO_2}$ (in units of $\times 10^{-16}$ ppb molec^{-1} cm^2) and panel B displays $d\chi^*_{O_3}/d\overline{\chi}_{NO_2}$ (unit-less). This analysis includes only days in which a significant sustained sea breeze was observed.

iwack, and Hope exhibited a different trend. Hope had a negative slope (-0.03) showing that the local morning time NO_2 (NO_x) did not greatly influence the local O_3 production, while Chilliwack and Abbotsford had positive slopes of 0.98 and 1.52, well above the average $d\chi^*_{O_3}/d\overline{\chi}_{NO_2}$ value of 0.84. The trend between these stations is the reverse of the $\overline{\Delta SCD}$ case.

While the ΔSCDs provide a representative measure of the NO_2 in the Strait of Georgia they do not differentiate between the amount of NO_2 located over the water at one particular location vs. another. The NO_2 is likely not uniform over the Strait. For example, the NO_2 at Sandheads is likely not the same as the NO_2 at White Rock for a given ΔSCD. If there is actually significantly less NO_2 at Sandheads vs. White Rock it may be a potential reason for a lower $d\chi^*_{O_3}/d\overline{\Delta SCD}_{NO_2}$ values at urban stations (T1, T2, T17, T31) vs. rural stations (T33, T12, T29). Despite this drawback, a positive correlation between $d\chi^*_{O_3}$ and $d\overline{\Delta SCD}_{NO_2}$ for most stations in the LFV may imply that NO_2 transported from the Strait of Georgia, following a nighttime stagnation event in the region, has a positive effect on O_3 production in the LFV. To confirm this mathematically, statistics are presented and analyzed for the three types of regressions at each station (Table 3.4). Even if statistically significant, this is not definite proof of cause and effect since other species such as HONO or VOCs (that may be correlated with NO_2) may also lead to enhanced O_3, resulting in a positive $d\chi^*_{O_3}/d\overline{\Delta SCD}_{NO_2}$ correlation.

When considering the 1° elevation angle NO_2 $\overline{\Delta SCD}$s, 18 air quality stations (Table 3.4) shown in Figure 3.8 have a positive correlation between $\chi^*_{O_3}$ and $\overline{\Delta SCD}_{NO_2}$ within error (only T13 is excluded). Nine stations (T2, T4, T9, T12, T14, T20, T26, T30, T32) have slopes that are statistically different from zero as defined via the p-value criteria mentioned earlier (Table 3.4). The coefficients of determination (R^2 values) range from 0.09 for station T13 to 0.91 for station T14 in Burnaby. At Burnaby, this indicates that 91% of the variance in peak daily ozone levels is associated with the variance in NO_2 measured in the Strait the morning before. The large number of stations showing a positive correlation, with an average $d\chi^*_{O_3}/d\overline{\Delta SCD}_{NO_2}$ of $1.33\pm0.50\times10^{-16}$ ppb molec^{-1} cm^2, provides some confidence that this correlation is real.

Similar results are seen for the 5° elevation angle NO_2 ΔSCDs. Seventeen stations shown in Figure 3.8 have a positive correlation between $\chi^*_{O_3}$ and $\overline{\Delta SCD}_{NO_2}$. Stations T13 and T18 have negligible slopes within error. However only five stations (T12, T14, T20, T26, T30) have slopes that are statistically different than zero using the p-value criteria (Table 3.4). The coefficients of determination range from 0.05 for station T13 to 0.92 for station T14 in Burnaby. An average positive correlation for all the stations in the LFV again gives more statistical confidence that this effect is real. This time $d\chi^*_{O_3}/d\overline{\Delta SCD}_{NO_2}$ was $1.64\pm0.77\times10^{-16}$ ppb molec^{-1} cm^2.

For comparison purposes, only 15 stations shown in Figure 3.8 have a positive

Table 3.4: Correlation between $\chi^*_{O_3}$ and $\overline{\Delta SCD}_{NO_2}$ or $\overline{\chi}_{NO_2}$ measured on the same day at air monitoring stations in the LFV. The elevation angles for the $\overline{\Delta SCD}_{NO_2}$ values were either 1° or 5°.

Stn	$d\chi^*_{O_3}/d\overline{\Delta SCD}_{NO_2}$ ($\alpha = 1°$)	R^2	$d\chi^*_{O_3}/d\overline{\Delta SCD}_{NO_2}$ ($\alpha = 5°$)	R^2	$d\chi^*_{O_3}/\overline{\chi}_{NO_2}$ (ground level)	R^2
T17	1.33±0.58	0.51	1.75±0.75	0.52	1.59±1.21	0.26
T31	1.13±0.90	0.24	1.47±1.19	0.24	1.69±0.75	0.51
T02	0.79±0.29	0.60	0.99±0.40	0.56	0.37±0.19	0.43
T01	0.97±0.55	0.38	1.34±0.69	0.43	0.79±0.13	0.89
T26	1.37±0.45	0.65	1.70±0.65	0.58	0.77±0.34	0.51
T06	0.98±0.42	0.52	1.24±0.57	0.49	0.22±0.23	0.15
T18	0.48±0.34	0.29	0.43±0.49	0.13	0.51±0.26	0.42
T04	0.93±0.32	0.62	1.06±0.51	0.47	0.51±0.25	0.46
T13	0.31±0.44	0.09	0.31±0.59	0.05	-0.17±0.25	0.08
T14	1.35±0.20	0.91	1.78±0.23	0.92	0.92±0.29	0.67
T09	1.87±0.53	0.72	2.14±0.87	0.55	1.02±0.43	0.53
T32	1.44±0.48	0.68	1.69±0.70	0.54	1.04±0.46	0.50
T15	1.11±0.70	0.34	1.31±0.96	0.27	0.74±0.65	0.20
T20	1.80±0.44	0.77	2.16±0.71	0.65	0.91±0.28	0.68
T27	1.05±0.69	0.31	1.22±0.95	0.25	1.35±1.13	0.22
T30	2.18±0.60	0.73	2.72±0.88	0.66	1.27±0.56	0.51
T33	1.41±0.65	0.49	1.84±0.85	0.49	1.52±0.72	0.47
T12	2.19±0.75	0.63	2.75±1.04	0.58	0.98±1.45	0.08
T29	2.66±1.18	0.50	3.24±1.65	0.43	-0.03±3.22	0.00
Avg	1.33±0.50		1.64±0.77		0.84±0.67	

*The units for $d\chi^*_{O_3}/d\overline{\Delta SCD}_{NO_2}$ are $\times 10^{-16}$ ppb molec^{-1} cm^2, while $d\chi^*_{O_3}/\overline{\chi}_{NO_2}$ at ground level is unit-less.

correlation between $\chi^*_{O_3}$ and $\overline{\chi}_{NO_2}$ (T13 and T29 have negative slopes and T6 and T12 have a zero slope within error). Furthermore, only three stations have slopes that are statistically different than zero using the p-value criteria (T1, T14, T20). Station T1 exhibited the highest R^2 value of 0.89 and had a p-value of 0.001, suggesting that $\chi^*_{O_3}$ is highly correlated with $\overline{\chi}_{NO_2}$ at this station. This is in stark contrast to the insignificant correlations (p-values) between the $\chi^*_{O_3}$ at T1 and the $\overline{\Delta SCD_5}$ and the $\overline{\Delta SCD_1}$ measured at Saturna (p-values were 0.11 and 0.14 respectively). The average slope for $d\chi^*_{O_3}/d\overline{\chi}_{NO_2}$ was positive (0.84±0.67), but for most stations not statistically significant. To summarize, the maximum daily ozone measured at stations in the LFV appears to be more highly correlated with morning time columns densities of NO_2 measured in the Strait of Georgia at Saturna than it does with morning time mixing ratios of NO_2 measured at those individual stations, on days when sea breezes are active in the valley.

Lastly, to test the null hypothesis, the regression analysis using the NO_2 $\overline{\Delta SCD}$s was extended to include the $\chi^*_{O_3}$ formed at each station for the previous day, known as Day -1, and the next day, known as Day +1. This is called the null hypothesis since all else being equal, one would not necessarily expect a strong correlation between the ozone measured on these other days with the NO_2 ΔSCD on the given day under examination. These regressions were performed for each station in the same fashion as those done on the same day (Day 0). For both the 1° and 5° EA

cases all stations showed negligible slopes and low coefficients of determination on both Day -1 and Day +1 (not shown). The average $d\chi^*_{O_3}/d\overline{\Delta SCD}_{NO_2}$ when $\alpha =$ 1°, for all stations on Day -1, Day 0 and Day 1 is compared to three individual stations (T2, T33, T29) in Figure 3.13. The average $d\chi^*_{O_3}/d\overline{\Delta SCD}_{NO_2}$ when $\alpha =$ 1° was -0.28±1.02 and 0.10±0.82×10^{-16} ppb molec^{-1} cm^2 for Day -1 and Day +1 respectively. Similarly, the average $d\chi^*_{O_3}/d\overline{\Delta SCD}_{NO_2}$ when $\alpha = 5°$ was -0.45±1.33 and 0.48±1.05×10^{-16} ppb molec^{-1} cm^2 for Day -1 and Day +1 respectively (not shown). For every station the p-values on both Day -1 and Day +1 were > 0.1 suggesting the null hypothesis to be true in all cases. Figure 3.13 shows a large disparity between the representative stations shown and the average. Station T29 (Hope) had high slope values for Day 0 and Day 1 but a negative slope on Day -1. Station T33 (Abbotsford) had had high slopes on Day -1 and Day 1, while station T2 (Vancouver) had lower than average slopes on Day 0 and Day 1 and a slightly above average slope on Day -1. Errors bars for the individual stations were omitted on this figure for clarity, but it must be noted these error bars are quite high. For Days -1 and 1 they are in fact significantly higher than the slope values themselves and as such the average slopes were used to draw conclusions. The average slopes show that the formation of O_3 due to transport of the NO_2 from the Strait of Georgia into the LFV may be a daily effect on days with sustained sea breezes carrying enhanced NO_2 into the valley. The NO_2 ΔSCDs on any given day

do not significantly affect the formation of ozone in the valley on the day previous to it, or the day immediately following it, even though the average slope for the Day +1 regression when α is either 1° or 5° is slightly positive in both cases.

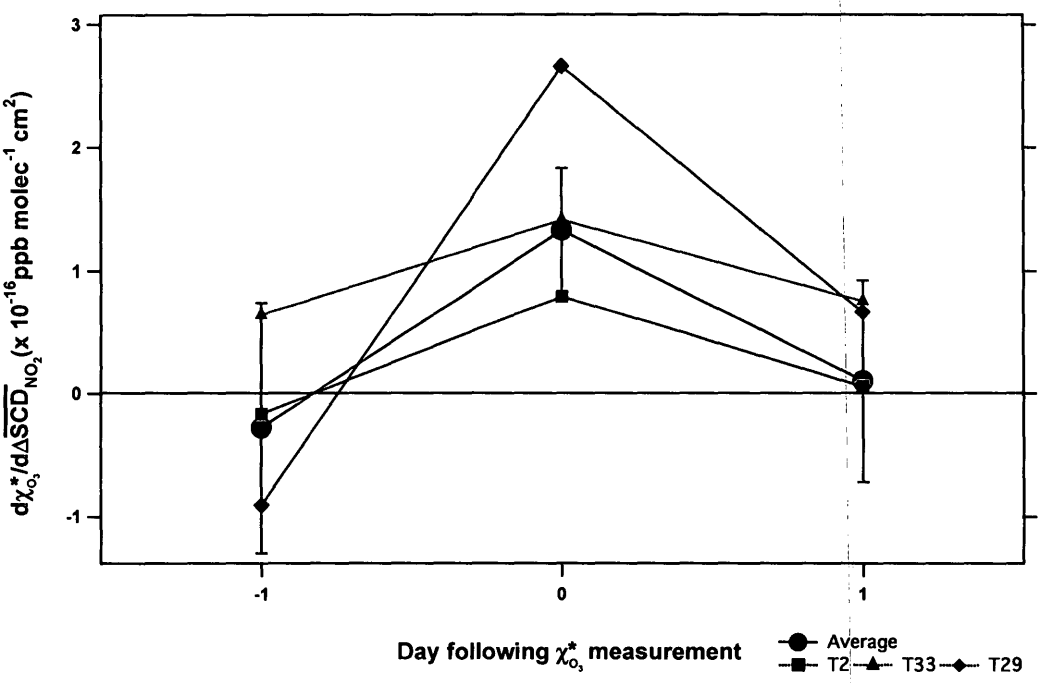

Figure 3.13: Response of $\chi^*_{O_3}$ at monitoring stations in the LFV to NO_2 $\overline{\Delta SCD}$s (when $\alpha = 1°$) over the daily 7:00-10:00 PDT time interval. Individual regressions were first performed for each station. Examples are shown for T2, T33 and T29. These values were then averaged for each Day as displayed in red. For Day 0, the $NO_2\overline{\Delta SCD}$s and $\chi^*_{O_3}$ are measured on the same day, while Day -1 and Day +1 contains $\chi^*_{O_3}$ measurements from one day earlier and one day later. These averages are taken from the seven selected days that have significant sustained sea breezes.

3.4 The Wake-Induced Stagnation Effect

The Wake-Induced Stagnation Effect (WISE) describes the stagnation of polluted air at night in the Strait of Georgia, close to Saturna Island. It is a result of light winds formed by the convergence of air flow from the Straits of Georgia and Juan de Fuca, coupled with the positions and topography of Vancouver Island, the Gulf Islands, and the San Juan Islands. During PACIFIC 2001, Brook et al. (2004) defined WISE and hypothesized that it may play a significant role in the build-up and photochemical processing of air pollutants. Emissions from the LFV, Vancouver, Victoria, Washington State and from marine vessels may collect in the Strait of Georgia creating the so-called "Saturna Cesspool", named for its close proximity to Saturna. One common transport scenario believed to exist consists of: (*i*) sea breezes carrying urban emissions into the valley, (*ii*) outflow of polluted air via land breezes at night into the MBL, (*iii*) stagnation of polluted air in the MBL overnight (WISE), and (*iv*) transport of this polluted overnight air back into the LFV the next day via sea breezes (Figure 3.14).

Backward and forward air trajectories were run by Bruce Ainslie with Environment Canada's Trajectory model, using Global Environmental Multi-scale model (GEM) output saved at 2 min intervals for the 7 days that exhibited prolonged sea breezes into the LFV. The GEM model used a 2.5 km domain over southern

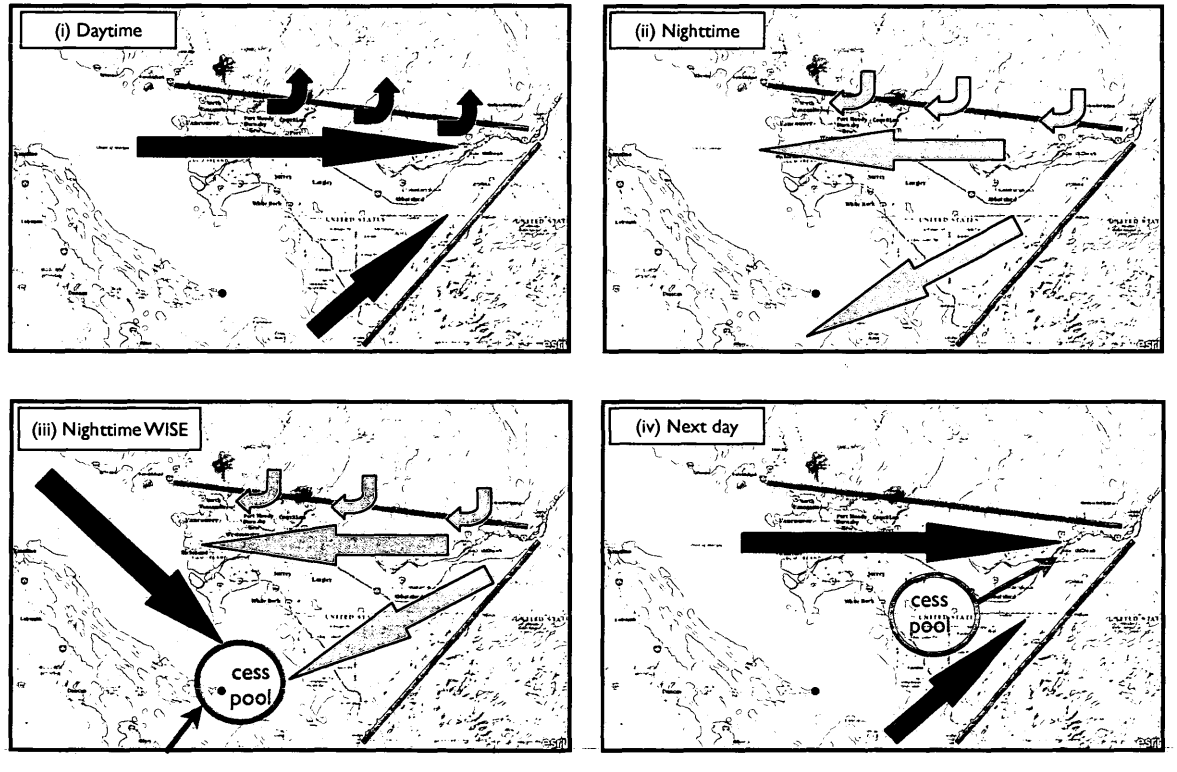

Figure 3.14: The Wake-Induced Stagnation Effect (WISE). Panel (*i*) shows sea breezes (blue) carrying urban emissions into the valley; panel (*ii*) shows outflow (green) of polluted air via land breezes at night into the MBL; panel (*iii*) shows stagnation of polluted air in the MBL overnight (WISE); and panel (*iv*) shows the transport of this polluted cesspool overnight air back into the LFV the next day via sea breezes.

BC, Washington State and the eastern Pacific Ocean. Figure 3.15 displays these trajectories, except for Aug 3 (not shown). The forward trajectories (green) started at East Point with a start time of 5:00 PDT on a given day, while the backward trajectories (blue) ended at the Chilliwack monitoring station at 17:00 PDT, and were launched at elevations of 1010, 1005, 1000, 995 and 990 mb for 12 h. Generally, the backward trajectories showed significant air transport from the Strait of Georgia to the LFV (as represented by Chilliwack); 3 days showed air coming from the north (July 27, Aug 5, Aug 7); 1 day showed air coming directly from the west (Aug 2); and 2 days in particular showed significant stagnation in the Strait (July 28, Aug 6). The forward trajectories also showed direct air transport from Saturna Island into the LFV on 4 days (July 28, Aug 5-7) with apparent stagnation, while for the remaining 3 days "Saturna-air" was transported southeast. These results provide further evidence that the NO_2 measured via MAX-DOAS at East Point was transported into the LFV and could be partly responsible for increased ozone production at stations like Abbotsford, Chilliwack and Hope.

Figure 3.15 also shows the daily maximum ozone value found in the LFV (Hope station) on each selected day. During the entire field study from July 25-Aug 8, $\chi^*_{O_3}$ levels in the LFV ranged from 39 to 76 ppb and $\chi^*_{O_3}$ with 1 h averages exceeding 65 ppb on 3 days: Aug 5 (66 ppb), July 27 (74 ppb) and Aug 4 (76 ppb). Generally the highest $\chi^*_{O_3}$ in the LFV was found at the Hope monitoring station (13 out of

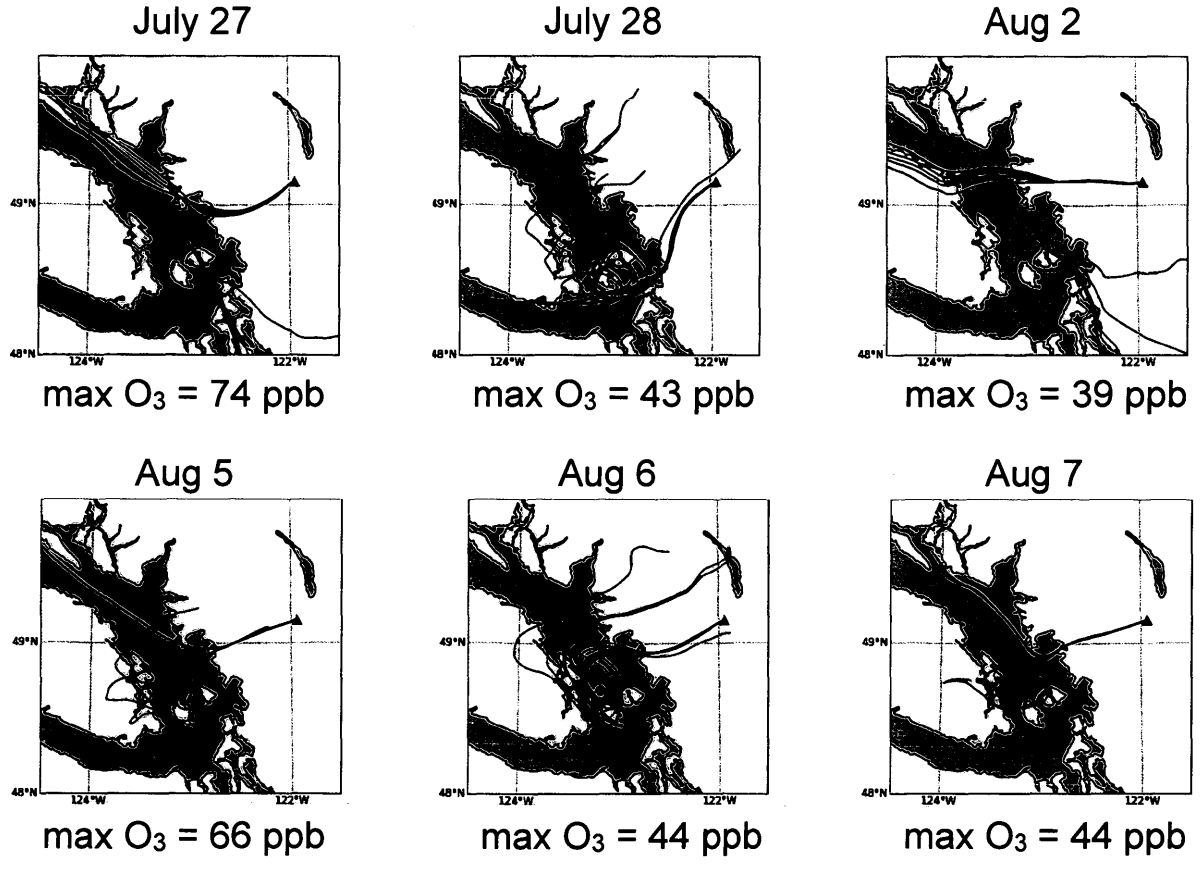

Figure 3.15: Air trajectories in the LFV. Forward trajectories (green) were run starting at East Point at 5:00 PDT daily. Backward trajectories (blue) were run ending at the Chilliwack at 17:00 PDT. Run times for both were 12 h. The maximum ozone found in the LFV (Hope) is also shown daily at the bottom of each sub-figure.

15 days), but on July 31 the highest $\chi^*_{O_3}$ was found at the Coquitlam station (T32) and on Aug 4 the highest $\chi^*_{O_3}$ was found at the Chilliwack station. Unlike the situation on Aug 5 or July 27, sustained strong sea breezes with wind speeds > 5 km h^{-1} were not present at all 6 met-stations in the LFV on Aug 4. This particular day had weaker sea breezes in the LFV, with the average wind speeds at the closest available met-station (Abbotsford) between 12:00 and 16:00 PDT slightly above the 5 km h^{-1} threshold (5.4 km h^{-1}). This day represented an example of extreme stagnation where NO_x and VOCs were allowed to build up in the LFV without any significant inflow. The WISE did not seem to play a large role in the build-up and photochemical processing of pollutants in the LFV during the field study, on the seven days with significant sea breezes (aside perhaps from on Aug 5 where forward trajectories showed significant stagnation and a maximum $\chi^*_{O_3}$ of 66 ppb at Hope).

The overall transport scenario described in detail earlier (and seen in Figure 3.14) may however indeed exist. The CO distribution in the LFV and Strait of Georgia on August 9 was modelled by Bruce Ainslie, with Environment Canada's AURAMS model at 4 km resolution over a domain that was nested within the GEM domain and had 27 vertical levels. AURAMS uses meteorology generated from GEM and emissions based on the Canadian 2006 and US 2005 inventory, generated from the Sparse Matrix Operation Kernel Emissions (SMOKE) processing system. Using the AURAMS-calculated concentrations at the lowest model level,

CO mixing ratios were saved at one hour intervals and snapshots from Aug 9 are shown in Figure 3.16. Model results showed strong evidence for the WISE. At 0:00 PDT significant amounts of CO are located in the LFV, while outflow overnight carries this CO into the Strait. By early morning (8:00 PDT) most is in the Strait, and by 11:00 PDT most of the CO is in the WISE zone. However, the CO that stagnates in this area begins to spin around itself due to a W/NW air flow around 13:00 PDT and ultimately is dissipated between 14:00-20:00 PDT. As was seen in the AURAMS model for Aug 9, something as simple as a change in wind direction could ultimately lead to a dissipation of the photochemical plume before it is able to impact the LFV. Yet, in other cases with a different wind direction (e.g. SW), the transport of pollutants from the WISE zone to the LFV could greatly impact the ozone levels and particulate matter in the valley, as hypothesized by Brook et al. (2004).

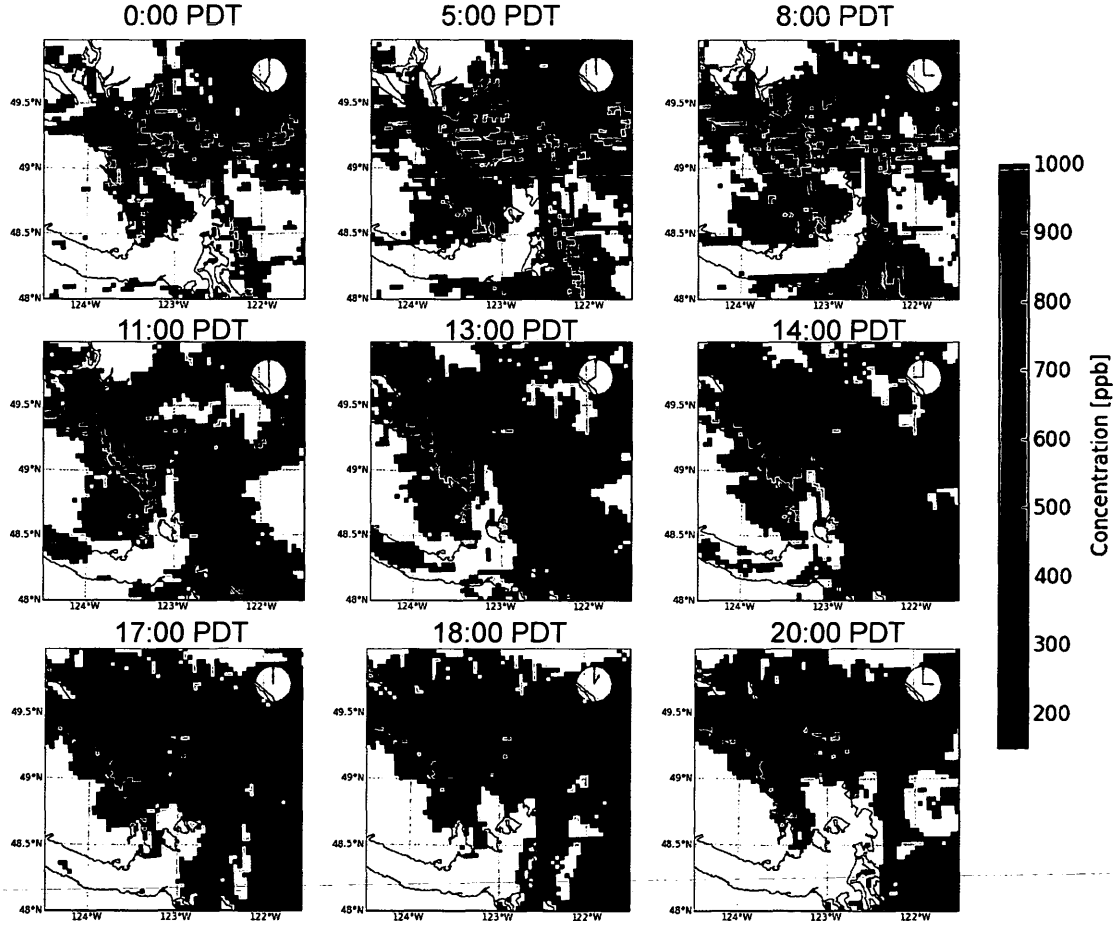

Figure 3.16: Snapshots of the CO distribution in the Strait of Georgia as modelled using AURAMS on Aug 9, 2005. At 0:00 PDT significant amounts of CO are located in the LFV, while outflow overnight carries this CO into the Strait. By morning (8:00 PDT) most is in the Strait, and by 11:00 PDT most of the CO is in the WISE zone. A W/NW air flow begins around 13:00 PDT and CO is ultimately dissipated between 14:00-20:00 PDT

3.5 Case Study: August 5, 2005

Figure 3.17 displays concurrent active and MAX-DOAS measures of NO_2 taken at East Point on Aug 5, 2005. The active DOAS NO_2 mixing ratio provides a measurement that essentially considers local sources only, while the MAX-DOAS slant column density represents an average value of NO_2 over a light path tens of kilometers in length (depending on the EA chosen). Nonetheless, in the morning hours between 7:30 and 10:00 PDT a similar temporal variation is seen in the NO_2 mixing ratio and ΔSCD. This is likely because most of the NO_2 present locally and within the differential slant column is contained in a low MBL. A possible indication that the MBL is low is that the NO_2 ΔSCDs decrease as a function of increasing EA, providing evidence for decreasing tropospheric paths. The active DOAS is not sensitive to any tropospheric NO_2 above the height of the instrument's light beam (average height $\sim$15 m *asl*) while the MAX-DOAS instrument has the capability of measuring the total vertical column of NO_2 as the EAs are varied.

MAX-DOAS also has the potential to capture spatial inhomogeneities in the Strait of Georgia. In the morning of Aug 5, the instrument's telescope was pointed at Heading 65° towards Blaine, USA. However, a distinct difference in visibility in the Strait was seen throughout the morning whereby a light brown haze was clearly more visible towards Heading 330° (and downtown Vancouver) than Heading

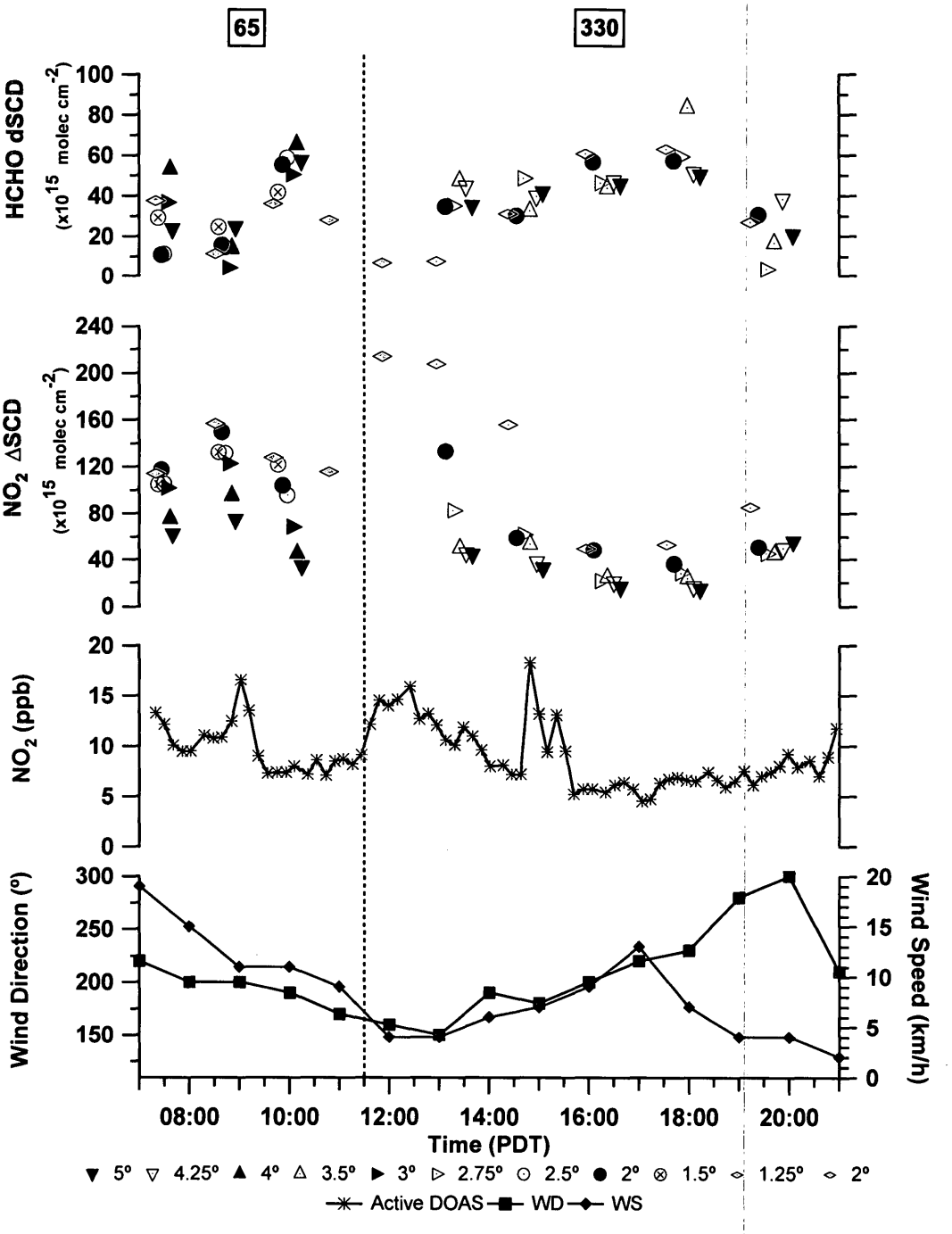

Figure 3.17: Active DOAS NO_2 mixing ratio, MAX-DOAS NO_2 and HCHO DSCDs, wind speed and wind direction at East Point, Saturna Island on Aug 5, 2005.

65°. Successive measurements with $\alpha = 1°$ were taken, first at 65° then at 330°, to determine if the MAX-DOAS instrument could quantify this visual difference. Figure 3.17 shows that the NO_2 ΔSCD at 330° is approximately two times higher (from ~1 to 2×10^{16} molec cm^{-2}) than the ΔSCD at 65°. This difference is believed to be real since the difference in the RAZI (between headings) at this time of day would not change the average light path greatly. However, temporal changes in NO_2 during the time taken for these $DSCD_1$ measurements may play a role in this difference.

When comparing NO_2 and HCHO DSCDs (Figure 3.17) it is apparent that their diurnal behaviour on Aug 5 is different. While the NO_2 peaks in the early afternoon ~12:00 PDT, the HCHO peaks late in the day ~18:00 PDT due to its increased photochemical production. The profiles of these species as a function of height likely differ as well. When the MAX-DOAS telescope was pointed to Heading 65° the NO_2 ΔSCDs showed a clear dependence on EA, as mentioned earlier, while the HCHO dSCDs displayed higher values at higher EAs (e.g. at times $DSCD_4$ and $DSCD_5$ were greater than the lower angle DSCDs like $DSCD_1$). When the MAX-DOAS telescope was pointed to Heading 330° in the afternoon there was a substantial time period from ~14:00-20:00 PDT when there was little variation between EAs for both NO_2 and HCHO, potentially giving them similar vertical profiles. If aerosol levels were extremely high this could lead to equating the effective path length for

all EAs, but at this time aerosol levels measured at Saturna (NASA, 2010c) were believed to be moderate (e.g. the aerosol optical depth at 340 nm ranged from 0.08 to 0.13 on July 29-31 and Aug 8). Assuming that the NO_2 and HCHO profiles are the same during this time period, the ratio of $HCHO/NO_2$ (with equal EAs) may be used to estimate whether the ozone formation in the air mass is VOC or NO_x limited (Sillman, 1999). Using the GEOS-CHEM global 3-D model of ozone-NO_x-VOC chemistry, Martin et al. (2004) defined a NO_x limited region to be located in areas where a similar ratio of the VCD_{HCHO}/VCD_{NO_2}, determined via the GOME satellite, to be equal or greater than 1.0. Applying this criteria to the last five EA sequences of the day at each available angle, Figure 3.18 shows the $HCHO/NO_2$ DSCD ratios for various EAs. Based on the rationale of Martin et al. (2004) it appears that O_3 formation in the Strait of Georgia is likely NO_x limited in the afternoon after ~16:30 PDT on Aug 5, 2005 but VOC limited in early afternoon from ~13:00 PDT to 16:00 PDT, although this assumes that HCHO and NO_2 are good representations of the VOCs and NO_x respectively, and the HCHO and NO_2 vertical profiles are identical. In the future it would be better to use the HCHO and NO_2 MAX-DOAS-RTM derived VCDs (Chapter 4) to determine the $HCHO/NO_2$ ratio since the VCD would be independent of the trace gas profile (as the DSCDs are not). Yet, this is the first known attempt (to one's knowledge) to determine NO_x and VOC limited regimes for ozone formation using MAX-DOAS.

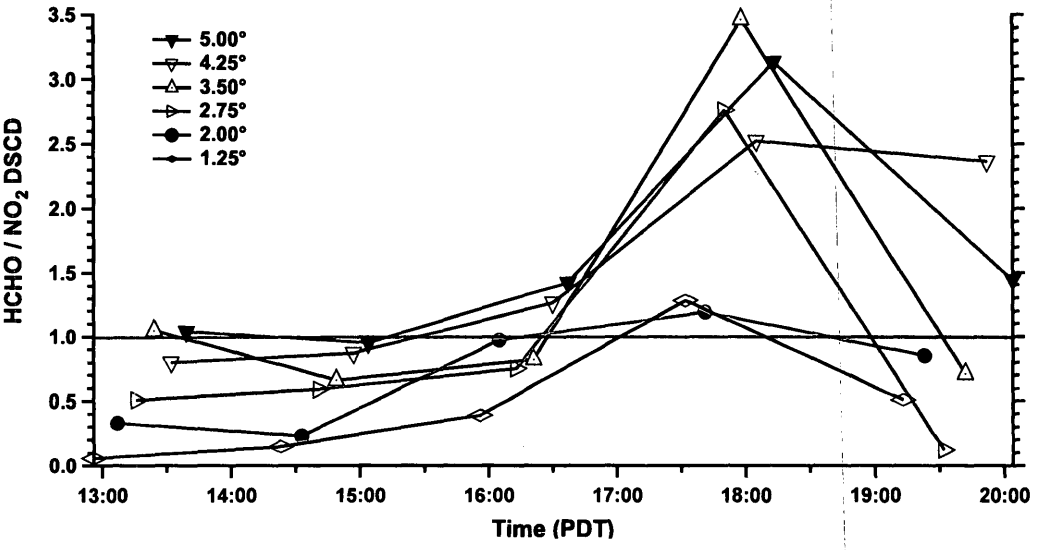

Figure 3.18: $HCHO/NO_2$ DSCD ratios for the afternoon of Aug 5, 2005, as a function of elevation angle.

3.6 Conclusions

MAX-DOAS measurements were taken at East Point, Saturna Island for three weeks during the summer of 2005. Average NO_2 slant column densities, represented by ΔSCDs, showed maximum values during the early morning and late afternoon/early evening time periods, similar to what was seen at station T13 in North Delta approximately 30 km NE of Saturna. The evening increase was also similar to what was seen from active DOAS measurements located concurrently at the East Point site. Furthermore, an "NO_2 weekend effect" was seen in both the

active and MAX-DOAS measurements whereby the median values for NO_2 mixing ratios and ΔSCDs were lower on the weekend days than weekdays. The statistics are somewhat limited for this analysis since only four weekend days occurred in the study. As such, further measurements would be needed to verify this tentative result. NO_2 mixing ratios in the LFV also exhibited this trend, leading to higher O_3 levels at urban sites (T1, T4) that are VOC limited but lower O_3 at more rural locations that are NO_x limited (T33, T12 and T29).

The relationship between NO_2 ΔSCDs ($\alpha = 1°$ or $5°$) and the maximum ozone formed in the Lower Fraser Valley was examined and statistically significant correlations were seen for several stations in the valley. The greatest effect seemed to be for stations further into the LFV such as Chilliwack and Hope. Areas such as this are likely NO_x limited and the introduction of extra NO_2 and photochemically processed ozone precursors into these areas are likely to result in enhanced ozone production. Forward and backward air trajectory analysis using Environment Canada's Trajectory model showed significant air transport from the Strait of Georgia to the Chilliwack monitoring station. These trajectories, at times, showed direct evidence for stagnation in the Strait. However, the significance of the wake-induced stagnation effect to the overall ozone production in the LFV is still debatable. During the field study, high ozone levels above 65 ppb were present on three days in the LFV; the highest maximum daily ozone was found on Aug 4, a day when sus-

tained sea breezes were insignificant. As such, the data set is not ideally suited to examine the WISE. However, AURAMS model results that used CO as a tracer for air pollutants in the LFV and Strait of Georgia did show a WISE-type stagnation on Aug 9. Unfortunately, in this case, the stagnation seen in the WISE zone was not transported into the LFV due to a change in wind direction in the early afternoon. Further field campaigns and modelling studies should be performed in order to examine the WISE further.

Finally, Aug 5 was used for a case study to show the differences between information gleaned via MAX-DOAS and ground-based techniques. Active NO_2 mixing ratios were compared to ΔSCDs and showed similar temporal variations in the early morning. The MAX-DOAS telescope was pointed in two separate headings and showed a large difference in sequential ΔSCDs, likely reflecting spatial inhomogeneity that was visually seen as a light brown haze from Saturna. Differential slant columns of both HCHO and NO_2 were compared when it was believed that both gases had similar vertical profiles. The HCHO/NO_2 DSCD ratio was calculated for several low EAs (e.g. 5°, 4.25°, 3.5°, 2.75°, 2°, and 1.25°), and although this ratio changed as a function of EA, for most EAs it was found to be greater than 1 in the afternoon after 16:30 PDT, possibly signifying, as suggested by Martin et al. (2004), a NO_x limited O_3 environment in the Strait of Georgia. Future studies should use VCDs for this ratio since they do not depend on trace gas profiles.

4 BAQS-Met Field Study

4.1 Introduction

In this chapter, an original two-step approach to determine NO_2 VCDs from MAX-DOAS measurements is outlined, applied to a data set on a routine basis, and validated with other field measurements.[1] The first step makes use of measured O_4 DSCDs and the RTM McArtim (Monte carlo Atmospheric radiative transfer inversion model) to obtain aerosol conditions for each MAX-DOAS measurement, following the approach introduced by Li et al. (2010). This aerosol information is then used as input to McArtim for the calculation of NO_2 AMFs that are ultimately compared to the measured MAX-DOAS SCDs to obtain NO_2 VCDs. In addition to the NO_2 VCDs, aerosol optical depth (τ) values, aerosol layer heights (H_{aer}) and gas layer heights (H_{gas}) are also determined. A full description and comprehensive analysis of the methodology is described within this chapter and in Halla et al. (2011), with further details in Wagner et al. (2011).

[1] Published in Halla et al. (2011).

Complex meteorological phenomena imposed by lake breezes interacting with anthropogenic sources are known to modify the air quality in southern Ontario (Hastie et al., 1999; Reid et al., 1996; Sills et al., 2011). One goal of the 2007 Border Air Quality and Meteorology Study (BAQS-Met) was to examine such interactions. This was accomplished using a three-week MAX-DOAS dataset collected in a rural region of southwestern Ontario that was supported by ground and aircraft-based measurements of trace gases and aerosols. The methodology outlined here for the determination of NO_2 VCDs is validated against experimentally derived composite profiles of NO_2 (aircraft + ground measurements) collected during BAQS-Met, compared to spatially and temporally coincident NO_2 VCDs determined from the satellite instruments OMI and SCIAMACHY, and compared to modelled NO_2 VCDs found from the AURAMS model. The aerosol optical depth values determined are compared to spatially relevant OMI, MODIS, AERONET and $PM_{2.5}$ measurements. Lastly, case studies are presented to demonstrate the ability of MAX-DOAS to characterize the complex transport of NO_2 in this region.

4.2 Experimental

4.2.1 BAQS-Met Ridgetown Supersite

During the BAQS-Met field study, measurements were acquired from June 20-July 10, 2007, at the Ridgetown ground site (Figure 4.1). Ridgetown is a small farming community with a population of ~3,500. The measurement site (42.45°N, 81.89°W), at an elevation of 202 m *asl*, was located in an agricultural field at the far north end of the University of Guelph (Ridgetown campus) away from the town center, with very limited local effect from direct anthropogenic influences. Surrounding anthropogenic influences (distance and direction) that can influence the site include a major highway, HWY 401 (4 km N), major refineries and chemical industry in Sarnia, ON (70 km NW), two major coal-fired power plants (65 km NW), Detroit/Windsor (100 km W), Cleveland, OH (100 km S) and the Golden Horseshoe (Toronto/Hamilton) urban area (200 km NE). Numerous urban areas and coal-fired power plants are also located in the Ohio valley region (100-500 km, S-SW). The site was 10 km from the north shoreline of Lake Erie.

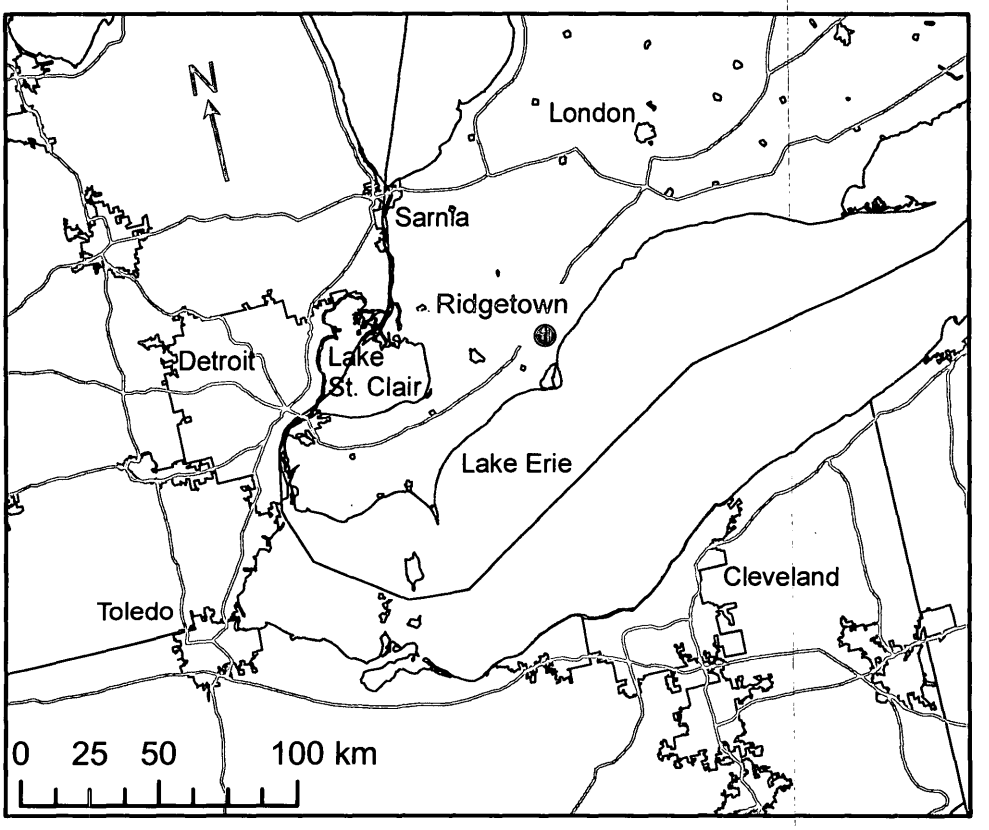

Figure 4.1: BAQS-Met Ridgetown supersite and other areas of interest in south-western Ontario and adjacent areas in the USA.

4.2.2 The MAX-DOAS Instrument and Retrieval

The MAX-DOAS instrument (Chapter 2, Figure 2.1) used to measure scattered sunlight at Ridgetown was described previously (Chapter 3, Section 3.2.2). This time however the spectrometer used was an Ocean Optics USB 2000^{+} (323-471 nm, grating #7, 2400 lines mm^{-1}, 50 μm slit, UV4 upgrade, L4 lens, $\sim$0.5 nm FWHM).

This new spectrometer was housed in a Peltier cooling thermoelectric unit (Resonance Inc.) to achieve a stable temperature of 15±0.2°C. The spectrometer data was transferred to a PC via USB connection, while the elevation angles were varied and the data acquired using the custom LabVIEW program described in Chapter 2, Section 2.1. During the field study, one complete cycle, lasting approximately 30 minutes, consisted of a series of measurements with the following elevation angles: 90°, 30°, 10°, 6°, 4°, 2°. Each measurement typically consisted of 2000 averages with integration times ranging from 30-300 ms at midday to between 500-2000 ms later in the afternoon, depending on light conditions. In most cases, with the rationale of studying the passage of lake breeze fronts at the site, the MAX-DOAS telescope was pointed in the SW direction ($\beta = 235°$, parallel to the shoreline of Lake Erie), where β is the direction the telescope is pointed. Yet, in order to examine the ability of MAX-DOAS to determine spatial inhomogeneities, for one complete day during BAQS-Met (July 8, 2007), MAX-DOAS measurements were taken using two different elevation angle sequences and headings. For 50% of the time the MAX-DOAS telescope was pointed to the SW ($\beta = 235°$), while the remaining time the instrument was pointed NE ($\beta = 55°$). One complete measurement sequence here consisted of a 2°, 4°, 6°, 10° and 30° measurement cycle facing SW followed directly by 90° measurement, and a 30°, 10°, 6°, 4°, and 2° measurement cycle facing NE. This routine was repeated 17 times throughout the course of the day on July 8.

Each measured spectrum was corrected by subtracting an electronic offset (IT = 3 ms, 10,000 averages, without light). Another measurement without light (IT = 30,000 ms, and only 1 average) was used to correct for dark current. A customized j-script routine within the DOASIS software package (Kraus, 2006), was used to correct for the offset and dark current for each measurement spectrum (see Chapter 2, Equation 2.1 for details). These corrected spectra were then analyzed using the well-known DOAS technique (Plane and Smith, 1995; Platt, 1994; Platt and Stutz, 2008). A wavelength calibration using WinDOAS (Fayt and van Roozendael, 2011) was performed by fitting a noon-time FRS_k ($\alpha = 90°$) taken on a clean day (June 20) to a high resolution solar spectrum (Kurucz et al., 1984) that was convolved with the instrument's slit function. A Ring spectrum (Grainger and Ring, 1962) was then calculated from the FRS_k with DOASIS (Kraus, 2006). The NO_2 and O_3 (223 K and 243 K) absorption cross sections (Bogumil et al., 2003; Vandaele et al., 1998) were convolved using WinDOAS to match the instrument's resolution, while the O_4 cross section (Greenblatt et al., 1990) was interpolated.

To determine the NO_2 $DSCD_k$ for each spectrum, a 3rd order polynomial, the logarithm of the FRS_k, the Ring spectrum, convolved NO_2, convolved O_3 (223 K) and an additive polynomial were fit to the logarithm of the corrected measurement spectrum using WinDOAS in the fit range 410-435 nm. Figure 4.2 gives a sample NO_2 fit for June 20, 9:46 EDT (Eastern Daylight Time = UTC-4) with an elevation

angle of 4°, yielding a NO_2 $DSCD_k$ of 8.78×10^{16} molec cm^{-2}. The NO_2 $DSCD_k$ detection limit was $\sim2\times10^{15}$ molec cm^{-2} calculated using two times the average fit error. To determine the O_4 $DSCD_d$ for each spectrum, a 4th order polynomial, the logarithm of the FRS_d, the Ring spectrum, interpolated O_4, convolved NO_2, convolved O_3 (223 K and 243 K) and an additive polynomial were fit to the logarithm of the corrected measurement spectrum using WinDOAS in the fit range 355-385 nm. Figure 4.3 gives a sample O_4 fit for June 20, 9:29 EDT with an elevation angle of 30°, yielding a O_4 $DSCD_d$ of 2.22×10^{43} $molec^2$ cm^{-5}. Table 4.1 gives a complete summary of the fit ranges, absorption cross sections, FRS, Ring, and polynomials used for NO_2 and O_4.

Table 4.1: MAX-DOAS fit scenario overviews for NO_2 and O_4.

Trace Gas Fit	Fit Range (nm)	Cross Sections in the fit scenario	FRS and Ring	Degree of Polynomials	Offset Polynomial
NO_2	410-435	NO_2 & O_3(223 K)	June 20	3rd	constant
O_4	355-385	O_4, NO_2, O_3 (223 K)	Daily	4th	constant

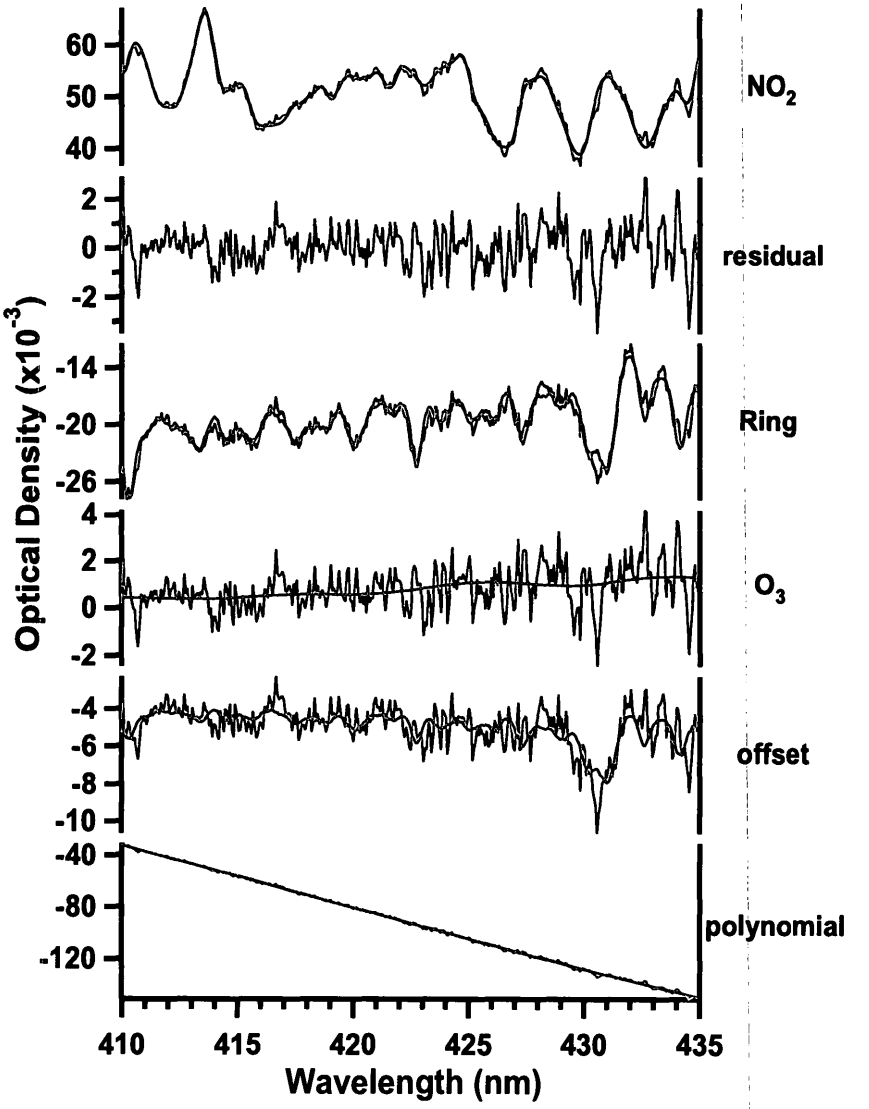

Figure 4.2: NO_2 MAX-DOAS fit retrieval for a measurement with $\alpha = 4°$ on June 20, 2007, 9:46 EDT. This fit, performed between 410-435 nm, includes the NO_2 and O_3 absorption cross sections, plus a 3rd order polynomial, offset polynomial, FRS_k, and Ring. The residual of the fit is shown in the second panel. For each remaining panel the black line represents the DOAS fit, and the red line represents the DOAS fit plus the residual of the species examined.

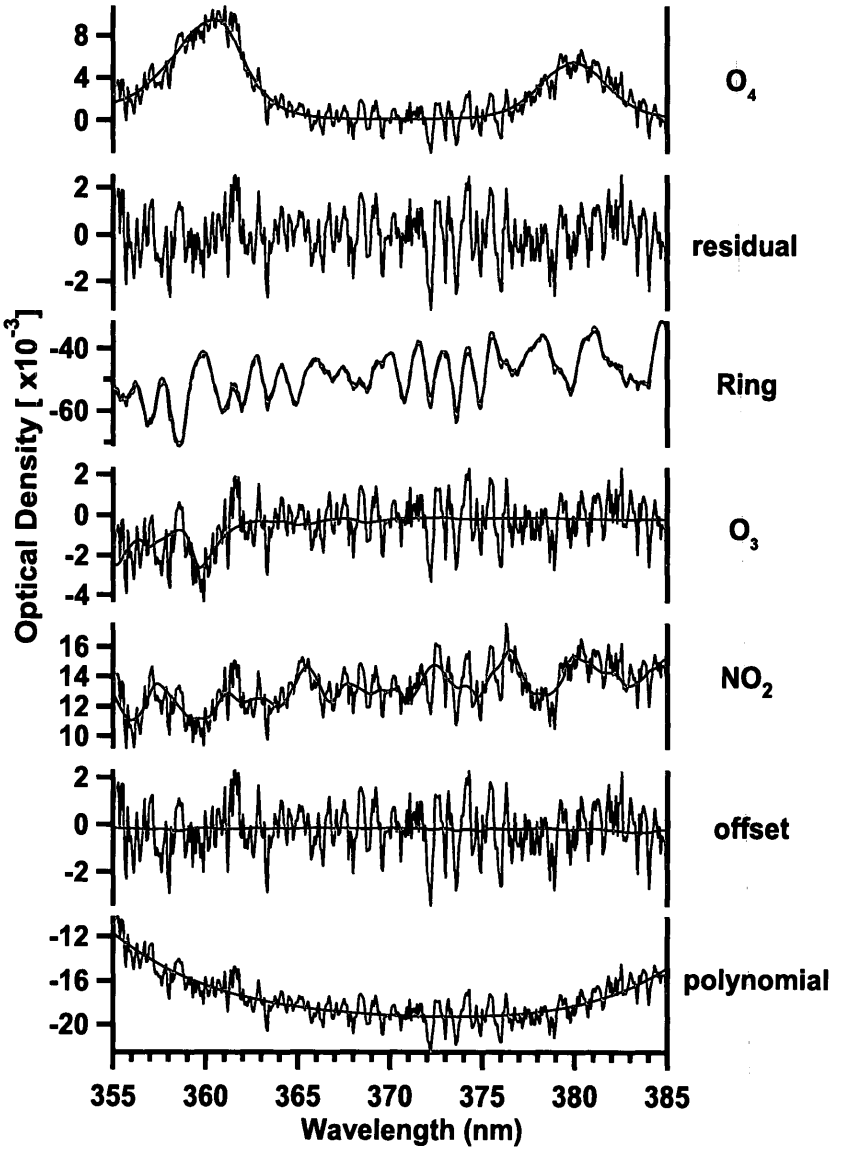

Figure 4.3: O_4 MAX-DOAS fit retrieval for a measurement with $\alpha = 30°$ on June 20, 2007, 9:29 EDT. This fit, performed between 355-385 nm, includes the O_4, NO_2, and O_3 absorption cross sections, plus a 4th order polynomial, offset polynomial, FRS_d, and Ring. The residual of the fit is shown in the second panel. For each remaining panel the black line represents the DOAS fit, and the red line represents the DOAS fit plus the residual of the species examined.

4.2.3 The Active DOAS Instrument and Retrieval

Measurements of ground-based NO_2 were made using an active DOAS instrument (Chapter 1, Figure 1.4) that has been described in detail previously (Chapter 3, Section 3.2.3). Briefly, the instrument utilized a 150 W high pressure Xe-arc lamp and a coaxial Cassegrain telescope. A corner cube retro-reflector was located 1.06 km SW of the site (β = 235°) on the top of a building at an elevation of 6 m *agl*, giving a total path length of 2.12 km and an average beam height of 3.5 m *agl*. The active DOAS instrument was located inside a shed adjacent to the MAX-DOAS instrument. The return beam was focused onto a 200 μm diameter quartz fiber optic (Ocean Optics), which coupled the light into a miniature spectrometer (Ocean Optics USB2000, grating #10, 295-492 nm, 1800 lines mm^{-1}, 2048 element CCD, 25 μm slit, UV2 upgrade, L2 lens, resolution ~0.5 nm). The spectrometer was cooled to -5°C in a portable freezer.

Custom acquisition software was written in LabVIEW to acquire spectra with typical integration times of 150-350 ms and 4000 scans, for spectra with a time resolution of 7-13 minutes. Mercury lamp reference spectra were collected periodically for wavelength calibration and for convolving molecular reference spectra to the slit function of the spectrometer. Xenon lamp spectra were collected for use in fitting to the measured spectra and each ambient spectrum was corrected for

electronic offset and dark current (Chapter 2, Equation 2.1). All spectra were fit using DOASIS (Kraus, 2006) in the wavelength range of 422-450 nm. The NO_2 fit scenario included a lamp reference spectrum, convolved spectra of NO_2 (Vandaele et al., 1998) and O_3 at 223K (Bogumil et al., 2003), and a 3rd order polynomial. The detection limit (3σ) for NO_2 was 1.1 ppb, determined by repetitive determination of a low concentration sample.

4.2.4 SCIAMACHY Satellite DOAS

The SCanning Imaging Absorption spectroMeter for Atmospheric CHartographY (SCIAMACHY) on board the European Space Agency's ENVIronmental SATellite (ENVISAT) (Bovensmann et al., 1999) measures Earthshine spectra from the UV to the NIR with a spectral resolution of 0.22-1.48 nm. It is operated in different viewing geometries, including nadir and limb. In nadir geometry (directed vertically down), the footprint of a single pixel is $\sim 30 \times 60$ km^2. Global coverage of nadir measurements is achieved every six days. In standard operation mode, the measurement state alternates between limb geometry (directed horizontally, tangential to the Earth's surface), and nadir in such a way that limb measurements probe almost the same stratospheric air mass as subsequent nadir measurements.

From the Earthshine spectra measured by SCIAMACHY, total slant column

densities of NO_2 were determined by Steffen Beirle, MPI für Chemie, Mainz, Germany, using the DOAS fitting technique (Platt and Stutz, 2008). For the NO_2 fit in the spectral range 431-460 nm, appropriately convolved absorption cross sections of O_3, NO_2, O_4, H_2O, H_2O (liquid), and CHOCHO, Ring spectra accounting for vibrational and rotational Raman scattering, and a 5th order polynomial are included (Beirle et al., 2010). In order to extract tropospheric column densities, the stratospheric fraction is estimated and subtracted. This was done using the Reference Sector Method (Beirle et al., 2010). Stratospheric column densities are estimated over the remote Pacific and the remaining tropospheric residuals are corrected for longitudinal variations using the limb measurements of SCIAMACHY. For the conversion of tropospheric SCDs into vertical column densities of NO_2 (VCD_{SCIA} values), tropospheric AMFs are calculated via the RTM McArtim (Deutschmann et al., 2011), assuming a fixed tropospheric profile with 80% of the tropospheric NO_2 within a constant boundary layer with a height of 1 km (Chen et al., 2009). Figure 4.4 gives an example of the averaged NO_2 VCD_{SCIA} values from 2003-2010 on a global scale, as seen in Beirle et al. (2010).

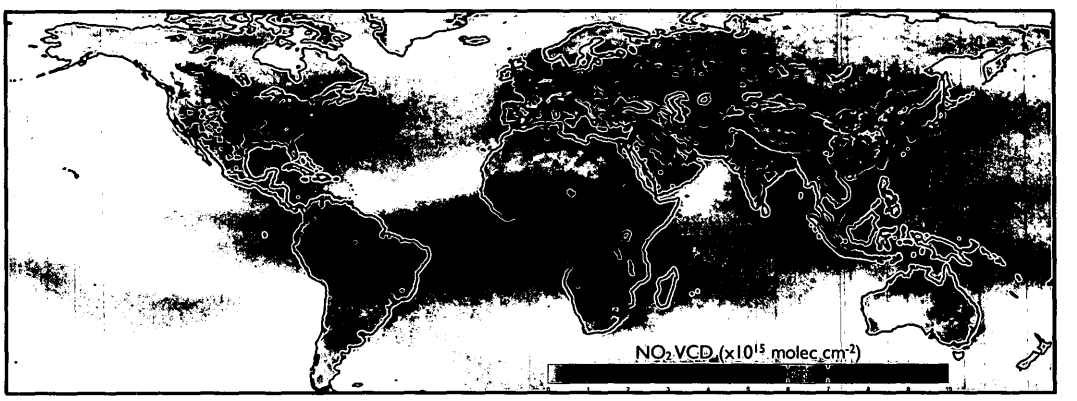

Figure 4.4: World map of averaged NO_2 tropospheric VCDs from SCIAMACHY for 2003-2010, courtesy of S. Beirle, MPI-Mainz, Germany (personal communication).

4.2.5 OMI Satellite DOAS

Onboard the Aura satellite, the Ozone Monitoring Instrument (OMI) is a nadir-viewing spectroradiometer that uses a 2-D CCD to simultaneously measure the Earthshine spectra in the ultraviolet-visible (UV-Vis) range from 270-500 nm (Levelt et al., 2006). Specifically, OMI measures in three broad spectral regions (UV-1, UV-2, and VIS) with a spectral resolution between 0.45 and 1.0 nm. It provides complete global coverage daily with a pixel size of 13×24 km^2 (312 km^2) at nadir increasing to $\sim40\times160$ km^2 (6,400 km^2) at the two ends of the scan line.

The present study uses the NASA standard product (overpass version) of the VCD of NO_2 (VCD_{OMI}) obtained from the NASA Aura Validation Data Centre

(AVDC) website (NASA, 2010b). From the Earthshine spectra measured by OMI, total slant column densities of NO_2 are determined using the DOAS fitting technique (Platt and Stutz, 2008). For the NO_2 fit in the spectral range 405-465 nm, appropriately convolved absorption cross sections of O_3 (Burrows et al., 1999), NO_2 (Vandaele et al., 1998), H_2O (Harder and Brault, 1997), a Ring spectrum (Chance and Spurr, 1997) and a cubic polynomial are included. To convert these SCDs into VCD_{OMI} values, different types of AMFs were calculated using geographically gridded (2.5°×2.0°) annual mean NO_2 profiles (GEOS-Chem was used for tropospheric, and the Goddard Chemical Transport model was used for stratospheric profiles (Bucsela et al., 2006)). Details of the algorithm used for the retrieval of the VCD_{OMI} may be found in Boersma et al. (2001); Bucsela et al. (2006); Celarier et al. (2008) and Wenig et al. (2008).

4.2.6 MODIS and OMI Aerosol Products

The MODerate resolution Imaging Spectroradiometer (MODIS) provides the ambient aerosol optical depth over portions of the continents and over oceans, from two satellites (Terra, Aqua). Daily level 2 data products give the highest resolution possible, and are produced at the spatial resolution of a 10×10 1 km pixel array (nadir). Two MODIS aerosol level 2 data products, collection 5, MOD04_L2

and MYD04_L2, from the Terra and Aqua satellites respectively, are available from the LAADS (Level 1 and Atmospheric Archive and Distribution System) website (NASA, 2010a). Only those data products that overlapped Ridgetown were used. All MODIS aerosol optical depth values were found at $\lambda = 550$ nm, and had a maximum sensitivity over land of 0.05±15% (Levy et al., 2007). OMI aerosol optical depth (τ) values were taken from the NASA AVDC (NASA, 2010b). The OMAERUV L2 product was selected ($\lambda = 388$ nm) for a satellite overpass of Ridgetown. Information on this OMI near-UV retrieval algorithm may be found in Torres et al. (1998).

4.2.7 AERONET Aerosol Products

AErosol RObotic NETwork (AERONET) aerosol optical depth (τ) values were taken from direct solar measurements using CIMEL sun photometers at two measurement sites (Kellogg, Michigan, USA – 42.41°N, 85.37°W, 293 m *asl*, and Egbert, Ontario, Canada – 44.23°N, 79.75°W, 264 m *asl*) (NASA, 2010c). All τ values have an uncertainty of ~0.01 to 0.02 ($\lambda = 340$ and 380 nm) and were AERONET Version 2.0, Level 2.0 – quality assured data, meaning they were pre- and post-field calibrated, automatically cloud cleared and manually inspected. Details regarding the AERONET network and the procedures used to calculate aerosol optical depths

may be found in Dubovik and King (2000), and Holben et al. (1998, 2001).

4.2.8 Additional Supporting Measurements

The NO_2, SO_2 and $PM_{2.5}$ were measured at ground level using a chemiluminescence NO_x analyzer with Mo converter (Thermo Model TE42C), trace level pulsed fluorescence SO_2 analyzer (Thermo Model TE43C-TL), and Tapered Element Oscillating Microbalance (TEOM) ambient $PM_{2.5}$ monitor (R&P Model 1400B with sample equilibration system) respectively. The data from these measurement devices, located in the Ontario Ministry of the Environment's (OME's) mobile particulate laboratory at the Ridgetown site, were supplied by Andy Ng, OME.

Measurements of NO_2 and other meteorological measurements were made onboard the NRC Twin Otter Aircraft that was dedicated to the BAQS-Met field campaign, and supplied by Kathy Hayden, EC. The NO_2 measurements were performed with a chemiluminescence NO_x instrument (TECO 42S) retrofit with a photolytic converter, for measurement of "true" NO_2 ($\pm$15%), with a detection limit of 60 pptv (3σ, 1 min). More details on the aircraft campaign measurements are provided elsewhere (Hayden et al., 2011).

The scanning LIDAR facility (RASCAL - Rapid Acquisition SCanning Aerosol LIDAR), capable of fast azimuth and elevation scanning of the lower troposphere,

was present at the Ridgetown site. A full description of its operation is also given elsewhere (Strawbridge and Snyder, 2004). All LIDAR data was supplied by Kevin Strawbridge, EC, and was used to aid in the determination of boundary layer heights for the composite profiles described in Section 4.5.5 and for the comparison of boundary layer heights to H_{aer} and H_{gas}, as described in Section 4.5.6.

4.2.9 AURAMS Model Results

AURAMS stands for A Unified Regional Air-quality Modelling System, and it is made up of three key components: (*i*) a prognostic meteorological model, GEM (Global Environmental Multi-scale model); (*ii*) an emissions processing system, SMOKE (Sparse Matrix Operator Kernel Emissions); and (*iii*) an off-line regional chemical transport model, the AURAMS chemical transport model. Using AURAMS, custom routines were made by Paul Makar, EC, to extract ground level NO_2, NO_x, and NO_y mixing ratios, and NO_2 VCDs as a function of time at the Ridgetown location. Further details with regards to AURAMS may be found elsewhere (Makar et al., 2009, 2010a,b).

4.3 Methodology for Determining τ and NO_2 VCDs from MAX-DOAS

The primary result of a MAX-DOAS retrieval is the DSCD:

$$DSCD_\alpha = SCD_\alpha - SCD_{90} \tag{1.14}$$

where SCD_α and SCD_{90} are the slant column densities of measurements with $\alpha < 90°$ and $\alpha = 90°$ respectively. The DSCD represents the difference in the column amount of the absorber integrated along the light path through the atmosphere and the column amount of the absorber in the SCD_{90}. It depends not only on the trace gas amount, but also on the elevation angle (α) of the measurement, the solar zenith angle (SZA) of the sun, and relative azimuth angle (RAZI) between the sun and the direction the telescope is pointed (β). As described in more detail in Section 4.2.2, for the BAQS-Met campaign all NO_2 DSCDs were determined using a fixed Fraunhofer Reference Spectrum (FRS_k) and, as such, are considered $DSCD_k$ values. In this chapter any reference to a NO_2 DSCD will more specifically signify a reference to a NO_2 $DSCD_k$ value. When calculating NO_2 VCDs using the inversion process described later in Section 4.3.1, NO_2 dSCDs were used from each measurement series. For a comprehensive description and clarification of the different ways of calculating differential slant column densities please consult Chapter 2, Section 2.2.1.

The Air Mass Factor (AMF) may be considered as the average light path

enhancement for solar light travelling through the atmosphere as compared to a straight vertical path orthogonal to the ground (Perliski and Solomon, 1993; Solomon et al., 1987) and is defined as the ratio of the slant column density (SCD) to the vertical column density (VCD) of a trace gas absorber:

$$AMF \equiv \frac{SCD}{VCD} \tag{1.17}$$

Similarly, the differential air mass factor (DAMF) may be calculated as the ratio between the differential slant column density (DSCD) and the vertical column density (VCD_{trop}) of an absorber in the troposphere:

$$DAMF = \frac{DSCD}{VCD_{trop}} \tag{4.1}$$

Since the DSCD contains only the tropospheric trace gas absorptions, for the calculation of the DAMF, only the tropospheric profiles of the trace gases have to be taken into account (Sinreich et al., 2005). Rearranging and expanding Equation 4.1 gives:

$$VCD_{trop} = \frac{DSCD}{DAMF} = \frac{SCD_{\alpha} - SCD_{90}}{AMF_{\alpha} - AMF_{90}} \tag{4.2}$$

Unfortunately the conversion from DSCD to VCD is not trivial, because the accurate determination of the DAMF is often difficult.

4.3.1 Radiative Transfer and Inversion

In southwestern Ontario, conditions with low aerosol levels are infrequently encountered during the summer and so the geometrical approximation (Chapter 1, Equation 1.19) often does not hold. Instead, a radiative transfer model was used to determine the required AMFs (Hendrick et al., 2006; Wagner et al., 2007). The Monte carlo Atmospheric radiative transfer inversion model (McArtim) is a backward model that calculates the photon flux at a certain location (latitude, longitude, altitude) in the atmosphere depending on several parameters and treats multiple scattering with full spherical geometry (Deutschmann et al., 2011). Operated in backward mode, it assumes that a photon emerges from the MAX-DOAS detector and follows an individual trajectory through the atmosphere until it leaves the top of the atmosphere or is absorbed. Probability distributions define the various events that may happen as the photon leaves the detector, and randomly generated numbers decide on the occurrence of events. At each scattering event a weight is calculated from two terms, the probability that sunlight reaches the scatter event, and the phase function of the scatter event. For each trajectory an estimate of the sun normalized radiance is obtained by adding all the weights of the scattering orders together. Many photon paths may be generated in order to reproduce the light of the simulated measurement. From the simulated radiances, AMFs for the

trace gases in question (O_4 and NO_2) are calculated. Input parameters to McArtim for each calculation include α, SZA, RAZI, altitude, pressure, temperature, surface albedo = 0.05, single scattering albedo (SSA) = 0.95, asymmetry parameter (g), under the Henyey-Greenstein approximation = 0.68 (Henyey and Greenstein, 1941), as well as parameters for the absorbing trace gases. The values used for these parameters were selected to be representative of a typical urban area (Dubovik et al., 2002). Of particular importance is the level of aerosol present in the atmosphere, as this will greatly alter the most probable light path from the sun to the MAX-DOAS detector (Frieß et al., 2006; Wagner et al., 2002, 2004).

Wagner et al. (2004) introduced the concept of using the oxygen dimer (O_2-O_2, or O_4) absorption to retrieve aerosol profiles (Frieß et al., 2006; Li et al., 2010; Wittrock et al., 2004). O_4 results from the bimolecular association of O_2:

$$O_2 + O_2 \rightleftharpoons O_4 \tag{R79}$$

is temperature and pressure dependent with a scale height of approximately 4 km, and is mainly independent of other atmospheric constituents including other trace gases and aerosols. This property allows it to serve as a gauging gas in order to calculate the effective path length of scattered light using the RTM McArtim. The variability in the O_4 profile due to pressure variations has a small effect on the final modelled aerosol parameters (Frieß et al., 2006). Thus, an estimated O_4 VCD (expressed as the integrated quadratic O_2 concentration) may be calculated

if temperature and pressure values as a function of height are known (Greenblatt et al., 1990). In order to get an estimated O_4 VCD, the following approach was used. The number densities of air (n_{air}), O_2 (n_{O_2}), and O_4 (n_{O_4}) as a function of height (z), may be calculated according to the following equations:

$$n_{air}(z) = \frac{A_v P(z)}{RT(z)} \tag{4.3}$$

$$n_{O_2}(z) = n_{air}(z) \cdot C_{O_2} \tag{4.4}$$

$$n_{O_4}(z) = K(T) \cdot [n_{O_2}]^2 \tag{4.5}$$

where A_v is Avagadro's number, $P(z)$ the height dependent pressure, R the universal gas constant, $T(z)$ the temperature, z the height *asl*, C_{O_2} (0.21) the mixing ratio of O_2 in the air, and K(T) the equilibrium constant for Reaction (R79). Since K(T) is unknown, the equilibrium constant is included in the O_4 VCD value (Greenblatt et al., 1990).

Although the height dependent pressure and temperature profiles could be estimated from assuming the Barometric Law and an adiabatic lapse rate respectively, radiosonde data from White Lake, Michigan: Station 72632/DTX (UWYO, 2010) that includes temperature and pressure values as a function of height, was used in order to calculate a more accurate O_4 VCD. An estimated O_4 VCD for Ridgetown may now be defined as:

$$VCD_{O_4} = \int_{200m}^{30{,}000m} n_{O_4} dz \tag{4.6}$$

Alternatively, substituting in Equations 4.3-4.5 into 4.6 yields:

$$VCD_{O_4} = K(T) \int_{200m}^{30,000m} \left[\frac{A_v P(z)}{RT(z)} \cdot C_{O_2} \right]^2 dz \tag{4.7}$$

The exact values from the radiosonde data were not integrated in this case because the ground elevation of Station 72632 at White Lake, Michigan was 329 m *asl*, while the ground elevation at Ridgetown was 202 m *asl*. Therefore, a sixth order polynomial was fit to the n_{air} vs. height curve (Figure 4.5) created using the radiosonde data (Equation 4.3). The resulting polynomial was then used to perform a numerical integration using Equation 4.7, from a starting height of 200 m to a final height of 30,000 m, using 100 m steps.

The result of this integration yielded an estimated O_4 VCD of 1.28×10^{43} molecules^2 cm^{-5}. This value agrees with other calculated values using similar approaches at similar elevations: 1.30×10^{43} molec^2 cm^{-5} (Wagner et al., 2009), 1.26×10^{43} molec^2 cm^{-5} (Heckel et al., 2005; Wagner et al., 2002). Since most O_4 is predominately in the lowest part of the troposphere, this is the region where O_4 DSCDs are most sensitive to changes in the light path due to varying levels of aerosols. As such, the amount of aerosol present for a given time and location also has a very large effect on the DAMFs. Under low aerosol conditions where most photons reaching the detector are single scattered, both the penetration depth of direct sunlight, and the direct line of site to the telescope have long paths (Figure 4.6A). Conversely, under high aerosol conditions, multiple scattering dominates, and both the penetration

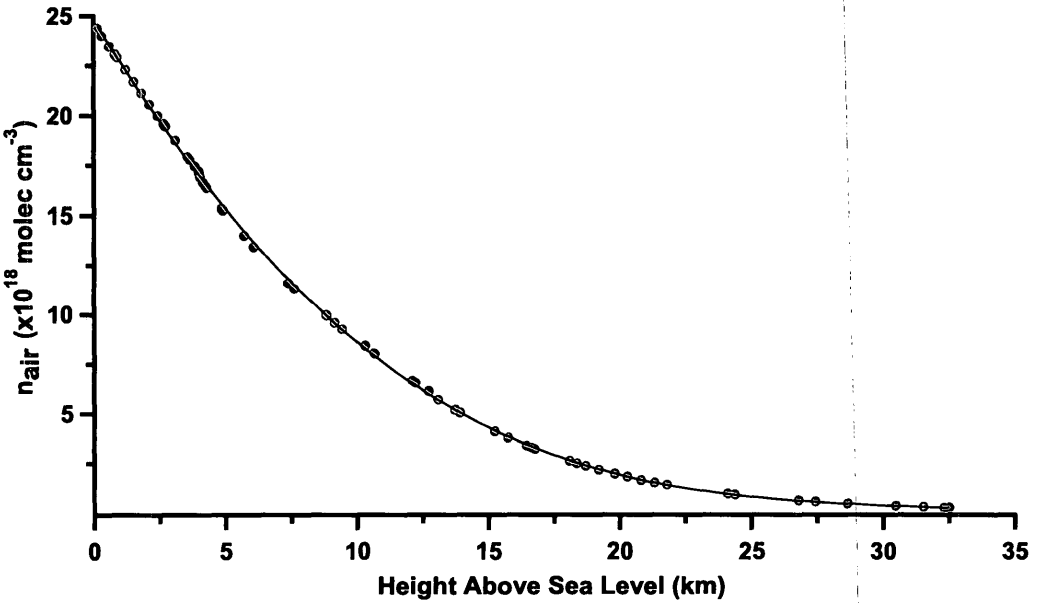

Figure 4.5: The n_{air} vs. Height (*asl*) profile used to calculate the estimated O_4 VCD value for the Ridgetown location. Red points represent values calculated directly from the radiosonde data, which was then fit to a 6th order polynomial (black line).

depth, and the direct line of site to the telescope have much shorter path lengths (Figure 4.6B). There will be a decrease in the O_4 DSCDs, particularly those at lower elevation angles, because higher aerosol extinction reduces the distance that photons travel through the lower atmosphere where most of the O_4 is concentrated. The difference between O_4 DSCDs measured with different elevation angles becomes less obvious and, because the penetration depth of the incident sunlight is reduced, the diurnal variation for the O_4 DSCDs is reduced as well (Wagner et al., 2004). Using this knowledge, a quick qualitative assessment plus a more comprenhensive

calculation of aerosol optical depths were performed to describe the aerosol conditions of cloud-free measurement sequences at Ridgetown (see Sections 4.3.1.1 and 4.5.3).

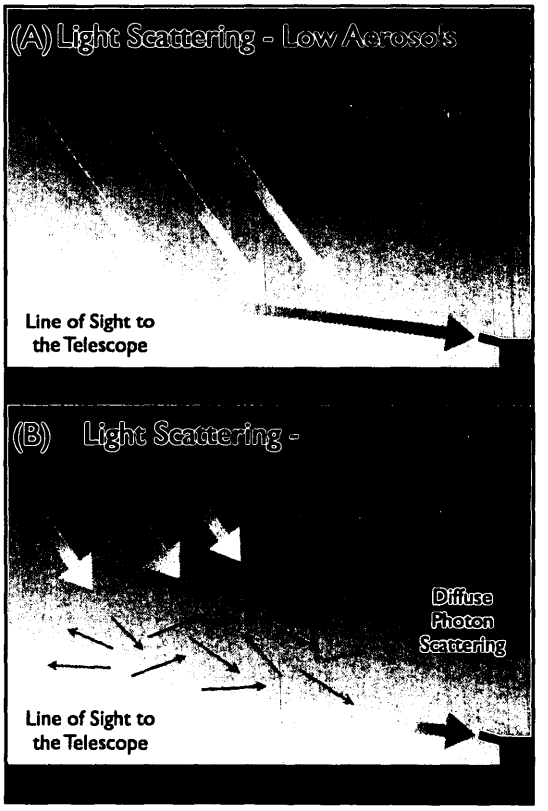

Figure 4.6: The effect of aerosols on scattered sunlight. Panel (A) shows the case where low aerosol levels are present, while panel (B) shows the case where high aerosol levels are present.

4.3.1.1 Aerosol Optical Depth (τ)

Aerosol optical depth, τ, refers to the attenuation of light due to aerosol extinction. In the following defining equation, I_0 is the original intensity of light, I is the intensity after travelling a distance x, through the atmospheric column, and E is the aerosol extinction coefficient:

$$\frac{I}{I_0} = e^{-\tau} = e^{-Ex} \tag{4.8}$$

Typically, aerosol optical depth is defined for light travelling through a vertical column of the atmosphere from sea level to infinity (top of the atmosphere), in which E is not constant with height. In order to model conditions with varying degrees of aerosol load, an integrated aerosol optical depth (τ), from sea level to above the troposphere (~20 km) was defined as:

$$\tau = \int_{0km}^{20km} E(z)dz \tag{4.9}$$

where z is the height *asl.* In the radiative transfer modelling performed in this dissertation, *E(z)* was divided into two layers (Figure 4.7), as developed by Li et al. (2010):

$$E(z) = \frac{\tau}{f \cdot H_{aer}}, z \leq H_{aer} \tag{4.10}$$

$$E(z) = \frac{\tau}{f \cdot H_{aer} e^{\gamma}}, z > H_{aer} \tag{4.11}$$

$$\gamma = \left[\frac{-1}{(H_{aer}/f) - H_{aer}}\right] \cdot [z - H_{aer}] \tag{4.12}$$

where τ is the integrated aerosol optical depth, H_{aer} the aerosol layer height, f the shape parameter that describes the relative shape of the aerosol profile, and γ is as defined in Equation 4.12 .

All aerosol profiles modelled in this study may then be described by the three parameters: τ, f, and H_{aer}. While τ represents the vertically integrated total aerosol optical depth for aerosols, the H_{aer} parameter describes the aerosol layer height of the profile. Within H_{aer}, the aerosol level is assumed to be constant and the values of the aerosol extinction above H_{aer} decrease depending on the last defined parameter, f. The shape parameter (f) gives the relative shape of the aerosol profile. By varying f, various aerosol profiles may be modelled. When $f>0$ and $f<1$, a quasi-exponential situation may be modelled. For example, if $f = 0.8$, 80% of the aerosol is present from ground level until H_{aer}, the remaining 20% is above H_{aer} (and decays exponentially from H_{aer} until the top of the troposphere). If $f = 1$ a box profile is modelled where 100% of the aerosol is located from ground level until H_{aer}. In this scenario there is no aerosol above H_{aer}. By using the above three parameters to describe the aerosol profile, a wide variety of scenarios may be described. Unfortunately, certain complex situations, such as multiple layers could not be modelled under this parameterization scheme. Furthermore, due to the limited information content of the MAX-DOAS measurements in the UV, the accurate determination of all three parameters (f, τ, and H_{aer}) is often difficult. As

such, for this study, f was set to one to create a box profile for the analysis of this data set. A sensitivity study for the f parameter will be presented later for both the aerosol and NO_2 VCD determinations (Section 4.5.4).

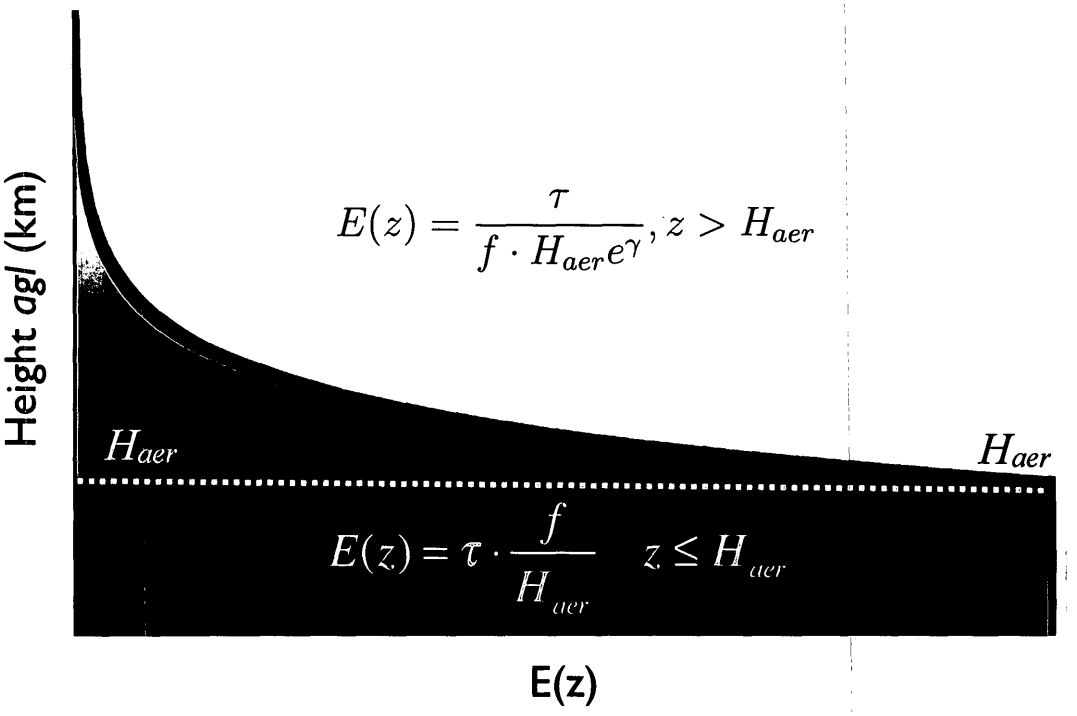

Figure 4.7: Modelled E(z) profiles in McArtim. The parameters f, τ, and H_{aer} are varied to obtain different profiles. For the BAQS-Met data set f was fixed to one (box profile, as outlined in white).

The RTM McArtim was run in order to calculate various O_4 AMFs at a wavelength of 360 nm, for 50,000 photon paths. A wavelength of 360 nm was chosen because it is in the DOAS fitting range (355-385 nm) for O_4, and 50,000 photon paths gave a good estimate of the most probable light paths present coupled with

reasonable computer computation times. From these multiple McArtim calculations a comprehensive set of O_4 DAMFs was catalogued (as a function of the input parameters mentioned earlier, see Table 4.2) and used to construct an O_4 DAMF look up table. For most days, the MAX-DOAS instrument was facing SW (β = 235°), except on July 8 when it alternated between SW and NE (β = 55°). The select pairings of SZA and RAZI values used to represent different periods of the day are shown in Figure 4.8. A MATLAB routine, designed by S. Beirle, was used to minimize the difference, measured by the residual sum of squares (RSS), between the O_4 DAMFs in the look up table (L_α), as a function of τ and H_{aer}, and the O_4 DAMFs (M_α) found via the measured DSCDs and their corresponding VCDs:

$$RSS(\tau, H_{aer}) = \sum_{\alpha=2°}^{30°} [M_\alpha - L_\alpha(\tau, H_{aer})]^2 \tag{4.13}$$

The results of this minimization yielded O_4 DAMF, τ, and H_{aer} values that may be used to describe the aerosol conditions for a given time period (one measurement series). Figure 4.9 shows a sample fit between measured O_4 DAMFs and those calculated via radiative transfer on June 20 from 9:54 to 10:05 EDT. The τ values determined in this way are henceforth labeled as τ_{RTM}. This procedure is repeated for each measurement series on a given day, under cloud-free conditions. In addition to the value of finding τ in itself, the determination of aerosol properties from the above procedure is a crucial intermediate step in determining the final NO_2 VCDs. Figure 4.10 provides a complete schematic for this whole procedure.

Table 4.2: Parameters used in McArtim and values selected for model runs.

Parameter	Unit	Number of Values	Selected Values
α	deg	6	90°, 30°, 10°, 6°, 4°, 2°
SZA	deg	7	80°, 70°, 60°, 50°, 40°, 30°, 18°
RAZI	deg	13	−167°, −159°, −149°, −141°, −131°, −117°, −53°, 1°, 19°, 30°, 41°, 49°, 58°
H_{aer}	km	9	0.1, 0.2, 0.3, 0.5, 0.7, 1.0, 1.5, 3.0, 5.0
H_{gas}	km	9	0.1, 0.2, 0.3, 0.5, 0.7, 1.0, 1.5, 3.0, 5.0
τ	-	10	0.05, 0.1, 0.2, 0.3, 0.5, 0.7, 1, 1.5, 2.0, 3.0
f	-	7	0.1, 0.2, 0.3, 0.4, 0.5, 0.7, 1.0

*Due to the systematic relationship between the diurnal variation of SZA and RAZI, calculations were only performed for appropriate pairs of SZA and RAZI (see Figure 4.8).

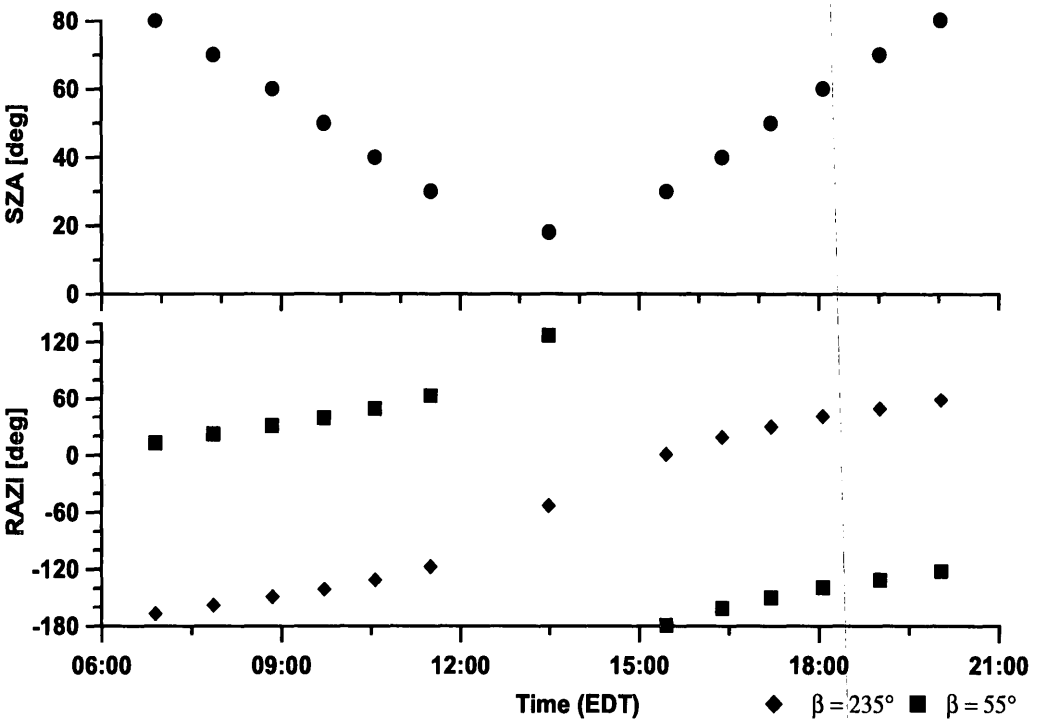

Figure 4.8: Systematic diurnal variation between SZA and RAZI at Ridgetown. The MAX-DOAS instrument was pointed both SW ($\beta = 235°$) and NE ($\beta = 55°$) on July 8, 2007 only.

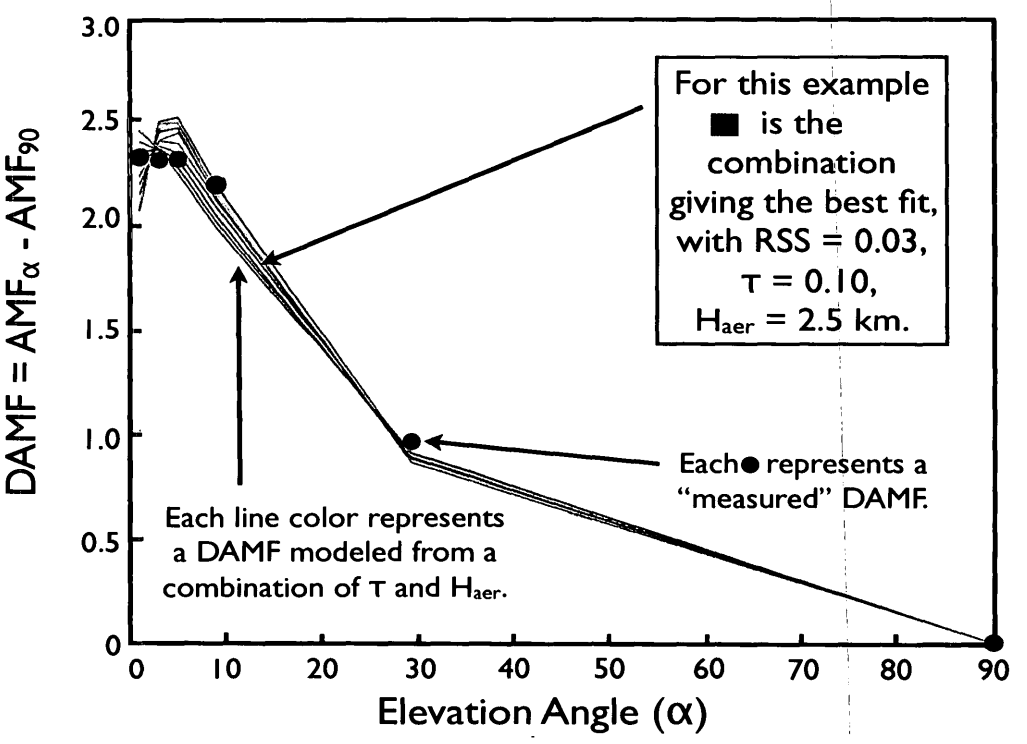

Figure 4.9: Sample fit between measured O_4 DAMFs and modelled O_4 DAMFs on June 20, 2007 from 9:54 to 10:05 EDT. The result of such fits yield τ and H_{aer}, while the RSS is used to determine the quality of the fits.

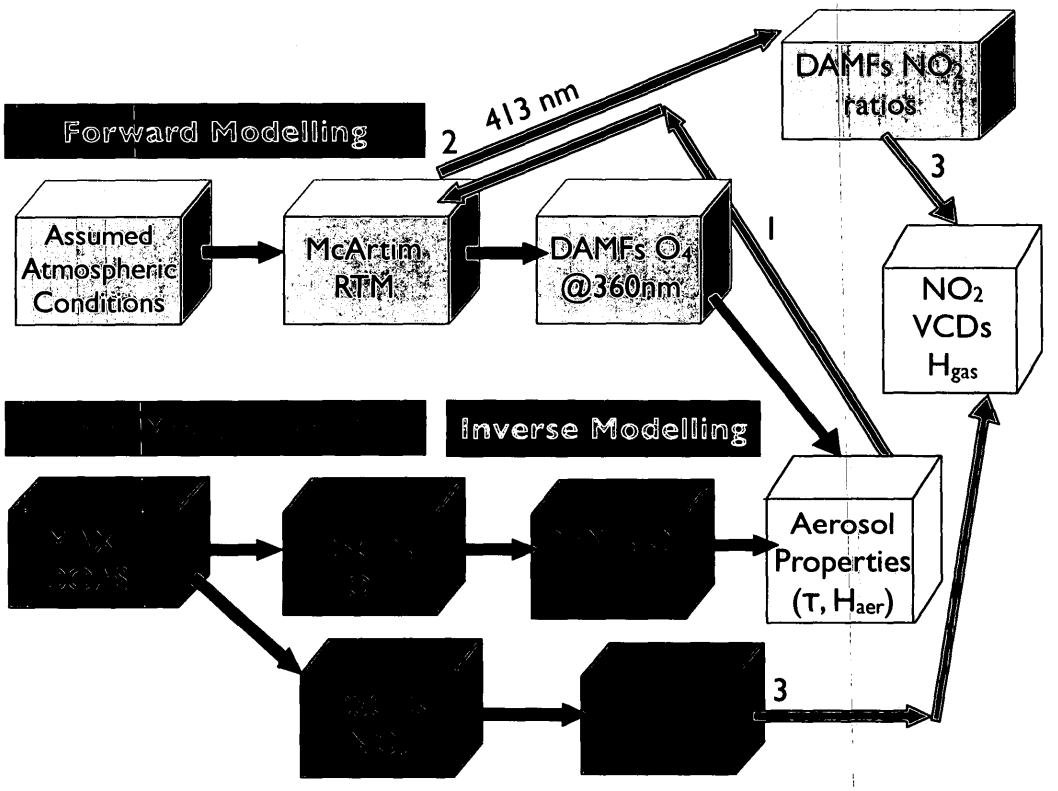

Figure 4.10: Flowchart of methodology for determination of NO_2 VCDs and aerosol properties from MAX-DOAS measurements, RTM and inverse modelling. Measurements in green boxes represent products obtained from direct MAX-DOAS measurements in the field, while parameters and products shown in the grey boxes represent modelled quantities and results only. The quantities in the yellow boxes are obtained from inverse modelling.

4.3.1.2 NO_2 Vertical Column Densities

In addition to the dependence on the aerosol profile, NO_2 DAMFs are also a function of the vertical concentration profile of NO_2. Under the assumption of a horizontally homogeneous trace gas distribution, the atmosphere may be divided vertically into several layers of height, h. Each "box" will then have its own DAMF that may then be defined as:

$$DAMF_{box_i} = \frac{dDSCD_i}{dVCD_i} \tag{4.14}$$

where $dDSCD_i$ is the partial differential slant column density, and $dVCD_i$ is the partial vertical column density for box_i. Within the layer the trace gas concentration is assumed to be constant. The $DAMF_{box}$ describes the DSCD's sensitivity to changes in the VCD for a given box within the total atmospheric column. Total DAMFs may then be calculated from the $DAMF_{box}$ values and the respective trace gas profile as the sum of $DAMF_{box}$ over the whole atmosphere weighted by the respective partial trace gas VCD:

$$DAMF_{total} = \frac{\sum_0^{TOA} DAMF_{box_i} \cdot VCD_i}{\sum_0^{TOA} VCD_i} \tag{4.15}$$

The $DAMF_{box_i}$ and VCD_i refer to the box DAMF and the partial VCD for layer i, respectively. The layer of trace gas concentration is assumed to be constant within the box. The sum is carried out for 95 i layers that start at ground level and finish at the top of the atmosphere (TOA). Layers 1-60 consists of individual boxes each

with a height of 0.2 km (ending at 12 km *agl*), layers 61-73 consists of individual boxes each with a height of 1 km (ending at 25 km *agl*), layers 74-83 consists of individual boxes each with a height of 2 km, layers 84-94 consists of individual boxes each with a height of 5 km, and layer 95 is a individual box with a starting height of 100 km *agl* and end height of 1000 km *agl*.

McArtim was run in order to calculate NO_2 $DAMF_{box}$ values at a wavelength of 413 nm (DOAS fitting range for NO_2 was 410-435 nm) using 50,000 photons for NO_2. These $DAMF_{box}$ values were catalogued and a new MATLAB routine, designed by S. Beirle, MPI-Mainz, was used to construct a $DAMF_{box}$ look up table. This routine subsequently selects the appropriate subset of $DAMF_{box}$ from the NO_2 look up table, based on the aerosol scenario previously determined (Equation 4.13). In order to minimize the effect of stratospheric NO_2, NO_2 $dSCD_{meas}$ ratios were prepared by taking individually measured SCD_α values ($\alpha \leq 30°$) and subtracting the SCD_{90} values of each measurement series from them to yield NO_2 dSCD values (see Chapter 2, Section 2.2.1). These NO_2 dSCD values were divided by the $dSCD_{10}$ values similarly prepared, for each series. These $dSCD_{meas}$ ratios (M_α) were then compared to their corresponding NO_2 $DAMF_{total}$ ratios (L_α). The quality of this fit was again expressed by the RSS:

$$RSS(H_{gas}) = \sum_{\alpha=2°}^{30°} [M_\alpha - L_\alpha(H_{gas})]^2 \tag{4.16}$$

This "best fit" between the $dSCD_{meas}$ ratios and the possible $DAMF_{total}$ ratios provided the NO_2 layer height, H_{gas} (where 100% of the NO_2 present is below H_{gas}), and the NO_2 DAMF for a given measurement series, as well as the NO_2 VCD_α values via the following equation:

$$VCD_\alpha = \frac{DSCD_{meas}}{DAMF_{total}} = \frac{SCD_{meas}(\alpha) - SCD_{meas}(90°)}{AMF_{total}(H_{gas}, \alpha) - AMF_{total}(H_{gas}, 90°)} \tag{4.17}$$

Figure 4.11 provides a sample fit for June 20 using a measurement sequence that was taken from 13:51 to 14:05 EDT. The average NO_2 VCD (henceforth called NO_2 VCD_{RTM}) values were calculated for each series using all elevation angle measurements ($\alpha < 90°$):

$$VCD_{RTM} = VCD_{avg} = \overline{VCD}_{(2°,4°,6°,10°,30°)} \tag{4.18}$$

The average NO_2 number density (n_{gas}) can then be found as:

$$n_{gas} = \frac{VCD_{RTM}}{H_{gas}} \tag{4.19}$$

and the average mixing ratio (C_{gas}) as:

$$C_{gas} = \frac{n_{gas}}{n_{air}} \tag{4.20}$$

where the number density of air, $n_{air} = 2.46 \times 10^{19}$ molec cm^{-3}, was calculated using Equation 4.3 assuming a constant temperature of 25°C and constant pressure of 1 atm.

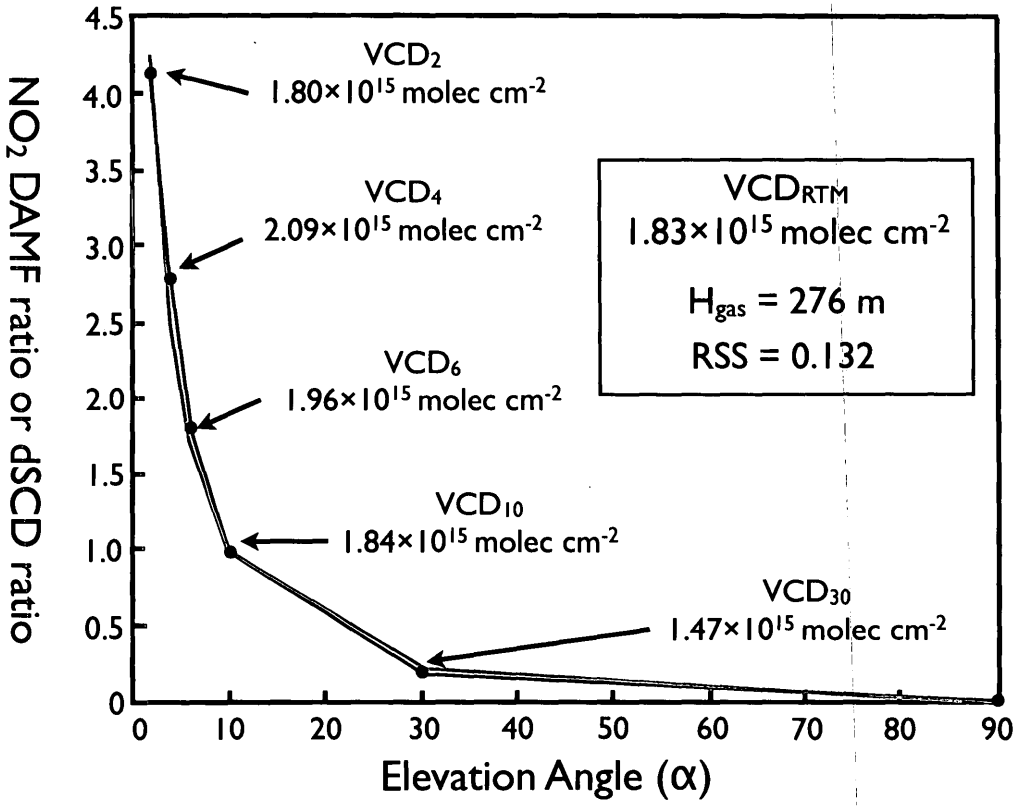

Figure 4.11: Sample fit between measured NO_2 DAMF ratios and NO_2 dSCD ratios on June 20, 2007 from 13:51 to 14:05 EDT. The result of such fits yield individual VCD_α values which are averaged to obtain VCD_{RTM}. H_{gas} is also found, while the RSS is used to determine the quality of the fits.

4.4 Other Considerations used for Data Interpretation

4.4.1 The Geometrical Approximation

Using a simple geometrical consideration, first proposed by A. Richter, Universität Bremen, Germany (personal communication), the AMF for a gas located in the troposphere may be approximated (Chapter 1, Figure 1.6A), assuming that the trace gas layer is located below the scattering altitude:

$$AMF_{GEO} = \frac{1}{sin\alpha} \tag{4.21}$$

Conveniently a dSCD measured at 30° then equals the geometric VCD:

$$VCD_{GEO} = \frac{dSCD}{DAMF_{GEO}} = \frac{dSCD_{30}}{\frac{1}{sin(30°)} - \frac{1}{sin(90°)}} = \frac{dSCD_{30}}{2-1} = dSCD_{30} \tag{4.22}$$

This geometrical approximation assumes that the stratospheric absorption is similar in the horizontal-viewing and zenith directions (essentially cancelling each other out), and the geometric light path enhancement is a good approximation of the actual light path enhancement exhibited. If there is a large amount of aerosol present and hence a high degree of Mie scattering present, this approximation becomes inaccurate. As such, in most cases a RTM must be employed to obtain an accurate AMF (Hendrick et al., 2006; Wagner et al., 2007). In general, this approximation would only hold under clear sky and low aerosol conditions. For this study, geometrically approximated VCDs were determined using NO_2 dSCDs at both 30° and 10°. If a pair of geometric VCDs at these elevation angles in the same measurement

sequence agreed to within 15%, then the VCD_{GEO}, as defined in Equation 4.22, was retained. This criterion ensures that the geometrical approximation is valid, and eliminates measurement points greatly affected by horizontal inhomogeneites, aerosols or clouds (Brinksma et al., 2008; Celarier et al., 2008).

4.4.2 Cloud Discrimination Scheme

Clouds have strong, systematic effects on MAX-DOAS observations and thus the radiative transfer modelling required for cloudy days is substantially more complex than for clear days (Wagner et al., 2011). Different types of clouds will have different effects on the light path retrieved by the MAX-DOAS instrument and cloud coverage may vary thoughout any given day. It is therefore very important to have a quick and simple means of distinguishing between clear and cloudy conditions. The scheme used in this dissertation makes use of the MAX-DOAS observations themselves to classify time periods as either cloudy or clear. If a particular measurement sequence was deemed to be in a cloudy period that sequence was eliminated from further processing (i.e. only measured data from clear periods was used for the RTM component that ultimately helped to determine the final τ_{RTM} and VCD_{RTM} values).

Three different MAX-DOAS retrieved quantities were studied for this scheme:

the O_4 DSCDs, the observed radiance at 360 nm, and the color ratio. The color ratio was defined as the ratio between low and high wavelengths (λ_{avg} = 365 nm / 467 nm). Figure 4.12 provides a representative example of these quantities on June 20. Most of the day was clear. Only six complete measurement sequences were discarded, due to changes in the O_4 DSCD, radiance or color ratio, while the remaining O_4 and NO_2 DSCD sequences were all used for radiative transfer modelling. A substantial increase or decrease in the O_4 DSCDs may represent a cloudy period, while a decrease in the radiance or color ratio could signal the presence of a cloud, as increased Mie scattering (at higher wavelengths) would occur.

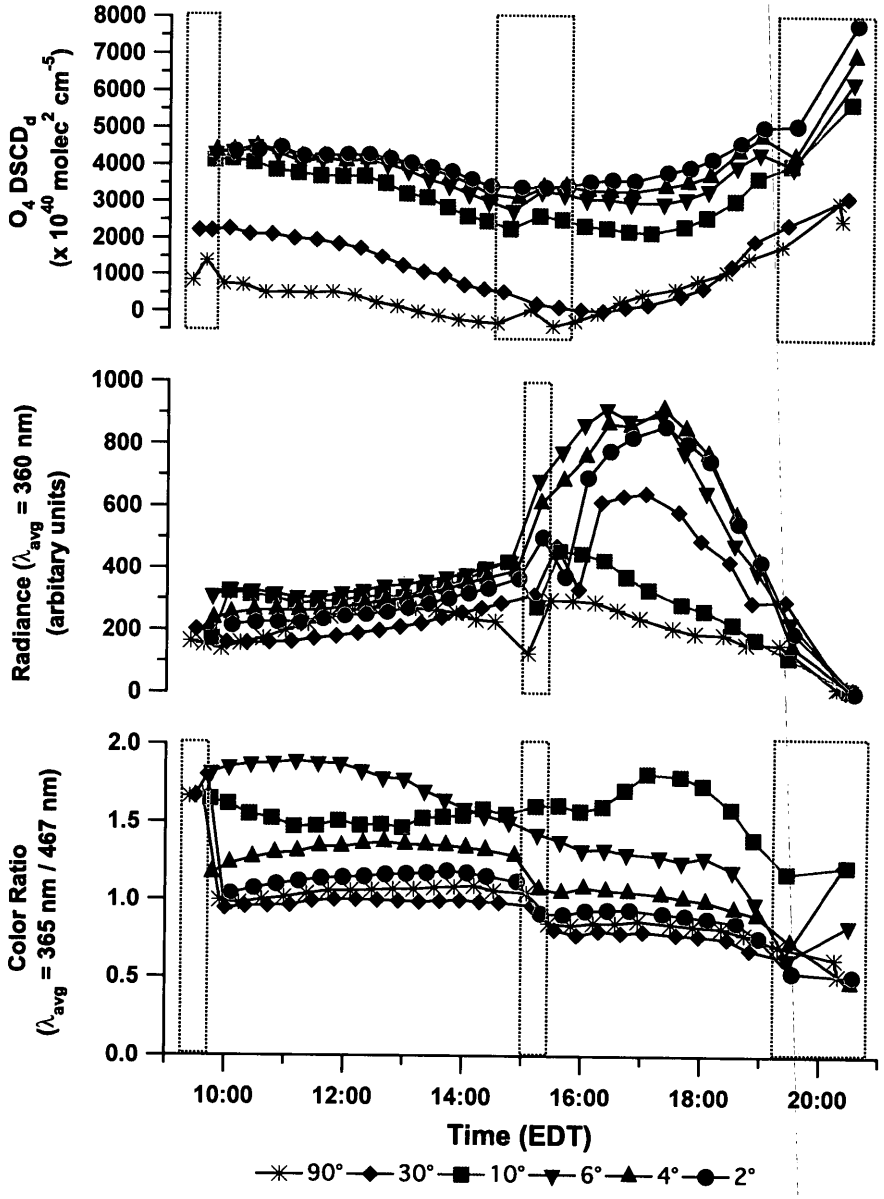

Figure 4.12: Cloud discrimination for sequences on June 20, 2007. O_4 $DSCD_d$ values, radiance at 360 nm, and the color ratio (365 nm/467 nm) are shown for the entire day. Boxed areas represent measurement series that were discarded due to potential cloud cover.

4.5 Results and Discussion

4.5.1 Comparison of Ground Measurements of NO_2

Figure 4.13 provides a comparison of NO_2 mixing ratios calculated from active DOAS and MAX-DOAS-RTM inversions at Ridgetown with those from the chemiluminescence instrument described earlier (Thermo Model TE42C, Section 4.2.8). The time stamp for each active DOAS value was the mid-point time of the measurement, with an average measurement time lasting approximately 10 minutes. The time stamp for each MAX-DOAS-RTM value was the mid-point time of each measurement series in the inversion (~30 mins). Two minute average values are displayed for the chemiluminescence measurements. Qualitatively the general temporal shape of the three measures appear to agree quite well, providing local maxima and minima at approximately the same times. The active DOAS and chemiluminescence measures often show NO_2 peaking during the nighttime. For example, on the nights of June 29/30, July 5/6, and July 6/7, NO_2 values upwards of 15 ppb are seen. This is not surprising since at night NO_2 photolysis is absent, leading to higher levels of NO_2 and hence a higher NO_2/NO (Leighton) ratio, in addition to NO_x emissions being confined to a shallow nighttime inversion layer.

Generally, the NO_2 measured by chemiluminescence appears to be higher than the active DOAS and MAX-DOAS-RTM values (e.g. June 26, 27, 28, and July 6, 7). The lower MAX-DOAS-RTM values may be due to unrealistic H_{gas} values

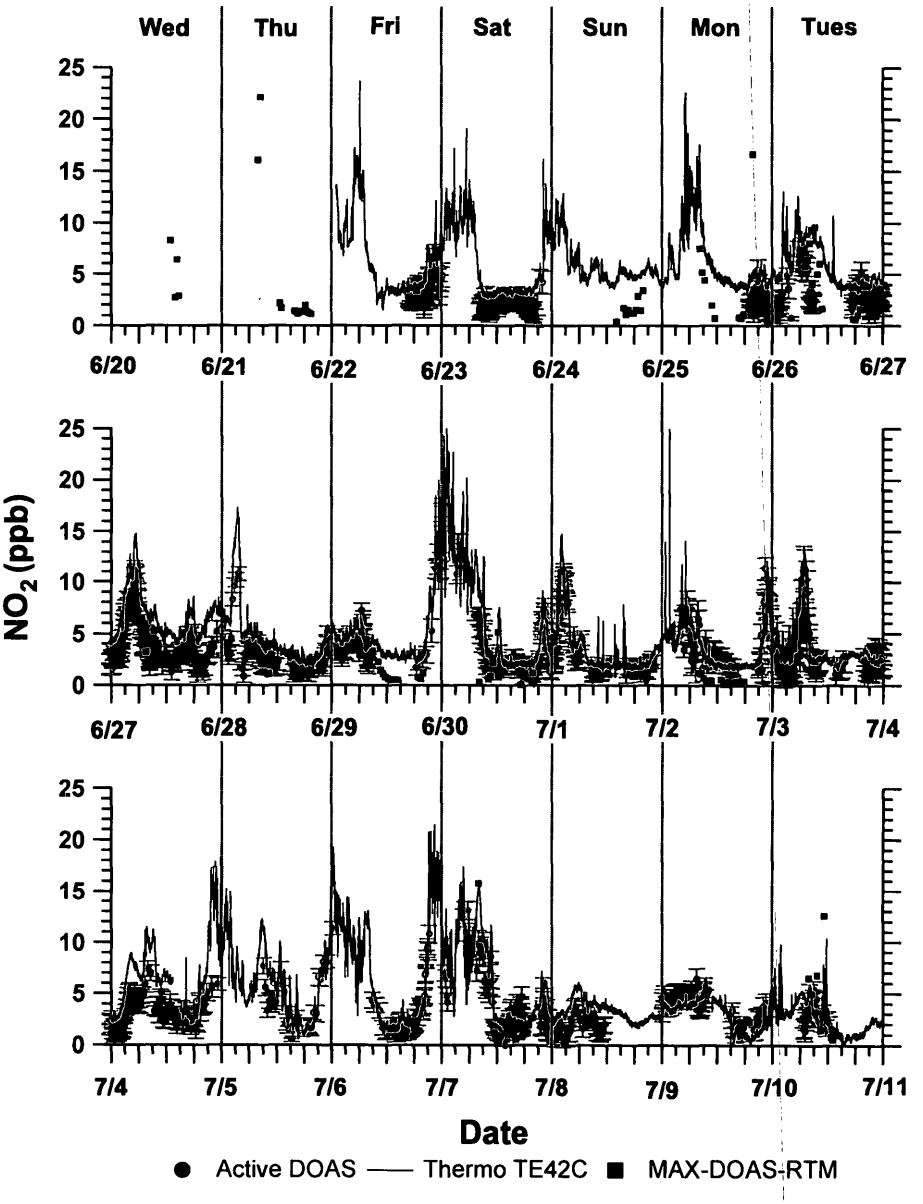

Figure 4.13: Overview of NO_2 ground measurements at Ridgetown. Red points represent active DOAS mixing ratios, blue points represent mixing ratios calculated from the MAX-DOAS-RTM inversion and the black line represents chemiluminescence measurements.

(which will be examined in detail in Section 4.5.6). However, it has already been determined that chemiluminescence instruments often over estimate NO_2 mixing ratios, since they do not provide a true measure of NO_2, but rather a surrogate NO_2 value. These instruments measure NO_2 by using molybdenum converters to catalytically convert NO_2 to NO. Unfortunately, other oxidized nitrogen compounds (NO_z = HNO_3 + PAN + HONO + HO_2NO_2 + NO_3 + N_2O_5 + $ClNO_2$ + other organic nitrates) may also be converted to NO, which leads to NO_2 being overestimated in cases where a lot of NO_z is present. In city sites where NO_x is dominant, this overestimation is minimal. In remote or rural sites, or in the presence of aged air masses, where NO_x is a lot smaller compared to NO_y, this error may become quite significant. Steinbacher et al. (2007) estimate that, at times, only 70-80% of the surrogate NO_2 may be attributed to true NO_2 during long term measurements at two rural sites in Switzerland and determine that this difference is greatest in the spring/summer due to enhanced seasonal photochemistry. Since two of the above criteria (rural site, summer season) are in place at Ridgetown, the possibility of the chemiluminescence instrument overestimating true NO_2 should not be ignored. Yet, the exact percentage of true NO_2 measured at different times is difficult to predict without the measurements of other NO_z species as well.

4.5.2 Interpretation of NO_2 DSCDs

NO_2 $DSCD_k$ values were determined from the raw spectra according to the procedure described in Section 4.2.2. Figure 4.14 provides an overview of all NO_2 DSCDs obtained during the entire field study. Periods where DSCDs are missing are due to either rain or instrumental difficulties. On most days a diurnal variation is present whereby higher NO_2 DSCDs are seen in the morning and evening, when the photolysis of NO_2 is low. For most measurement series the DSCDs are larger at low elevation angles (ie. $DSCD_2 > DSCD_4 > DSCD_6 > DSCD_{10} > DSCD_{30} > DSCD_{90}$) since the geometric path through the troposphere is larger at low elevation angles. Figure 4.15 plots the NO_2 DSCDs vs. EA (α = 2°, 4°, 6°, 10° and 30°) in a box and whisker format whereby the top of each box represents the 75th percentile, the bottom of each box is the 25th percentile and the error bars represent the 95th and 5th percentile for each EA. This figure clearly shows that the 95th, 75th, 50th, 25th and 5th percentile NO_2 DSCD levels all become progressively smaller when α is increased from 2° to 30°, illustrating that, as theory dictates, the average tropospheric light path lengths increase with decreasing EA. The values of the DSCDs range from ~0-1.4×10^{17} molec cm^{-2} (a similar range to what was found at Saturna), depending on the EA, which is indictative of a rural area without substantial NO_x sources close by. However, the average NO_2 $DSCD_2$ was 2.4×10^{16} molec cm^{-2}

considerably lower than the average NO_2 ΔSCD_2 measured at Saturna (8.5×10^{16} molec cm^{-2})

Qualitatively it can be seen that certain days (June 23, 24, and July 1) have low NO_2 levels, while other days (June 21, 30, July 7-10) appear to be impacted by pollution sources. The changes in NO_2 DSCDs with elevation angle give qualitative information on the vertical distribution of NO_2. This can be better visualized in the contour plots shown in Figure 4.16, where certain days appear to stand out. For example, on June 30, a short duration event between 12:00 and 13:00 EDT is apparent, with large DSCDs for all elevation angles, while clean conditions prevail in the afternoon. July 1 is noticeably clean and from July 8-10 high NO_2 DSCDs are seen for the majority of the day. Care should be taken when interpreting this figure quantitatively since aerosol levels change on a daily basis and could significantly affect the DSCD values. This figure should not be taken as an NO_2 profile because each elevation angle does not represent a constant height above ground for different time periods. Nonetheless, it is a simple approach that allows better visualization of the data compared to Figure 4.14. For a more quantitative analysis, the NO_2 VCDs determined using the DSCDs and the full radiative transfer modelling approach are discussed in Section 4.5.9, along with case studies for June 30, July 2 and July 9 in Section 4.5.9.1

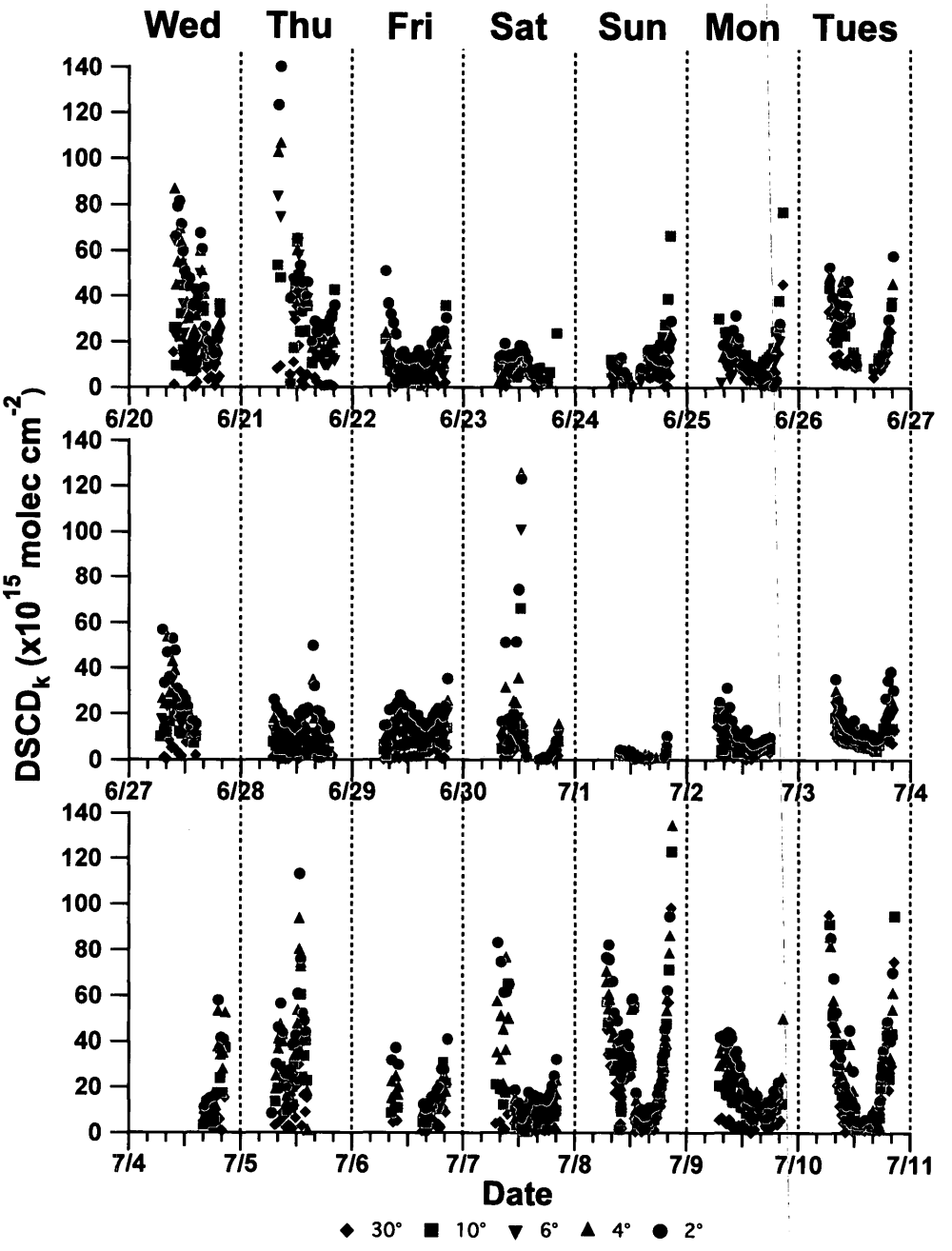

Figure 4.14: Overview of NO_2 DSCDs at Ridgetown during BAQS-Met. All $DSCD_k$ values shown here are retrieved using one FRS from June 20, 2007.

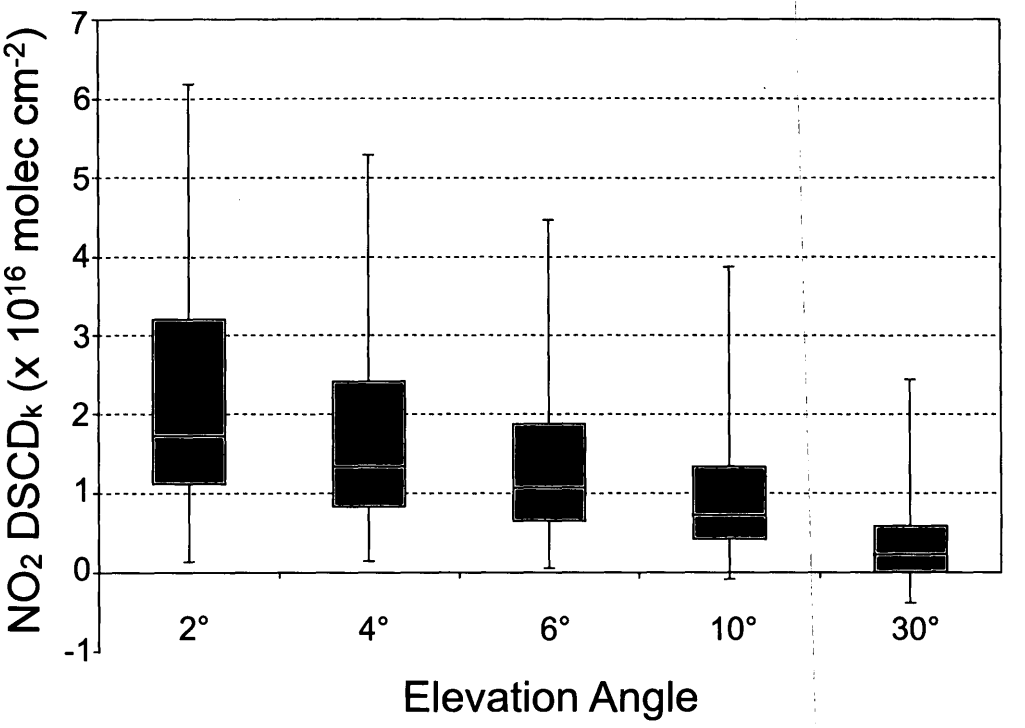

Figure 4.15: Box and whisker plot of NO_2 $DSCD_k$ vs. Elevation Angle at Ridgetown, Ontario. The solid horizontal line within each box represents the median, the top and bottom of the boxes represent the 75th and 25th percentiles, and the error bars correspond to the 95th and 5th percentile.

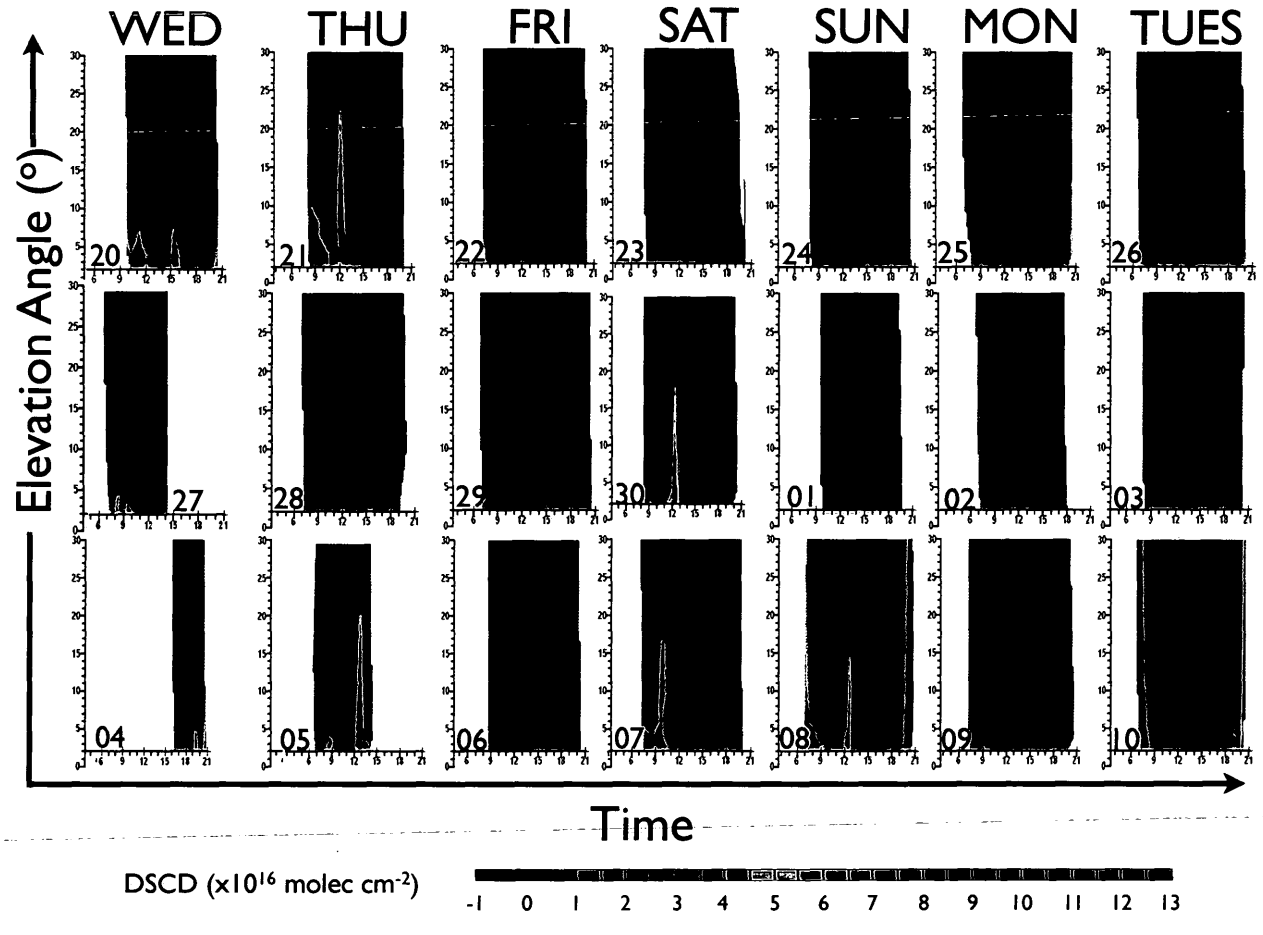

Figure 4.16: NO_2 DSCDs vs. Time (EDT) and Elevation Angle for Ridgetown: June 20-July 10, 2007.

4.5.2.1 Effect of RAZI on DSCDs and Radiative Transfer

In order to examine the ability of MAX-DOAS to determine spatial inhomogeneities of NO_2, for one complete day during BAQS-Met (July 8) measurements were taken using two different elevation angle sequences, headings, and SZA-RAZI pairings (Figure 4.8). For 50% of the time the MAX-DOAS telescope was pointed to the SW (β = 235°), while for the remaining time the instrument was pointed NE (β = 55°). One complete measurement cycle consisted of a 2°, 4°, 6°, 10° and 30° measurement sequence facing SW followed by a 90° measurement, and a 30°, 10°, 6°, 4° and 2° measurement sequence facing NE. This cycle was repeated 17 times throughout the course of the day.

Figure 4.17 displays the NO_2 DSCDs for July 8 for both headings for the selected EAs of 30°, 10° and 2°. There is no significant difference between NO_2 DSCDs obtained from the SW and NE direction, apart from two cases (~10:00 EDT for all EAs and 13:00 EDT for the 10° EAs). Unfortunately, any difference in DSCD between measurements at the same elevation angle but pointed in different headings could not only be explained by spatial inhomogeneity of NO_2 at Ridgetown, but could also be attributed to the temporal differences in these measurements and more importantly to changes in the effective path length seen by the MAX-DOAS instrument at the two different headings. Therefore, direct interpretation using

the NO_2 DSCDs to examine spatial differences is not believed to be an accurate method.

As described in more detail in Section 4.3.1, differences in aerosol level greatly affect the path length seen by the MAX-DOAS instrument. When examining the light paths in a pure Rayleigh atmosphere for the telescope pointed both SW and NE at Ridgetown in the afternoon, the effective path length for each heading would not differ significantly (Wagner et al., 2004). This is simply because Rayleigh scattering does not prefer one direction over another (Figure 4.18A). However, if aerosols are present (as is the case at Ridgetown), forward scattering becomes more pronounced, so that in the SW direction the telescope receives significantly more single scattered photons than the NE direction (Figure 4.18B). This in turn leads to lower O_4 DSCDs in the SW direction than the NE direction because the SW heading has a higher fraction of single scattered photons than multiple scattered photons (that have much longer paths through the atmosphere). To confirm this the O_4 DSCDs on July 8 were examined as well. Figure 4.19 shows the O_4 DSCDs at elevation angles of 30°, 10° and 2° in the SW and NE direction. Aside from a significant peak between (~12:00-14:00 EDT), which may be due to a cloud presence, the O_4 absorptions seem to follow this predicted trend. In particular for the higher angle measures, SW absorptions are significantly smaller than the NE absorptions in the afternoon (when the sun is facing W), while the converse is seen in the morn-

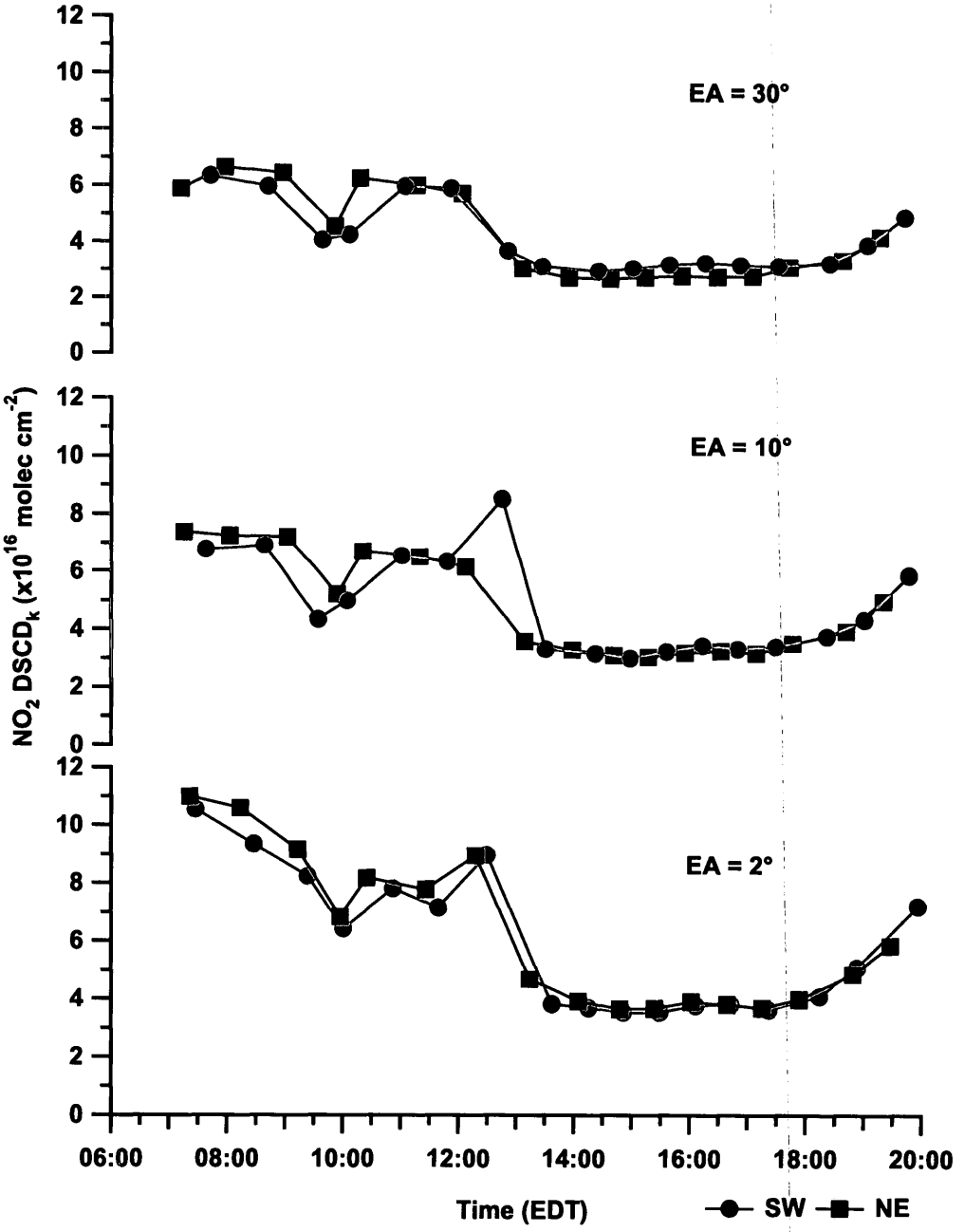

Figure 4.17: NO_2 $DSCD_k$ values for the NE and SW Headings on July 8, 2007 for 30°, 10° and 2° elevation angles.

ing. The differences between the NE and SW O_4 absorptions are the smallest for the 2° case. This is believed to be because at lower elevation angles there is an increased influence due to multiple scattering (from more aerosols in the effective path) and consequently less relative contribution from single scattering making the O_4 DSCDs determined for the NE and SW headings quite similar.

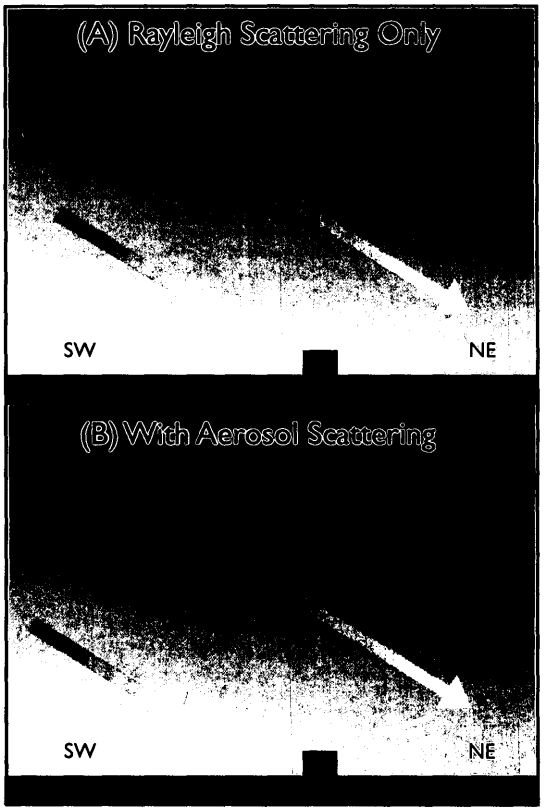

Figure 4.18: Single light scattering in the troposphere. Panel A shows scattering under clear conditions (Rayleigh only), while panel B shows light scattering with aerosols present.

To more quantitatively determine any spatial heterogeneity in NO_2 a full radiative transfer approach (as described in Section 4.3) was performed separately for all SW and NE measurements. Figure 4.20 shows the VCD_{RTM} values found along with the NO_2 DSCDs. NO_2 VCD_{RTM} values are enhanced for both headings in the afternoon, with no noticeable change in the DSCDs or ground level NO_2 found via active DOAS or chemiluminescence (not shown). Despite having lower O_4 DSCDs absorptions in the afternoon at the SW heading, the VCD_{RTM} values are, at times, higher in the SW versus the NE heading. Figure 4.21 shows a correlation plot for the SW-NO_2 VCD_{RTM} vs. the NE-NO_2 VCD_{RTM} (colour-coded for time of day) for each measurement series. From the 11 compared points, 7 fall along the the 1:1 slope line within error, while the remaining 4 points deviate from this line. For these points, three SW-VCDs are higher and one NE-VCD is higher in the afternoon period. These examples (aside from the higher NE-VCD in the afternoon) provide possible evidence that the differences in NO_2 VCDs are not primarily due to differences in the light path seen by the MAX-DOAS instrument, but rather due to inhomogeneities in the NO_2 as a function of heading. It should be noted however that these differences are relatively small and temporal changes in NO_2 were not considered. Further investigations should be done to verify this approach in cases where larger spatial inhomogeneities in NO_2 are visually apparent and thus highly probable.

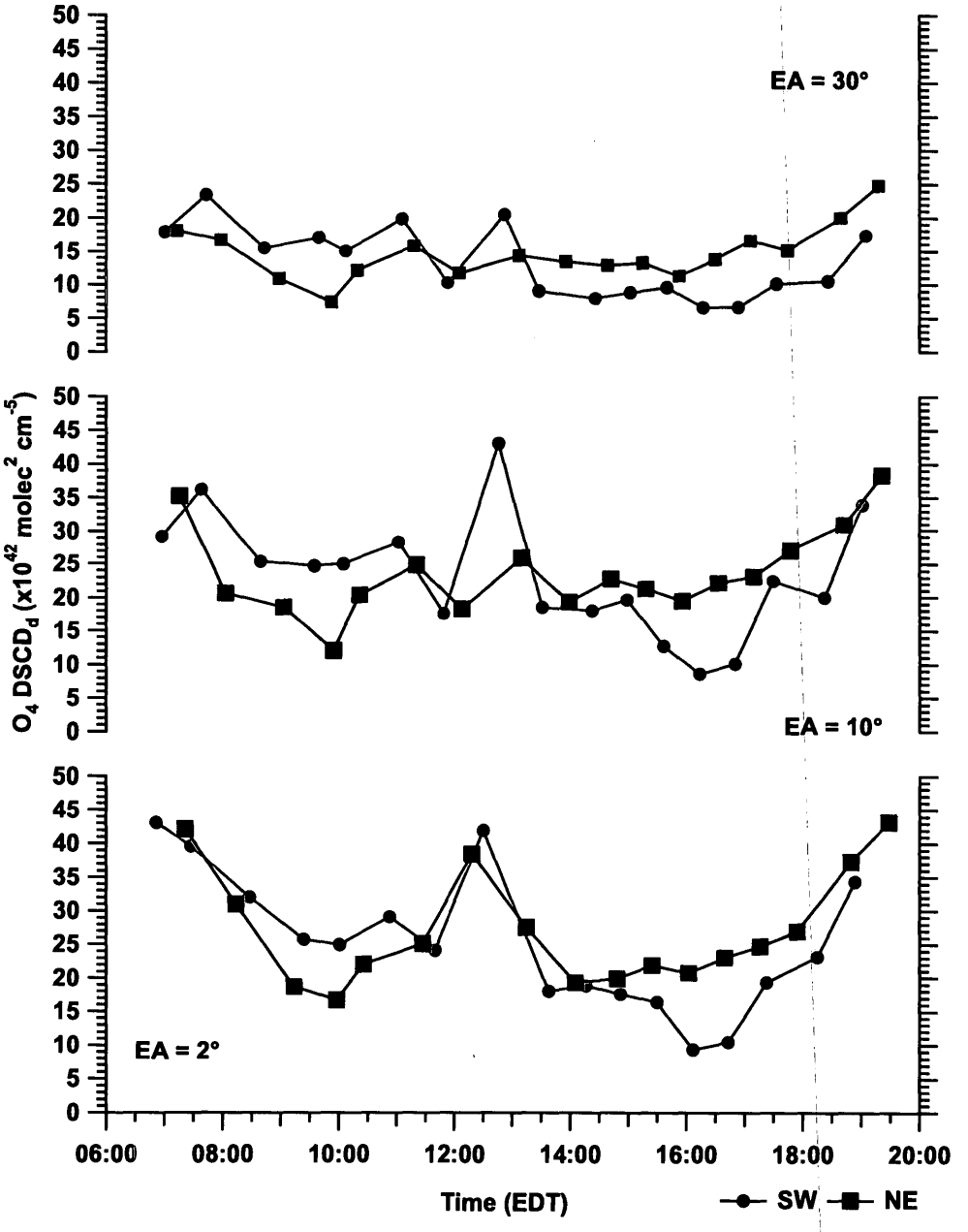

Figure 4.19: O_4 $DSCD_d$ values for the NE and SW Headings on July 8, 2007 for 30°, 10° and 2° EAs.

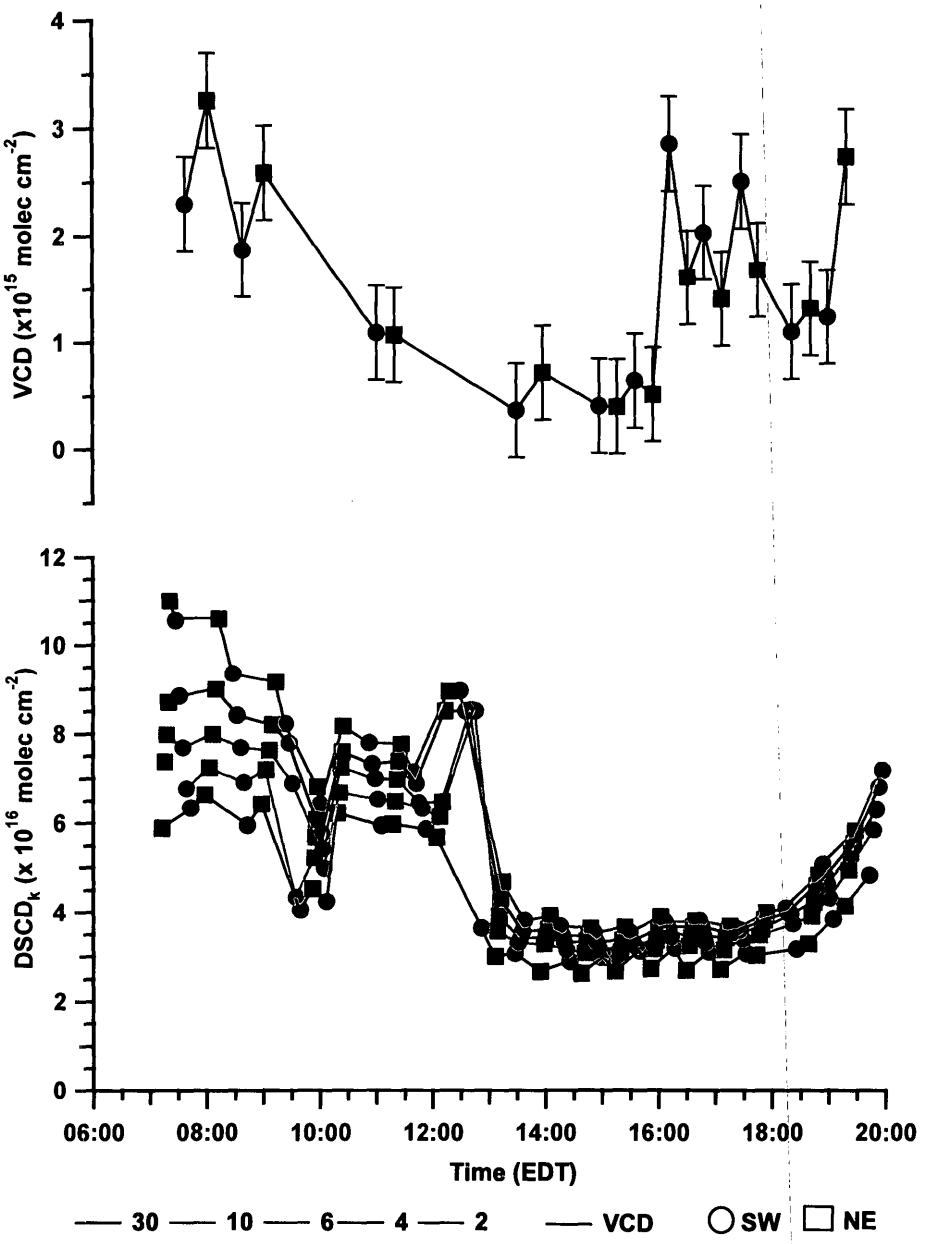

Figure 4.20: NO_2 VCDs and $DSCD_k$ values for SW and NE Headings on July 8, 07. All VCDs were determined using a full radiative transfer approach that considered the different RAZI-SZA combinations for each measurement.

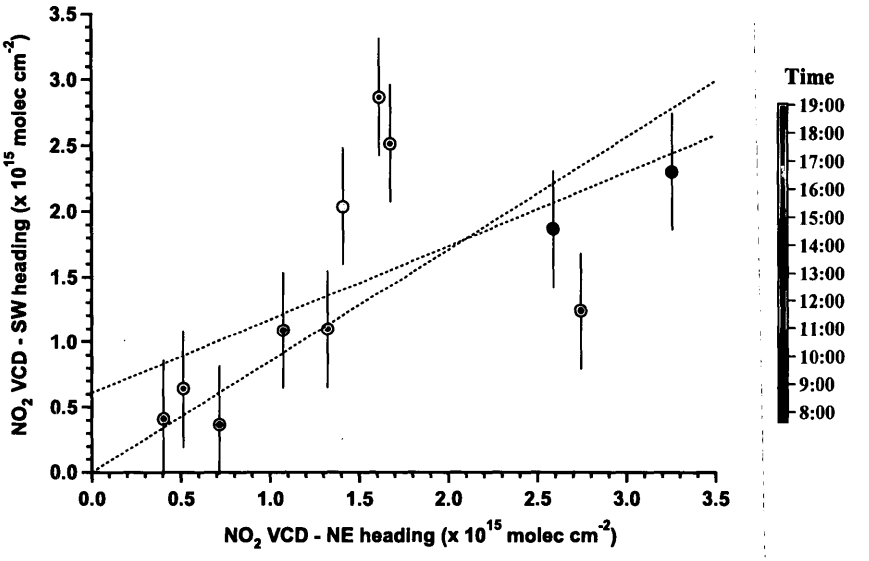

Figure 4.21: Correlation plot of NO_2 VCDs determined in NE and SW directions on July 8, 2007. The zero-forced slope is in black, while the red represents the non-forced slope.

4.5.3 Aerosol Optical Depth and Aerosol Extinction Coefficient

Figure 4.22 displays the O_4 $DSCD_d$ values at Ridgetown for the entire field campaign, under cloud-free conditions. The O_4 DSCDs typically show increasing values with decreasing elevation angles, indicative of a tropospheric absorber, such as on June 20, 22, 23, 29 and July 2 and 7. However, in several cases (parts of June 25, 26, 27, and July 4, 5, 9, and 10) there appears to be little dependence of the DSCDs on elevation angle. This phenomenon occurs when high levels of aerosol and/or clouds are present and the light path from the last scattering event to the

detector becomes effectively equal, regardless of the elevation angle of the observation. As only cloud-free conditions are presented here, the effect is largely due to the presence of aerosols. As such, when qualitatively comparing aerosol levels during the campaign, days such as June 20 appear to contain low aerosol extinction, while days such as July 9 contain elevated aerosol extinction.

In order to assess conditions on a more quantitative level, the aerosol optical depth (τ_{RTM}) for each cloud-free measurement series was determined at 360 nm as described in Section 4.3.1.1 (Figure 4.23). The τ_{RTM} varied from 0.05 to 2.93, with a mean and median value of 0.41 and 0.46 respectively. The average relative error of each τ_{RTM} value was estimated at 26% (Wagner et al., 2011). The τ_{RTM} values were compared to those τ values found from satellite measurements (τ_{MODIS}: λ = 550 nm, τ_{OMI}: λ = 388 nm), and AERONET ground-based measurements at Egbert and Kellogg (τ_{EGB}, τ_{KEL}, λ_{avg} = 360 nm for each location). Satellite measurements were only optimally available on a daily basis, while the comparison of τ_{RTM} with the τ values derived from the two satellites was somewhat limited due to the different wavelengths used (particularly for τ_{MODIS}) and the fact that the satellites only provide one or two comparison points daily. Although the measurements were made at similar λ for the AERONET locations, they are relatively far from Ridgetown (Egbert ~320 km NE, Kellogg ~330 km W), yet Ridgetown is approximately centralized between the two locations. The above factors limit the

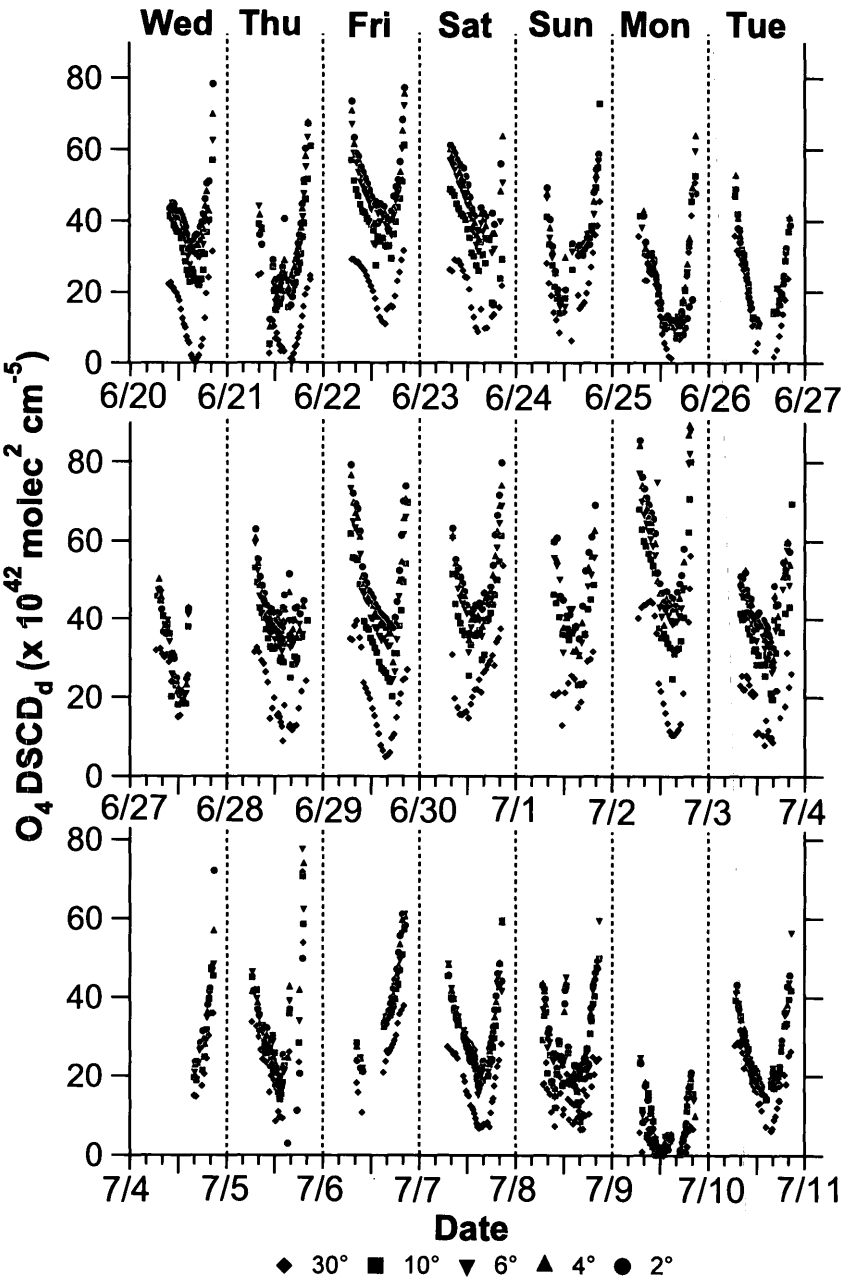

Figure 4.22: O_4 DSCD$_d$ values for cloud-free conditions during the BAQS-Met campaign at the Ridgetown supersite. Major ticks represent midnight and noon EDT, while minor ticks indicate every four hour increment.

ability to make direct comparisons of τ_{RTM} at Ridgetown, yet the values of τ_{RTM} do lie within the range of the other measurements, as might be expected during times when the high aerosol loading is associated with regional pollution events that affect eastern North America over large spatial distances. Such regionally polluted conditions were observed from June 24-27 and July 8-10. It should also be noted here that there was significantly more variability in the τ_{RTM} than the other measures of τ. There is no explanation for this phenomena at this time.

Spatially, it would be better to compare the τ_{RTM} values with aerosol levels measured directly at Ridgetown. Although another measure of τ is not available at the site, $PM_{2.5}$ mass was measured. When the $PM_{2.5}$ was compared to the corresponding τ_{RTM} values, a low level of correlation was found ($R^2 = 0.068$). This is not surprising since $PM_{2.5}$ is a ground point-source measurement of particulate mass, while τ_{RTM} represents an integrated column quantity of aerosol extinction. A more appropriate comparison of the aerosol properties may be done by examining the aerosol extinction coefficient, E. In this study $E = \tau_{\mathrm{RTM}}/H_{\mathrm{aer}}$, as described in detail in Section 4.3.1.1.

Figure 4.24A shows the time series comparing the aerosol extinction coefficient calculated via Equation 4.10 and the $PM_{2.5}$ measured at Ridgetown. A correlation plot for these two related properties is shown in Figure 4.24B using data from the entire study. Both panels show that there is a high degree of correlation between

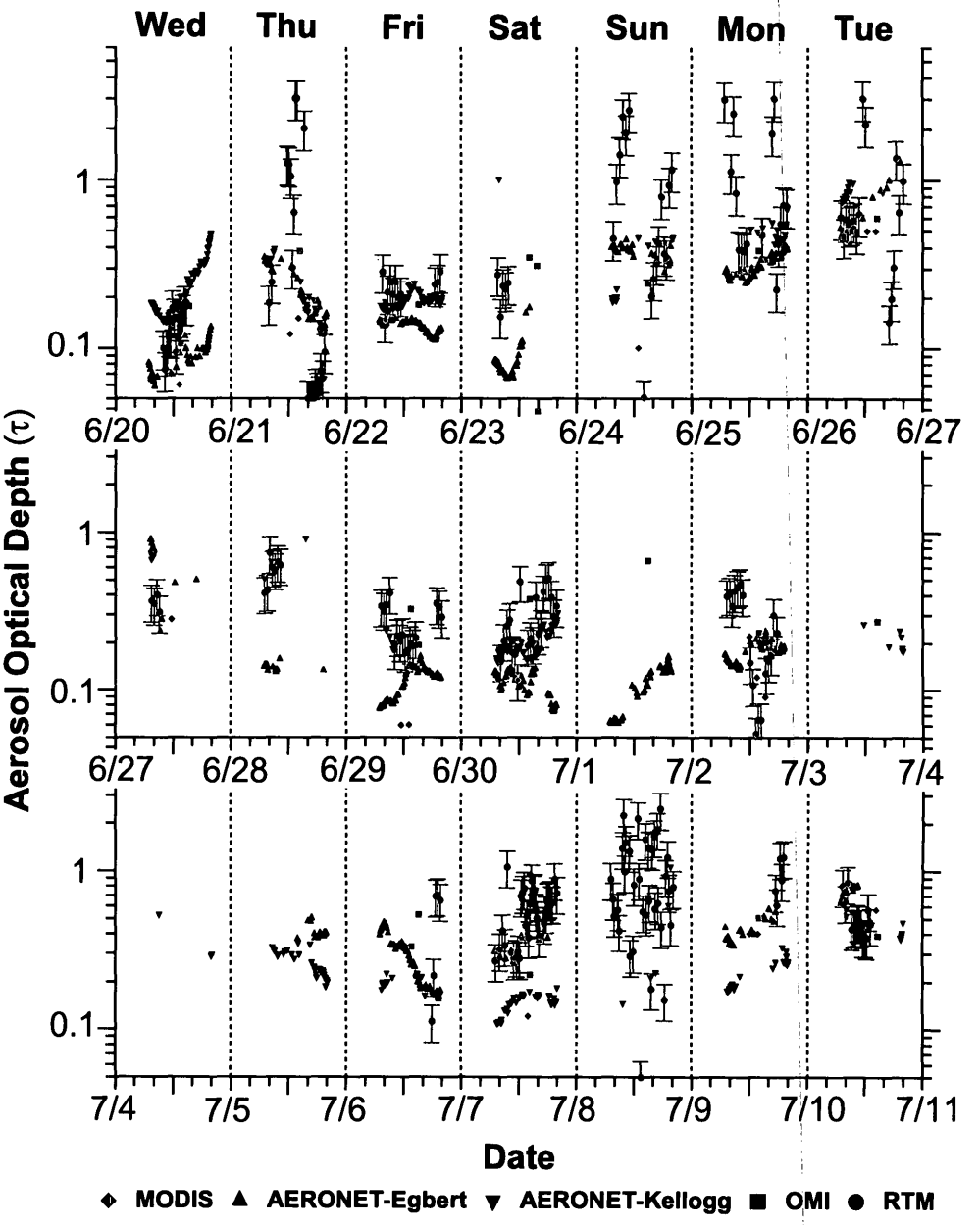

Figure 4.23: Aerosol optical depth for the BAQS-Met campaign. For AERONET locations $\lambda_{avg} = 360$ nm, for satellite measurements $\lambda = 388$ nm (OMI), $\lambda = 550$ nm (MODIS) and for the MAX-DOAS-RTM values $\lambda = 360$ nm. Major ticks represent midnight and noon EDT, while minor ticks indicate every four hours.

aerosol extinction, determined from the MAX-DOAS measurements plus radiative transfer and $PM_{2.5}$ mass ($R^2 = 0.75$, similar to what was found by Zieger et al., 2011). This improved correlation shows that the MAX-DOAS-RTM aerosol inversions are sensitive to the total concentration of aerosol at Ridgetown. In order to determine the sensitivity of the retrieval to aerosol optical depth, ideally a sun photometer would be co-located with the MAX-DOAS instrument.

Recent studies have compared local PM_{10} and $PM_{2.5}$ measurements to τ values determined from MODIS (Chu et al., 2003; Engel-Cox et al., 2004, 2006; Gupta and Christopher, 2008; Kacenelenbogen et al., 2006; Pelletier et al., 2007; Schaap et al., 2009; Wang and Christopher, 2003). The extent of correlation they found between τ_{550} (MODIS) and $PM_{2.5}$ varied, with R^2 values ranging from 0.27 to 0.60. This range is not entirely surprising as variations in local meteorology, differing aerosol composition, and the distribution of the aerosol layer(s) may all play roles in this relationship. In particular, if aerosols are concentrated in the boundary layer, and the boundary layer is highly variable, a poor relationship between τ and $PM_{2.5}$ would be expected. If the boundary layer height is known, this correlation may be greatly improved through calculation of E. For example, Koelemeijer et al. (2006) found that there was a better correlation ($R^2 = 0.59$) between $PM_{2.5}$ measurements and the modified aerosol extinction from MODIS, E^*:

$$E^* = \frac{\tau}{BLH \cdot f(RH)} \tag{4.23}$$

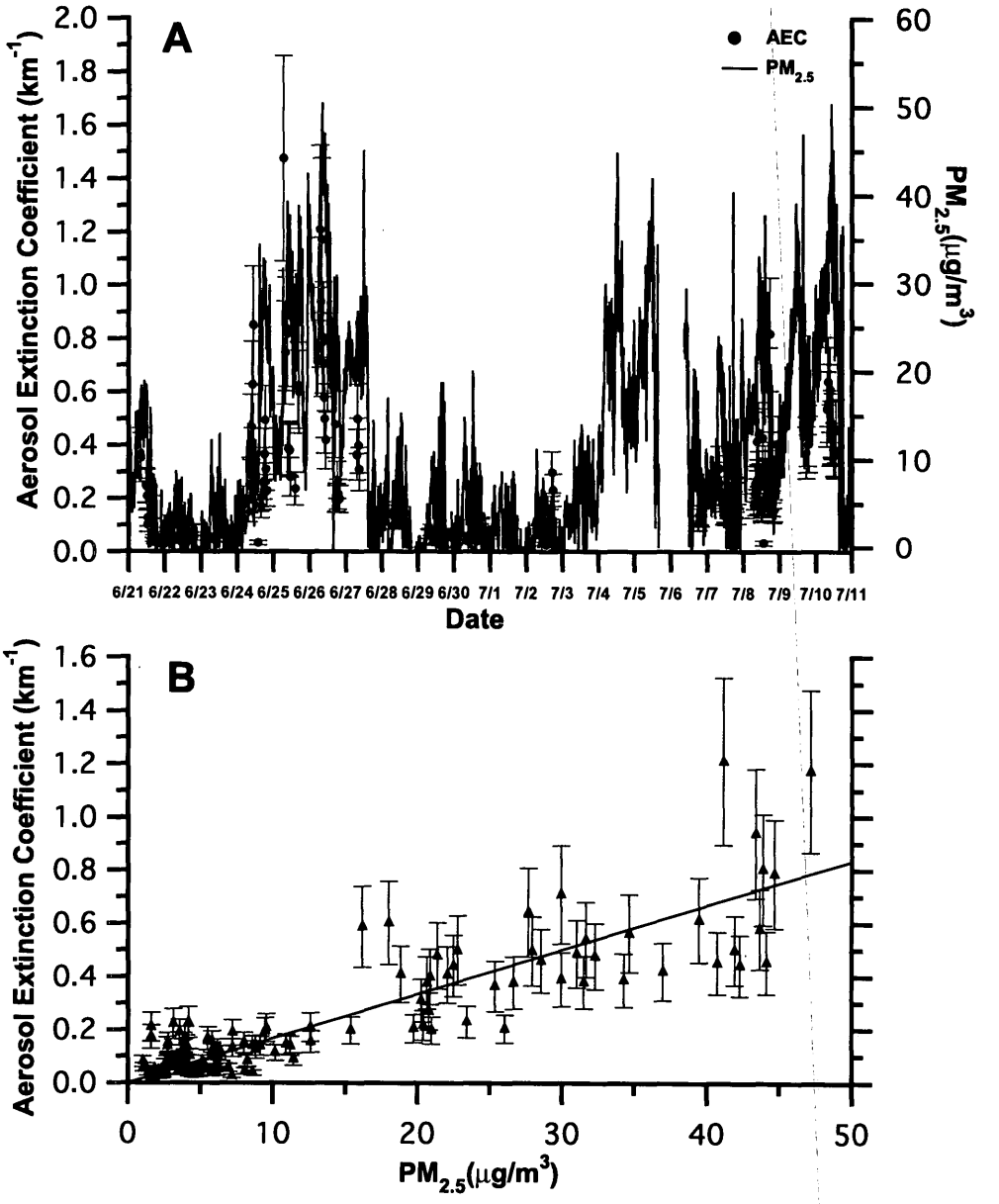

Figure 4.24: Time Series for the aerosol extinction coefficient (red) and $PM_{2.5}$ (grey) at Ridgetown (A) and Aerosol Extinction Coefficient vs. $PM_{2.5}$ (B). Slope of the trend line for B (y-intercept zero-forced) is 16 ± 1 m^2 g^{-1}, $R^2 = 0.75$.

with BLH being the boundary layer height, and $f(\mathrm{RH})$ a factor that takes into account the increase of aerosol extinction from hygroscopic growth of aerosols, as opposed to directly comparing hourly $PM_{2.5}$ and τ ($R^2 = 0.38$). Their result implied that most of the aerosol was found within the boundary layer, but that the boundary layer height is variable, preventing an easy measurement of aerosol mass through satellite-derived quantities. Unfortunately, in most of the other above-mentioned studies accurate boundary layer determinations were not given or were unavailable, and as such the relationship between aerosol extinction and $PM_{2.5}$ was not examined.

Further studies have determined aerosol extinction coefficients and aerosol optical depths from MAX-DOAS O_4 measurements and radiative transfer modelling, and compared them to PM_{10}, LIDAR calculated extinction coefficients, and aerosol optical depths from sky radiometers. Irie et al. (2008) compared extinction coefficients from MAX-DOAS-RTM inversions run at 476 nm with LIDAR calculated extinction coefficients (slope = 1.01, $R^2 = 0.85$) and compared τ values found from these MAX-DOAS-RTM inversions with τ values from a sky radiometer. Both comparisons agreed to within 30% for values determined from ground level to a height of 1 km. Lee et al. (2009) compared extinction coefficients found from a MAX-DOAS-RTM inversion run at 356 nm to LIDAR calculated extinction coefficients ($R^2 = 0.70$), and they agreed to within 50%, while a comparison between MAX-

DOAS-RTM derived extinction coefficients and PM_{10} also showed a relatively good correlation. The results presented here appear to be consistent with these studies.

4.5.4 Radiative Transfer Sensitivity Studies

As described in its entirety in Section 4.3, the determination of the NO_2 VCDs from NO_2 dSCDs is a two step process. First, according to Equation 4.13, τ_{RTM} and H_{aer} are determined for each measurement series. Second, this aerosol information was used as input to compare measured NO_2 dSCD ratios to modelled NO_2 DAMFs. The aerosol extinction coefficient (E) has been modelled with McArtim using three parameters (f, H_{aer}, and τ), while the NO_2 number density may be similarly modelled using f, H_{gas}, and VCD. Because of ambiguities in the retrieval of all three parameters, and the limited information content of NO_2 dSCDs in the UV region, the shape parameter (f) was set to 1 for all the retrievals (both aerosol and gas). It is acknowledged here that this "box profile" may not represent the best distribution of aerosols or NO_2 at any given time. As such, a sensitivity study was carried out to see the effects of lowering the shape parameter to $f = 0.8$ and $f = 0.5$ for both the aerosol and VCD retrievals, modelling pseudo-exponential profiles. For this investigation three days were chosen from the study period; June 20, June 29, and July 10. These days were chosen as representative days from each week, June

20 was the first day of the study where low τ values under 0.30 were determined. June 29 represented a day in the middle of the study period with moderate τ values ranging between 0.10-0.50, while on July 10, the last day of the study, relatively high τ values (over 0.90) were found. Figure 4.25 displays all τ values found for each day when the shape parameter (f) was set to either 1.0, 0.8, or 0.5. As can be seen in the figure, with just a few exceptions, most τ values were in close agreement with each other regardless of the f value prescribed. The slope (zero-forced intercept) between τ ($f = 0.5$ or 0.8) vs. τ ($f = 1$) varied from a maximum of 1.18 to a minimum of 0.97, and R^2 ranged from 0.88 to 0.99 (Table 4.3). This relative error is significantly lower than the calculated relative error for τ_{RTM} of 26% previously mentioned. Additionally, when varying f for both the aerosol and VCD retrievals the final NO_2 VCD determined had an even lower variance and sensitivity to the chosen f combinations, versus the combination $f = 1$ for both aerosol and NO_2 modelling (Figure 4.26 and Table 4.4). In every case, the NO_2 VCD was found to be within 6% of the value achieved when $f = 1$ for both retrievals. This was substantially lower than the relative error of each column, and therefore the choice of setting f to 1 should not be taken as a major source of error in determining the NO_2 vertical column densities.

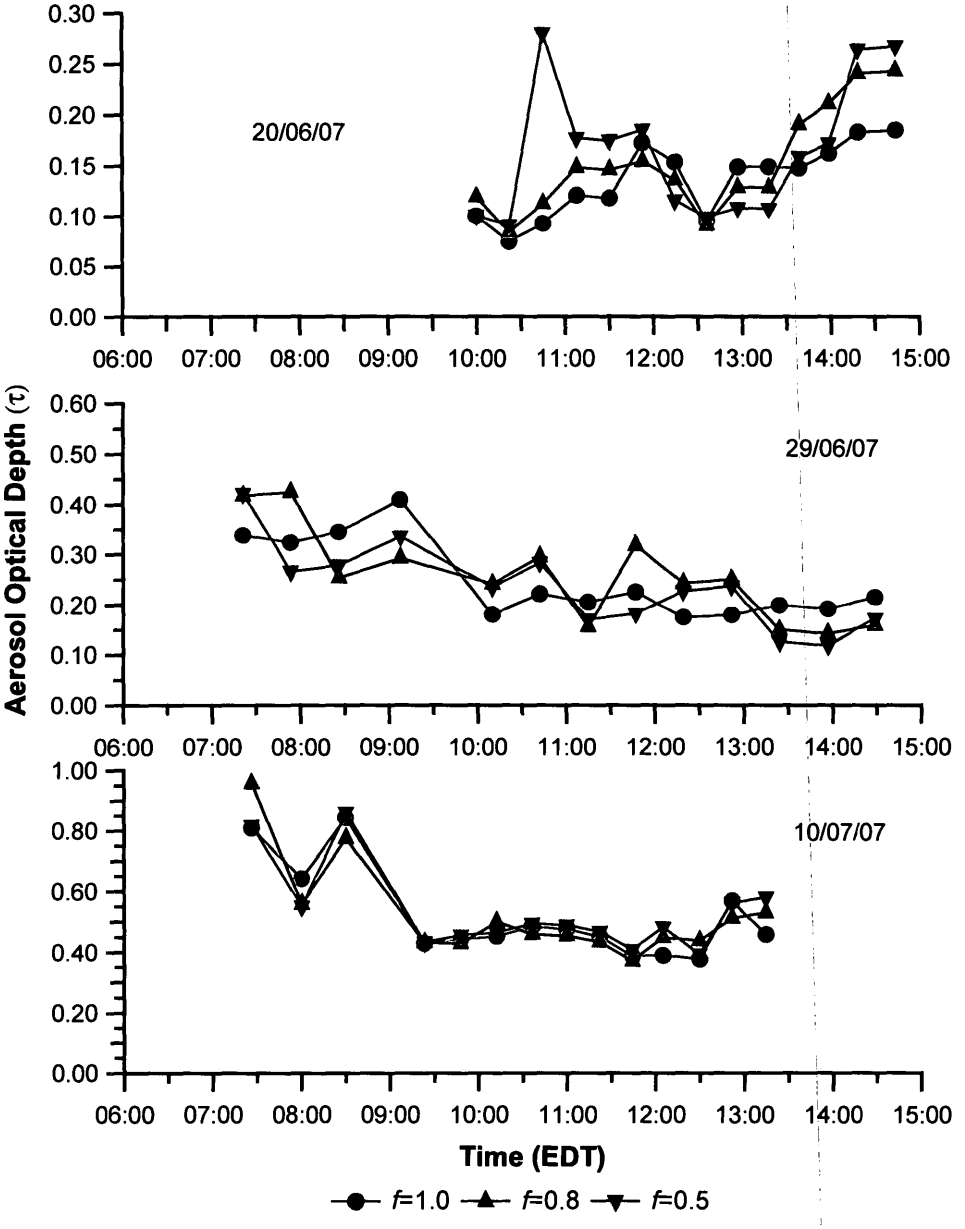

Figure 4.25: Aerosol optical depth values on June 20, June 29 and July 10, 2007 for various f values. The shape parameter (f) was set to 1.0, 0.8 or 0.5.

Table 4.3: Comparison of τ_{RTM} values when the shape parameter (f) is varied.

	June 20	June 29	July 10
Number of Data Pairs, N	14	16	14
τ_{RTM} (f=0.8) / τ_{RTM} (f=1.0)	1.12	1.01	1.01
Slope* (forced zero intercept)	1.12±0.05	0.98±0.07	1.01±0.03
Correlation*, R^2	0.97	0.92	0.99
τ_{RTM} (f=0.5) / τ_{RTM} (f=1.0)	1.21	0.99	1.02
Slope† (forced zero intercept)	1.18±0.12	0.97±0.08	1.02±0.02
Correlation†, R^2	0.88	0.91	0.99

*refers to $f = 0.8$ vs. $f = 1$ and † refers to $f = 0.5$ vs. $f = 1$.

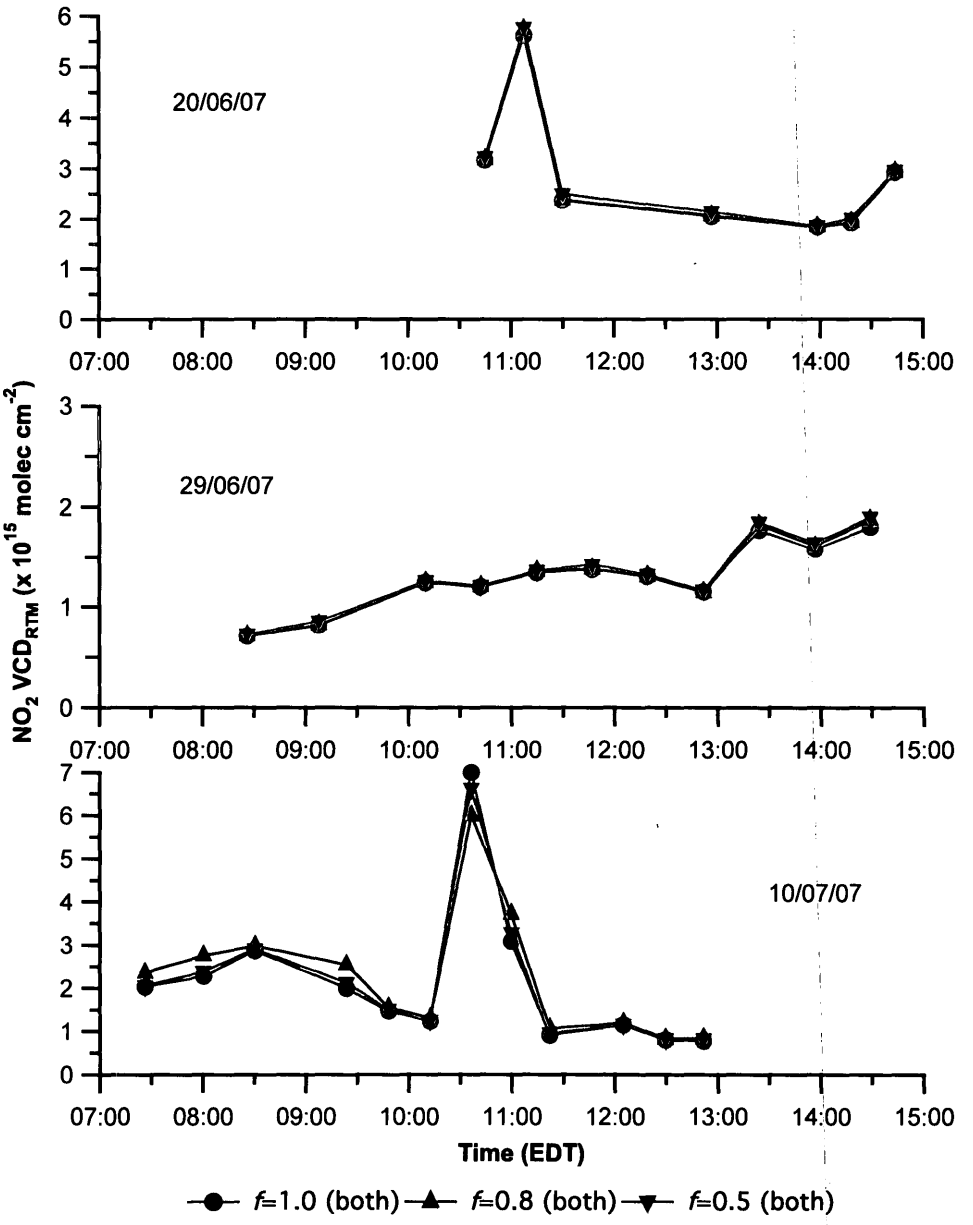

Figure 4.26: NO_2 VCD_{RTM} values on June 20, June 29 and July 10, 2007 for various f values. The shape parameter (f) was set to either 1.0, 0.8 or 0.5 for both the aerosol and gas modelling performed.

Table 4.4: Comparison of NO_2 VCD_{RTM} values when the shape parameter (f) is varied vs. NO_2 VCDs with f set to 1 for both the aerosol and NO_2 modelling.

	20/6 NO_2 (f=0.8)	20/6 NO_2 (f=0.5)	29/6 NO_2 (f=0.8)	29/6 NO_2 (f=0.5)	10/7 NO_2 (f=0.8)	10/7 NO_2 (f=0.5)
Aerosol (f=1.0) Slope (forced zero intercept)	1.00	1.03	1.00	1.02	1.00	1.03
Correlation*, R^2	1.00	1.00	1.00	1.00	1.00	0.98
Aerosol (f=0.8) Slope (forced zero intercept)	1.01	1.03	1.02	1.03	0.98	1.02
Correlation*, R^2	1.00	1.00	1.00	1.00	0.99	0.96
Aerosol (f=0.5) Slope (forced zero intercept)	1.00	1.03	1.02	1.03	0.94	0.98
Correlation*, R^2	1.00	1.00	1.00	1.00	0.97	0.92

*Note: for 20/6, N=7, 29/6, N=14, and 10/7, N=12.

4.5.5 Validation of MAX-DOAS-RTM against Vertical Measurements of NO_2

In order to validate the method for deriving NO_2 VCDs using MAX-DOAS and RT calculations, comparative VCDs of NO_2 were derived from a composite of ground-based and aircraft-based NO_2 measurements in the vicinity of Ridgetown during the same time frame as the MAX-DOAS measurements. The composite profiles included ground-based NO_2 measurements at Ridgetown via active DOAS, vertical measurements of NO_2 when the aircraft was in the vicinity of Ridgetown, and suitable estimates of NO_2 in the free troposphere above the maximum height of the aircraft. Suitable temporal and spatial overlapping data were found for one day: June 26. Four composite profiles of NO_2 were derived for this day, two in the morning when the boundary layer height was still low, and two in the late afternoon, when the boundary layer had maximized. The morning profiles were split into three discrete sections. For the boundary layer (Section I), the NO_2 mixing ratio was assumed to be homogeneous and equivalent to the NO_2 measured at ground level by DOAS. Boundary layer heights for this time period were determined through a combination of LIDAR, vertical temperature profiles measured by tethersonde at the site, and by aircraft in the vicinity of the site. For Section II, the portion of the column from the top of the boundary layer to the maximum height of the aircraft, NO_2 measured onboard the aircraft was used when the aircraft was within

a suitable criteria distance of the Ridgetown site. In general, the degree of spatial homogeneity in NO_2 increases with height, in the absence of elevated sources, and the criteria for inclusion of data in the composite profile reflected this. From the top of the boundary layer to 800 m *agl*, only aircraft data collected within 30 km of the site was included, while from ~800 m to 1600 m *agl* aircraft data within 80 km of the site was included (Figure 4.27A). The assumption here is that above the boundary layer in the morning, the NO_2 mixing ratio in the residual layer is regionally homogeneous. For Section II, NO_2 number densities were calculated as a function of height accounting for the non-linearity of pressure and temperature, then fit to an exponential function, and integrated over the appropriate range to yield the NO_2 column density. For Section III, the portion of the column above the top of the aircraft measurements (free troposphere), a constant NO_2 mixing ratio of 50 ppt was assumed (Blond et al., 2007).

For the afternoon profiles, the boundary layer was much higher and the assumption of a homogeneous layer of NO_2 was found to be invalid on this day. Mixing ratios of NO_2, measured when the aircraft penetrated into the boundary layer (~315 m *agl*) over land close to Ridgetown, were much lower than values measured at ground level. The boundary layer at this time was 797±45 m *agl*, determined by potential temperature profiles measured by the aircraft. For this reason, the PM profiles were split into just two sections, with Sections I and II combined in

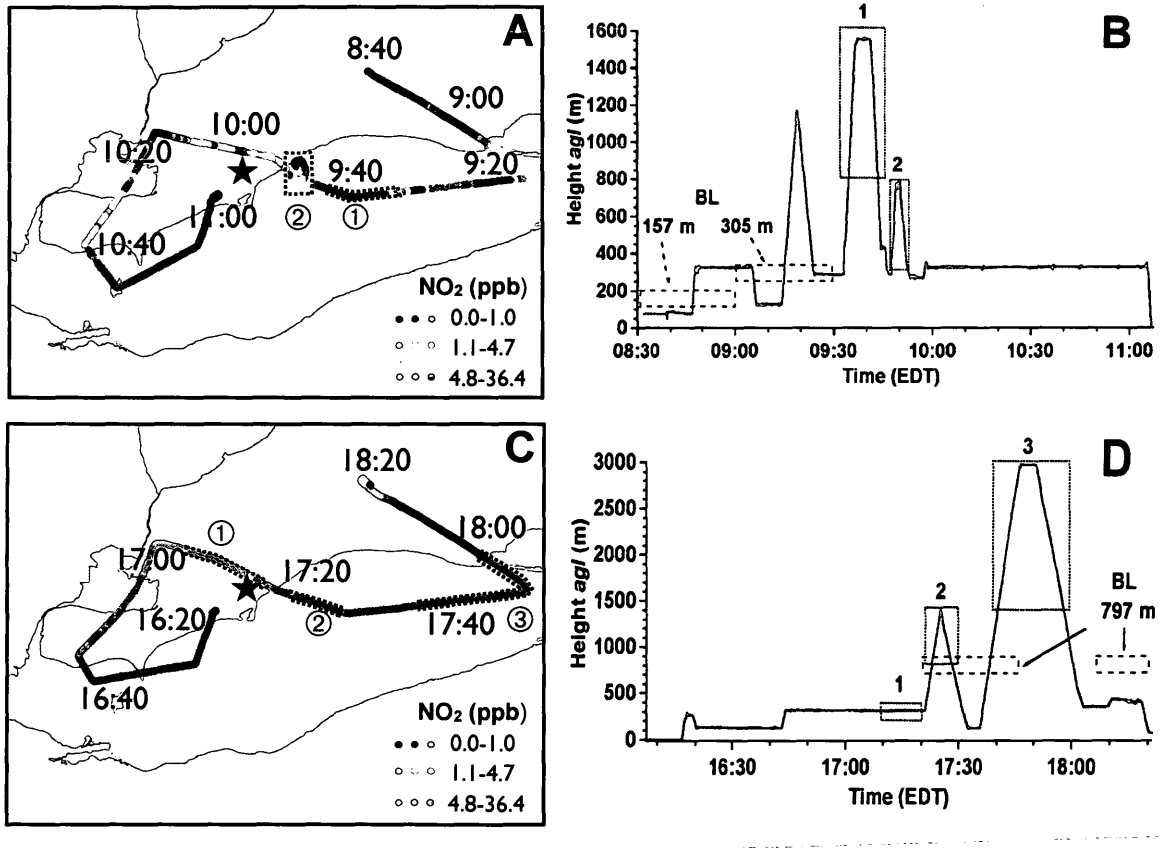

Figure 4.27: AM flight path (8:32-11:07 EDT) and PM flight path (16:07-18:21 EDT) on June 26, 2007. Panel A and C show the NO_2 mixing ratios and the aircraft location every 20 minutes. Panel B and D show the aircraft elevation and BLH (*agl*) as a function of time. The numbered sections on all figures show the locations, elevations, and approximate mixing ratios used for constructing the composite NO_2 profiles. The Ridgetown supersite location is starred.

this case. Section (I+II) consisted of the portion of the column from ground level to the top of the aircraft measurements. The criteria for inclusion of aircraft data in the profile was that the aircraft had to be within 30 km of the site over land for the boundary layer, within 50 km of the site for heights from the top of the boundary layer to 1400 m *agl*, and within 140 km of the site for heights between 1400 and 2980 m *agl* (Figure 4.27C). To determine the total column density of this section, an exponential was fit to all NO_2 data from ground level to the top of the available aircraft measurements. This exponential fit was then integrated to obtain the total NO_2 column density for this section. A sensitivity calculation is included later on to explore the uncertainty in this approach. Section III, the portion of the free troposphere above the top of the aircraft measurements was again assumed to have a constant NO_2 mixing ratio of 50 ppt.

Data from the two aircraft flights coupled with ground-based measurements were used to construct four different NO_2 vertical profiles on June 26, coincident in time with four VCD_{RTM} determinations. The vertical column densities of NO_2 were calculated from these profiles using Equation 4.24 and are henceforth called composite VCDs (VCD_{COMP}):

$$VCD_{COMP} = \int_0^{BL} n^{I}_{NO_2} dz + \int_{BL}^{TOAc} n^{II}_{NO_2} dz + \int_{TOAc}^{10km} n^{III}_{NO_2} dz \qquad (4.24)$$

where n_{NO_2} is the number density of NO_2 for Sections I, II, III, and TOAc represents the top of available aircraft measurements. Figure 4.27A (8:32-11:07 EDT) and

Figure 4.27C (16:07-18:21 EDT) show the flight paths for each flight. In each figure, the NO_2 mixing ratio is displayed as a function of time and location. The exact position of the aircraft for every 20 min interval of flying time is also marked. Figures 4.27B and 4.27D show the altitude profiles for these flights with respect to time of day and include ascending, descending, and stable height time periods. The closest available NO_2 mixing ratios for each given height have been selected based on both time and location considerations, as discussed previously (the flight segments used for profiles are highlighted on the figures). Figure 4.28 displays the two sample NO_2 profiles for June 26 (AM period: 8:31-8:57 EDT and PM period: 17:52-18:15 EDT) that were used to calculate VCD_{COMP} values. Error bars in the y dimension represent uncertainties in the boundary layer heights (AM period only), while error bars in the x dimension represent uncertainties in the NO_2 mixing ratios.

Four VCD_{COMP} values were determined for the AM and PM flights on this day, to be compared to four VCD_{RTM} values coincident in time (Table 4.5). The uncertainty in the VCD_{RTM} values in Table 4.5 is dictated by two factors. The first is the uncertainty in the NO_2 DSCD determined by the DOAS fit, which has a typical absolute uncertainty of $\pm 7 \times 10^{15}$ molec cm^{-2}. The second factor is the uncertainty in the NO_2 AMF, which is more difficult to gauge, although we estimate the relative uncertainty to be $\pm 30\%$. Together this yielded an absolute and relative uncertainty for the VCD_{RTM} values of $0.9\text{-}1.9 \times 10^{15}$ molec cm^{-2} and

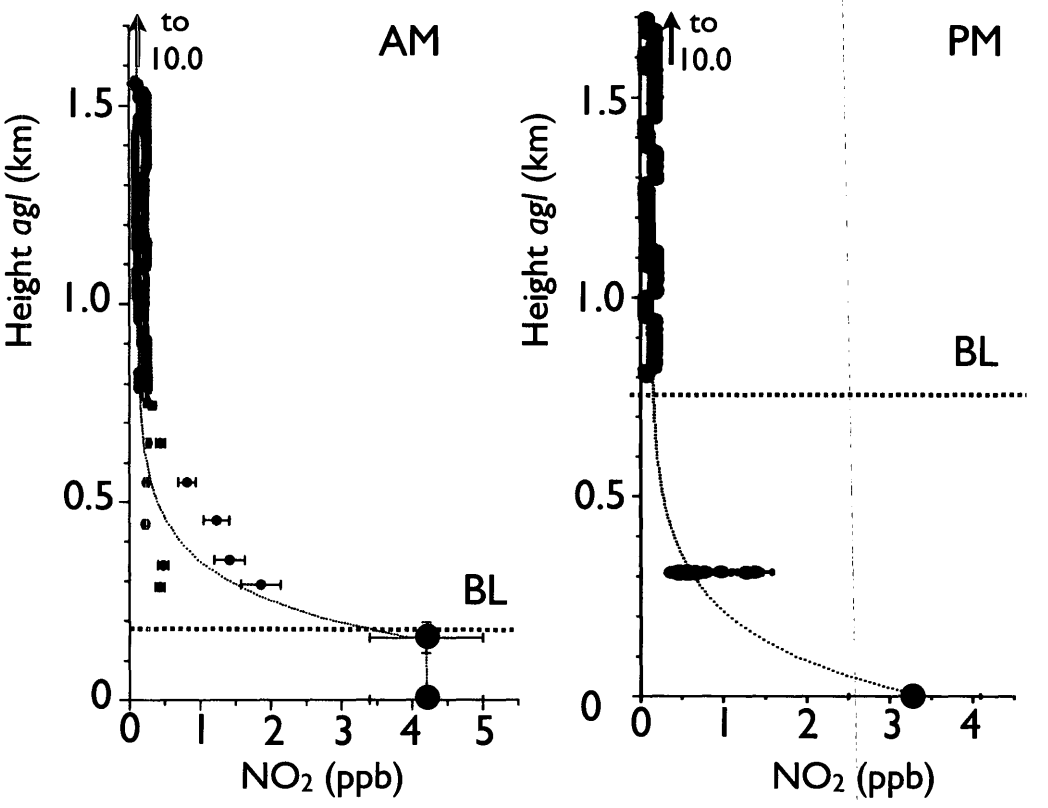

Figure 4.28: NO_2 concentration profiles used to construct the composite NO_2 VCDs for the AM flight path (8:31-8:57 EDT) are in red and the PM flight path (17:52-18:10 EDT) are in blue, on June 26, 2007. Colored circles represent NO_2 aircraft measurements, while dark grey circles represent ground-based NO_2 by active DOAS. The boundary layer height (BLH) for each case is also marked with the horizontal dashed line.

32-36%, respectively.

The uncertainties in the VCD_{COMP} presented in Table 4.5 were determined from several sources. For Section I (AM) the contributing factors were the uncertainty in the boundary layer height and the uncertainty in the NO_2 concentration determined by DOAS. These two uncertainties were propagated to give the total uncertainty for Section I. For each AM measurement the boundary layer was determined from LIDAR with uncertainty and verified using temperature profiles from tethersonde/aircraft measurements. For Section II the uncertainty in the exponential fit of the NO_2 mixing ratio vs. height was key. For Section III the uncertainty in the assumed NO_2 mixing ratio (50 ppt) was assumed to be $\pm$100%. For Section (I+II, PM) the uncertainty in the exponential fit was key, and for Section III (PM) the uncertainty in the NO_2 mixing ratio was again assumed to be $\pm$100%. Other uncertainties in the determination of the VCD_{COMP}, such as those due to spatial and temporal differences between the aircraft measurements and the MAX-DOAS column, were not considered.

The mean value of the VCD_{COMP} values in Table 4.5 was $3.54\pm0.59\times10^{15}$ molec cm^{-2}, which is reasonable for a rural region (Heland et al., 2002; Irie et al., 2009; Ladstätter-Weißenmayer et al., 2003). The mean value of the VCD_{RTM} values was $4.03\pm0.71\times10^{15}$ molec cm^{-2}. The ratio of VCD_{RTM} / VCD_{COMP} = 1.14$\pm$0.27, while the regression of VCD_{RTM} vs. VCD_{COMP} indicates a slope of 1.16$\pm$0.12 (standard

Table 4.5: Comparison of RTM and composite NO_2 VCDs on June 26, 2007.

Point	Time (EDT)	VCD_{COMP} (10^{15} molec cm^{-2})	VCD_{RTM} (10^{15} molec cm^{-2})	Error (10^{15} molec cm^{-2})	VCD_{RTM} vs. VCD_{COMP}
1	8:31-8:57	4.06±1.11	5.84±1.92	1.78	
2	9:03-9:29	3.85±1.19	4.18±1.37	0.33	
3	17:25-17:46	3.06±1.22	2.59±0.93	-0.47	
4	17:52-18:15	3.18±1.22	3.50±1.25	0.32	
Mean		3.54±0.59	4.03±0.71	0.49	1.14±0.27
RMSE				0.95	
				Slope (forced zero intercept)	1.16±0.12 (0.39)
				Correlation, R	0.77

*All errors are standard errors except those in brackets, which are at the 95% confidence level.

error) that is not statistically different from 1.0 at the 95% confidence level. The regression was forced to zero because the intercept in a two parameter (slope and intercept) linear regression did not show an intercept that was statistically different from zero. The mean bias in the VCD_{RTM} values compared to the VCD_{COMP} values is $+0.49\times10^{15}$ molec cm^{-2}, not statistically different from zero. Although only a limited number of points were compared, the comparison above serves as a preliminary validation for the MAX-DOAS-RTM method used to determine NO_2 VCDs, as outlined in Section 4.3 . There is no evidence of a statistically significant bias in the determination of VCD using this method at the moderate NO_2 column levels that existed during the comparison.

4.5.6 Comparison of Boundary Layer Heights to H_{aer} and H_{gas}

Although the focus in this study was not the determination of accurate boundary layer heights (BLHs), it is instructive to compare the retrieved aerosol and gas heights, H_{aer} and H_{gas}, and BLHs determined by LIDAR backscatter measurements. LIDAR data was available on six days (8:00-16:00 EDT), simultaneous with MAX-DOAS-RTM determinations. There were 25 simultaneous determinations of BLH, ranging from 0.1 km-2.0 km *agl*, from early morning to late afternoon respectively. Figure 4.29 shows the correlations between the retrieved heights and the BLH from

LIDAR, zero-forced since the intercepts were not statistically different from zero.

The correlation coefficients are low ($R^2 = 0.17$ for H_{aer}; 0.08 for H_{gas}), indicating that the retrievals only capture a small amount of the variance associated with the backscattered BLHs. It is also apparent that the values of H_{aer} are significantly higher than the BLHs, by almost a factor of two, and that the H_{gas} values are significantly lower than the BLHs, by a factor of two. The correlation coefficients are improved by applying a more rigid set of criteria for inclusion of data pairs, such as using a lower RSS value, as shown in Wagner et al. (2011). However, the slopes still remain much the same, which requires an explanation. The H_{aer} slope of 1.92±0.21 likely results from the fact that aerosols are not exclusively confined to the boundary layer, especially in early morning periods when significant amounts of aerosols left over from the previous day can exist in the residual layer, as was directly observable in LIDAR images. This is partly attributable to the longer lifetime of aerosols in the atmosphere, compared to NO_x, and partially attributable to the ubiquitous secondary source of aerosols throughout the atmospheric column. On the other hand, the sources of NO_x are predominantly surface-based within the boundary layer, which combined with its shorter lifetime than aerosols gives rise to a negative gradient of NO_2 in the boundary layer (see Fig. 4.28). When modelled as a homogeneous layer, the H_{gas} height is lower than the BLH (slope = 0.43±0.08); however an accurate VCD can still be obtained. As mentioned earlier

in Section 4.5.4, a sensitivity analysis was performed in which the fraction of NO_2 (f_{gas}) and aerosols (f_{aer}) confined to the homogeneous layer were allowed to vary from 0.5 to 1.0. The τ_{RTM} values were found to agree quite well ($\pm 2\%$) for moderately and highly polluted days, but less so for a low aerosol day with a maximum difference of 21% on a very clean day ($\tau \approx 0.05$). The variance in VCD_{RTM} was $\pm 6\%$ under all aerosol conditions tested in this sensitivity study. Thus, accurate values of τ and VCD are still obtained using the current methodology. If this method is to be used for accurate determinations of BLH however, then time dependent values of f_{aer} and f_{gas} would be needed. A more thorough discussion of the sensitivity of the retrievals to f_{aer} and f_{gas} is given elsewhere (Wagner et al., 2011).

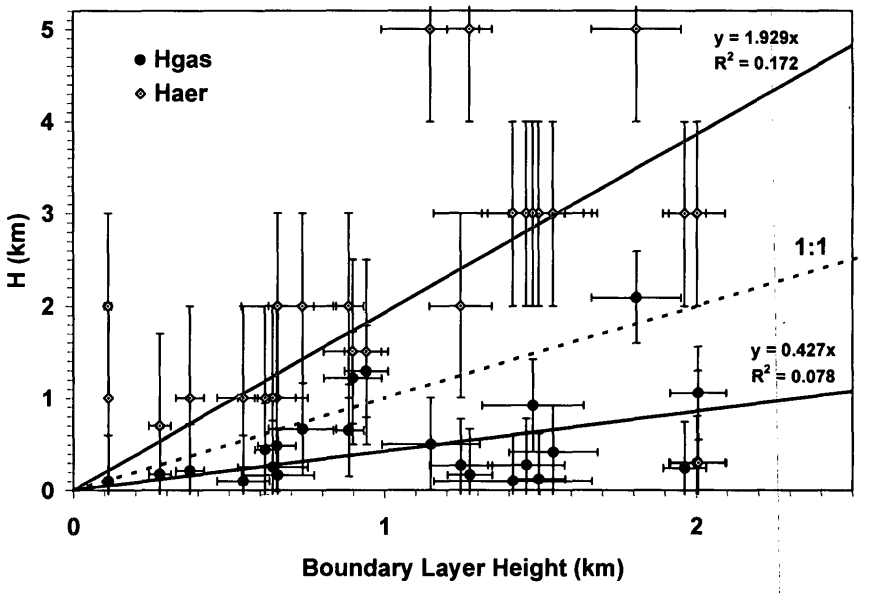

Figure 4.29: Correlation between MAX-DOAS-RTM retrieved layer heights and boundary layer heights determined by LIDAR backscatter determinations.

4.5.7 Comparison between MAX-DOAS-RTM and Satellite VCDs of NO_2

Figure 4.30 displays all tropospheric NO_2 VCDs for the Ridgetown site throughout the study. The VCD_{RTM}, VCD_{GEO} and VCD_{COMP} (June 26 only) are shown, along with the satellite-derived measures VCD_{OMI} and VCD_{SCIA}. Only nine VCD_{SCIA} measurements were available during the study period due to the limited temporal sampling of the ENVISAT satellite. There were 31 measurements from the OMI instrument on the Aura satellite as it provides daily global coverage with successive orbits separated by 100 mins providing 1-2 measurements per day at a specified location. To facilitate comparisons between VCD_{RTM} and $VCD_{satellite}$, measurements were paired only when the two measurements were made within one hour of each other. Only one comparison pair was available for SCIAMACHY while eight comparisons were available for the OMI instrument. The statistical comparison is provided in Table 4.6, where all VCDs are compared to VCD_{RTM}.

The comparison in Table 4.6 indicates that the NO_2 VCDs derived by satellite were higher than those of the VCD_{RTM}. Presuming a proportionate error, the two satellites determinations are about 50% higher than VCD_{RTM}, but only statistically so for the OMI instrument due to a lack of comparison points for SCIAMACHY. The proportionate error for OMI was determined in two ways: *i)* the ratio of the averages, VCD_{OMI} / VCD_{RTM} and *ii)* the slope of the regression of VCD_{OMI} vs.

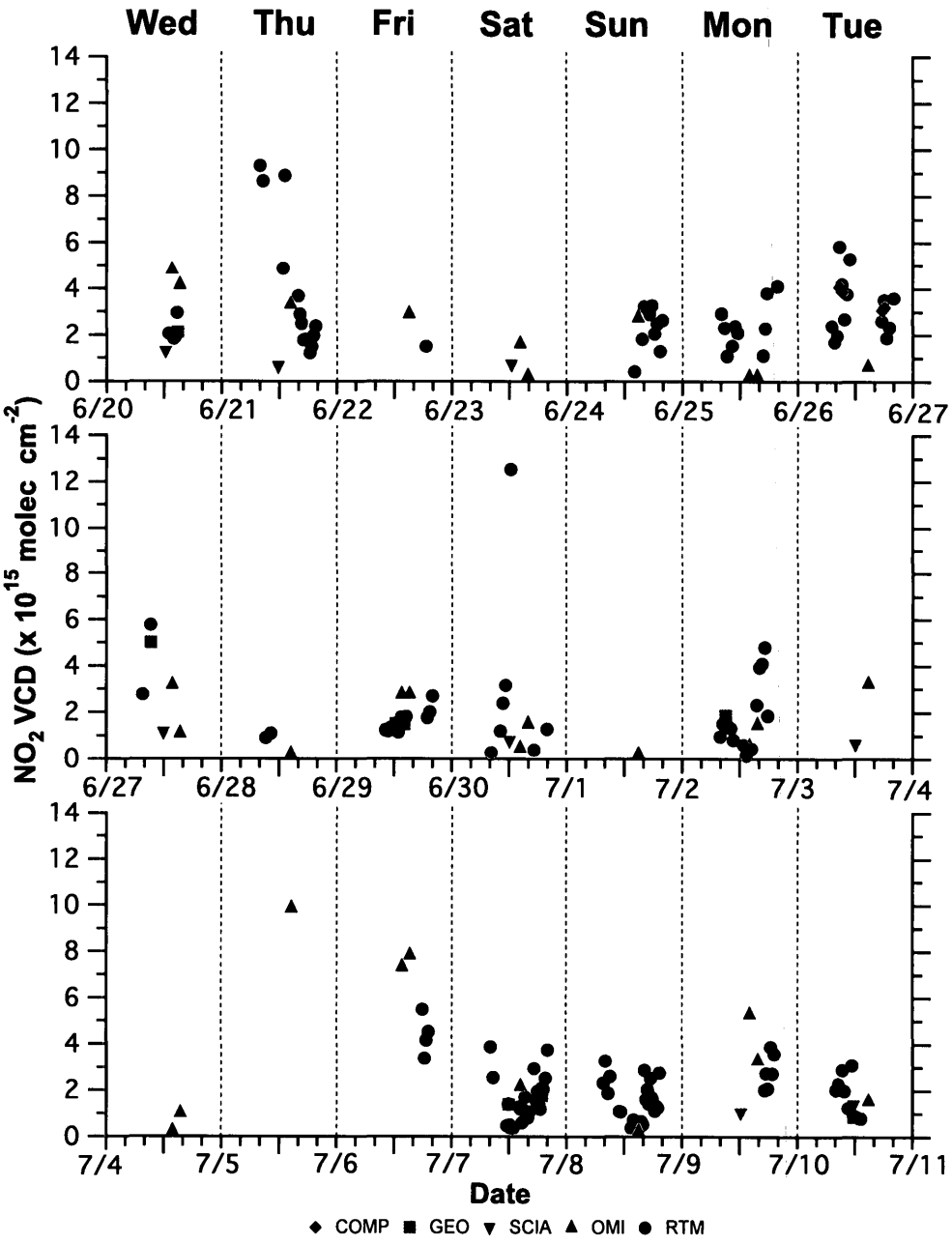

Figure 4.30: Comparison of NO_2 tropospheric VCDs derived from aircraft/ground, satellite and MAX-DOAS-RTM measurements.

Table 4.6: Comparison of various NO_2 VCDs with VCD_{RTM}

	OMI AURA*	SCIAMACHY ENVISAT	Geometric Approximation*	Aircraft Composite*	AURAMS model
Number of Data Pairs, N	8	1	10	4	131
$\overline{VCD}_{measured}$ ($\times 10^{15}$ molec cm^{-2})	2.67±0.18	1.39	1.88±0.05	3.54±0.59	1.85
$\overline{VCD}_{RTM}$ ($\times 10^{15}$ molec cm^{-2})	1.76±0.16	0.92±0.44	2.05±0.14	4.03±0.71	2.38
$\overline{VCD}_{measured}/\overline{VCD}_{RTM}$	1.52±0.17	1.5	0.92±0.07	0.88±0.09	0.78
Slope (forced zero intercept)	1.47±0.20	N/A	0.88±0.04	0.83±0.09	0.69
Correlation, R	0.63	N/A	0.97	0.77	0.57
Mean Absolute Error ($\times 10^{15}$ molec cm^{-2})	1.12	0.48	0.30	0.49	0.53
RMSE ($\times 10^{15}$ molec cm^{-2})	1.33	N/A	0.41	0.95	1.60
Mean Bias ($\times 10^{15}$ molec cm^{-2})	+0.91	+0.48	-0.17	-0.49	-0.53

*All errors are standard errors (1σ).

VCD_{RTM}, with the y-intercept forced to zero (intercept was equal to zero within error). If one presumes a constant bias in the satellite retrievals, the mean bias is $+0.91\times10^{15}$ molec cm^{-2} for OMI, and $+0.48\times10^{15}$ molec cm^{-2} for SCIAMACHY. These results do not provide sufficient statistical evidence as to whether the satellite error is proportionate or absolute. However, it should be noted that the total VCDs experienced at this rural site are relatively small. Thus, the apparently large relative overprediction for the satellite retrievals (+50%) is not necessarily a result that is transferable to more polluted regions with higher NO_2 VCDs. Further comparisons at different sites containing varying levels of NO_2 would be required to investigate this relationship further.

Earlier studies (Brinksma et al., 2008; Celarier et al., 2008; Chen et al., 2009; Irie et al., 2009), including the Saturna Island study, found satellite-derived NO_2 VCDs to be substantially lower than MAX-DOAS derived NO_2 VCDs. In those studies the MAX-DOAS VCDs were geometrically approximated (similar to VCD_{GEO}) and the distinction from a full MAX-DOAS with radiative transfer derived VCD (VCD_{RTM}) should be taken into account in these comparsions. The observation of satellite VCDs with a positive bias compared to MAX-DOAS-RTM and aircraft-derived VCDs is in contrast to these previous studies. One possible explanation for this is that previous comparisons have frequently focused on urban and suburban areas where average NO_2 VCDs were significantly higher. For example, the VCD of NO_2

ranged from 0.5-5$\times10^{16}$ molec cm^{-2} during DANDELIONS at Cabauw, Netherlands (Brinksma et al., 2008; Celarier et al., 2008) with a median of $\sim$1.5$\times10^{16}$ molec cm^{-2}, whereas the VCD range in the current study is 0.01-1.25$\times10^{16}$ molec cm^{-2} with a median of 2.00$\times10^{15}$ molec cm^{-2}. In that study, the MAX-DOAS instruments measured very high NO_2 VCDs in a polluted region, which could not be completely captured by the satellite, due to the regional averaging implicit with a large pixel size. Under such conditions, the satellite will measure lower values than the more localized *in situ* measurement. The opposite would be true here. Being situated in a rural region, the local measurements of NO_2 made by MAX-DOAS and the aircraft are relatively low. In contrast, the large pixel area coverage of the satellite instruments (OMI - 13$\times$24 km^2, SCIAMACHY - 30$\times$60 km^2) will be higher than the local measurement when the pixel is impacted by surrounding urban areas, as may occur when prevailing westerly winds carry pollutants from Windsor-Detroit towards Ridgetown. If a significant amount of a given pixel lies within a position west of Ridgetown, it may be detect NO_2 from this urban outflow and thus overestimate the actual NO_2 present at the site (see Figure 4.31). Additionally, the satellite retrievals used here do not consider aerosol conditions or temporal changes in the NO_2 profile. Uncertainties in these parameters could lead to uncertainties in the overall satellite-derived VCD and, with low levels of NO_2, this may lead to large relative uncertainties in these VCDs.

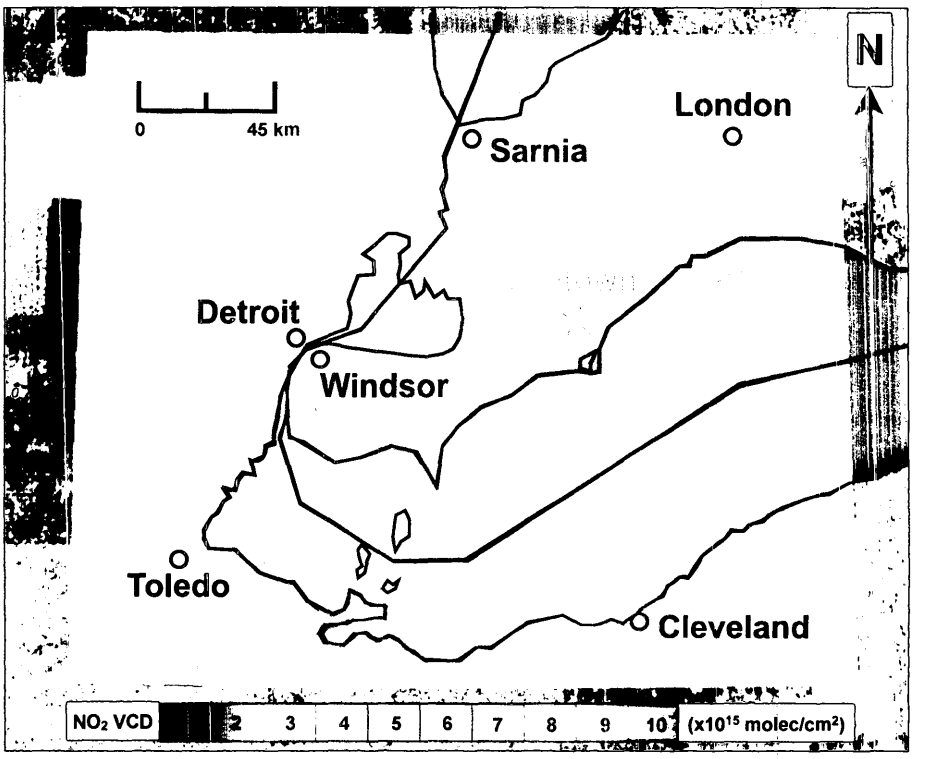

Figure 4.31: Averaged OMI tropospheric NO_2 VCDs for the intensive field study period (June 20-July 10, 2007) in southwestern Ontario. Ridgetown supersite is starred. Figure provided courtesy of M. Wenig, LMU-Munich, Germany (personal communication).

Also included in Table 4.6 is a statistical comparison of VCD_{GEO} to VCD_{RTM}, where the conservative selection criterion for inclusion was fulfilled, namely that the values of geometrically approximated VCDs for elevation angles of 10° and 30° in the same measurement series agreed to within 15%. This selection criterion is quite limiting and was fulfilled for 10 data pairs only, as seen in the table. Similar criteria has been used in past studies to ensure that the VCDs determined by the geometric approximation are not heavily influenced by aerosols, thus making them appropriate for comparison to satellite measures (Brinksma et al., 2008; Celarier et al., 2008). Although the method with full radiative transfer is favoured, the VCD_{GEO} comparison allows benchmarking to previous literature. The comparison indicates that VCD_{GEO} is lower than VCD_{RTM} by 8-12%, presuming a proportional error, or with a mean bias of -0.17×10^{15} molec cm^{-2}, presuming an absolute error. Since both of these VCDs are derived either partly or entirely from the same set of MAX-DOAS measurements, they have nearly identical measurement times, and the compared pairs show a high correlation between VCD_{GEO} and VCD_{RTM} (R^2 = 0.97).

The average NO_2 VCD retrieved from OMI measurements during the study period (June 20-July 10) for the BAQS-Met study domain is mapped on a $0.002°\times0.002°$ grid, as described in Wenig et al. (2008), in Figure 4.31. The highest VCDs are seen over the metropolitan area of Detroit/Windsor with average VCDs up to $\sim1\times10^{16}$

molec cm^{-2}. Other areas with enhanced NO_2 columns include the cities of Toledo, Sarnia, and Cleveland. The waterways between Lake Huron and Lake Erie, one of the busiest waterways in the world, (St. Clair River and Detroit River) are also hot spots for enhanced columns of NO_2 and likely indicative of the heavy ship traffic and associated industrial activities supported by the presence of the waterway transport. Also visible from the satellite are enhanced NO_2 columns extending well out into the lakes at the ends of these waterways; Lake Erie (south of Detroit) and Lake Huron (north of Sarnia) which are likely indicative of the emissions from underway vessels, anchored vessels awaiting entry into the waterways and recreational boating activities. Considering just the NO_2 VCDs over Lake Erie, the western region of the Lake appears to be the most polluted. In contrast to the previously mentioned regions, the measurement site at Ridgetown can be seen to be in a relatively rural area with a study average NO_2 VCD of $\sim$2-3$\times10^{15}$ molec cm^{-2}. The lowest average NO_2 VCDs in the domain are seen over Lake Erie south of London and in regions surrounding London to the north and west ($\sim$1-2$\times10^{15}$ molec cm^{-2}).

4.5.8 Comparison between NO_2 Measurements and Modelled NO_2 from AURAMS

Figure 4.32 compares the NO_2 VCDs for columns calculated from ground level to $\sim$18 km obtained from the AURAMS model (VCD_{AUR}) to the previously discussed

NO_2 VCDs from satellite, ground-aircraft composite and MAX-DOAS-RTM. The advantages that the model has over the other measures are that it has better time resolution (2 min) and there are with no gaps in the time series. The largest VCDs from the model occur during dark hours, when other measurements of VCD cannot be made. For the time periods in common, the VCD_{AUR} values often seem to match the other measures qualitatively. To assess things on a quantitative level, VCD_{AUR} is compared to VCD_{RTM} in Figure 4.33, with the averaging of AURAMS values into the time periods of the corresponding VCD_{RTM} values. The slope suggests that AURAMS underpredicts the NO_2 VCD at Ridgetown by a significant amount (~47%), with an intercept of 5.9×10^{14} molec cm^{-2}, while the correlation was somewhat moderate ($R^2 = 0.37$). When the slope was zero-forced, AURAMS underpredicts the NO_2 VCD by 31% with $R^2 = 0.32$, and the ratio of average VCD_{AUR} to average VCD_{RTM} was 0.78 (Table 4.6). There are several potential reasons for the underprediction of NO_2 in the model, both chemical and physical.

To examine possible causes for this underprediction, ground level NO_2 from AURAMS (at an average height of 3.5 m) was compared to ground level measurements of NO_2 from chemiluminescence and active DOAS (Figure 4.34). For the majority of days, ground level NO_2 peaks at the same or similar times, yet there are some cases such as on June 26, 27, July 4, and 6, where peak NO_2 times do not coincide. It is clear that AURAMS generally underpredicts ground level NO_2 versus both ex-

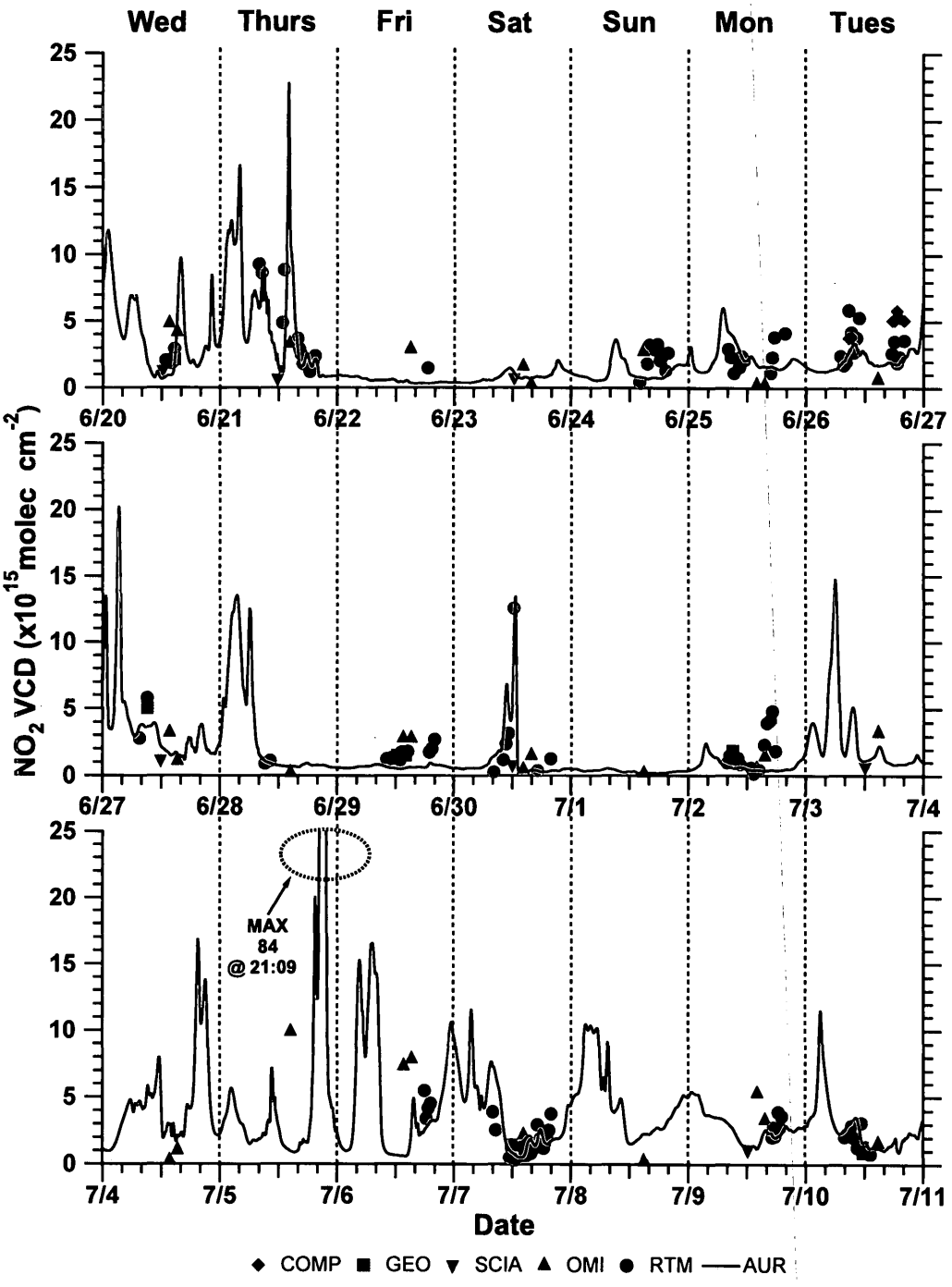

Figure 4.32: Comparison of all NO_2 VCDs at Ridgetown. Composite, geometric, satellite, MAX-DOAS-RTM and AURAMS-derived VCDs are displayed.

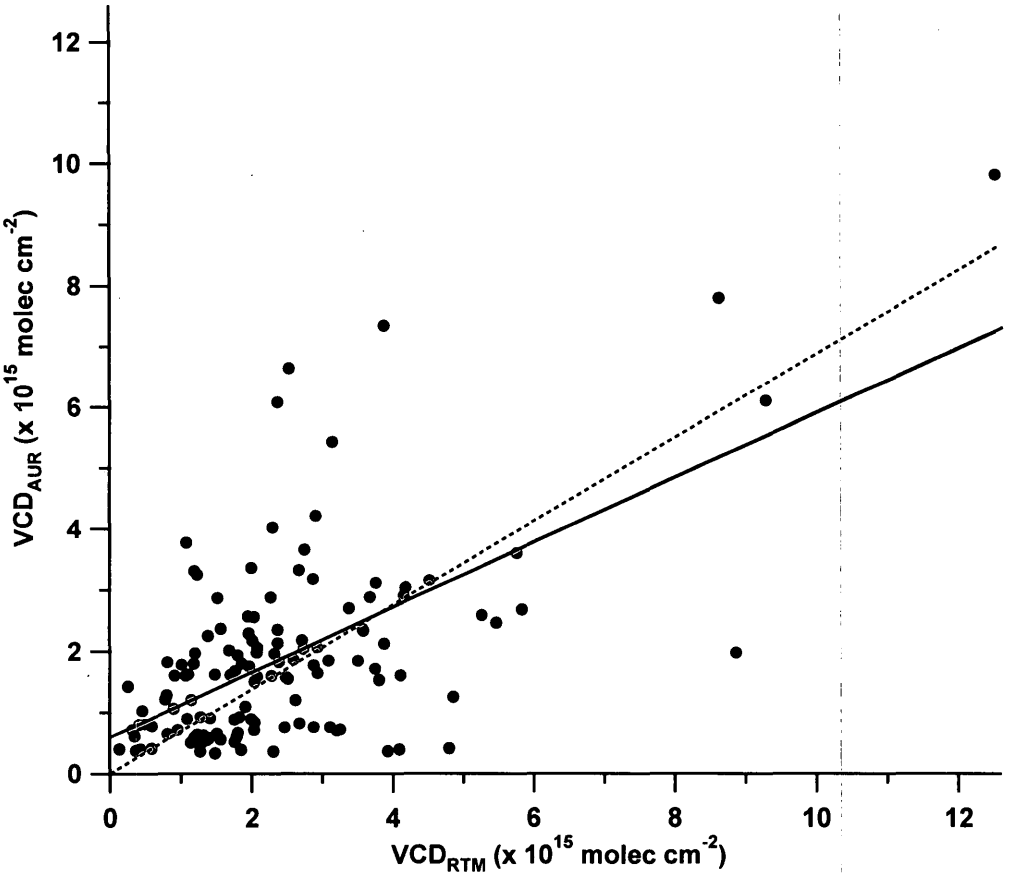

Figure 4.33: Correlation plot of VCD_{AUR} vs. VCD_{RTM} at Ridgetown. The solid line represents the linear regression, while the dotted line represents the linear regression with a zero-forced intercept.

perimental measures. Examining this further, 10 minute averaged AURAMS NO_2 data and chemiluminescence NO_2 values were compared (Figure 4.35). Chemiluminescence values were used here instead of active DOAS values because a much greater number of values could be compared (several active DOAS spectra were discarded due to the presence of strong absorption features from scattered sunlight). AURAMS was significantly lower than chemiluminescence NO_2 measures on average (60% lower) with an intercept of 0.70 ppb, and only moderately correlated (R^2 = 0.33). When the y-intercept was zero-forced this underprediction was lowered to 51%, and the ratio of the average ground level AURAMS NO_2 to NO_2 from chemiluminescence was 0.53. In this case, the AURAMS NO_2 could be expected to be significantly lower than the chemiluminescence values, as it has been well documentated that chemiluminescence devices may overpredict NO_2 (and NO_x) due to interference from other oxidized nitrogen species [NO_z = HNO_3 + HONO + N_2O_5 + $RONO_2$ + others] (Steinbacher et al., 2007). As such, the "NO_2" reported from the chemiluminescence instrument is often higher than the true NO_2 present.

The comparisons between VCDs and mixing ratios both indicate that the model underpredicts NO_2. It is possible that the chemical mechanism in the model distributes NO_x incorrectly. An excess of OH in the model could convert daytime NO_2 to HNO_3 too quickly, or photolysis rates that are too high in the model could affect the photostationary state of O_3, decreasing the NO_2/NO (Leighton) ratio in

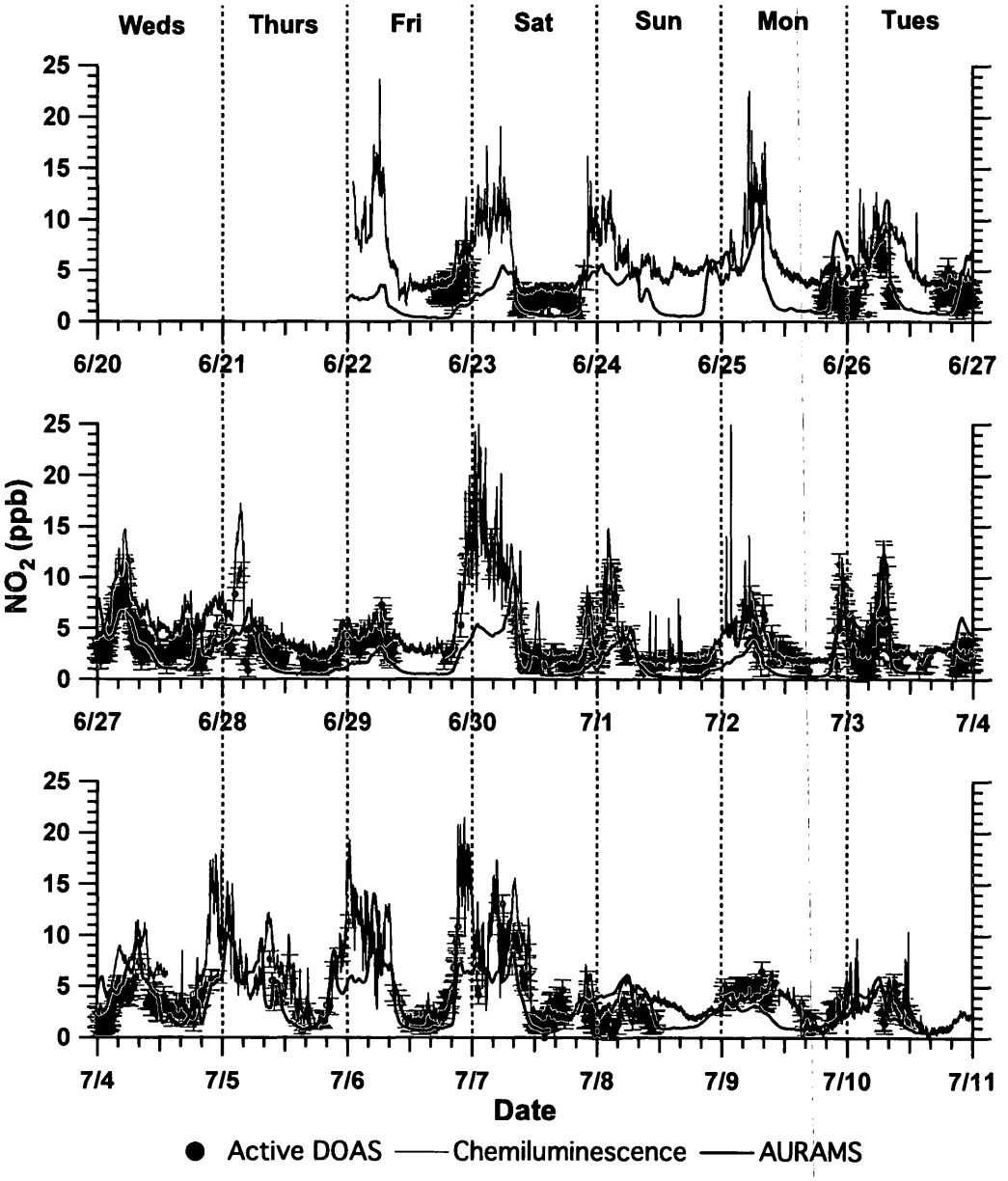

Figure 4.34: Comparison of ground level NO_2 from active DOAS, chemiluminescence and AURAMS at Ridgetown.

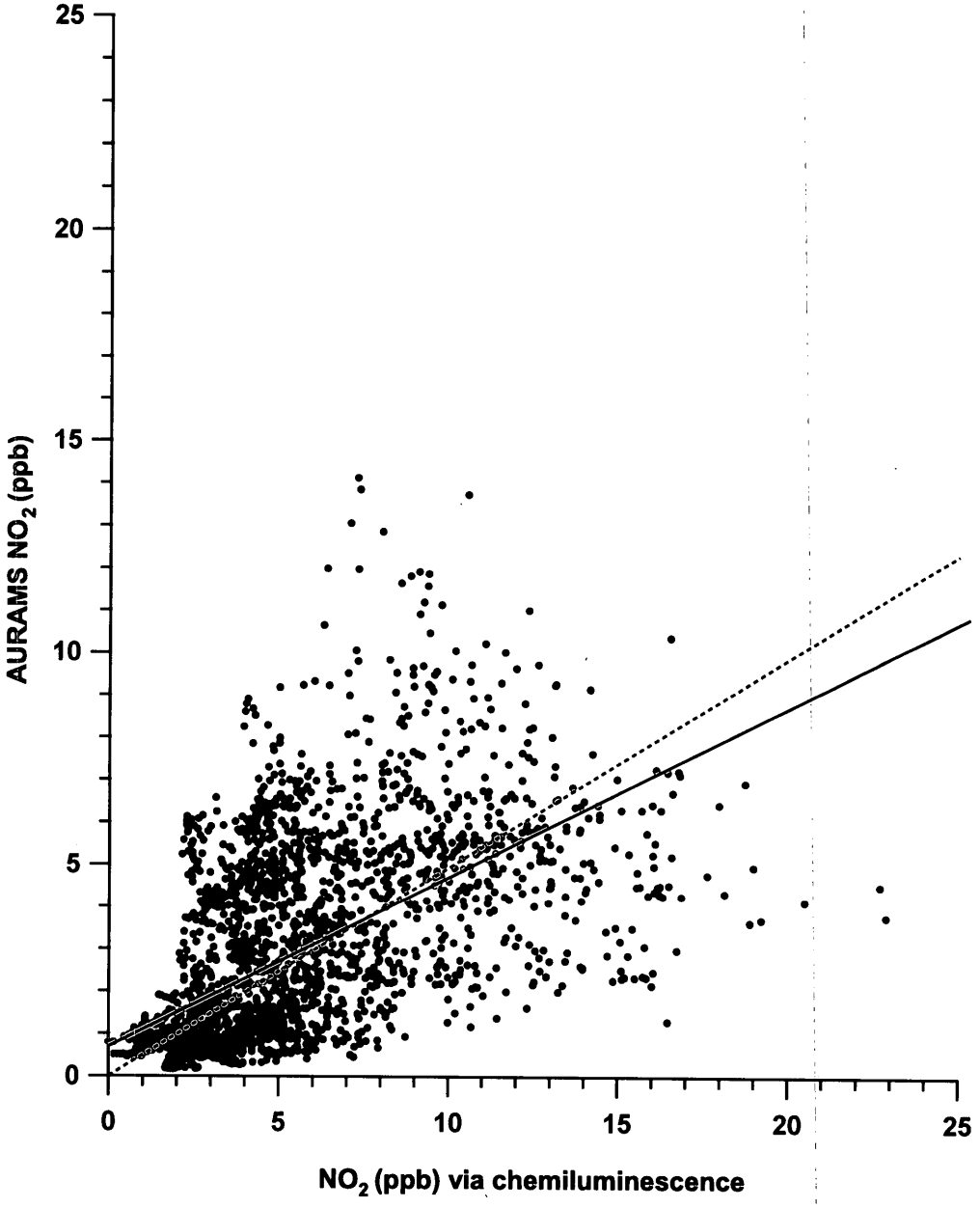

Figure 4.35: Correlation plot of AURAMS ground level NO_2 and ground level NO_2 from chemiluminescence at Ridgetown. The solid line represents the linear regression, while the dotted line represents the linear regression with a zero-forced intercept.

the model. To examine such chemical potentialities, chemiluminescence NO_x values were compared to the AURAMS NO_y output values, for an average height of 3.5 m (Figure 4.36). AURAMS NO_y in this case was defined as: [$NO_y = NO_2 + NO + HNO_3 + CH_3COOONO_2 + HONO + RNO_3 + NO_3 + 2N_2O_5 + HNO_4 + RO_2N$]. The timing of the AURAMS NO_y peaks sometimes coincide with the NO_x peaks, but not always. In most cases the AURAMS NO_y values are substantially lower than the measured NO_x, but there are also periods that agree quite nicely on June 25 and 26, July 3, 8 and 10. To examine this quantitatively, AURAMS NO_y was compared to chemiluminescence NO_x values during the same time periods for the entire campaign in Figure 4.37. This figure clearly shows that there is very little correlation between the two measures ($R^2 = 0.09$) and that NO_y is lower than NO_x, while there is a significant intercept (3.43 ppb). This offset may be due to nitrogen compounds emitted from surrounding agricultural fields close to the measurement site.

In the above comparisons AURAMS underpredicts both NO_2 VCDs and ground measures of NO_2. This underprediction is unlikely due to the partitioning of the nitrogen species studied. Likely the emissions inventories used by AURAMs are too low for NO_x or the loss of NO_2 is overestimated. Further investigations with other nitrogen species should be conducted to find the exact cause for this discrepancy.

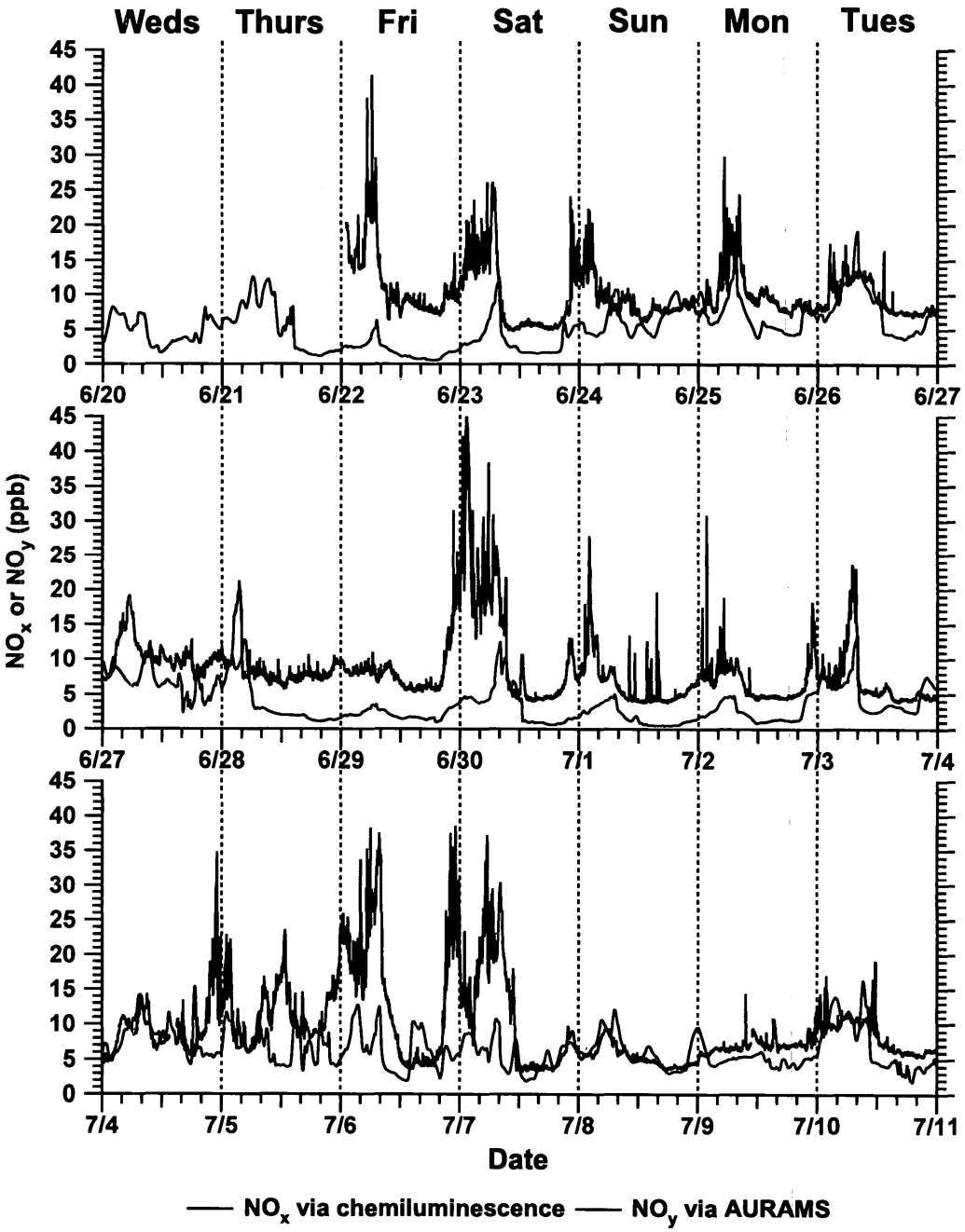

Figure 4.36: Comparison of NO_x via chemiluminescence and NO_y via AURAMS at Ridgetown.

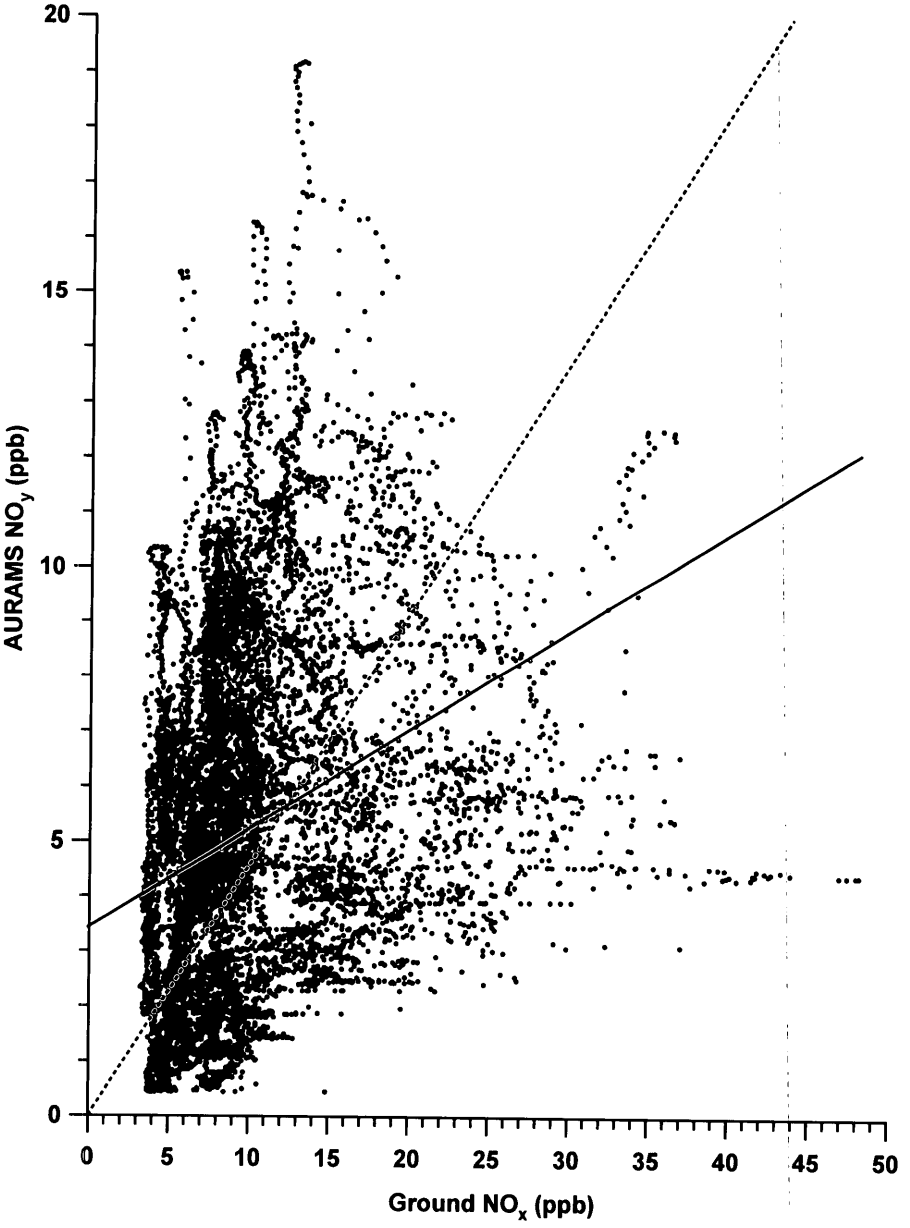

Figure 4.37: Correlation plot of AURAMS ground level NO_y and ground level NO_x from chemiluminescence at Ridgetown. The solid line represents the linear regression, while the dotted line represents the linear regression with a zero-forced intercept.

4.5.9 Comparison between Tropospheric VCDs and Ground Level NO_2

To examine the relationship between NO_2 vertical columns and NO_2 concentrations measured at ground level, average ground level NO_2 measurements were calculated for the time periods of all VCD_{RTM} determinations. In this analysis and in the case studies to follow, the NO_2 ground level values were determined from the chemiluminescence instrument due to its continuous measurement and high temporal resolution (and also due to a shortage of quality active DOAS spectra). It is well known that the "NO_2" reported for these instruments may be biased high since they may contain some contribution from NO_z species due to reduction of NO_z by the Mo convertor. However, for most of the periods of discussion to follow, we generally found good agreement between the NO_2 reported by the chemiluminescence and active DOAS instrument, apart from some early morning periods when we suspect that HONO and HNO_3 accumulated overnight may have contributed to the signal. Figure 4.38 shows three polar class scatter plots using the various NO_2 measures, where the NO_2 VCD_{RTM}, NO_2 number density (n_{NO_2}), and the ratio VCD_{RTM} / n_{NO_2} are plotted on the radial axis respectively, as a function of the average wind direction during the measurement period, and the time of day, color-coded into four binned daytime periods. The temporal behavior of the NO_2 measures within each time bin are also tabulated in Table 4.7, irrespective of wind direction.

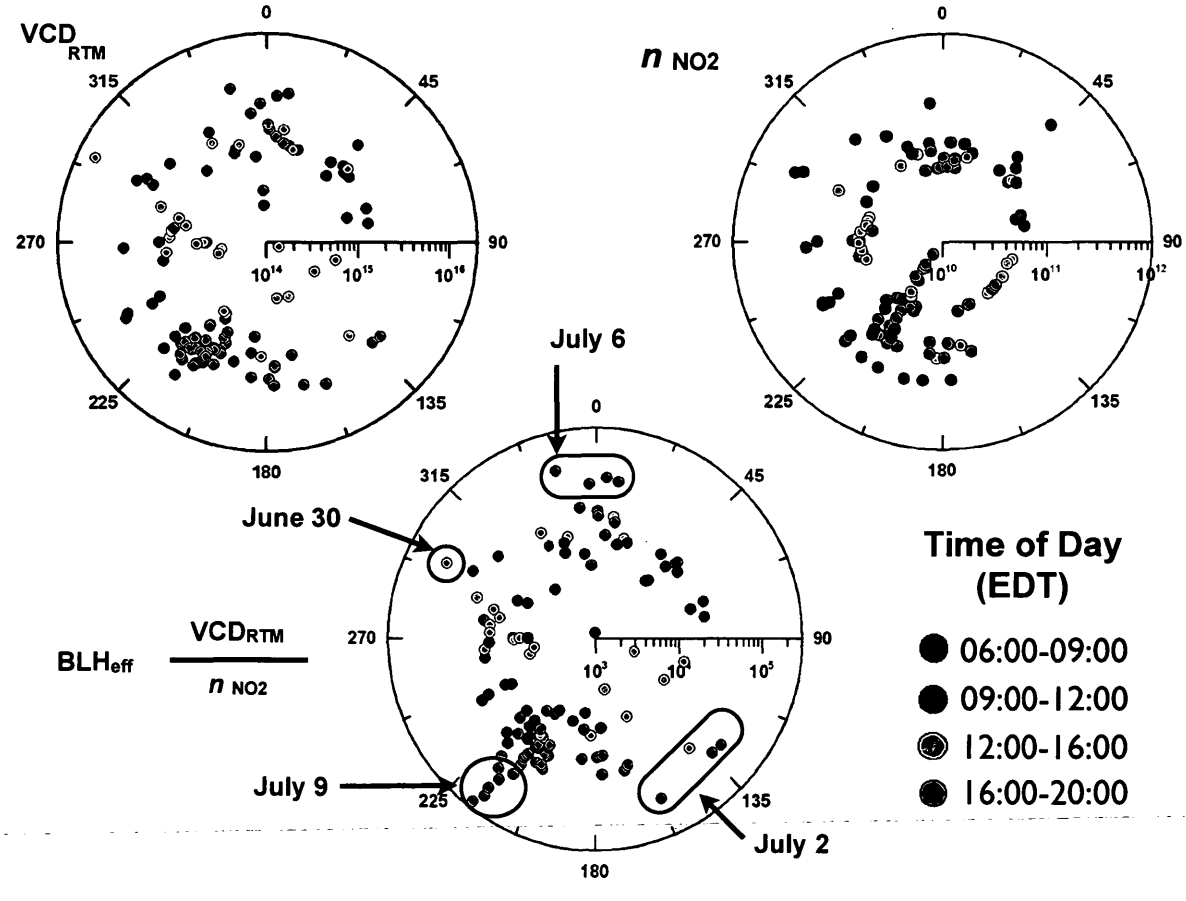

Figure 4.38: Polar class scatter plot diagrams for Ridgetown. The NO_2 VCD_{RTM} (molec cm^{-2}), the NO_2 number density (molec cm^{-3}), and the BLH_{eff} = ratio of NO_2 VCD_{RTM}/NO_2 number density (cm), are plotted on the radial axis vs. the wind direction and color-coded for the time of day of each measurement.

Four dominant factors can contribute to the daytime temporal trends in NO_2 observed at the site: *i)* temporal changes in emission rates of local NO_x sources, *ii)* changes in dilution effects of boundary layer NO_2 brought about by changes in the boundary layer height, *iii)* changes in the Leighton ratio, $[NO_2]/[NO]$, brought about by changes in the photolysis rate of NO_2, and *iv)* changes in advection patterns. The ground-based NO_2 concentrations show a clear dependence on the time of day, both in Figure 4.38 and Table 4.7. The highest concentrations are seen in the early morning decreasing by a factor of $\sim$3 by the afternoon. The decrease in NO_2 from early morning to afternoon is likely indicative of a combination of increased dilution in a growing boundary layer, as well as increased photoylsis of NO_2. The photolysis of NO_2 would give highest losses around solar noon (13:31 EDT at this site), and a corresponding minimum in the middle of the day. The lack of a significant minimum in the central bins of n_{NO_2} in Table 4.7 indicates that increased dilution in a growing boundary layer is the dominant factor that contributes to the temporal pattern seen for the NO_2 concentration. Conversely, the VCD_{RTM} shows less dependence on the time of day (Table 4.7 and Figure 4.38), compared to the NO_2 concentration, and the temporal trend contains a minimum in the middle of the day. This is to be expected, as the column density of a pollutant in the boundary layer should be independent of dilution effects resulting from changes in the boundary layer height. The minimum VCD (1.5×10^{15} molec cm^{-2})

is observed in the bin that contains solar noon (Table 4.7) when NO_2 photolysis would be at its highest rate, while the highest VCD averages (2.4 and 2.7×10^{15} molec cm^{-2}) were found in the early morning and early evening periods, when the NO_2 photolysis rate is significantly less than at solar noon. These observations indicate that the photolysis of NO_2 and consequent lowering of the NO_2/NO ratio likely play a more dominant role in the temporal behavior of the NO_2 VCD.

Table 4.7: Average VCD_{RTM}, ground NO_2, and BLH_{eff} for selected time periods at Ridgetown.

Time Period (EDT)	VCD_{RTM} ($\times10^{15}$ molec cm^{-2})	n_{NO_2} ($\times10^{10}$ molec cm^{-3})	BLH_{eff} (m)
6:00-9:00	2.4±0.8	21.4±3.2	119±45
9:00-12:00	2.1±0.7	10.6±1.7	203±77
12:00-16:00	1.5±0.5	6.4±1.0	201±77
16:00-20:00	2.7±0.9	7.1±1.0	521±198

To examine the differences between NO_2 vertical columns and NO_2 concentrations measured at ground level, the following ratio was calculated:

$$Ratio = \frac{VCD_{RTM}}{n_{NO_2}} = BLH_{eff} \tag{4.25}$$

whereby the VCD_{RTM} and n_{NO_2} for identical time ranges were compared. The

BLH_{eff} may be considered analogous to H_{gas} except that H_{gas} is calculated solely from the MAX-DOAS-RTM inversion, while BLH_{eff} is determined using both the inversion and an additional ground level measurement (in this case chemiluminescence). In general, one would expect the NO_2 vertical column density and NO_2 concentration at ground level to be correlated with one another. If NO_2 is well mixed within a homogeneous boundary layer, and the vertical column is dominated by NO_2 within the boundary layer, then this ratio will be approximately equal to the boundary layer height. However, as we have already seen (Section 4.5.5), the boundary layer is not always well mixed and free tropospheric NO_2 can also contribute to the vertical column of NO_2, creating a deviation of the ratio from the true boundary layer height. For these reasons, this ratio is named the effective boundary layer height, BLH_{eff}. A value of BLH_{eff} higher than the actual boundary layer height would be observed under the following conditions: *i)* an elevated plume of NO_2 exists above the surface site, or *ii)* the column of NO_2 in the free troposphere is a significant fraction of the total tropospheric column (e.g. likely applies under conditions when the boundary layer is relatively unpolluted). Conversely, values of BLH_{eff} lower than the actual boundary layer would be observed when surface sources of NO_2 are not well mixed in the boundary layer, which could occur under conditions of relative atmospheric stability. In addition to these deviations of BLH_{eff}, one would also expect that the temporal pattern of BLH_{eff} will generally

follow the temporal pattern of the real boundary layer height.

The values of BLH_{eff} observed during this study ranged from 12 m (observed in early morning) to 2.54 km (observed in late afternoon). In general the BLH_{eff} increased from early morning to the end of the day (Table 4.7, Figure 4.38), although the average values observed in the early afternoon (~200 m) are less that one would expect for continental boundary layer heights in midsummer in this region. This likely indicates that NO_2 is not homogeneously mixed in the boundary layer, as we directly observed by aircraft measurements on June 26 (Section 4.5.5). Instructive here is to identify cases where the VCD measured by MAX-DOAS shows something different than what is measured by the more conventional surface-based point-source measurement of NO_2. These cases would be indicated by the highest and lowest values of BLH_{eff}. The periods of low BLH_{eff} are somewhat trivial and are all isolated to early morning events, when a nocturnal inversion is still intact. During such periods, the NO_2 accumulated throughout the night from regional surface sources are trapped in the low inversion creating relatively high concentrations of NO_2 but only low or moderate tropospheric VCDs. More interesting are periods with high levels of BLH_{eff}, during which a ground-based measurement of NO_2 concentration would underestimate the total amount of NO_2 in the troposphere and transport of NO_2 into the region, with subsequent impacts on regional air quality. In Figure 4.38, four such cases are identified as a function of the wind direction

measured at ground level. The highest values of BLH_{eff} occurred on June 30, July 2, July 6, and July 9.

On June 30 (between 12:00-12:40 EDT), the highest value of VCD_{RTM} determined in the study was recorded (1.25×10^{16} molec cm^{-2}) and the BLH_{eff} rose to 998 m. During this case, an elevated plume of NO_2 impacted the site from the NW that we attribute to industrial point sources in Sarnia. This case is discussed in further detail in the next section. On July 2 (between 15:00-18:00 EDT), on an otherwise cool, clear and clean day, the VCD_{RTM} increased to 5×10^{15} molec cm^{-2} and $BLH_{eff} = 991$ m with virtually no increase in the ground level concentration of NO_2. This case is attributed to the impact of elevated forest fire plumes, originating in northern Ontario that moved southward, while the ground level at Ridgetown experienced a clean lake breeze inflow from the southeast. On July 6, the BLH_{eff} had a maximum of 1.08 km early in the evening (17:00-19:00 EDT). Winds during this time were from the N-NW and the presence of elevated SO_2 indicates that the site was impacted by a mixture of industrial emissions from Sarnia, and possibly marine vessel emissions from ships on Lake Huron heading for or exiting the St Clair River. The high boundary layer height would be typical of a lake breeze layer thermally modified after travelling 70 km inland (Sills et al., 2011). On July 9, late in the afternoon, the highest values of BLH_{eff} (up to 2.5 km) were seen. This case was characterized by strong surface winds from the SW that is characteristic

for southern Ontario, evidence for strong convection and extremely high pollution levels, a classic case of a pollution episode with long-range transport of pollutants from the SW. This case will also be discussed in more detail in the next section.

4.5.9.1 Case studies

For the case studies that follow, the residual sum of squares (RSS), as described in the Section 4.3, was used as an indicator for the quality of the fits between measured and modelled τ_{RTM} and $\mathrm{VCD}_{\mathrm{RTM}}$ values. Values of RSS <0.25 were deemed to be good fits; values with 0.25< RSS <2.5 were more uncertain. Values of RSS >2.5 were very uncertain and were removed from the data set. These thresholds were chosen based on empirical considerations to differentiate between fits with low and high uncertainty. Values with 0.25< RSS <2.5 are marked accordingly on Figures 4.39, 4.41, and 4.42. Values with RSS >0.25 are more uncertain, usually as the atmosphere was not behaving as per the assumption in the RTM (e.g. horizontal inhomogeneity). Data points with these intermediate RSS values do not necessarily represent poor results, but they indicate values that can have larger uncertainties due to limitations in the forward model, measurement errors, or temporal variations of the atmospheric properties during an elevation sequence.

June 30, 2007

Figure 4.39 summarizes various measurements made on June 30 at Ridgetown. The synoptic flow was gentle and from the northwest in the morning period. Relatively high levels of ground level NO_2 (8-12 ppb) but low levels of SO_2 were seen in the morning period 8:00-10:00 EDT. At the same time, the NO_2 VCD_{RTM} was quite low ($<1\times10^{15}$ molec cm^{-2}), and BLH_{eff} was $\leq$150 m, indicating a shallow inversion layer. Ground level NO_2 mixing ratios decreased rapidly due to the breakup of the nocturnal inversion at about 9:30 EDT and leveled off for the remainder of the morning at $\sim$2 ppb. The characteristic feature on this day was a pollution plume of $\sim$1 hour duration that impacted the site between 12:00-13:00 EDT. During this short interval, daily maxima were observed for DSCDs (α = 2°, 4°, 6°, 10°), VCD_{RTM}, τ_{RTM}, $PM_{2.5}$, SO_2, BLH_{eff} (see Figure 4.39), and O_3 (52 ppb, not shown). The maximum of the pollution plume coincided with the arrival of a lake breeze front from Lake Huron to the north. Evidence for this was an increase in the relative humidity, a slight drop in temperature, and a subtle, gradual but discernible shift in wind direction towards the north. It also coincided with arrival from the north of a thin east-west line of cumulus clouds that moved across Ridgetown between 12:00 and 13:00 EDT. The thin line of clouds provides evidence for enhanced lift along the line of this feature, typical of a lake breeze front (Sills et al., 2011). While final results from an observational analysis by Sills et al. (2011) did not specifically

identify a feature with gradients that were sharp enough to be called a lake breeze front, there is consensus that the Ridgetown site was experiencing a Lake Huron lake breeze by 14:00 EDT, and this meteorological feature with enhanced lift preceded the arrival of the lake breeze. The results from the MAX-DOAS measurements are particularly informative at this time. For example, while the DSCDs of NO_2 increased at all elevation angles, the DSCD with $\alpha = 4°$, $DSCD_4$, was marginally higher than the $DSCD_2$ (although the difference is not statistically significant). This is an observation that rarely occurs, even under high aerosol conditions when the absorption length through the lower atmosphere becomes similar at all elevation angles, making all DSCDs similar. This result can be contrasted to the result early in the morning when the nocturnal boundary layer was still intact. During that early morning period, we observed the typical situation in which $DSCD_2 > DSCD_4 > DSCD_6 > DSCD_{10} > DSCD_{30}$, commonly seen when a polluted layer exists at the surface, where larger DSCDs are observed at lower elevation angles due to the larger effective path length of scattered light through the polluted layer (Hönninger et al., 2004). In addition, it can be observed during the time just preceding the pollution plume peak that the $DSCD_2$ and $DSCD_4$ increase before the other DSCDs and well before the ground level *in situ* observations of NO_2 and SO_2 show any detectable increase. This points towards a temporal effect whereby an inhomogeneous plume moves into the complex viewing geometry of the MAX-

DOAS. Both effects strongly suggest that the polluted layer was elevated from the surface or had higher concentrations above the surface than at ground level (Hönninger et al., 2004). Other evidence that the pollution plume was elevated was the rapid increase in the value of BLH_{eff}. Despite the presence of an elevated plume, increases in SO_2, NO_2, and NO_x were still seen at ground level during this time period of the plume, which coincided with the arrival of the lake breeze. This suggests that the elevated plume was mixed partially to the surface (but not homogeneously) through a process similar to fumigation, where smokestack effluent brought inland in stable stratified marine air is mixed to the surface when it intersects the convective mixed layer at the lake breeze front (Lyons and Cole, 1973; Sills et al., 2011).

Wind Directions on June 30 were N-NW (Figure 4.39) and the pollutant plume between 12:00-13:00 EDT may be traced back to the region of Sarnia, Ontario $\approx$70 km away, using the NOAA HYSPLIT (Draxler and Rolph, 2011) back trajectory analysis (Figure 4.40). Many anthropogenic sources with elevated stack emissions are located close to the Lake Huron shoreline close to Sarnia, including petrochemical refineries, other chemical industries, and a major coal fired electric generation facility in Lambton, Ontario. The excess SO_2/NO_x ratio (mole/mole) in the pollution plume at ground level during the pollution event was calculated to be 2.21 ± 0.08 mole mole^{-1}. This can be compared to emissions from the largest

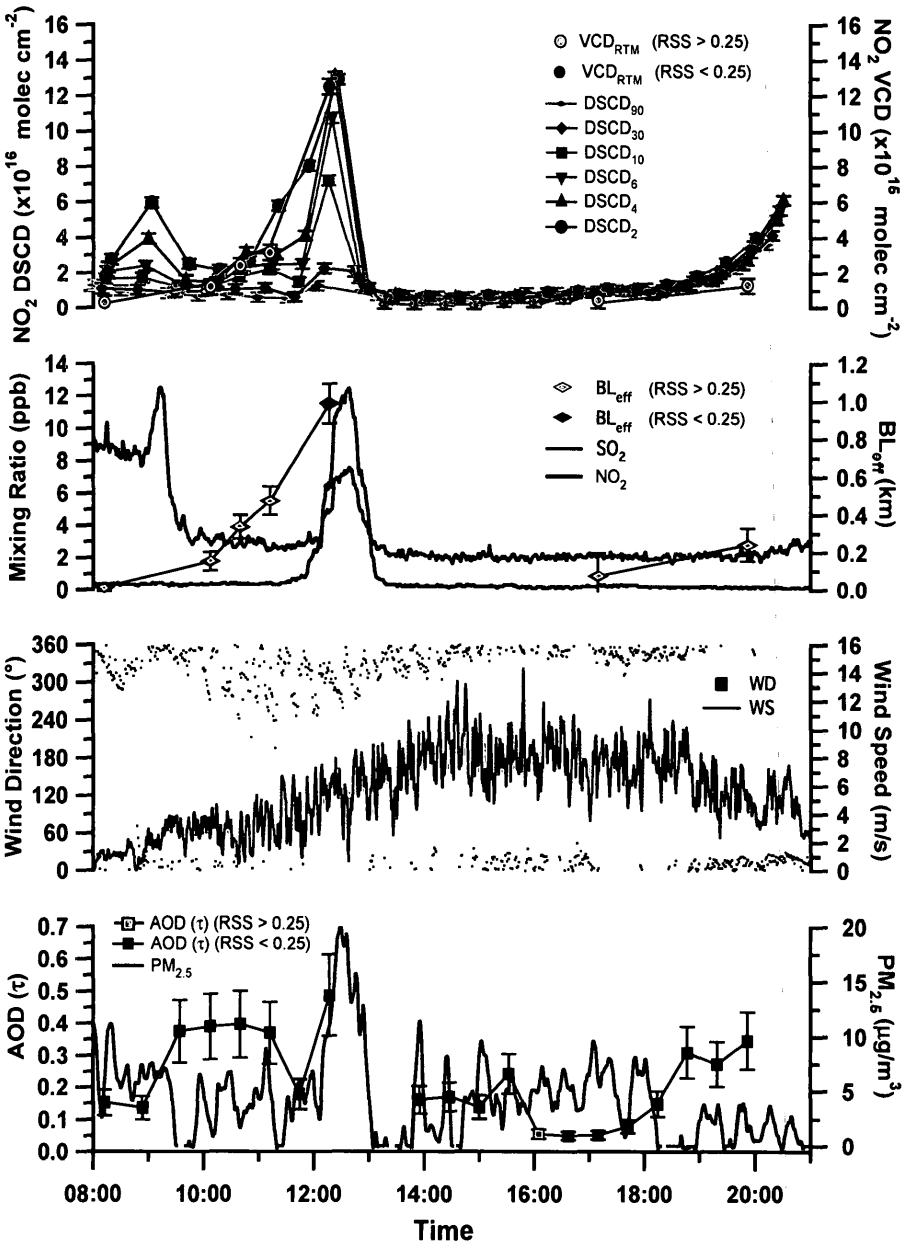

Figure 4.39: In situ and column measurements at Ridgetown on June 30, 2007. NO_2 MAX-DOAS DSCDs with NO_2 VCD_{RTM} values are followed by ground level measurements of SO_2 and NO_2, BLH_{eff}, wind direction, wind speed, $PM_{2.5}$ and AOD (τ_{RTM}).

point sources within a 5 km radius of Sarnia that contain stacks. According to the National Pollutant Release Inventory (EC, 2011), the total emissions of SO_2 and NO_x from the top 10 point sources in Sarnia are 23.9 ktonnes yr^{-1} and 5.82 ktonnes yr^{-1} respectively, with a SO_2/NO_x ratio of 2.95 mole $mole^{-1}$, dominated by refinery emissions. The corresponding emissions of SO_2 and NO_x from the stack of the Lambton coal-fired electric utility ($\approx$16 km south of the major refineries in Sarnia) are 6.19 ktonnes yr^{-1} and 3.96 ktonnes yr^{-1}, with a SO_2/NO_x ratio of 1.10 mole $mole^{-1}$. Although a single source cannot be identified by this, the evidence suggests that the plume impacting the site during this period was from either one or several elevated fuel combustion sources that fumigated to the surface as the lake breeze front passed Ridgetown. After this time, the winds at the site continued to shift towards a more northerly direction and the site experienced a clean lake breeze from Lake Huron for the rest of the afternoon, devoid of surface or elevated pollution sources of NO_2. While the evidence points to the fact that the plume arriving at the site was elevated, an explanation is still required for the large increase in the NO_2 VCD as the plume arrives and its simultaneous arrival with the lake breeze front. A lake breeze front is known to be a narrow convergence zone with enhanced lift that can transport pollutants upward (Sills et al., 2011). The front can also result in a region of spatial stagnation, with respect to the inflow layer, if the speed of the front moves slower than the inflow layer. The

dynamics of both lift, and recirculation that exist at the front (Lyons and Cole, 1973; Sills et al., 2011) can thus result in a higher concentration of pollutants at the leading edge of a lake breeze, that is still not completely understood. This result presents evidence (perhaps for the first time) that these dynamics can lead to an overall increase in not only the concentration of pollutants by late morning and throughout the afternoon but also the vertical column of pollutants at the front as well. It is believed to be the first demonstration of such an effect using MAX-DOAS.

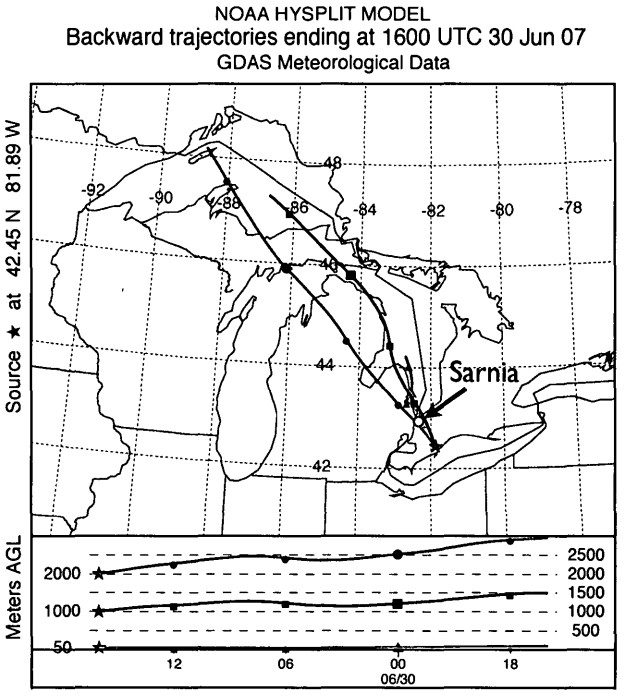

Figure 4.40: HYSPLIT back trajectory for Ridgetown (starred) on June 30, 07. Time scale in UTC (EDT = UTC-4).

July 2, 2007

Figure 4.41 summarizes various measurements made on July 2. The area was under the influence of a regional high pressure system on this day with light winds, sunshine, cool temperatures (< 21°C) and low deformation lake breeze conditions (Sills et al., 2011). Ground level pollution (SO_2, NO_2, $PM_{2.5}$, O_3) was low throughout most of the day, as was O_3 (<35 ppb, not shown). The MAX-DOAS measurements indicated a clean troposphere with VCDs $<2\times10^{15}$ molec cm^{-2} and BLH_{eff} <200 m prior to 15:00 EDT, indicating either a shallow or inhomogeneously mixed boundary layer with NO_2 confined to the surface. By late morning and throughout the afternoon the site was experiencing a moderate lake breeze from the S-SE (Lake Erie) although satellite imagery indicates that upper air movement was from the W-NW. After 15:00 EDT the NO_2 VCDs showed an appreciable increase from $\sim5\times10^{14}$molec cm^{-2} up to 5×10^{15} molec cm^{-2} while the BLH_{eff} increased from less than 100 m to greater than 1 km. A close examination showed that the ground level mixing ratio of NO_2 remained unchanged at ~2 ppb throughout this period, indicating that the increase in vertical column of NO_2 was not due to a surface source of NO_2. Unlike the elevated plume seen on June 30, in this case the DSCDs at lower elevation angles ($DSCD_2$, $DSCD_4$) did not show any appreciable increase. Further examination indicates that the increase in the VCD_{RTM} was being largely driven by increase in $DSCD_{30}$ (VCD_{30}). In a qualitative sense, this indicates that

the elevated NO_2 must be at very high elevation from the surface, much higher than seen on June 30. Indeed, elevated forest fire plumes, visible as brown streaks high in the sky, and originating from northern Canada (Saskatchewan), were reported this day in southern Ontario and were clearly visible in the sky, moving south at high altitude, likely in the upper free troposphere. An analysis of satellite imagery and fire occurrences using the Canadian Wildland Fire Information System (CWFIS, 2011) for several days prior and following this date indicated the most likely source to be an intense line of boreal forest fires that had started on or about June 28 close to the Saskatchewan/Northwest Territories border approximately 2500 km northwest of the site. Although the aerosol optical depth was higher in the morning ($\tau_{\mathrm{RTM}} = 0.4$), likely due to anthropogenic aerosol pollution from urban areas to the northeast, the τ_{RTM} also increased marginally ($\Delta\ \tau_{\mathrm{RTM}} = +0.2$) during the biomass burning plume event while $PM_{2.5}$ remained unchanged. This indicated that only a small amount of aerosol was associated with the plume, perhaps due to sedimentation during the approximately two day transport time. Despite this, particle-based receptor modelling of aerosol time of flight mass spectrometry data identified the beginning of an event of aged biomass burning particles at Harrow, ON, late in the day or early morning on July 2/3 (McGuire et al., 2011). It is acknowledged that the determination of τ using the method outlined here is highly uncertain in a case such as this and would likely benefit from a two level retrieval

system as there are likely two distinct layers of NO_2 and aerosols. As O_4 has a scale height of ~4 km in the atmosphere, the use of changes in the O_4 absorption to predict the presence of aerosols will be much less sensitive with aerosol layers in the upper troposphere. Therefore, the value of τ_{RTM} will likely underestimate the true tropospheric aerosol optical depth in such cases. This could be the situation for the current case study. The VCD_{RTM} could also be uncertain due to multiple scattering events in a mixed aerosol-NO_2 plume in the upper troposphere. However, it is unlikely to be as sensitive as the aerosol optical depth and the prediction of the direction of bias in NO_2 VCD is uncertain without further two level radiative transfer modelling. Despite this, this case illustrates a situation where transport of pollution through the region at high altitude was detected by MAX-DOAS, which would be virtually undetectable at ground level using standard air quality instrumentation.

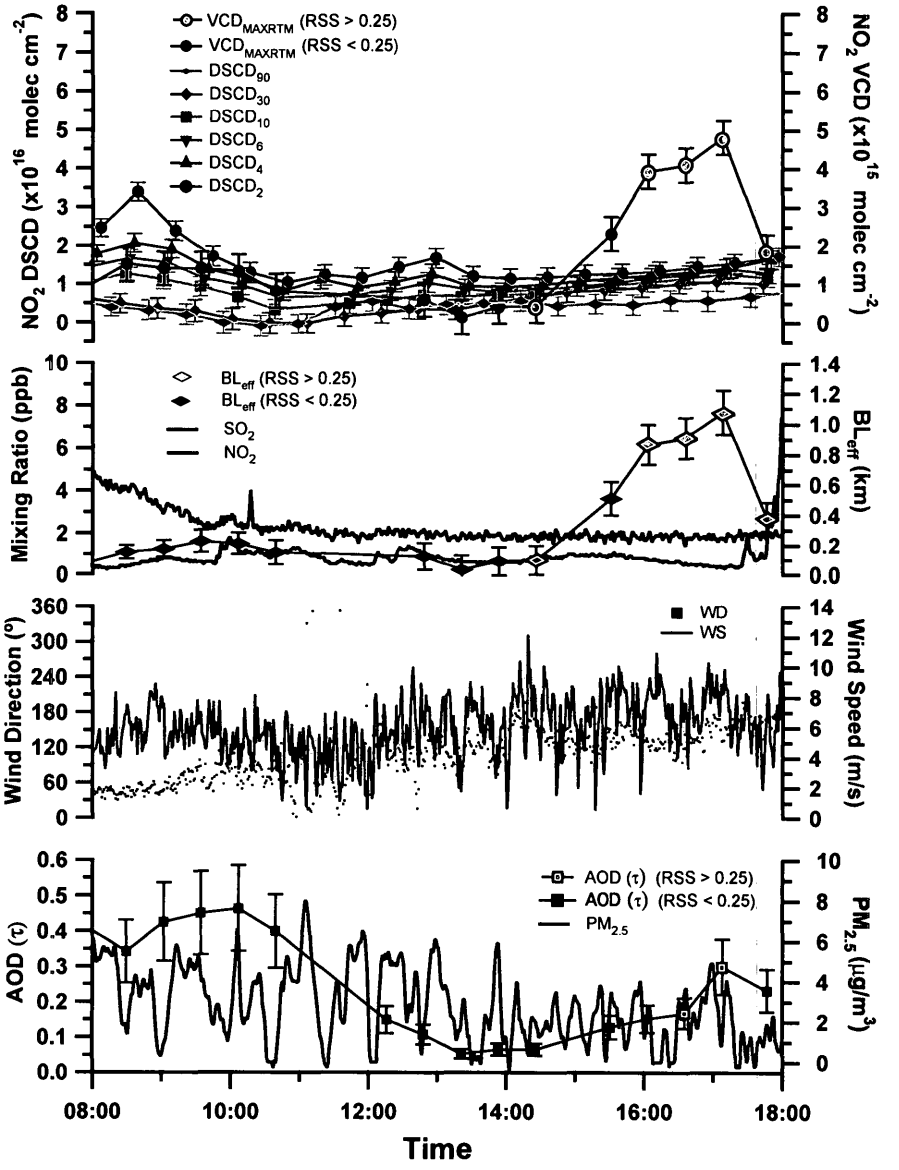

Figure 4.41: In-situ and column measurements at Ridgetown on July 2, 2007. NO_2 MAX-DOAS DSCDs with NO_2 VCD_{RTM} values are followed by ground level measurements of SO_2 and NO_2, BLH_{eff}, wind direction, wind speed, $PM_{2.5}$ and AOD (τ_{RTM}).

July 9, 2007

Figure 4.42 summarizes various measurements made on July 9. This day was characterized by warm temperatures (33°C maximum), hazy conditions with strong W-SW synoptic flow, high deformation lake breezes circulations, and enhanced turbulence (Sills et al., 2011). High pressure existed southeast of the Great Lakes, a typical situation for the transport of ozone and aerosol precursors into southern Ontario from the SW (MOE, 2011). Indeed, aerosols were abundant with $PM_{2.5}$ levels in the range of 10-50 μg m^{-3} and τ_{RTM} $\sim$1.0$\pm$0.2 in late afternoon, apart from a single value of 2.8 at 17:00 EDT. Ozone (not shown) also recorded a maximum of 87 ppb a few minutes prior to the passage of a lake breeze front. Due to the cumulus clouds in the vicinity for much of the day, VCD_{RTM} could not be determined until after 17:00 EDT. Winds that were from the W-SW (260°) at 9 m s^{-1} switched to S-SW (215°) at 13 m s^{-1} with gusts up to 17 m s^{-1} at 15:10 EDT, indicating the passage of the lake breeze front (Lake Erie) and accompanied with an increase in relative humidity, spikes in $PM_{2.5}$, O_3 and CO (not shown), and a drop in NO_2. Between 17:00 and 19:15 EDT conditions were hazy but cloud-free such that MAX-DOAS-RTM inversions that yielded VCD_{RTM} values were determinable. The NO_2 was relatively low, between 0.5 and 1.5 ppb, while VCDs ranged from 2-4$\times$10^{15} molec cm^{-2}, and BLH_{eff} increased from 800 m to 2600 m at 17:10 EDT. The DSCDs do not give any indication of an elevated plume and a measure of the

true boundary layer height was not available at Ridgetown on this day. However, the potential temperature profile measured by sonde release at White Lake, Michigan, just west of Detroit (Station DTX, #72632), indicated a subsidence inversion at 1.90 km at 20:00 EDT that was comparable to the average BLH_{eff} measured between 18:20 and 19:20 EDT (1.93 km). Thus, on this particular day, when strong wind speeds and strong convection would support a well mixed boundary layer, the value of BLH_{eff} was comparable to the true boundary layer height measured in a continental region close to the site. This provides an opportunity to further validate our VCD_{RTM} determinations during this time period. Between 18:00 and 19:00 the average VCD_{RTM} was $3.4\pm0.5\times10^{15}$ molec cm^{-2}. The tropospheric NO_2 VCD estimated from the average NO_2 mixing ratio (0.8 ppb) in a homogeneous boundary layer of 1.9 km was 3.8×10^{15} molec cm^{-2}. These numbers agree reasonably well. This case, where the boundary layer is relatively homogeneous and well mixed, is one of the few situations during the study where one would expect this to be true. In such a case, the mixing ratio of NO_2 measured at ground level is quite low and may not indicate the total amount of NO_2 being transported into the region in the deep boundary layer. To estimate the total transport of tropospheric NO_2 across a boundary tangential to the wind direction during this pollution event, the flux of tropospheric NO_2 perpendicular to the wind direction, F_{NO_2} (molec s^{-1}), could be

calculated according to the following equation:

$$F_{NO_2} = VCD_{NO_2} \times L \times u_{trop} \tag{4.26}$$

where L is the length of a border and u_{trop} is the average flow rate of the troposphere. Using the wind speed at 10 m height (12 m s^{-1} in late afternoon) as a lower limit of the flow rate in the lower troposphere, and the average VCD_{RTM} in the later afternoon period (3.4×10^{15} molec cm^{-2}), we conservatively estimate the line flux ($F_{NO_2}/\ L$) of NO_2 through the region to be greater than 4.1×10^{18} molec cm^{-1} s^{-1}, or 112 kg NO_2 km^{-1} hr^{-1}, during the pollution event. This may be a useful parameter to compare with model estimates of transport fluxes where they exist.

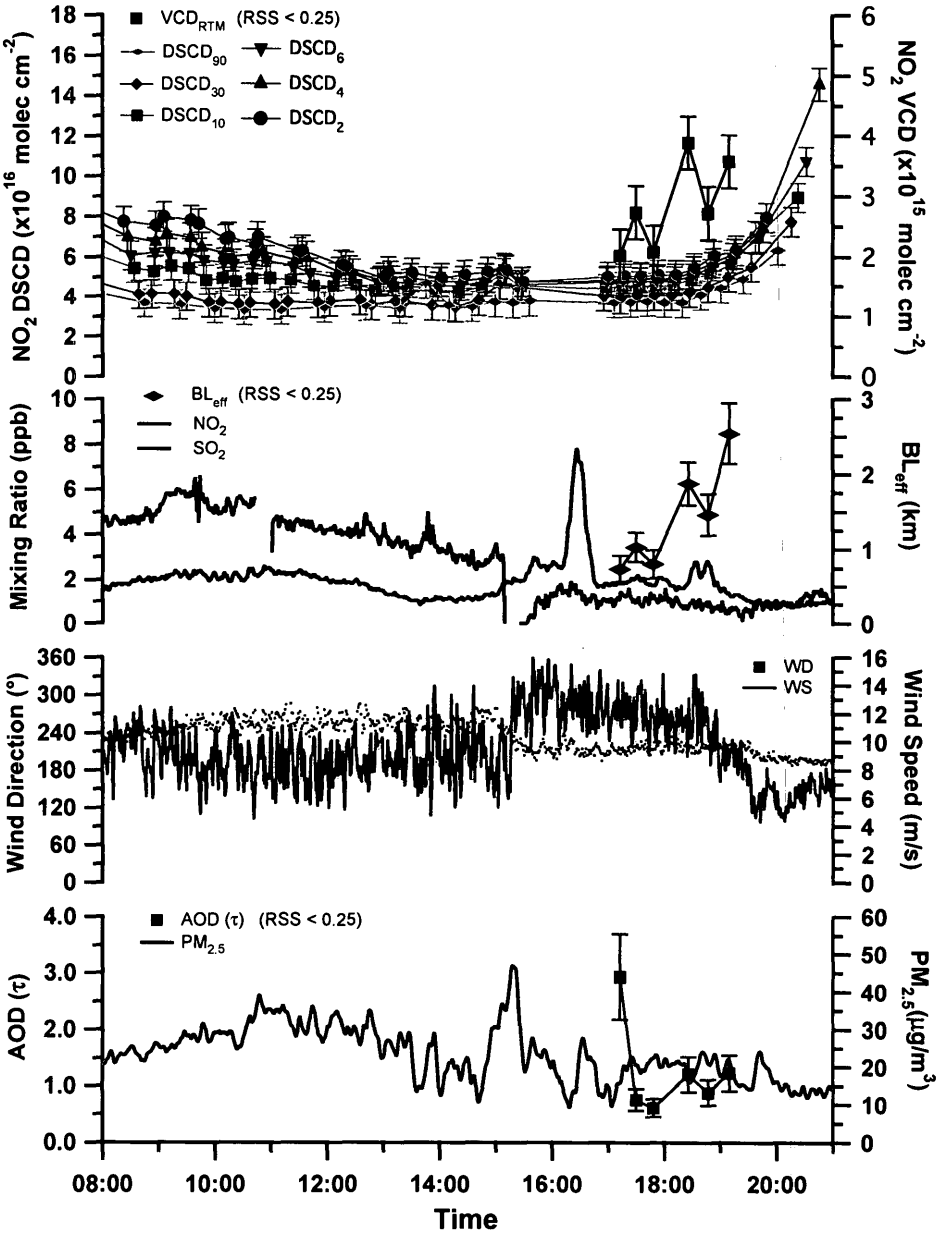

Figure 4.42: In-situ and column measurements at Ridgetown on July 9, 2007. NO_2 MAX-DOAS DSCDs with NO_2 VCD_{RTM} values are followed by ground level measurements of SO_2 and NO_2, BLH_{eff}, wind direction, wind speed, $PM_{2.5}$, and AOD (τ_{RTM}).

4.6 Conclusions

MAX-DOAS measurements were made at a rural site in southwestern Ontario during the BAQS-Met study. Using these measurements, a method for the determination of aerosol optical depths and vertical column densities of NO_2 using a combination of DOAS fitting of the MAX-DOAS spectra for NO_2 and O_4, radiative transfer modelling, and inversion modelling was outlined. The aerosol optical depths (λ = 360 nm) determined with this method were compared to other measures of aerosol optical depth regionally available (OMI, MODIS, AERONET) with some qualitative agreement, although differences in the wavelengths used and spatial locations prevented a more direct comparison of these measures. A direct comparison between τ_{RTM} and $PM_{2.5}$ measured at the site gave a very low level of correlation while a direct comparison between the calculated aerosol extinction coefficient ($E = \tau_{\mathrm{RTM}} \ / \ H_{aer}$) and $PM_{2.5}$ gave a much higher correlation and a mass specific extinction coefficient of 16$\pm$1 $m^2\ g^{-1}$. While this value is quite high (most likely because the boundary layer heights predicted by H_{aer} are too low), it emphasizes the importance of taking into account boundary layer heights in any attempt to link aerosol optical depths determined by satellite, for example, with human exposure of aerosols at ground level.

The tropospheric vertical column densities of NO_2 derived this way, VCD_{RTM},

were compared to tropospheric vertical column densities, compiled through a composite of measurements of NO_2 at ground level and vertical measurements of NO_2 via aircraft close to the site, VCD_{COMP}. On average, VCD_{RTM} was 15% higher than VCD_{COMP} but the difference was not statistically significant (95% confidence level), which we take as a validation for the method outlined here for determining NO_2 VCDs. Intercomparison of satellite instrument derived measures of NO_2 VCD with a limited number of comparison points from OMI (N=8) and SCIAMACHY (N=1) indicate that the satellite derived measures were overall ~50% higher than VCD_{RTM}, with a mean bias of between 0.9×10^{15} molec cm^{-2} for OMI (statistically significant) and 0.5×10^{15} molec cm^{-2} for SCIAMACHY (not statistically significant). It should be taken in context that the apparently large relative overprediction by the satellites retrievals (+50%) could easily be due to a small constant bias coupled with the overall relatively small tropospheric NO_2 VCDs that were experienced in this rural region. The relevance of the result to more polluted regions with higher VCDs should be verified.

Previous literature has reported the opposite, namely that satellite-derived measures of VCD are on average smaller than VCDs found via MAX-DOAS. The root cause for these differences probably is the different nature of the measurement sites; rural in this study compared to more urban in previous reports, with overall NO_2 VCDs that were much lower in this study compared to previous reports. Typically,

VCDs derived from MAX-DOAS in previous comparisons with satellite measures of NO_2 have used a geometrical approximation to estimate the AMF and VCD, similar to the VCD_{GEO} values reported here. These VCD_{GEO} values were marginally lower than the VCD_{RTM} values but only for a small subset of comparisons with a stringent criteria, namely that the VCDs determined using a geometric approximation with elevation angles of 10° and 30° agreed to within 15%. The methodology outlined here to determine VCD_{RTM} was not as stringent and has allowed for the determination of VCDs over a much wider range of aerosol conditions than would have otherwise been possible using the geometric approximation alone.

The NO_2 VCD_{RTM} values were also compared to vertical column densities determined with the AURAMS model (VCD_{AUR}). The VCDs from AURAMS were substantially lower: ~31% when the intercept of the graph of VCD_{AUR}/VCD_{RTM} was zero-forced; ~47% when the intercept was not forced. AURAMS also underpredicted ground level NO_2 versus chemiluminescence measurements by ~60%. This underprediction was not believed to be due to NO_y, but rather the possibility that the chemical mechanism in the model does not distribute NO_x properly (e.g. the loss of NO_2 may be overestimated) or perhaps it uses emission data that is too low.

The ratio of the tropospheric VCD and ground level concentration of NO_2 was defined as the effective boundary layer height, BLH_{eff}. The diurnal pattern of BLH_{eff} generally followed the expected pattern for the boundary layer height during the

day; although we found values of BLH_{eff} were generally lower than expected for continental boundary layer heights in late afternoon, likely due to surface sources in a boundary layer that was not well mixed. Exceptions to this were illustrated in three case studies. In two cases, high values of BLH_{eff} were due to elevated plumes of NO_2, one from elevated stack emissions from industry and one from biomass burning plumes that were transported through the region. In the third case, the BLH_{eff} was very high ($\sim$2 km) and similar to the measured continental boundary layer height just west of the study region, likely as a result of instability in the atmosphere that promoted convection and efficient mixing throughout the boundary layer. The variations of BLH_{eff} with time of day and conditions should be considered in attempts to determine ground level concentrations of NO_2 from satellite derived measures or in attempts to validate satellite measurements through use of ground-based measurements.

The case studies examined here also provide some interesting examples of transport of pollutants in this region and the interaction with lake breezes that exist due to the presence of the three surrounding lakes. In the first case study, a convincing example of fumigation of elevated industrial pollutants brought to the surface at a lake breeze front, and an increase in the total NO_2 VCD at the lake breeze front, was presented. The last case study occurred during a regional smog event with transport of ozone and aerosol precursors from the southwest. Although ground

level concentrations of NO_2 were quite low during this event (<1.5 ppb), the column amount of NO_2 was more substantial than otherwise suspected due to a deep and well mixed boundary layer. The line flux of NO_2 during the latter part of the day during this event was estimated to be greater than 112 kg NO_2 km^{-1} hr^{-1}. Multiplication of the line flux by the width of a boundary line perpendicular to the prevailing wind direction would give the total mass transport of tropospheric NO_2 across the boundary line during the regional pollution event.

5 Conclusions and Future Work

5.1 Overall Conclusions

A MAX-DOAS instrument was successfully deployed during two extensive Canadian field campaigns: one from Saturna Island, BC; the other from Ridgetown, ON. Spectra were collected and DSCDs of NO_2, O_4 and HCHO were determined using the conventional DOAS analysis procedure. Using the multi-axis feature of this technique, these trace gas absorbers were probed along multiple paths, depending on the elevation angles chosen.

When the measured DSCDs from Ridgetown were compared with DAMFs calculated using a Monte Carlo RTM (McArtim), the average light paths travelled were determined, allowing MAX-DOAS spectra to yield NO_2 VCDs, aerosol optical depths, and NO_2 and aerosol layer heights. Determination of DSCDs and VCDs have advantages over point-source measurements in that they are more sensitive to the total atmospheric load of a pollutant and are relatively insensitive to variations in the boundary layer height. The method of determining NO_2 VCDs in this way was validated for the first time by comparison to composite VCDs derived from

aircraft and ground-based measurements of NO_2, satellites, and a chemical model (AURAMS). The usefulness of the MAX-DOAS technique was extended further, using both DSCDs and VCDs, to include the interpretation of pollutant transport at Saturna and Ridgetown, and to provide an example of fumigation of elevated industrial pollutants brought to the surface at a lake breeze front at Ridgetown.

5.2 Instrumental Improvements

Some important improvements were made to the original MAX-DOAS instrument used for the Saturna Island field study. The Ocean Optics USB 2000 spectrometer with a 25 μm slit was replaced with a USB 2000$^+$ spectrometer that had an increased entrance slit width of 50 μm. The grating was changed from #10 to #7 in order to optimize the light collection in the spectral fitting window of NO_2. The original Ocean Optics fiber optic (λ = 400 nm) was replaced with a larger fiber optic (λ = 1000 nm) and a more precise temperature control unit replaced the fridge as the method of keeping the spectrometer temperature stable. These upgrades resulted in better signal to noise and stability, allowing a greater number of measurements to be made during the BAQS-Met campaign for a similar time frame (~3 weeks). Furthermore, by using a consistent set of EAs that included a high angle measurement (α = 30°) in each series, the data set was now well suited for

use in determining VCDs when comparing measured DSCDs to DAMFs calculated via radiative transfer modelling.

Yet, there are still some recommended upgrades and recommendations for future MAX-DOAS experiments. First, the original device is not extremely portable and the stepper motor that moves the telescope does not move very quickly (e.g. it takes ~6 minutes to move 90°); the telescope is not able to point in different headings unless moved manually; and the end of the 1000 μm fiber optic has a circular slit fitting into the rectangular 50 μm slit of the USB 2000$^+$ spectrometer, resulting in large light collection losses.

To solve the above-mentioned problems, the current device will be replaced with a mini-MAX-DOAS designed by Hoffmann Messtechnik. This mini-MAX-DOAS is more portable, has excellent temperature control, and has a custom fiber optic that ends in a slit formation that matches the entrance to the USB 2000$^+$. With its small size the instrument is able to rotate between EAs at great speeds and has been designed to integrate completely with DOASIS so that temperature control, EA movement, the measurements of dark current and offset, and even spectral fitting maybe performed automatically using customized j-script routines.

Future field studies will take advantages of these new improvements. Perhaps with further development of DOASIS j-scripts, "quick fits" may be performed for individual trace gas species automatically. This could allow for greater optimization

of the fit parameters such as wavelength range and polynomial order. A visualization scheme could also be used to refine these parameters more effectively, as done recently for BrO by Vogel et al. (2013). Another feasible improvement would be the addition of horizontal stepper motors that would allow the MAX-DOAS telescope to automatically move to different pre-selected headings to examine spatial pollutant differences. A video monitor could be placed either on or nearby to the mini-MAX-DOAS device to record the "real time" cloud and aerosol conditions, in the appropriate viewing directions. These instrumental improvements could result in a more flexible instrument with better detection limits, making the DOAS fits for NO_2, O_4, and in particular HCHO, more accurate. Perhaps it would also allow for the future detection of other trace gas species, such as BrO, IO and CHOCHO.

Lastly, with the remaining "MAX-DOAS" telescope, additional retro-reflectors and an appropriate LED, a new active DOAS instrument could be constructed that would be more mobile than the current instrument. If the correct LED and spectrometer are chosen for this device, long path lengths may be probed allowing for excellent detection limits, as done by Tschritter (2007). Alternatively, the remaining telescope could be mounted with a moon tracker and be used for lunar DOAS measurements.

5.3 Future Work

Radiative transfer modelling under cloudy conditions represents a significant challenge to the MAX-DOAS inversion technique used to determine VCDs. In this dissertation, spectra under cloudy conditions were discarded. For the BAQS-Met field study this led to a significant loss of information and may have biased the data set somewhat. Future work could be directed into developing an algorithm that would allow the analysis of MAX-DOAS data under both clear and cloudy conditions. As shown in Chapter 4, O_4 DSCDs and radiance measurements may be used to classify these conditions. However, there are several other techniques used to measure cloud properties. These include LIDAR, a ceilometer, a sunphotometer, a hyper-spectral camera, or even a specialized RADAR that could be used to measure the vertical distribution of clouds. With the help of these devices and video images, perhaps an automated procedure could be created to group conditions according to cloud cover and then process the spectra accordingly.

The radiative transfer model employed in this dissertation (McArtim) does not currently have the capability of determining AMFs under cloudy conditions, however it could be modified to analyze cloudy spectra. Alternatively, other more "cloud-friendly" RTMs could be employed to calculate the necessary AMFs. Regardless of the RTM used, there is still some debate as to which approach is best

when performing inversions between measurements and modelled data. The method used in this thesis used three parameters to model both aerosol and gas profiles, but was further limited to two parameter "box profiles" due to instabilities in the inversion when all three parameters were allowed to free-float. The calculated VCDs were shown to be relatively insensitive to the aerosol and gas profile shapes but, if a chemical model (e.g. GEOS-Chem) was used to determine more accurate profiles, better results may be achievable. Other groups use optimal estimation and incorporate *a priori* assumptions for aerosol and trace gas profiles into their inversion retrievals. This may lead to more accurate gas profile retrievals, especially if additional aerosol information (found via alternative measurements such as from a sky radiometer) is incorporated into the retrieval. Future work could compare both inversion approaches and these results could be compared to true profiles found from LIDAR, radiosondes, balloons, and aircraft measurements with flight patterns dedicated solely to VCD validation, to determine which inversion approach is more favourable. In particular, the aerosol and trace gas layer heights could be compared to LIDAR and NO_2 balloon measurements. When these measures are in good agreement the ground level NO_2 mixing ratios calculated from the MAX-DOAS-RTM inversion procedure would also likely be in agreement with the NO_2 concentrations determined from other point-source techniques. This could perhaps provide insight into developing a standard technique to be used by the

satellite DOAS community for effectively calculating ground level NO_2 world-wide, which is of great importance today for its health implications.

Both the Saturna and Ridgetown locations are rural areas. Although done in the past by other groups, an examination of more urban locations, including Toronto, would prove useful for satellite validation purposes and the examination of more novel species including BrO and CHOCHO could also be done. A long term MAX-DOAS study could be implemented from York University in order to collect an extensive data set (e.g. seasonally, yearly) that could be used to compare with active DOAS and satellite DOAS measurements under both cloudy and clear conditions. Assuming higher levels of pollutants in the city and better detection limits using the new mini-MAX-DOAS, BrO may potentially be found in the wintertime due to roadsalt on the roadways. Finally, Saturna Island could be revisited with the intention of probing the WISE once more and using a MAX-DOAS-RTM inversion to determine true NO_2 and HCHO VCDs and examine their effects on ozone formation in the LFV.

References

Ahmed, S. and Kumar, V.: Measurement of photoabsorption and fluorescence cross-sections for CS_2 at 188.2-213 and 287.5-339.5 nm, *Pramana*, 39, 367–380, 1992.

Alicke, B., Hebestreit, K., Stutz, J., and Platt, U.: Iodine oxide in the marine boundary layer, *Nature*, 397, 572–573, 1999.

Alicke, B., Platt, U., and Stutz, J.: Impact of nitrous acid photolysis on the total hydroxyl radical budget during the Limitation of Oxidant Production/Pianura Padana Produzione di Ozono study in Milan, *Journal of Geophysical Research-Atmospheres*, 107, LOP 9–1–LOP 9–17, 2002.

Alicke, B., Geyer, A., Hofzumahaus, A., Holland, F., Konrad, S., Pätz, H. W., Schafer, J., Stutz, J., Volz-Thomas, A., and Platt, U.: OH formation by HONO photolysis during the BERLIOZ experiment, *Journal of Geophysical Research-Atmospheres*, 108, PHO 3–1–PHO 3–17, 2003.

Allan, B. J., McFiggans, G., Plane, J. M. C., Coe, H., and McFadyen, G. G.: The nitrate radical in the remote marine boundary layer, *Journal of Geophysical Research*, 105, 24 191–24 204, 2000.

Beirle, S., Kühl, S., Puķīte, J., and Wagner, T.: Retrieval of tropospheric column densities of NO_2 from combined SCIAMACHY nadir/limb measurements, *Atmospheric Measurement Techniques*, 3, 283–299, 2010.

Blacet, F. E.: Photochemistry in the Lower Atmosphere, *Industrial & Engineering Chemistry*, 44, 1339–1342, 1952.

Blond, N., Boersma, K. F., Eskes, H. J., van der A, R. J., van Roozendael, M., Smedt, I. D., Bergametti, G., and Vautard, R.: Intercomparison of SCIAMACHY nitrogen dioxide observations, in situ measurements and air quality modeling results over Western Europe, *Journal of Geophysical Research-Atmospheres*, 112, D10 311, 2007.

Boersma, K. F., Bucsela, E. J., Brinksma, E. J., and Gleason, J. F.: NO_2, OMI-EOS Algorithm, *Theoretical Basis Document: Trace Gas Algorithms: NO_2*, pp. 12–35, 2001.

Bogumil, K., Orphal, J., Homann, T., Voigt, S., Spietz, P., Fleischmann, O. C., Vogel, A., Hartmann, M., Kromminga, H., Bovensmann, H., Frerick, J., and Burrows, J. P.: Measurements of molecular absorption spectra with the SCIAMACHY pre-flight model: instrument characterization and reference data for atmospheric remote-sensing in the 230-2380 nm region, *Journal of Photochemistry and Photobiology A-Chemistry*, 157, 167–184, 2003.

Bovensmann, H., Burrows, J. P., Buchwitz, M., Frerick, J., Noel, S., Rozanov, V. V., Chance, K. V., and Goede, A. P. H.: SCIAMACHY: Mission objectives and measurement modes, *Journal of the Atmospheric Sciences*, 56, 127–150, 1999.

Brauer, M. and Brook, J. R.: Ozone personal exposures and health effects for selected groups residing in the Fraser Valley, *Atmospheric Environment*, 31, 2113 – 2121, 1997.

Brinksma, E. J., Pinardi, G., Volten, H., Braak, R., Richter, A., Schönhardt, A., van Roozendael, M., Fayt, C., Hermans, C., Dirksen, R. J., Vlemmix, T., Berkhout, A. J. C., Swart, D. P. J., Oetjen, H., Wittrock, F., Wagner, T., Ibrahim, O. W., de Leeuw, G., Moerman, M., Curier, R. L., Celarier, E. A., Cede, A., Knap, W. H., Veefkind, J. P., Eskes, H. J., Allaart, M., Rothe, R., Piters, A. J. M., and Levelt, P. F.: The 2005 and 2006 DANDELIONS NO_2 and aerosol intercomparison campaigns, *Journal of Geophysical Research-Atmospheres*, 113, D16S46, 2008.

Brook, J. R., Strawbridge, K. B., Snyder, B. J., Boudries, H., Worsnop, D., Sharma, S., Anlauf, K., Lu, G., and Hayden, K.: Towards an understanding of the fine particle variations in the LFV: integration of chemical, physical and meteorological observations, *Atmospheric Environment*, 38, 5775–5788, 2004.

Bucsela, E., Celarier, E., Wenig, M., Gleason, J., Veefkind, J., Boersma, K. F., and Brinksma, E.: Algorithm for NO_2 vertical column retrieval from the Ozone Monitoring Instrument, *IEEE Transactions on Geoscience and Remote Sensing*, 44, 1245–1258, 2006.

Burrows, J. P., Richter, A., Dehn, A., Deters, B., Himmelmann, S., and Orphal, J.: Atmospheric remote-sensing reference data from GOME 2. Temperature-dependent absorption cross sections of O_3 in the 231-794 nm range, *Journal of Quantitative Spectroscopy & Radiative Transfer*, 61, 509–517, 1999.

Celarier, E. A., Brinksma, E. J., Gleason, J. F., Veefkind, J. P., Cede, A., Herman, J. R., Ionov, D., Goutail, F., Pommereau, J. P., Lambert, J. C., van Roozendael, M., Pinardi, G., Wittrock, F., Schönhardt, A., Richter, A., Ibrahim, O. W., Wagner, T., Bojkov, B., Mount, G., Spinei, E., Chen, C. M., Pongetti, T. J., Sander, S. P., Bucsela, E. J., Wenig, M. O., Swart, D. P. J., Volten, H., Kroon, M., and Levelt, P. F.: Validation of Ozone Monitoring Instrument nitrogen dioxide columns, *Journal of Geophysical Research-Atmospheres*, 113, D15S15, 2008.

Chance, K. V. and Spurr, R. J. D.: Ring effect studies: Rayleigh scattering, including molecular parameters for rotational Raman scattering, and the Fraunhofer spectrum, *Applied Optics*, 36, 5224–5230, 1997.

Chen, D., Zhou, B., Beirle, S., Chen, L. M., and Wagner, T.: Tropospheric NO_2 column densities deduced from zenith-sky DOAS measurements in Shanghai, China, and their application to satellite validation, *Atmospheric Chemistry and Physics*, 9, 3641–3662, 2009.

Chu, D. A., Kaufman, Y. J., Zibordi, G., Chern, J. D., Mao, J., Li, C. C., and Holben, B. N.: Global monitoring of air pollution over land from the Earth Observing System-Terra Moderate Resolution Imaging Spectroradiometer (MODIS), *Journal of Geophysical Research-Atmospheres*, 108, 4661, 2003.

Clémer, K., van Roozendael, M., Fayt, C., Hendrick, F., Hermans, C., Pinardi, G., Spurr, R., Wang, P., and Mazière, M. D.: Multiple wavelength retrieval of tropospheric aerosol optical properties from MAXDOAS measurements in Beijing, *Atmospheric Measurement Techniques*, 3, 863–878, 2010.

Cleveland, W. S., Graedel, T. E., Kleiner, B., and Warner, J. L.: Sunday and Workday Variations in Photochemical Air Pollutants in New Jersey and New York, *Science*, 186, 1037–1038, 1974.

CWFIS: Canadian Wildland Fire Information System, URL `http://cwfis.cfs.nrcan.gc.ca/en_CA/index`, 2011.

Davies, J.: Correlation Spectroscopy, *Analytical Chemistry*, 42, 101A–112A, 1970.

Dentener, F. J. and Crutzen, P. J.: Reaction of N_2O_5 on Tropospheric Aerosols: Impact on the Global Distributions of NO_x, O_3, and OH, *Journal of Geophysical Research*, 98, 7149–7163, 1993.

Deutschmann, T., Beirle, S., Frieß, U., Grzegorski, M., Kern, C., Kritten, L., Platt, U., Prados-Román, C., Puķīte, J., Wagner, T., Werner, B., and Pfeilsticker, K.:

The Monte carlo Atmospheric radiative transfer model McArtim: Introduction and validation of Jacobians and 3D features, *Journal of Quantitative Spectroscopy and Radiative Transfer*, 112, 1119–1137, 2011.

Dodge, M. C.: Combined use of modeling techniques and smog chamber data to derive ozone-precursor relationships, in: *International Conference on Photochemical Oxidant Pollution and its Control: Proceedings, Vol. II.*, 881-889, B. Dimitriades, ed. EPA/600/3-77-001b. U.S., 1977.

Draxler, R. R. and Rolph, G. D.: HYbrid Single-Particle Lagrangian Integrated Trajectory Model, URL `http://ready.arl.noaa.gov/HYSPLIT.php`, 2011.

Dubovik, O. and King, M. D.: A flexible inversion algorithm for retrieval of aerosol optical properties from Sun and sky radiance measurements, *Journal of Geophysical Research-Atmospheres*, 105, 20 673–20 696, 2000.

Dubovik, O., Holben, B., Eck, T. F., Smirnov, A., Kaufman, Y. J., King, M. D., Tanré, D., and Slutsker, I.: Variability of Absorption and Optical Properties of Key Aerosol Types Observed in Worldwide Locations, *Journal of the Atmospheric Sciences*, 59, 590–608, 2002.

EC: Environment Canada, National Pollutant Release Inventory, URL `http://www.ec.gc.ca/inrp-npri/default.asp?lang=Enn=4A577BB9-1`, 2011.

EC: Environment Canada, National Climate Data and Information Archive, URL `http://climate.weatheroffice.gc.ca/Welcome_e.html`, 2012.

Edner, H., Sunesson, A., Svanberg, S., Uneus, L., and Wallin, S.: Atmospheric NH_3 monitoring by long-path UV absorption spectroscopy, in: *Proceedings of International Congress on Optical Science and Engineering. Environment and Pollution Measurement Sensors and Systems*, 1990.

Engel-Cox, J. A., Holloman, C. H., Coutant, B. W., and Hoff, R. M.: Qualitative and quantitative evaluation of MODIS satellite sensor data for regional and urban scale air quality, *Atmospheric Environment*, 38, 2495–2509, 2004.

Engel-Cox, J. A., Hoff, R. M., Rogers, R., Dimmick, F., Rush, A. C., Szykman, J. J., Al-Saadi, J., Chu, D. A., and Zell, E. R.: Integrating lidar and satellite optical depth with ambient monitoring for 3-dimensional particulate characterization, *Atmospheric Environment*, 40, 8056–8067, 2006.

Fayt, C. and van Roozendael, M.: WinDOAS 2.1 - 2001, URL `http://bro.aeronomie.be/WinDOAS-SUM-210b.pdf`, 2011.

Finlayson-Pitts, B., Wingen, L., Sumner, A., Syomin, D., and Ramazan, K.: The heterogeneous hydrolysis of NO_2 in laboratory systems and in outdoor and indoor atmospheres: An integrated mechanism, *Physical Chemistry Chemical Physics*, 5, 223–242, 2003.

Finlayson-Pitts, B. J. and Pitts, J. N.: *Chemistry of the Upper and Lower Atmosphere*, Academic Press, San Diego, 1999.

Frieß, U., Monks, P. S., Remedios, J. J., Rozanov, A., Sinreich, R., Wagner, T., and Platt, U.: MAX-DOAS O_4 measurements: A new technique to derive information on atmospheric aerosols: 2. Modeling studies, *Journal of Geophysical Research-Atmospheres*, 111, D14 203, 2006.

Geyer, A., Alicke, B., Konrad, S., Schmitz, T., Stutz, J., and Platt, U.: Chemistry and oxidation capacity of the nitrate radical in the continental boundary layer near Berlin, *Journal of Geophysical Research*, 106, 8013–8025, 2001.

Götz, F., Dobson, G., and Meetham, A.: Vertical distribution of ozone in the atmosphere, *Nature*, 132, 281–281, 1933.

Grainger, J. F. and Ring, J.: Anomalous Fraunhofer Line Profiles, *Nature*, 193, 762, 1962.

Greenblatt, G. D., Orlando, J. J., Burkholder, J. B., and Ravishankara, A. R.: Absorption Measurements of Oxygen Between 330 nm and 1140 nm, *Journal of Geophysical Research-Atmospheres*, 95, 18 577–18 582, 1990.

Gupta, P. and Christopher, S. A.: Seven year particulate matter air quality assessment from surface and satellite measurements, *Atmospheric Chemistry and Physics*, 8, 3311–3324, 2008.

Halla, J. D., Wagner, T., Beirle, S., Brook, J. R., Hayden, K. L., O'Brien, J. M., Ng, A., Majonis, D., Wenig, M. O., and McLaren, R.: Determination of tropospheric vertical columns of NO_2 and aerosol optical properties in a rural setting using MAX-DOAS, *Atmospheric Chemistry and Physics*, 11, 12 475–12 498, 2011.

Harder, J. W. and Brault, J. W.: Atmospheric measurements of water vapor in the 442 nm region, *Journal of Geophysical Research-Atmospheres*, 102, 6245–6252, 1997.

Harris, G. W., Carter, W. P. L., Winer, A. M., Pitts, J. N., Platt, U., and Perner, D.: Observations of nitrous acid in the Los Angeles atmosphere and implications for predictions of ozone-precursor relationships, *Environmental Science & Technology*, 16, 414–419, 1982.

Harrison, R. and Kitto, A.: Evidence for a Surface Source of Atmospheric Nitrous Acid, *Atmospheric Environment*, 28, 1089–1094, 1994.

Harrison, R., Peak, J., and Collins, G.: Tropospheric cycle of nitrous acid, *Journal of Geophysical Research-Atmospheres*, 101, 14 429–14 439, 1996.

Hastie, D. R., Narayan, J., Schiller, C., Niki, H., Shepson, P. B., Sills, D. M. L., Taylor, P. A., Moroz, W. J., Drummond, J. W., Reid, N., Taylor, R., Roussel, P. B., and Melo, O. T.: Observational evidence for the impact of the lake breeze circulation on ozone concentrations in Southern Ontario, *Atmospheric Environment*, 33, 323–335, 1999.

Hausmann, M. and Platt, U.: Spectroscopic measurement of bromine oxide and ozone in the high Arctic during Polar Sunrise Experiment 1992, *Journal of Geophysical Research*, 99, 25 399–25 413, 1994.

Hayden, K., Anlauf, K., Hoff, R., Strapp, J., Bottenheim, J., Wiebe, H., Froude, F., Martin, J., Steyn, D., and McKendry, I.: The vertical chemical and meteorological structure of the boundary layer in the Lower Fraser Valley during Pacific '93, *Atmospheric Environment*, 31, 2089–2105, 1997.

Hayden, K. L., Sills, D. M. L., Brook, J. R., Li, S.-M., Makar, P. A., Markovic, M. Z., Liu, P., Anlauf, K. G., O'Brien, J. M., Li, Q., and McLaren, R.: Aircraft study of the impact of lake-breeze circulations on trace gases and particles during BAQS-Met 2007, *Atmospheric Chemistry and Physics*, 11, 10 173–10 192, 2011.

Heckel, A., Richter, A., Tarsu, T., Wittrock, F., Hak, C., Pundt, I., Junkermann, W., and Burrows, J. P.: MAX-DOAS measurements of formaldehyde in the Po-Valley, *Atmospheric Chemistry and Physics*, 5, 909–918, 2005.

Heicklen, J., Westberg, K., and Cohen, N.: *Center for Air Environmental Studies Report No. 115-69*, Technical report, 1969.

Heland, J., Schlager, H., Richter, A., and Burrows, J. P.: First comparison of tropospheric NO_2 column densities retrieved from GOME measurements and in situ aircraft profile measurements, *Geophysical Research Letters*, 29, 44–1–44–4, 2002.

Hendrick, F., van Roozendael, M., Kylling, A., Petritoli, A., Rozanov, A., Sanghavi, S., Schofield, R., von Friedeburg, C., Wagner, T., Wittrock, F., Fonteyn, D., and Mazièrere, M. D.: Intercomparison exercise between different radiative transfer models used for the interpretation of ground-based zenith-sky and multi-axis DOAS observations, *Atmospheric Chemistry and Physics*, 6, 93–108, 2006.

Henyey, L. and Greenstein, J.: Diffuse radiation in the Galaxy, *Astrophysical Journal*, 93, 70–83, 1941.

Hoff, R. M.: Differential SO_2 column measurements of the Mt. Pinatubo volcanic plume, *Geophysical Research Letters*, 19, 175–178, 1992.

Holben, B. N., Eck, T. F., Slutsker, I., Tanré, D., Buis, J. P., Setzer, A., Vermote, E., Reagan, J. A., Kaufman, Y. J., Nakajima, T., Lavenu, F., Jankowiak, I., and Smirnov, A.: AERONET - A federated instrument network and data archive for aerosol characterization, *Remote Sensing of Environment*, 66, 1–16, 1998.

Holben, B. N., Tanré, D., Smirnov, A., Eck, T. F., Slutsker, I., Abuhassan, N., Newcomb, W. W., Schafer, J. S., Chatenet, B., Lavenu, F., Kaufman, Y. J., Castle, J. V., Setzer, A., Markham, B., Clark, D., Frouin, R., Halthore, R., Karneli, A., O'Neill, N. T., Pietras, C., Pinker, R. T., Voss, K., and Zibordi, G.: An emerging ground-based aerosol climatology: Aerosol optical depth from AERONET, *Journal of Geophysical Research-Atmospheres*, 106, 12 067–12 097, 2001.

Hönninger, G. and Platt, U.: Observations of BrO and its vertical distribution during surface ozone depletion at Alert, *Atmospheric Environment*, 36, 2481–2489, 2002.

Hönninger, G., von Friedeburg, C., and Platt, U.: Multi axis differential optical absorption spectroscopy (MAX-DOAS), *Atmospheric Chemistry and Physics*, 4, 231–254, 2004.

Irie, H., Kanaya, Y., Akimoto, H., Iwabuchi, H., Shimizu, A., and Aoki, K.: First retrieval of tropospheric aerosol profiles using MAX-DOAS and comparison with lidar and sky radiometer measurements, *Atmospheric Chemistry and Physics*, 8, 341–350, 2008.

Irie, H., Kanaya, Y., Akimoto, H., Iwabuchi, H., Shimizu, A., and Aoki, K.: Dual-wavelength aerosol vertical profile measurements by MAX-DOAS at Tsukuba, Japan, *Atmospheric Chemistry and Physics*, 9, 2741–2749, 2009.

Jacob, D. J.: *Introduction to Atmospheric Chemistry*, Princeton University Press, Princeton, NJ, 1999.

Jiang, W., Singleton, D. L., Hedley, M., and McLaren, R.: Sensitivity of ozone concentrations to VOC and NO_x emissions in the Canadian Lower Fraser Valley, *Atmospheric Environment*, 31, 627–638, 1997.

Johnston, P.: *Making UV/Vis Cross Sections, Reference Fraunhofer and Synthetic Spectra*, unpublished manuscript, 1996.

Kacenelenbogen, M., Leon, J. F., Chiapello, I., and Tanré, D.: Characterization of aerosol pollution events in France using ground-based and POLDER-2 satellite data, *Atmospheric Chemistry and Physics*, 6, 4843–4849, 2006.

Kleffmann, J., Kurtenbach, R., Lorzer, J., Wiesen, P., Kalthoff, N., Vogel, B., and Vogel, H.: Measured and simulated vertical profiles of nitrous acid - Part I: Field measurements, *Atmospheric Environment*, 37, 2949–2955, 2003.

Koelemeijer, R. B. A., Homan, C. D., and Matthijsen, J.: Comparison of spatial and temporal variations of aerosol optical thickness and particulate matter over Europe, *Atmospheric Environment*, 40, 5304–5315, 2006.

Kraus, S.: *DOASIS, A Framework Design for DOAS*, Ph.D. thesis, Universität Heidelberg, 2006.

Kreher, K., Fiedler, M., Gomer, T., Stutz, J., and Platt, U.: The Latitudinal Distribution (50-Degrees-N-50-Degrees-S) of NO_2 and O_3 in October November 1990, *Geophysical Research Letters*, 22, 1217–1220, 1995.

Kurtenbach, R., Becker, K., Gomes, J., Kleffmann, J., Lorzer, J., Spittler, M., Wiesen, P., Ackermann, R., Geyer, A., and Platt, U.: Investigations of emissions and heterogeneous formation of HONO in a road traffic tunnel, *Atmospheric Environment*, 35, 3385–3394, 2001.

Kurucz, R. L., Furenlid, I. J., and Testerman, L.: *Solar Flux Atlas from 296 to 1300 nm, National Solar Observatory*, Technical report, 1984.

Ladstätter-Weißenmayer, A., Heland, J., Kormann, R., von Kuhlmann, R., Lawrence, M. G., Meyer-Arnek, J., Richter, A., Wittrock, F., Ziereis, H., and Burrows, J. P.: Transport and build-up of tropospheric trace gases during the MINOS campaign: comparision of GOME, in situ aircraft measurements and MATCH-MPIC-data, *Atmospheric Chemistry and Physics*, 3, 1887–1902, 2003.

Lammel, G.: *Formation of nitrous acid: parameterisation and comparison with observations*, Technical report 286, Max-Planck-Insitut für Meteorologie, 1999.

Lebron, F.: A comparison of weekend-weekday ozone and hydrocarbon concentrations in the Baltimore-Washington metropolitan area, *Atmospheric Environment*, 9, 861–863, 1975.

Lee, H., Irie, H., Kim, Y. J., Noh, Y., Lee, C., Kim, Y., and Chun, K. J.: Retrieval of Aerosol Extinction in the Lower Troposphere Based on UV MAX-DOAS Measurements, *Aerosol Science and Technology*, 43, 502–509, 2009.

Leighton, P. A.: *Photochemistry of Air Pollution*, Academic Press, New York, 1961.

Levelt, P. F., den Oord, G. H. J. V., Dobber, M. R., Malkki, A., Visser, H., de Vries, J., Stammes, P., Lundell, J. O. V., and Saari, H.: The Ozone Monitoring Instrument, *IEEE Transactions on Geoscience and Remote Sensing*, 44, 1093–1101, 2006.

Levenberg, K.: A method for the solution of certain non-linear problems in least squares, *Quarterly of Applied Mathematics*, 2, 164–168, 1944.

Levy, R. C., Remer, L. A., and Dubovik, O.: Global aerosol optical properties and application to Moderate Resolution Imaging Spectroradiometer aerosol retrieval over land, *Journal of Geophysical Research-Atmospheres*, 112, D13 210, 2007.

Li, S.-M.: A concerted effort to understand the ambient particulate matter in the Lower Fraser Valley: the Pacific 2001 Air Quality Study, *Atmospheric Environment*, 38, 5719–5731, 2004.

Li, X., Brauers, T., Shao, M., Garland, R. M., Wagner, T., Deutschmann, T., and Wahner, A.: MAX-DOAS measurements in southern China: retrieval of aerosol extinctions and validation using ground-based in-situ data, *Atmospheric Chemistry and Physics*, 10, 2079–2089, 2010.

Lippmann, M.: Health Effects of Ozone A Critical Review, *Journal of the Air Pollution Control Association*, 39, 672–695, 1989.

Lyons, W. A. and Cole, H. S.: Fumigation and Plume Trapping on the Shores of Lake Michigan During Stable Onshore Flow, *Journal of Applied Meteorology*, 12, 494–510, 1973.

Macfarlane, M. L. S., Campbell, M., and Basrur, S. V.: *Toronto Public Health Report - Toronto's Air: Let's Make it Healthy*, Technical report, 2000.

Makar, P. A., Moran, M. D., Zheng, Q., Cousineau, S., Sassi, M., Duhamel, A., Besner, M., Davignon, D., Crevier, L. P., and Bouchet, V. S.: Modelling the impacts of ammonia emissions reductions on North American air quality, *Atmospheric Chemistry and Physics*, 9, 7183–7212, 2009.

Makar, P. A., Gong, W., Mooney, C., Zhang, J., Davignon, D., Samaali, M., Moran, M. D., He, H., Tarasick, D. W., Sills, D., and Chen, J.: Dynamic adjustment of climatological ozone boundary conditions for air-quality forecasts, *Atmospheric Chemistry and Physics*, 10, 8997–9015, 2010a.

Makar, P. A., Zhang, J., Gong, W., Stroud, C., Sills, D., Hayden, K. L., Brook, J., Levy, I., Mihele, C., Moran, M. D., Tarasick, D. W., He, H., and Plummer, D.: Mass tracking for chemical analysis: the causes of ozone formation in southern Ontario during BAQS-Met 2007, *Atmospheric Chemistry and Physics*, 10, 11 151–11 173, 2010b.

Martin, R. V., Fiore, A. M., and van Donkelaar, A.: Space-based diagnosis of surface ozone sensitivity to anthropogenic emissions, *Geophysical Research Letters*, 31, L06 120, 2004.

McGuire, M. L., Jeong, C. H., Slowik, J. G., Chang, R. Y. W., Corbin, J. C., Lu, G., Mihele, C., Rehbein, P. J. G., Sills, D. M. L., Abbatt, J. P. D., Brook, J. R., and Evans, G. J.: Elucidating determinants of aerosol composition through particle-type-based receptor modeling, *Atmospheric Chemistry and Physics*, 11, 8133–8155, 2011.

McGwin, Jr., G., Lienert, J., and Jr., J. I. K.: Formaldehyde Exposure and Asthma in Children: A Systematic Review, *Environmental Health Perspectives*, 118, 313–317, 2010.

McLaren, R., Wojtal, P., Majonis, D., McCourt, J., Halla, J. D., and Brook, J.: NO_3 radical measurements in a polluted marine environment: links to ozone formation, *Atmospheric Chemistry and Physics*, 10, 4187–4206, 2010.

Meena, G. S.: *Study of Atmospheric Constituents by Visible Spectroscopy*, Ph.D. thesis, Indian Institute of Tropical Meteorology, 2005.

Meller, R. and Moortgat, G. K.: Temperature dependence of the absorption cross sections of formaldehyde between 223 and 323 K in the wavelength range 225-375 nm, *Journal of Geophysical Research-Atmospheres*, 105, 7089–7101, 2000.

Mentel, T., Bleilebens, D., and Wahner, A.: A study of nighttime nitrogen oxide oxidation in a large reaction chamber - the fate of NO_2, N_2O_5, HNO_3, and O_3 at different humidities, *Atmospheric Environment*, 30, 4007–4020, 1996.

Mielke, L. H., Furgeson, A., and Osthoff, H. D.: Observation of $ClNO_2$ in a Mid-Continental Urban Environment, *Environmental Science & Technology*, 45, 8889–8896, 2011.

MOE: Ministry of the Environment, Ontario (MOE): Air Quality in Ontario 2005 Report and Appendix, URL http://www.ene.gov.on.ca/environment/en/resources/STD01076445.html, 2011.

Mueller, J. F. and Stavrakou, T.: Inversion of CO and NO_x emissions using the adjoint of the IMAGES model, *Atmospheric Chemistry and Physics*, 5, 1157–1186, 2005.

NASA: NASA Goddard Space Flight Center LAADS Web - Level 1 and Atmosphere Archive and Distribution System, URL http://ladsweb.nascom.nasa.gov/, 2010a.

NASA: NASA Goddard Space Flight Center Aura Validation Data Center, URL http://avdc.gsfc.nasa.gov/, 2010b.

NASA: NASA Goddard Space Flight Center AERONET - Aerosol Robotic Network, URL http://aeronet.gsfc.nasa.gov/, 2010c.

Noël, S., Bovensmann, H., Burrows, J. P., Frerick, J., Chance, K. V., and Goede, A. H. P.: Global Atmospheric Monitoring with SCIAMACHY, *Physics and Chemistry of the Earth, Part C: Solar, Terrestrial Planetary Science*, 24, 427–434, 1999.

Noxon, J., Norton, R., and Marovich, E.: NO_3 in the Troposphere, *Geophysical Research Letters*, 7, 125–128, 1980.

Noxon, J. F.: Nitrogen-Dioxide in Stratosphere and Troposphere Measured by Ground-Based Absorption Spectroscopy, *Science*, 189, 547–549, 1975.

Noxon, J. F., J., E. C. W., and Hyde, R. S.: Stratospheric NO_2 1. Observational Method and Behavior at Mid-Latitude, *Journal of Geophysical Research*, 84, 5047–5065, 1979.

Pelletier, B., Santer, R., and Vidot, J.: Retrieving of particulate matter from optical measurements: A semiparametric approach, *Journal of Geophysical Research-Atmospheres*, 112, D06 208, 2007.

Perliski, L. M. and Solomon, S.: On the Evaluation of Air Mass Factors for Atmospheric Near-Ultraviolet and Visible Absorption Spectroscopy, *Journal of Geophysical Research-Atmospheres*, 98, 10 363–10 374, 1993.

Perner, D. and Platt, U.: Detection of Nitrous Acid in the Atmosphere by Differential Optical Absorption, *Geophysical Research Letters*, 6, 917–920, 1979.

Perner, D., Ehhalt, D. H., Pätz, H. W., Platt, U., Röth, E. P., and Volz, A.: OH - Radicals in the Lower Troposphere, *Geophysical Research Letters*, 3, 466–468, 1976.

Phillips, G. J., Tang, M. J., Thieser, J., Brickwedde, B., Schuster, G., Bohn, B., Lelieveld, J., and Crowley, J. N.: Significant concentrations of nitryl chloride observed in rural continental Europe associated with the influence of sea salt chloride and anthropogenic emissions, *Geophysical Research Letters*, 39, L10 811, 2012.

Plane, J. M. C. and Smith, N.: *Atmospheric Monitoring By Differential Optical Absorption Spectroscopy*, vol. 24 of *Spectroscopy in Environmental Science*, pp. 223–262, John Wiley & Sons, Inc., West Sussex, 1995.

Platt, U.: *Differential Optical Absorption Spectroscopy (DOAS)*, vol. 127 of *Air Monitoring by Spectroscopic Technique, Chemical Analysis Series*, pp. 27–84, John Wiley & Sons, Inc., Hoboken, 1994.

Platt, U. and Perner, D.: Direct Measurements of Atmospheric CH_2O, HNO_2, O_3, NO_2, and SO_2 by Differential Optical Absorption in the Near UV, *Journal of Geophysical Research*, 85, 7453–7458, 1980.

Platt, U. and Stutz, J.: *Differential Optical Absorption Spectroscopy: Principles and Applications*, Springer, Berlin, 2008.

Platt, U., Perner, D., and Pätz, H. W.: Simultaneous Measurement of Atmospheric CH_2O, O_3, and NO_2 by Differential Optical Absorption, *Journal of Geophysical Research-Oceans and Atmospheres*, 84, 6329–6335, 1979.

Platt, U., Perner, D., Harris, G., Winer, A. M., and Pitts, J. N.: Observations of Nitrous Acid in an Urban Atmosphere by Differential Optical Absorption, *Nature*, 285, 312–314, 1980a.

Platt, U., Perner, D., Winer, A. M., Harris, G. W., and Jr., J. N. P.: Detection of NO_3 in the polluted troposphere by differential optical absorption, *Geophysical Research Letters*, 7, 89–92, 1980b.

Ravishankara, A. R., Daniel, J. S., and Portmann, R. W.: Nitrous Oxide (N_2O): The Dominant Ozone-Depleting Substance Emitted in the 21st Century, *Science*, 326, 123–125, 2009.

Reid, N. W., Niki, H., Hastie, D., Shepson, P., Roussel, P., Melo, O., Mackay, G., Drummond, J., Schiff, H., Poissant, L., and Moroz, W.: The southern Ontario oxidant study (SONTOS): Overview and case studies for 1992, *Atmospheric Environment*, 30, 2125–2132, 1996.

Riedel, T. P., Bertram, T. H., Crisp, T. A., Williams, E. J., Lerner, B. M., Vlasenko, A., Li, S.-M., Gilman, J., de Gouw, J., Bon, D. M., Wagner, N. L., Brown, S. S., and Thornton, J. A.: Nitryl Chloride and Molecular Chlorine in the Coastal Marine Boundary Layer, *Environmental Science & Technology*, 46, 10 463–10 470, 2012.

Rozanov, A., Rozanov, V., and Burrows, J. P.: A numerical radiative transfer model for a spherical planetary atmosphere: combined differential-integral approach involving the Picard iterative approximation, *Journal of Quantitative Spectroscopy and Radiative Transfer*, 69, 491–512, 2001.

Sanders, R. W., Solomon, S., Carroll, M. A., and Schmeltekopf, A. L.: Ground based measurements of O_3, NO_2, OClO and BrO during the Antarctic Ozone Depletion Event, in: *Ozone in the Atmosphere, Quadrennial Ozone Symposium 1988*, edited by Bjokov, R. D. and Fabian, P., pp. 65–70, Deepak Publishing, Hampton, 1988.

Sanders, R. W., Solomon, S., Smith, J. P., Perliski, L., Miller, H. L., Mount, G. H., Keys, J. G., and Schmeltekopf, A. L.: Visible and Near-Ultraviolet Spectroscopy at McMurdo Station, Antarctica 9. Observations of OClO from April to October 1991, *Journal of Geophysical Research*, 98, 7219–7228, 1993.

Schaap, M., Apituley, A., Timmermans, R. M. A., Koelemeijer, R. B. A., and de Leeuw, G.: Exploring the relation between aerosol optical depth and $PM_{2.5}$ at Cabauw, the Netherlands, *Atmospheric Chemistry and Physics*, 9, 909–925, 2009.

Senne, T., Stutz, J., and Platt, U.: Measurement of the latitudinal distribution of NO_2 column density and layer height in Oct Nov 1993, *Geophysical Research Letters*, 23, 805–808, 1996.

Sillman, S.: The relation between ozone, NO_x and hydrocarbons in urban and polluted rural environments, *Atmospheric Environment*, 33, 1821–1845, 1999.

Sills, D. M. L., Brook, J. R., Levy, I., Makar, P. A., Zhang, J., and Taylor, P. A.: Lake breezes in the southern Great Lakes region and their influence during BAQS-Met 2007, *Atmospheric Chemistry and Physics*, 11, 7955–7973, 2011.

Sinreich, R., Frieß, U., Wagner, T., and Platt, U.: Multi axis differential optical absorption spectroscopy (MAX-DOAS) of gas and aerosol distributions, *Faraday Discussions*, 130, 153–164, 2005.

Sinreich, R., Volkamer, R., Filsinger, F., Frieß, U., Kern, C., Platt, U., Sebastián, O., and Wagner, T.: MAX-DOAS detection of glyoxal during ICARTT 2004, *Atmospheric Chemistry and Physics*, 7, 1293–1303, 2007.

Smith, J. and Solomon, S.: Atmospheric NO_3 3. Sunrise Disappearance and the Stratospheric Profile, *Journal of Geophysical Research-Atmospheres*, 95, 13 819–13 827, 1990.

Snyder, B. and Strawbridge, K.: Meteorological analysis of the Pacific 2001 air quality field study, *Atmospheric Environment*, 38, 5733–5743, 2004.

Solomon, S., Schmeltekopf, A. L., and Sanders, R. W.: On the Interpretation of Zenith Sky Absorption Measurements, *Journal of Geophysical Research*, 92, 8311–8319, 1987.

Solomon, S., Sanders, R. W., Carroll, M. A., and Schmeltekopf, A. L.: Visible and Near-Ultraviolet Spectroscopy at McMurdo Station, Antarctica 5. Observations of the Diurnal Variations of BrO and OClO, *Journal of Geophysical Research*, 94, 11 393–11 403, 1989.

Solomon, S., Sanders, R. W., Garcia, R. R., and Keys, J. G.: Increased chlorine dioxide over Antarctica caused by volcanic aerosols from Mount Pinatubo, *Nature*, 363, 245–248, 1993.

Steinbacher, M., Zellweger, C., Schwarzenbach, B., Bugmann, S., Buchmann, B., Ordóñez, C., Prevot, A. S. H., and Hueglin, C.: Nitrogen oxide measurements at rural sites in Switzerland: Bias of conventional measurement techniques, *Journal of Geophysical Research*, 112, D11 307, 2007.

Steyn, D., Bottenheim, J., and Thomson, R.: Overview of tropospheric ozone in the Lower Fraser Valley, and the Pacific '93 field study, *Atmospheric Environment*, 31, 2025–2035, 1997.

Stoiber, R. and Jepsen, A.: Sulfur-Dioxide Contributions to Atmosphere by Volcanos, *Science*, 182, 577–578, 1973.

Strawbridge, K. B. and Snyder, B. J.: Planetary boundary layer height determination during Pacific 2001 using the advantage of a scanning lidar instrument, *Atmospheric Environment*, 38, 5861–5871, 2004.

Stutz, J.: *Charakterisierung von Photodiodenzeilen zur Messung stratosphärischer Spurenstoffe*, Diplom thesis, University of Heidelberg, 1991.

Stutz, J. and Platt, U.: Improving long-path differential optical absorption spectroscopy with a quartz-fiber mode mixer, *Applied Optics*, 36, 1105–1115, 1997.

Stutz, J., Alicke, B., and Neftel, A.: Nitrous acid formation in the urban atmosphere: Gradient measurements of NO_2 and HONO over grass in Milan, Italy, *Journal of Geophysical Research-Atmospheres*, 107, LOP 5–1 – LOP 5–15, 2002.

Torres, O., Bhartia, P. K., Herman, J. R., Ahmad, Z., and Gleason, J.: Derivation of aerosol properties from satellite measurements of backscattered ultraviolet radiation: Theoretical basis, *Journal of Geophysical Research*, 103, 17 099–17 110, 1998.

Tschritter, J.: *Entwicklung einer DOAS-Optik der 3. Generation und ein Vergleich mit herkömmlichen Systemen*, Diplom thesis, 2007.

Tuckermann, M., Ackermann, R., Gölz, C., Lorenzen-Schmidt, H., Senne, T., Stutz, J., Trost, B., Unold, W., and Platt, U.: DOAS observation of halogen radical-catalysed arctic boundary layer ozone destruction during the ARCTOC-campaigns 1995 and 1996 in Ny-Ålesund, Spitsbergen, *Tellus B*, 49, 533–555, 1997.

UWYO: University of Wyoming (UWYO), College of Engineering, Department of Atmospheric Science Atmospheric Soundings, URL `http://weather.uwyo.edu/upperair/sounding.html`, 2010.

Vandaele, A. C., Hermans, C., Simon, P. C., Carleer, M., Colin, R., Fally, S., Merienne, M. F., Jenouvrier, A., and Coquart, B.: Measurements of the NO_2 absorption cross-section from 42 000 cm^{-1} to 10 000 cm^{-1} (238-1000 nm) at 220 K and 294 K, *Journal of Quantitative Spectroscopy & Radiative Transfer*, 59, 171–184, 1998.

Vogel, L., Sihler, H., Lampel, J., Wagner, T., and Platt, U.: Retrieval interval mapping: a tool to visualize the impact of the spectral retrieval range on differential optical absorption spectroscopy evaluations, *Atmospheric Measurement Techniques*, 6, 275–299, 2013.

Voigt, S., Orphal, J., and Burrows, J.: The temperature and pressure dependence of the absorption cross-sections of NO_2 in the 250-800 nm region measured by Fourier-transform spectroscopy, *Journal of Photochemistry and Photobiology A: Chemistry*, 149, 1–7, 2002.

Volkamer, R., Molina, L. T., Molina, M. J., Shirley, T., and Brune, W. H.: DOAS measurement of glyoxal as an indicator for fast VOC chemistry in urban air, *Geophysical Research Letters*, 32, L08 806, 2005.

Volz, A. and Kley, D.: Evaluation of the Montsouris Series of Ozone Measurements made in the 19th Century, *Nature*, 332, 240–242, 1988.

von Friedeburg, C.: *Derivation of Trace Gas Information combining Differential Optical Absorption Spectroscopy with Radiative Transfer Modelling*, Ph.D. thesis, Institut für Umweltphysik, Universität Heidelberg, 2003.

von Friedeburg, C., Pundt, I., Mettendorf, K. U., Wagner, T., and Platt, U.: Multi-axis-DOAS measurements of NO_2 during the BAB II motorway emission campaign, *Atmospheric Environment*, 39, 977–985, 2005.

Wagner, T., von Friedeburg, C., Wenig, M., Otten, C., and Platt, U.: UV-visible observations of atmospheric O_4 absorptions using direct moonlight and zenith-scattered sunlight for clear-sky and cloudy sky conditions, *Journal of Geophysical Research-Atmospheres*, 107, 4424, 2002.

Wagner, T., Dix, B., von Friedeburg, C., Frieß, U., Sanghavi, S., Sinreich, R., and Platt, U.: MAX-DOAS O_4 measurements: A new technique to derive information on atmospheric aerosols - Principles and information content, *Journal of Geophysical Research-Atmospheres*, 109, D22 205, 2004.

Wagner, T., Burrows, J. P., Deutschmann, T., Dix, B., von Friedeburg, C., Frieß, U., Hendrick, F., Heue, K. P., Irie, H., Iwabuchi, H., Kanaya, Y., Keller, J., McLinden, C. A., Oetjen, H., Palazzi, E., Petritoli, A., Platt, U., Postylyakov, O., Pukite, J., Richter, A., van Roozendael, M., Rozanov, A., Rozanov, V., Sinreich, R., Sanghavi, S., and Wittrock, F.: Comparison of box-air-mass-factors and radiances for Multiple-Axis Differential Optical Absorption Spectroscopy (MAX-DOAS) geometries calculated from different UV/visible radiative transfer models, *Atmospheric Chemistry and Physics*, 7, 1809–1833, 2007.

Wagner, T., Deutschmann, T., and Platt, U.: Determination of aerosol properties from MAX-DOAS observations of the Ring effect, *Atmospheric Measurement Techniques*, 2, 495–512, 2009.

Wagner, T., Beirle, S., Brauers, T., Deutschmann, T., Frieß, U., Hak, C., Halla, J. D., Heue, K. P., Junkermann, W., Li, X., Platt, U., and Pundt-Gruber, I.: Inversion of tropospheric profiles of aerosol extinction and HCHO and NO_2 mixing ratios from MAX-DOAS observations in Milano during the summer of 2003 and

comparison with independent data sets, *Atmospheric Measurement Techniques*, 4, 2685–2715, 2011.

Wang, J. and Christopher, S. A.: Intercomparison between satellite-derived aerosol optical thickness and $PM_{2.5}$ mass: Implications for air quality studies, *Geophysical Research Letters*, 30, 2095, 2003.

Wang, S., Ackermann, R., and Stutz, J.: Vertical profiles of O_3 and NO_x chemistry in the polluted nocturnal boundary layer in Phoenix, AZ: I. Field observations by long-path DOAS, *Atmospheric Chemistry and Physics*, 6, 2671–2693, 2006.

Weaver, A., Solomon, S., Sanders, R., Arpag, K., and Miller, H.: Atmospheric NO_3 5. Off-axis measurements at sunrise: Estimates of tropospheric NO_3 at 40 degrees N, *Journal of Geophysical Research-Atmospheres*, 101, 18 605–18 612, 1996.

Weinstock, B.: Carbon Monoxide: Residence Time in the Atmosphere, *Science*, 166, 224–225, 1969.

Wenig, M. O., Cede, A. M., Bucsela, E. J., Celarier, E. A., Boersma, K. F., Veefkind, J. P., Brinksma, E. J., Gleason, J. F., and Herman, J. R.: Validation of OMI tropospheric NO_2 column densities using direct-Sun mode Brewer measurements at NASA Goddard Space Flight Center, *Journal of Geophysical Research-Atmospheres*, 113, D16S45, 2008.

Wilmouth, D. M., Hanisco, T. F., Donahue, N. M., and Anderson, J. G.: Fourier Transform Ultraviolet Spectroscopy of the A $^2\Pi_{3/2} \leftarrow$ X $^2\Pi_{3/2}$ Transition of BrO, *The Journal of Physical Chemistry A*, 103, 8935–8945, 1999.

Witschi, H.: *Essays in Toxicology, Vol. 6*, Academic Press, New York, 1975.

Wittrock, F., Müller, R., Richter, A., Bovensmann, H., and Burrows, J.: Measurements of iodine monoxide (IO) above Spitsbergen, *Geophysical Research Letters*, 27, 1471–1474, 2000.

Wittrock, F., Oetjen, H., Richter, A., Fietkau, S., Medeke, T., Rozanov, A., and Burrows, J. P.: MAX-DOAS measurements of atmospheric trace gases in Ny-Ålesund - Radiative transfer studies and their application, *Atmospheric Chemistry and Physics*, 4, 955–966, 2004.

Wojtal, P., Halla, J. D., and McLaren, R.: Pseudo steady states of HONO measured in the nocturnal marine boundary layer: a conceptual model for HONO formation on aqueous surfaces, *Atmospheric Chemistry and Physics*, 11, 3243–3261, 2011.

Zhou, X., Civerolo, K., Dai, H., Huang, G., Schwab, J., and Demerjian, K.: Summertime nitrous acid chemistry in the atmospheric boundary layer at a rural site in New York State, *Journal of Geophysical Research-Atmospheres*, 107, ACH 13–1 – ACH 13–11, 2002.

Zieger, P., Weingartner, E., Henzing, J., Moerman, M., de Leeuw, G., Mikkilä, J., Ehn, M., Petäjä, T., Clémer, K., van Roozendael, M., Yilmaz, S., Frieß, U., Irie, H., Wagner, T., Shaiganfar, R., Beirle, S., Apituley, A., Wilson, K., and Baltensperger, U.: Comparison of ambient aerosol extinction coefficients obtained from in-situ, MAX-DOAS and LIDAR measurements at Cabauw, *Atmospheric Chemistry and Physics*, 11, 2603–2624, 2011.